Tunnelling and its effects on piles and piled structures

Andrea Franza

Department of Civil Engineering
University of Nottingham

This dissertation is submitted for the degree of
Doctor of Philosophy

November 2016

Ai miei genitori

Declaration

I hereby declare that except where specific reference is made to the work of others, the contents of this dissertation are original and have not been submitted in whole or in part for consideration for any other degree or qualification in this, or any other university. This dissertation is my own work and contains nothing which is the outcome of work done in collaboration with others, except as specified in the text and Acknowledgements. This dissertation contains less than than the revised limit of 120,000 words including appendices, bibliography, tables and equations.

Andrea Franza
November 2016

List of Publications

Journal articles

Franza, A., Marshall, A. M., Haji, T., Abdelatif, A. O., Carbonari, S., Morici M. (2017). A simplified elastic analysis of tunnel-piled structure interaction. *Tunnelling and Underground Space Technology*, 61:104–121.

Marshall, A. M. and Franza, A. (2016). Discussion of "Observation of Ground Movement with Existing Pile Groups Due to Tunneling in Sand Using Centrifuge Modelling" by Ittichai Boonsiri and Jiro Takemura. *Geotechnical and Geological Engineering*, pages 1–5.

Conference papers

Franza, A., Haji, T., and Marshall, A. M. (2016a). A Winkler-based method for the assessment of tunnelling-induced deformations on piled structures. In Ni, J. C., Yang, J., Chen, S.-l., and Qiu, T., editors, *Proceedings of 4th Geo-China International Conference*, number 260 GSP, pages 259–266, Shandong, China. American Society of Civil Engineers (ASCE).

Franza, A., Idinyang, S., Heron, C., and Marshall, A. M. (2016b). Development of a coupled centrifuge-numerical model to study soil-structure interaction problems. In Thorel, L., Bretschneider, A., Blanc, M., and Escoffier, S., editors, *Proceedings of the 3rd European Conference on Physical Modelling in Geotechnics (Eurofuge 2016)*, pages 135–140, Nantes, France.

Franza, A. and Marshall, A. M. (2015a). Analytical investigation of soil deformation patterns above tunnels in sandy soil. In *Proceedings of the XVI ECSMGE Geotechnical Engineering for Infrastructure and Development*, volume 2, pages 467–472, Edinburgh, United Kingdom.

Franza, A. and Marshall, A. M. (2015b). Semi-analytical prediction of ground movements due to shallow tunnels in sand. In *Proceedings of the XVI ECSMGE Geotechnical Engineering for Infrastructure and Development*, volume 2, pages 461–466, Edinburgh, United Kingdom.

Franza, A. and Marshall, A. M. (2016). Centrifuge modelling of piled structure response to tunnelling. In Thorel, L., Bretschneider, A., Blanc, M., and Escoffier, S., editors, *Proceedings of the 3rd European Conference on Physical Modelling in Geotechnics (Eurofuge 2016)*, pages 313–318, Nantes, France.

Franza, A., Zhou, B., and Marshall, A. M. (2016c). The effects of relative tunnel depth and volume loss on vertical settlements above tunnels in dense sands. In Ni, J. C., Yang, J., Chen, S.-l., and Qiu, T., editors, *Proceedings of 4th Geo-China International Conference*, number 260 GSP, pages 125–132, Shandong, China. American Society of Civil Engineers (ASCE).

Acknowledgements

This research thesis was done under the supervision of Dr Alec Marshall. I would like to sincerely thank my supervisor for his continuous guidance and support during the PhD study; he has encouraged me to develop my ideas and guided me throughout the early stages as a researcher.

For financial support and funding of this research, I would like to thank the University of Nottingham and the Engineering and Physical Sciences Research Council (EPSRC).

I would like to acknowledge the fellow researchers at the Nottingham Centre for Geomechanics (NCG) that contributed with their work to this research. The development of the coupled centrifuge and numerical modelling technique was carried out in collaboration with a multidisciplinary team consisting of Amged Abdelatif, Charles Heron, Solomon Idinyang, and Alec Marshall. In addition, part of the results presented in Chapters 4, 5 and 6 was obtained by Twana Haji, Alec Marshall, and Bo Zhou.

I am grateful to a number of colleagues that I had the privilege of working alongside during my time at NCG; I would like to thank them for their professional help, suggestions, and friendship. In particular, it has been a precious opportunity to work with Itai Elkayam, Pinqiang Mo, Vasileios Matziaris, James Meakin, Craig Cox, Luke Bedford, and Maurizio Tomeo.

During my years in Nottingham, I met many special people and had enjoyable experiences that made this period of my life unforgettable. I would like to thank them for their encouragement, the good times we had and all the laughs we shared.

Finally, thanks to my family for their continued support and love throughout this challenging period of my life; without them, I would have not been be able to complete this research.

Abstract

Current needs for infrastructure and services in urban areas often require the construction of tunnels that may affect existing surface and buried structures. In general, the construction of new tunnels in the proximity of deep foundations raises concerns related to pile failure and associated structural damage (in both the superstructure and the foundation). Despite its practical importance, few studies have investigated the global tunnel-pile-structure interaction (TPSI) and, thus, engineers generally compensate for the lack of understanding with an overly conservative design approach.

To provide insights into the interaction mechanisms of TPSI, this research used geotechnical centrifuge testing as the main investigation method to acquire data related to both greenfield tunnelling in sands and tunnel excavations beneath piles and piled buildings. In particular, a novel method was developed to study TPSI problems through the real-time coupling of numerical and centrifuge modelling, enhancing centrifuge modelling capabilities. Furthermore, empirical and closed-form solutions were used to study the tunnelling-induced displacement fields and simplified elastic analyses were used to provide insights into the global TPSI mechanisms.

Results from the greenfield tests illustrate that ground movement prediction in sands is very complex because of soil arching effects and changes that occur as tunnels transition from relatively shallow to deep depths, resulting in highly non-linear displacement mechanisms. Results also illustrate the correlation between vertical and horizontal displacement mechanisms. In particular, the influence of soil relative density and volume loss on deformation patterns is highly dependent on the tunnel relative depth. To provide simple tools for engineering practice, empirical and closed-form solutions are proposed. Predicted ground movements provide sufficient accuracy for preliminary assessments, though limitations of these methods should be considered.

The centrifuge tests on TPSI provide experimental evidence that tunnelling-induced pile displacements are affected by [i] pile installation method (displacement versus non-displacement piles), which affects the pre-tunnelling soil state and the distribution of loads between pile shaft and base, [ii] initial safety factor of the pile foundation, which is related to pile bearing capacity and superstructure self-weight, and [iii] superstructure stiffness and configuration, which results in pile load redistribution while minimising structural distortions. In addition, results show that potential for pile failure is a critical aspect for piles with relatively low initial safety factors and that pile failure may be prevented by a limited relative reduction in the pile load due to the superstructure.

Finally, the importance of superstructure stiffness and self-weight on tunnelling-induced structural distortions is confirmed. Piled buildings respond critically to tunnelling beneath the pile tip depth in terms of flexural deformations. In general, it is shown that [iv] piles increase structural distortions compared to shallow foundations and that [v] the superstructure stiffness and self-weight decrease and increase the superstructure distortions resulting from tunnelling, respectively. Results are also evaluated within the modification factor approach; parametric analyses of elastic soil-pile-structure interaction are used to develop simple design charts that can be used to estimate horizontal strains and deflection ratio modification factors based on newly defined relative axial and bending stiffness parameters. The envelopes compare well with deflection ratio modification factors measured from centrifuge tests. Further research is needed to include the effects of soil plasticity, building self-weight, superstructure configuration and tunnel-structure eccentricity in these design charts. This dissertation highlights the improvements in the design of underground constructions that can be achieved by combining ground and structural engineering.

Keywords: tunnel, pile, soil-structure interaction, building response, centrifuge, sand.

Table of contents

List of figures

List of tables

Nomenclature

Roman Symbols

a	acceleration	$[\mathrm{m/s^2}]$
a	radius of void representing tunnel ground loss (Chapter 2)	$[\mathrm{m}]$
b	beam width	$[\mathrm{m}]$
c_u	undrained shear strength	$[\mathrm{N/m^2}]$
d	beam depth	$[\mathrm{m}]$
d_{50}	average grain size diameter	$[\mathrm{m}]$
d_p	pile diameter	$[\mathrm{m}]$
e	building eccentricity to tunnel centreline (Chapters 2, 6)	$[\mathrm{m}]$
e	void ratio	$[-]$
f	frequency	$[\mathrm{Hz}]$
g	gap parameter (Chapter 2)	$[\mathrm{m}]$
g	standard gravity	$[\mathrm{m/s^2}]$
h	storey height	$[\mathrm{m}]$
h_m	height of soil in centrifuge model	$[\mathrm{m}]$
i	horizontal offset from tunnel centreline to point of inflexion	$[\mathrm{m}]$
k	variable related to Poisson's ratio	$[-]$
k_x	stiffness for horizontal shaft springs (per unit-length of pile)	$[\mathrm{N/m^2}]$
k_z	stiffness for vertical shaft springs (per unit-length of pile)	$[\mathrm{N/m^2}]$
l	beam span	$[\mathrm{m}]$
m	elastic constant	$[-]$
n	shape parameter used in modified Gaussian curve	$[-]$
p	current pressure	$[\mathrm{N/m^2}]$
p_0	initial pressure	$[\mathrm{N/m^2}]$
p_0	volumetric total stress component (Chapter 2)	$[\mathrm{N/m^2}]$
p_{atm}	atmospheric pressure	$[\mathrm{N/m^2}]$
p_{min}	minimum pressure	$[\mathrm{N/m^2}]$
p_{ult}	pressure at ultimate state	$[\mathrm{N/m^2}]$

q_0	deviatoric total stress component	$[\mathrm{N/m^2}]$
q_b	pile average base resistance pressure	$[\mathrm{N/m^2}]$
r	radial distance	[m]
r_m	empirically distance for pile-pile interaction	[m]
r_p	pile radius	[m]
t	distance between the neutral axis and the edge of the beam in tension (Chapter 2)	[m]
t	model plate thickness	[m]
t	time (Chapter 3)	[s]
u_{max}	maximum settlement at tunnel centreline	[m]
u_x	horizontal displacements	[m]
u_x^p	pile head horizontal displacement	[m]
u_z	vertical displacements	[m]
u_z^p	pile head vertical displacement	[m]
v	incremental model pile settlement	[m]
x	horizontal offset from tunnel centreline	[m]
x^{**}	horizontal offset from centreline to point on fitted curve where $u_z = 0.303u_{max}$	[m]
x^*	horizontal offset from centreline to point on fitted curve where $u_z = 0.606u_{max}$	[m]
z	depth	[m]
z_t	depth to tunnel axis	[m]
A	cross-sectional area	$[\mathrm{m^2}]$
A^*	cross-sectional area per m run	$[\mathrm{m^2/m}]$
A_E	material constant	$[\mathrm{N/m^2}]$
A_p	area of the pile cross-section	$[\mathrm{m^2}]$
A_s	pile shaft surface area	$[\mathrm{m^2}]$
B	transverse building width	[m]
B	trapdoor width (Chapter 2)	[m]
C	column influence factor (Chapters 2, 6)	[–]
C	cover, measured from surface of soil to crown of tunnel	[m]
DR	Deflection ratio	[–]
D_t	outer tunnel diameter	[m]
E	Young's modulus of building/superstructure	$[\mathrm{N/m^2}]$
EA	axial stiffness	[N]
EI	bending stiffness	$[\mathrm{Nm^2}]$
E_s	Young's modulus of soil	$[\mathrm{N/m^2}]$
$E_{s,b}$	Young's modulus of soil below the pile base	$[\mathrm{N/m^2}]$
$F\,[e]$	function of void ratio, e, used to determine stiffness	[–]

F_p	tunnelling-induced vertical force on a rigid isolated pile	[N]
G	shear modulus of building/superstructure	[N/m^2]
G_s	shear modulus of soil	[N/m^2]
H	building height	[m]
H	depth to tunnel axis (Chapters 2, 5)	[m]
H	soil overburden depth (Chapter 2)	[m]
I	moment of inertia	[m^4]
I^*	moment of inertia per m run	[m^4/m]
I_d	relative density	[−]
K	earth pressure coefficient	[−]
K	trough width parameter (Chapters 2, 4, 5)	[−]
K_b	beam stiffness parameter	[m]
K_c	column stiffness parameter	[m]
K_{LC}	column stiffness parameter of lower column in frame	[m]
K_{UC}	column stiffness parameter of upper column in frame	[m]
K_p	vertical stiffness of a rigid isolated pile	[N/m]
$K^p_{s,b}$	stiffness of the vertical spring at pile base	[N/m]
K^*	trough width parameter based on x^*	[−]
K^{**}	trough width parameter based on x^{**}	[−]
L	building length in the longitudinal direction	[m]
L_{hog}	length of the hogging settlement zone	[m]
L_p	pile length	[m]
L_{sag}	length of the sagging settlement zone	[m]
M	modification factor	[−]
N	centrifuge acceleration scale	[−]
N, N^*	tunnel stability factor (Chapter 2)	[−]
P	pile vertical load	[N]
P'	demanded pile vertical load in coupled-centrifuge numerical model	[N]
ΔP	$= P - P_0$ superstructure reaction force	[N]
δP	$= P' - P$	[N]
Q	pile bearing capacity	[N]
Q_s	pile shaft frictional capacity	[N]
Q_{tip}	pile base capacity	[N]
R	tunnel radius	[m]
R_e	effective centrifuge radius	[m]
R_{max}	roughness of the pile shaft	[m]

R_n	normalised roughness	[−]
$R_{Q,S}$	pile capacity reduction factor	[−]
R^2	coefficient of determination	[−]
R_t	centrifuge radius to top of model soil	[m]
S	settlement	[m]
ΔS	differential settlement	[m]
SF	pile safety factor	[−]
S_l, S_{lg}	pile row spacing in the longitudinal direction	[m]
S_t	pile spacing in the transverse direction	[m]
U	model pile settlement	[m]
U^e	error in the LVDT measurement of the model pile settlement	[m]
U^r	real model pile settlement	[m]
V_0	cross-sectional area of tunnel	[m^2]
$V_{l,s}$	soil volume loss, expressed as percentage of tunnel cross-sectional area	[%]
$V_{l,t}$	tunnel volume loss, expressed as percentage of tunnel cross-sectional area	[%]
V_s	soil ground loss per unit length of tunnel	[m^2]
ΔV	tunnel ground loss per unit length of tunnel	[m^2]
$\mathbf{f}_p$	external force vector	
$\mathbf{s}$	displacement vector of greenfield ground movements	
$\mathbf{u}_p$	displacement vector of the pile foundation	
$\mathbf{A}$	soil flexibility matrix	
$\mathbf{C}$	soil stiffness matrix	
$\mathbf{K}_p$	stiffness matrix of the pile group	
$\mathbf{K}_s$	condensed stiffness matrix of the structure	

Greek Symbols

α	compressibility parameter (Chapters 2, 5)	[−]
α	shape parameter used in modified Gaussian curve (Chapters 2, 5)	[−]
α_f^*	relative axial stiffness of piled building	[m]
α_{mod}^*	modified relative axial stiffness of building	[−]
α_f	frame axial stiffness	[N/m]
$\bar{\alpha}$	approximate compressibility parameter (Chapter 5)	[−]
β	angular distortion (Chapter 2)	[°]
β	limit angle (Chapter 2)	[°]
β	parameter used to normalise $V_{l,s}$ with C/D (Chapters 2, 4, 5)	[−]
Δ	relative deflection	[m]
δ	displacement (Chapter 2)	[m]

δ	tunnel ovalization parameter	[−]
γ	engineering shear strain (Chapters 4, 8)	[−]
γ	soil unit weight	[N/m^3]
λ	parameter used to predict $V_{l,s}$	[−]
ν	Poisson's ratio	[−]
ν_s	Poisson's ratio of the soil	[−]
$\nu_{s,b}$	Poisson's ratio of the soil below the pile base	[−]
ω	angular velocity (Chapter 3)	[rad/s]
ω	tilt (Chapters 2)	[°]
π	$\simeq 3.14\ldots$	
ϕ	friction angle	[°]
ϕ_{cv}	constant volume friction angle	[°]
ϕ_{max}	maximum friction angle	[°]
ρ	relative bending stiffness	[−]
ρ	relative distortion of a deep cavity (Chapters 2, 5)	[−]
ρ^*_{mod}	modified relative bending stiffness	[−]
ρ_{norm}	relative bending stiffness considering building self-weight	[−]
$\rho^{p;r}$	relative bending stiffness accounting for pile foundation	[m]
ρ_s	soil density	[kg/m^3]
σ	stress	[N/m^2]
σ_{norm}	normalised tunnel pressure	[N/m^2]
σ_s	surface surcharge pressure	[N/m^2]
σ_t	pressure in the model tunnel	[N/m^2]
σ_v	vertical stress	[N/m^2]
$\bar{\tau}_s$	average shaft friction	[N/m^2]
τ_s	shaft shear stress	[N/m^2]
ε	tunnel contraction parameter	[−]
ε_0	equivalent ground loss parameter	[−]
ε_b	bending tensile strain	[−]
ε_{bt}	bending tensile strain due to shearing, bending and horizontal deformations	[−]
ε_d	diagonal tensile strain	[−]
ε_{dt}	diagonal tensile strain due to shearing, bending and horizontal deformations	[−]
ε_{hc}	horizontal compressive building strain	[−]
ε_{ht}	horizontal tensile building strain	[−]
ε_{lim}	limiting tensile strain	[−]
ε_v	axial strain (Chapter 8)	[−]

ε_v	volumetric strain	[−]
$\varepsilon_{x,z}$	modified equivalent ground loss parameter	[−]
ε_{xx}	axial strain in x direction	[−]
ε_{zz}	shear strain	[−]
ε_{zz}	axial strain in z direction	[−]
φ^p	pile head rotation	[rad]
ξ	corrective term	[−]

Superscripts

an	analytical
$bldg$	building
el	elastic
exp	experimental
f	failure
gf	greenfield
r	pile row

Subscripts

0	initial/pre-tunnelling
b	beam
c	column
cr	critical
eq	equivalent
g	ground level
hog	hogging
i	subscript index
max	maximum
min	minimum
mod	modified
p	pile
s	surface
sag	sagging
t	tunnel
Vlt	at a given tunnel volume loss

Acronyms / Abbreviations

CCNM	coupled centrifuge-numerical modelling
FDM	finite difference method
FEM	finite element method

FDM	field programmable gate array
G	Gaussian curve
mG	modified Gaussian curve
LVDT	linear variable differential transformer
PIV	particle image velocimetry
PPT	pore pressure transducer
PTFE	polytetrafluoroethene
TPGI	tunnel-pile group interaction
TPI	tunnel-pile interaction
TPSI	tunnel-pile-structure interaction
TSAM	two-stage analysis method
TSI	tunnel-structure interaction

Chapter 1

Introduction

The expansion of cities and urban areas is resulting in an increased demand for environmentally and economically sustainable transport and services infrastructure (e.g water, waste, etc). Underground construction and infrastructure that often require the excavation of tunnels represent an ideal solution to satisfy these needs. However, tunnel construction is increasingly taking place in close proximity to buried and surface structures. If protective measures are not adopted, tunnelling inevitably affects existing structures because of the induced ground movements and stress relief, with serious potential for damage. On the other hand, the use of protection measures, such as compensation grouting, increases the costs associated with the project. Therefore, to optimise the design of tunnel excavations (which involves assessing tunnelling-induced greenfield soil movements, the deformations induced on structures resulting from soil-structure interactions, and the risk of failure) engineers need to be able to accurately estimate the response of structures, foundations, and infrastructure to tunnelling.

A frequent scenario that engineers face in urban areas is tunnelling beneath deep foundations and piled structures. In these cases, key concerns of tunnel engineers relate to the preservation of structural serviceability and the limitation of tunnel volume loss prior to reaching pile failure. Although various studies have considered the effect of excavations on either a building with shallow foundations or piles, a comprehensive understanding of the global tunnel-pile-structure interaction (TPSI) problem has not yet been achieved. Few researchers have addressed the problem, which is particularly challenging because of the complexity and non-linear response of the global system and the need to link concepts from tunnelling, ground and structural engineering. Therefore, engineers generally compensate for the lack of understanding with an overly conservative design, which often results in significant project costs associated with structural protection measures. This dissertation investigates tunnelling and its effects on piles and piled structures to achieve a better understanding of the global TPSI and the way it may affect/damage the superstructure.

This project used geotechnical centrifuge modelling as the main research tool. Geotechnical centrifuge modelling offers an efficient and cost-effective way to study tunnelling and soil-structure interaction (SSI) problems: it can provide high-quality data from experimental parametric studies, enabling isolation of simplified domains to gain understanding of individual

interaction mechanisms and parameter effects, or investigation of the entire domain. Furthermore, in this research, the real-time substructure testing approach was applied with centrifuge modelling to study a TPSI problem through the real-time coupling of numerical and centrifuge modelling. This advancement enhanced the capabilities of the centrifuge modelling and enabled an accurate representation of a complex ground-foundation-superstructure system to be achieved. The technique coupled experimental and numerical modelling tools in such a way that the strengths of the respective modelling techniques was exploited. [i] The numerical model allows accurate and efficient simulation of the structure. [ii] The tunnel-ground-foundation system is modelled within the centrifuge to accurately reproduce soil and soil-structure interaction behaviour. [iii] The two models run simultaneously and are coupled through a real-time data interfacing system that transmits the boundary conditions between the models (load-controlled system). In this dissertation, a wide range of greenfield tunnelling scenarios in sands, including relatively shallow and deep tunnels with variation of soil density between loose and dense states, are investigated to assess the magnitude and distribution of tunnelling-induced ground movements. The centrifuge modelling of piles and piled structure response to tunnelling contributes to the understating of TPSI and illustrates the importance of modelling pile installation method, the superstructure configuration, self-weight and stiffness distribution. Furthermore, empirical and closed-form solutions are used to study the tunnelling-induced displacement fields and elastic Winkler-based Two-Stage Analysis Methods (TSAMs) are used to analyse the TPSI problem. This dissertation is structured as follows.

- A review of the relevant literature to this research is provided in Chapter 2.
- The development of the centrifuge model, coupled centrifuge-numerical model, experimental methods, and test plan are shown in Chapter 3.
- The effects of relative tunnel depth, soil density and volume loss on vertical and horizontal ground movements due to greenfield tunnelling in sands are studied in Chapter 4; empirical formulas for the prediction of settlement troughs are also presented.
- Chapter 5 deals with analytical and semi-analytical predictions of soil deformation patterns above tunnels in sandy soil.
- A simplified elastic analysis of tunnel-piled structure interaction is carried out in Chapter 6.
- The effects of tunnelling beneath piles and piled frames are investigated in Chapter 7 using the coupled centrifuge-numerical modelling technique.
- Conventional centrifuge modelling of tunnelling beneath an equivalent piled plate is presented in Chapter 8.
- Conclusions and recommendations for further research are given in Chapter 9.

Chapter 2

Background

This chapter presents a review of the most relevant research carried out on tunnelling and its effects on existing piles and structures. Firstly, greenfield tunnelling is discussed with reference to tunnel stability, tunnelling-induced ground movements in clays and sands and their prediction methods. The subsequent sections discuss the effects of tunnelling on pile foundations considering both displacement and non-displacements piles with particular emphasis on pile settlements and pile failure due to tunnel excavations. Finally, the review addresses the problem of the global tunnel-structure interaction; in particular, the focus is on the response of structures with shallow and deep foundations to excavation-induced ground movements and the resulting distortions.

2.1 Greenfield tunnelling

Stress relief and ground over-excavation during tunnelling results in ground movements and strains within the soil that may lead to soil failure in the case of an insufficient support during the tunnelling stages. Important requirements for design and construction of tunnels are stability, ground movements, and performance of linings. Because in urban areas tunnel excavations are generally successfully performed in pre-collapse conditions, the main aim of the research is investigating tunnelling-induced ground movements, which represent a reference point for the tunnel-structure interaction problem. However, the stability problem is also reviewed to highlight some of the differences between tunnelling in fine and coarse soils.

In this thesis, the term greenfield is used to indicate a tunnelling scenario characterised by the absence of surface or buried structures. A qualitative description of surface greenfield settlements due to tunnelling is shown in Figure 2.1. To simplify the problem, engineers tend to study the three-dimensional distribution of ground movements considering the 2D cross sections corresponding to the transverse and longitudinal planes defined with respect to the tunnel axes. This research focuses on the steady-state condition obtained at a distance of several diameters from the tunnel face, in the transverse plane.

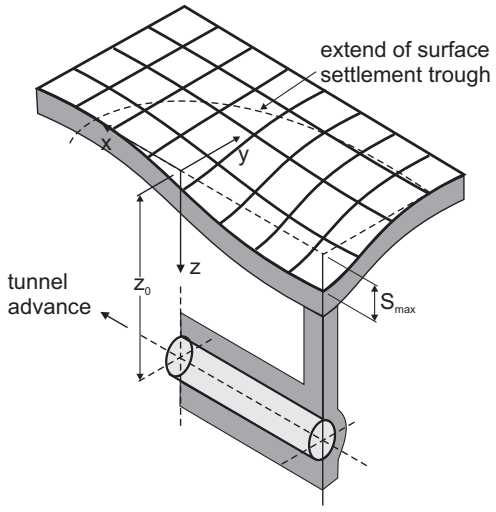

Fig. 2.1 Surface settlements induced by tunnelling [Attewell et al. (1986); Möller (2006)].

2.1.1 Tunnel stability

The problem of tunnel stability is particularly relevant at the tunnel heading where a portion of the soil is unsupported, if the temporary/permanent linings have not yet been placed, or only partially supported. To simplify a generally complex scenario depending on several technological and design aspects, engineers model the stability problem through the following parameters: the length of unsupported excavation (P), the cover to diameter ratio (C/D) or the depth to the tunnel axis (z_t), surface surcharge pressure (σ_s), the unit weight of the overburden material (γ), the soil strength, water pressure, and tunnel support pressure achieved with compressed

air or pressurised slurry (σ_t). The idealised geometry of a tunnel excavation progress in the longitudinal and transverse direction is shown in Figure 2.2.

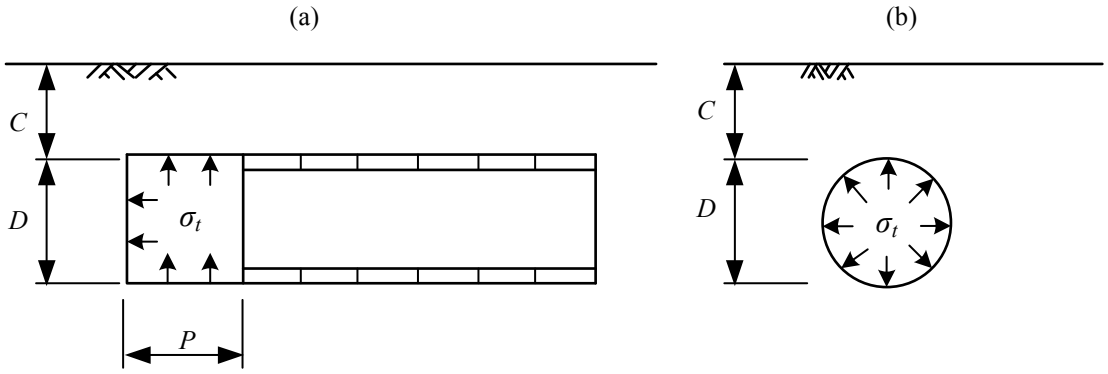

Fig. 2.2 (a) Tunnel heading; (b) 2D idealisation of tunnel heading in the transverse plane [Mair and Taylor (1999).

To evaluate tunnel stability in undrained conditions, Broms and Bennermark (1967) introduced the tunnel stability factor, N, defined as

$$N = \frac{\sigma_s + \gamma z - \sigma_t}{c_u} \tag{2.1}$$

where c_u is the undrained shear strength of the clay. The higher the stability ratio the more unstable is the tunnel heading. On the basis of laboratory tests and field observations, they stated that failure is associated with the critical stability ratio $N_c = 6$. According to a comprehensive review of latest findings performed by Leca et al. (2007), care is recommended in the evaluation of settlement risk when $3 < N \leq 6$, with particular attention to possible face ground loss if $N > 5$. Centrifuge model tests performed by Mair (1979) and Kimura and Mair (1981) displayed that the critical value N_c increases with cover to diameter ratio, C/D, and decreases with the unsupported length of the tunnel head, P. Theoretical solutions supporting these findings were developed by Davis et al. (1980).

A theoretical solution of the tunnel collapse pressure in cohesionless soils was proposed by Atkinson and Potts (1977) through upper and lower bound theorem solutions in plane-strain condition that agreed well with laboratory benchmark data. The application of the lower bound theorem through an admissible stress field that respects the failure criterion leads to the following safe tunnel pressure

$$\frac{\sigma_t}{2\gamma R} = max\left\{ \frac{1}{2(\mu-2)}\left(\left(\frac{R}{C+R}\right)^{\mu-2}\left(3-\frac{4}{\mu}\right)-1\right]; \frac{\mu}{\mu^2-1}\right\} \tag{2.2}$$

$$\mu = \frac{1+sin(\phi)}{1-sin(\phi)}$$

whereas the suggested upper-bound tunnel pressure is

$$\frac{\sigma_t}{2\gamma R} = \frac{1}{4\cos(\phi)}\left(\frac{1}{\tan(\phi)} + \phi - \frac{\pi}{2}\right) \tag{2.3}$$

where γ is the unit weight of the material, R is the tunnel radius, C is the cover above the tunnel crown, and ϕ is the friction angle.

Finally, it is important to note that failure mechanisms in clays and sands are remarkably different. In clays, the failure mechanism is wide and characterised by slip surfaces that propagate horizontally, whereas failure in sands results in a chimney mechanism with vertical slip surfaces where settlements propagate vertically from the tunnel (Figure 2.3). Note that the chimney mechanism is obtained at the ultimate state and deformation patterns pre-collapse are discussed in the following sections.

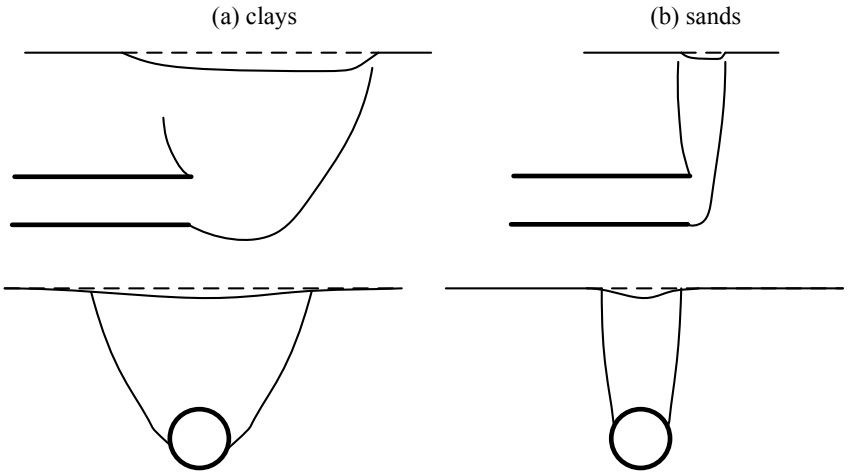

Fig. 2.3 Observed failure mechanisms based on centrifuge model tests in (a) clays and (b) sands [Chambon and Corte (1994); Mair (1979); Mair and Taylor (1999)].

2.1.2 Volume loss and its effects

2.1.2.1 The concept of volume loss, its magnitude and distribution

Ground movements are mainly caused by the soil moving towards the drilling machine due to the stress-relief, which results in a ground loss. In general, depending on the tunnel construction method (either open faced or closed-face excavation using tunnel boring machines (TBMs)), it is possible to identify the main sources of the ground loss, as listed by Mair and Taylor (1999) and shown in Figure 2.4.

Considering the transverse section and assuming plane-strain conditions, the magnitude of the ground loss is commonly described by tunnelling engineers with two parameters: the tunnel volume loss, $V_{l,t}$, and the soil volume loss, $V_{l,s}$. The concept of volume loss is illustrated in Figure 2.5(a). $V_{l,s}$ is defined as the ratio between the volume of the settlement trough per unit

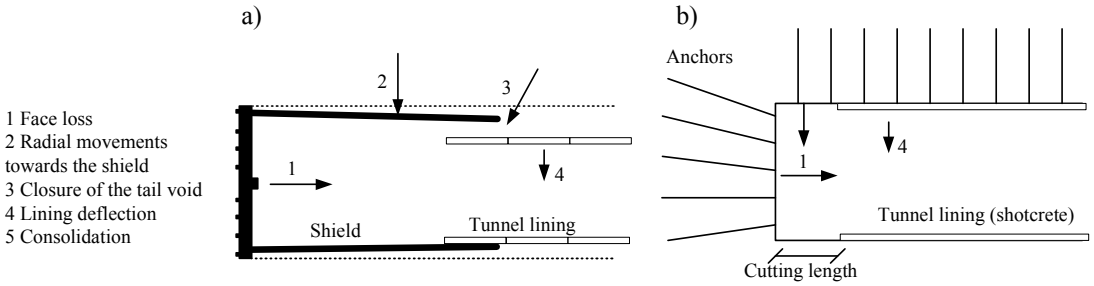

Fig. 2.4 Primary sources of ground deformation of (a) shield tunnels (Mair and Taylor, 1999) and (b) conventionally driven open face tunnels (Cording, 1991).

length of tunnel, V_s, and the notional final area of the tunnel cross section, V_0.

$$V_{l,s} = \frac{V_s}{V_0} \times 100 \qquad [\%] \tag{2.4}$$

In experimental, analytical and numerical studies, the ground loss is modelled through the tunnel volume loss, $V_{l,t}$, which is the ratio between the ground loss at the tunnel periphery, ΔV, and V_0.

$$V_{l,t} = \frac{\Delta V}{V_0} \times 100 \qquad [\%] \tag{2.5}$$

$V_{l,t}$ and $V_{l,s}$ are generally expressed as a percentage.

Tunnel engineers are generally interested in V_s to describe the overall effect of tunnelling. Because of the simplicity in the measurement of the surface V_s in the field and the fact that tunnelling is mostly performed in undrained conditions (i.e. the undrained condition allows assuming $V_{l,t} = V_{l,s}$ over the short-term scenario), $V_{l,t}$ is a widely used parameter in practice and it is a convenient reference for researchers. However, it is important to note that the relationship $V_{l,t} - V_{l,s}$ is affected by ground conditions and volumetric strains (Marshall et al., 2012).

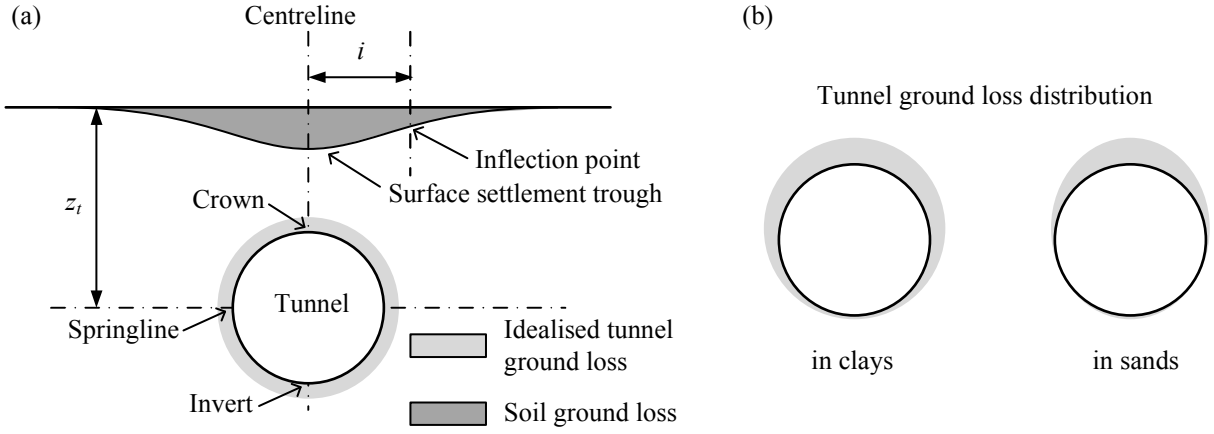

Fig. 2.5 (a) Illustration of the concept of soil and tunnel volume losses; (b) typical tunnel volume loss distribution according to Loganathan and Poulos (1998) and Zhou (2014).

Alternatively, in experimental studies and analytical methods, to model the ground loss it is assumed that the tunnel excavation induces a movement of the ground at the tunnel periphery

resulting in a reduced cross-section of the tunnel compared to the originally excavated area. $V_{l,t}$ is used to describe the magnitude of the tunnel contraction.

The implementation of a proper tunnel deformation shape assumes a fundamental role in the analytical analysis. Initially, in analytical works, the volume loss area has been attributed to a cavity contraction (Sagaseta, 1987), i.e. by an uniform tunnel convergence. Nevertheless, this straightforward assumption may not describe the actual field displacement adequately: centrifuge modelling confirmed that little ground displacement occurs at the tunnel invert (Mair, 1979; Potts, 1976). The actual tunnel ground loss is distributed according to a roughly elliptical shape in clays (Loganathan and Poulos, 1998; Rowe and Kack, 1983), whereas the ground loss should be concentrated at the tunnel crown in sands (Marshall, 2009; Zhou, 2014) (see in Figure 2.5 (b)).

The volume loss magnitude depends on the type of ground, constructor's skills and the adopted tunnelling technique. Mair and Taylor (1999) concluded the following based on a review of several papers and recent projects:

- volume losses in stiff clays, such as London Clay, are generally between 1% and 2% when the open-face tunnelling technique is adopted;
- sprayed concrete linings (NATM) in London Clay could provide a control of the ground movements with volume losses between 0.5% and 1.5%;
- earth pressure balance (EPB) and slurry machines can achieve a high degree of settlement control with volume losses of 0.5%, and 1-2%, respectively, for sands and soft clays (excluding consolidation settlements);
- in mixed face conditions volume loss may be higher for EPB and slurry machines.

Several cases of open-face tunnelling in London Clay were reviewed by Dimmock and Mair (2007). The authors proposed the empirical Equation (2.6) between $V_{l,t}$ and the load factor, N/N_c, derived from field monitoring data.

$$V_{l,t}\,[\%] = 0.23e^{4.8\cdot(N/N_c)} \text{ for } N/N_c \geq 0 \tag{2.6}$$

2.1.2.2 Soil arching and ground reaction curves

Soil arching consist in the mobilisation of shearing resistance of the soil. Its understanding can provide useful insights on ground reaction curves and ground movements resulting from underground excavations. Soil arching occurs within the ground when an underground deformable inclusion or an excavation causes deformations and strains of the soil mass resulting in local redistribution of the greenfield stresses. Soil arching is associated with the transfer of stresses from the deflecting or yielding areas towards the sides, where the ground is more stable. In tunnelling, this results in a variation of the inner tunnel pressure at the axis level, σ_t, with $V_{l,t}$ that defines the ground reaction curve. The qualitative trend of a ground reaction curve is presented

in Figure 2.6: at small yielding, the arch starts to mobilise inducing a drop of the loading on the intrusion; when the arch is fully active the loading reaches its minimum; further increases of yielding cause an increment in loading, defining a recovery stage, up to an asymptotic value associated with ultimate conditions in the soil mass.

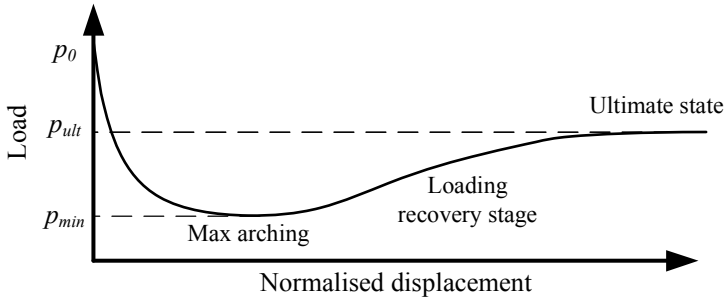

Fig. 2.6 Qualitative trend of a reaction curve and definitions.

.

In recent years, centrifuge testing has been performed to systematically investigate the deformation mechanisms of arching in granular soils subjected to a subsurface void using a trapdoor model (Dewoolkar et al., 2007; Iglesia et al., 2014). Dewoolkar et al. (2007) and Iglesia et al. (2014) described the formation above the trapdoor of a physical arch, which evolves from an initially curved configuration to a triangular shape and ultimately to a prismatic sliding mass with vertical sides (see Figure 2.7). This mechanism of the soil arch shape, as the displacement of the trapdoor progresses, was confirmed by da Silva et al. (2016) with measurements of the subsurface ground movements. Iglesia et al. (2014) assumed that, at its ends, the parabolic arch has an inclination to the horizontal equal to the complementary angle of the friction angle (see Figure 2.7), which agrees with da Silva et al. (2016) who suggested that the shape of the triangular arch may only be slightly influenced by the soil overburden depth, H, for a given soil density and inclusion width, B.

Regarding the effects of soil arching on ground reaction curves, the following main conclusions were drawn (Dewoolkar et al., 2007; Iglesia et al., 2014).

- The absolute value of the p_{min} and p_{ult} loadings are not dependent on H/B (depth-to-width ratio).
- For a given inclusion width, B, the deeper the soil overburden depth, H, the greater the relative reduction in the loading (p/p_0) with respect to the pre-tunnelling condition: the minimum and ultimate relative loadings (p_{min}/p_0 and p_{ult}/p_0) decrease with the increase of H/B to asymptotic values for $H/B > 5$. The variation rate is high for shallow intrusions, $H/B < 2$, and low for deep intrusions, $H/B > 2$.
- The higher arch efficiency, associated with the minimum loading p_{min}, is mobilised at a constant normalised trapdoor displacement (δ/B).
- The effects of the soil relative density are secondary to other parameters inducing a slight decrease of p_{min} and p_{ult} loadings.

- The evolution mechanism of the arch shape may be associated with the trend of the reaction curve because the load on the intrusion is mostly due to the weight of the soil beneath the arch. The formation of the initial triangular arch allows for the drop of the loading on the intrusion. The transition to a parabolic and, finally, rectangular shape results in the increase of the load because of the more volume of the ground without support (i.e. beneath the arch) overlying the intrusion. However, the shear stresses along the sides cause a final condition with a ratio $p_{ult}/p_0 < 1$.

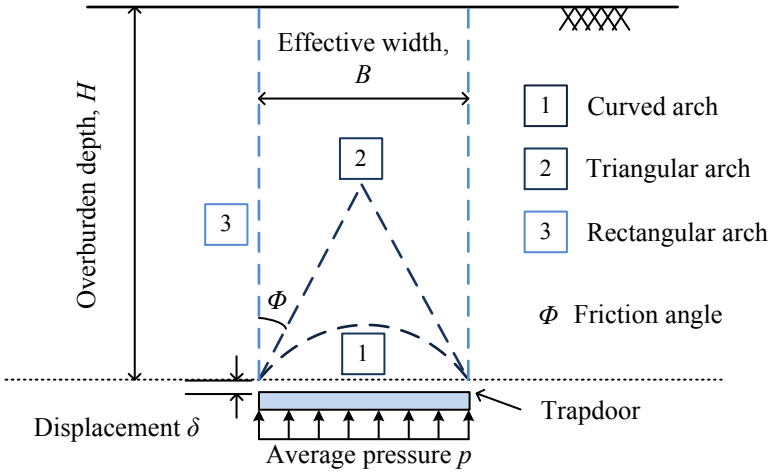

Fig. 2.7 Qualitative arching mechanism above a trapdoor (1) at relatively small, (2) intermediate, and (3) large displacements postulated by Iglesia et al. (2014).

.

A number of authors have measured ground reaction curves during centrifuge tests of tunnelling in sands (Marshall, 2009; Vorster et al., 2005; Zhou, 2014). They highlighted similar trends of the tunnel pressure to the curve displayed in Figure 2.6. 1) σ_t has a steep initial reduction with the increase in tunnel volume loss up to 1%; 2) this is followed by an approximately steady value. In the case of relatively shallow tunnels, 3) a gradual increase in tunnel pressure was measured at high volume loss. This result may be explained considering the soil arching and soil failure (i.e. critical state). Furthermore, Zhou (2014) noted identical reaction curves for three different relative densities at a given C/D ratio equal to 2.0.

2.1.3 Tunnelling-induced ground movements and empirical relations

The estimation of ground movements is the first step to perform a reliable risk-assessment of the potential effects on building and buried infrastructure, which is essential for the design of tunnelling in urban areas. Although a good understanding of the greenfield tunnel-induced settlements has been reached for tunnels in clay, where the soil conforms to constant volume conditions, so far there has been a limited discussion about ground movements in sandy soils.

Numerical methods have been extensively applied to tunnelling and the analysis of the induced soil deformation patterns because of the possibility to implement various geometries, details of the construction procedure and complex soil constitutive models. However, there are

many cases, especially in the preliminary stages of the design, in which the soil data are not adequate to characterise complex constitutive models and the excavation method is not fully defined. Therefore, empirical methods and closed-form solutions still represent an effective instrument to carry out low computational cost, approximate and sensible evaluation of practical study cases.

In this section, the available empirical and analytical methods to predict ground movements in the transverse plane are illustrated and discussed. This review is focused on the steady-state condition in the transverse plane because this research does not attempt to model and assess the effects of the tunnel excavation advancement. However, note that in the transitional phase of the tunnel advancement there is a longitudinal settlement trough developing ahead and above of the tunnel heading, which was described by O'Reilly and New (1982) with the use of a cumulative probability curve. Likewise, these differential settlements may result in potential damage of structures oriented in the longitudinal direction.

2.1.3.1 Transverse settlements in clay

Tunnelling-induced settlement troughs are generally described by tunnel engineers using simple empirical methods. As proposed by Peck (1969), in undrained conditions, the shape of transverse settlement troughs agrees with a standard Gaussian curve, with the maximum settlement, u_{max}, and the horizontal distance of the inflexion point from the tunnel centreline, i, defining the curve (i.e. the Gaussian curve has two degrees of freedom) .

$$u_z = u_{max} \exp\left(-\frac{x^2}{2i^2}\right) \tag{2.7}$$

where x is the horizontal distance from the tunnel centreline. The volume per meter of tunnel, V_s, calculated by integrating the above equation is

$$V_s = \sqrt{2\pi}\,(i u_{max}) \tag{2.8}$$

Because in this approach the shape of the settlement trough is only described by i and the curvature of the settlement curve may lead to potential for damage, it is interesting to investigate the parameter i. O'Reilly and New (1982) proposed a linear relationship between i at the surface and z_t

$$i = K z_t \tag{2.9}$$

where K is a trough width parameter and z_t the depth of the tunnel axis. They suggested assuming 0.4-0.5 for stiff fissured clay, 0.5-0.6 for glacial deposits, and 0.6-0.7 for soft silty clays. The value $K = 0.5$ in clays was confirmed by Mair et al. (1993).

To allow for the prediction of subsurface settlement curves, Mair et al. (1993) found that the value of i is proportional to the vertical distance between the tunnel and the depth of interest through the width parameter K (Equation (2.10)), whereas the parameter K was defined as a

function of the ratio between depth and tunnel depth, z/z_t, according to Equation (2.11). The predictions of Equations (2.10) and (2.11) were satisfactory when compared to the data of centrifuge tests performed in clays by Grant and Taylor (2000), despite the overestimation of i within a distance of $D_t/2$ from the tunnel crown.

$$i = K\left(z_t - z\right) \tag{2.10}$$

$$K = \frac{0.175 + 0.325\left(1 - \dfrac{z}{z_t}\right)}{1 - \dfrac{z}{z_t}} \tag{2.11}$$

In recent years, Jones (2010) displayed that the Mair et al. (1993) expression would overestimate the width parameter K in the case of deep tunnels. Based on field data measurements, the author proposed a logarithmic formula for the prediction of the width parameter depending on the height above the tunnel $z_t - z$ rather than the relative depth z/z_t.

$$K = -0.25\ln\left[z_t - z\right] + 1.234 \tag{2.12}$$

Interestingly, Equation (2.12) predicts a decrease of the surface width parameter with z_t. Therefore, according to Jones (2010), the settlement trough shape in clays is a function of depth, z, and tunnel depth, z_t. In general, it should be noticed that in both Equations (2.11) and (2.12) the settlement trough shape does not change with $V_{l,t}$ as confirmed by the centrifuge results of Grant and Taylor (2000).

It is worth noting that several authors have provided data suggesting that i is also a function of the tunnel diameter, especially for low cover-to-diameter ratios (Clough and Schmidt, 1981; Lee et al., 1999; Moh et al., 1996). For instance, Lee et al. (1999) derived the following empirical relation making use of centrifuge tests of tunnelling in soft clays

$$2\frac{i}{D_t} = 1 + 0.58\frac{z}{D_t} \tag{2.13}$$

During undrained tunnelling, there is the development of excess pore pressure that, dissipating with time, results in additional settlements with respect to the immediate displacement field. An overall description of the problem has been proposed by Mair and Taylor (1999), who pointed out that the consolidation settlements are influenced by magnitude and distribution of excess pore pressures, compressibility and permeability of the soil, and permeability ratio between soil and lining. Despite the complexity of the problem, in general, the consolidation settlement troughs tend to be wide because of a steady state seepage taking place towards the draining tunnel. Therefore, in several scenarios post-construction settlements are not a major concern for damage because wide settlement troughs (with modest differential settlements) do not induce distortions and strains in structures.

2.1.3.2 Transverse settlements in sand

The mechanism of tunnelling-induced ground displacements in sands is different to clays both in pre-collapse and ultimate conditions. Firstly, the displacement field in sands is the result of the dilative/contractile behaviour of the ground that adds additional complexity to the problem and that makes the constant volume assumption inaccurate. Secondly, as discussed in Cording (1991) and Marshall (2009), there is a variability of the deformation pattern with tunnel volume loss. In fact, at low volume loss and small strains the soil displays an elastic and stiff behaviour like a continuum, which allows a high propagation of deformations resulting in a wide settlement trough. As a consequence of the increase of volume loss, $V_{l,t}$, there is a narrowing of the settlement trough: large displacements associated with soil shearing occur above the tunnel crown. However, the chimney-like displacement mechanism does not necessarily form, as displayed by Figure 2.8. Furthermore, several studies highlighted that the width parameter i increases with C/D (Marshall et al., 2012; Sugiyama et al., 1999) and varies with the relative density, I_d (Zhou, 2014; Zhou et al., 2014). In general, the settlement curve shape and volume (i.e. the width parameter K and the soil volume loss $V_{l,s}$, respectively) are affected by the cover to diameter ratio, C/D, the magnitude of tunnel volume loss, $V_{l,t}$, depth, $z_t - z$, and the soil relative density, I_d. Despite previous works, there has not been a systematic investigation fully understanding the correlations between these variables.

To allow for the prediction of settlement troughs in sands, O'Reilly and New (1982) and Mair and Taylor (1999) carried out the interpolation of available field data assuming the standard Gaussian curve and Equation (2.9). Their work indicated scattered values of K in sands compared to the interpolation obtained in clays. These authors respectively proposed to adopt $K = 0.25$ and $K = 0.35$. Moh et al. (1996) analysed subsurface settlement data from the Tapei Mass Transit system within silty sands and proposed Equation (2.14), whose structure is based on the work of Clough and Schmidt (1981):

$$i = \left(\frac{D_t}{2}\right)\left(\frac{z_t}{D_t}\right)^{0.8}\left(\frac{z_t - z}{z_t}\right)^{m} \tag{2.14}$$

where m is 0.4 for silty sands and 0.8 for silty clays.

The use of the standard Gaussian curve was questioned by Celestino et al. (2000). In their paper, it was demonstrated that Gaussian curves do not always provide a good fit to settlement trough data in drained soils, which may explain the discrepancy and scatter between the K values. To overcome this problem, the yield-density curve was used by Celestino et al. (2000) whereas the modified Gaussian curve described by Equation (2.15) was suggested by Vorster et al. (2005) to obtain a better fit to observed centrifuge settlements in sands.

$$\begin{aligned} u_z &= u_{max}\frac{n}{(n-1)+exp\left[\alpha\left(x/i\right)^2\right]} \\ n &= e^{\alpha}\frac{2\alpha-1}{2\alpha+1}+1 \end{aligned} \tag{2.15}$$

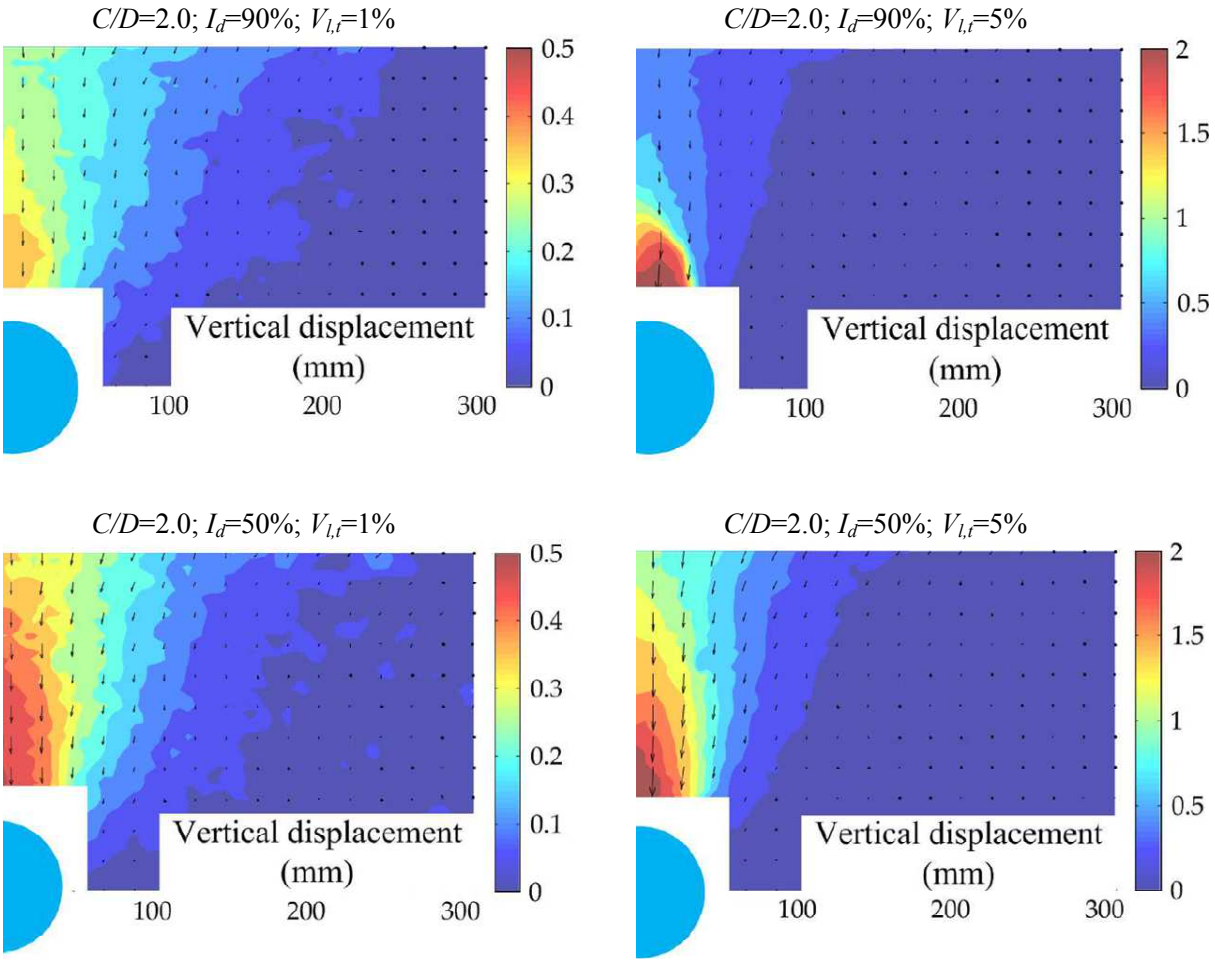

Fig. 2.8 Results from centrifuge tests in dry sands: effects of I_d and $V_{l,t}$ on settlement contours [Zhou (2014)].

where α is the additional parameter controlling the profile shape and ensuring i has the same definition as in the Gaussian distribution curve (Equation 2.7). α controls the vertical location of the inflexion point and allows for more effective curve fitting in the case of narrow settlement troughs. Equation (2.15) becomes the standard Gaussian curve when $n = 1$, as shown in Figure 2.9. Note that both the yield-density curve and the modified Gaussian curve are defined by three parameters (i.e. they have three degrees of freedom).

Despite its versatility, the use of the modified Gaussian curve is not as user-friendly as the standard Gaussian curve and the α parameter does not have a physical meaning. To overcome these drawbacks, to develop an approach able to determine the parameters of a generic three-degree-of-freedom curve and to allow comparing data from standard and modified Gaussian curves, Marshall et al. (2012) proposed to describe the curve through the position of two points and the soil volume loss $V_{l,s}$. The authors suggested to define the curve shape with the points $(x^*, 0.606u_{max})$ and $(x^{**}, 0.303u_{max})$, where $0.606u_{max}$ is the settlement corresponding to the inflection point of the standard Gaussian curve (i.e. if $n = 1$, $x^* = i$). In this way, the parameter x^* is comparable to the value i of the standard Gaussian curve because the same vertical displacement u_z corresponds to both offsets. Note that x^* and x^{**} can be derived from

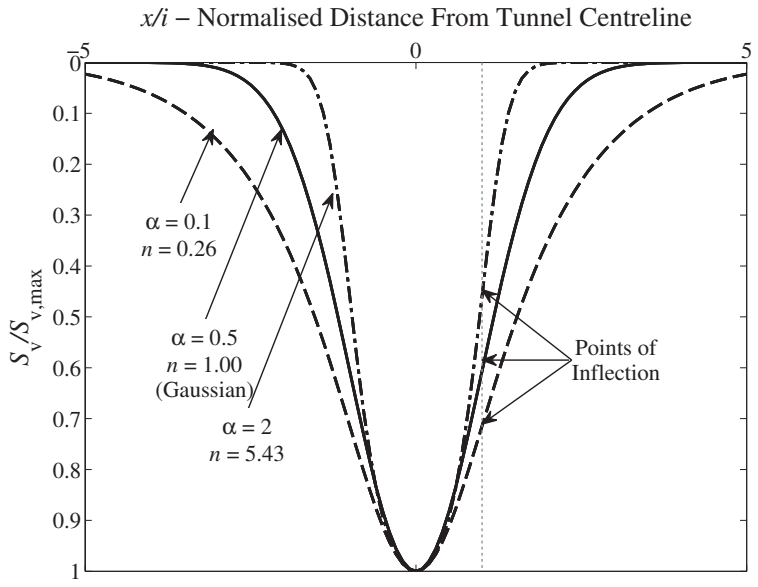

Fig. 2.9 Comparison between standard Gaussian and modified Gaussian settlement trough [Vorster et al. (2005); Williamson (2014)].

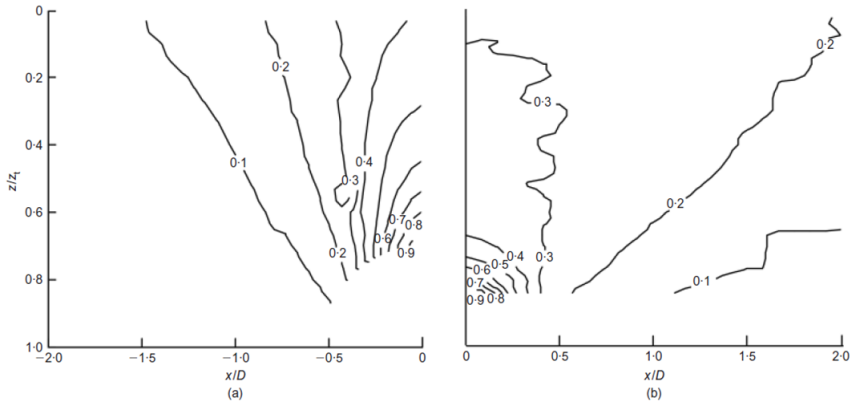

Fig. 2.10 Normalised settlement contours at 5% volume loss for: (a) $C/D = 1.3$ and (b) $C/D = 4.4$ [Marshall et al. (2012)].

the shape parameters i and α. As in the formulation proposed by Mair et al. (1993), x^* and x^{**} were related to the depth through

$$\begin{aligned} x^* &= K^*(z_t - z) \\ x^{**} &= K^{**}(z_t - z) \end{aligned} \tag{2.16}$$

Marshall et al. (2012) carried out centrifuge tests in dense sands ($I_d = 0.9$) to examine the effect of C/D and $V_{l,t}$ with three centrifuge tests ($C/D = 1.3, 2.4, 4.4$). The authors proved that the three-degrees-of-freedom curves fit the data better than the standard Gaussian curve and that trough width may vary within a wide range ($K^* = 0.25 - 0.75$) with high values at low volume loss. Furthermore, they provided evidence that the chimney mechanism is better recognisable for the relatively shallow tunnel than for the relatively deep excavations at a given volume loss (see Figure 2.10), which is probably due to soil arching.

Starting from the Equation (2.11), Marshall et al. (2012) proposed the following equations, based on the modified Gaussian curve and the offsets x^* and x^{**}, to predict surface and subsurface settlement trough shape in dense sands accounting for C/D ratio and tunnel volume loss value.

$$K^* = \frac{K_s^* + \left(\partial x^*/\partial z\right)\left(z/z_t\right)}{1 - z/z_t} \qquad K^{**} = \frac{K_s^{**} + \left(\partial x^{**}/\partial z\right)\left(z/z_t\right)}{1 - z/z_t} \tag{2.17}$$

$$K_s^* = K_{s,Vlt}^{*int} + K_{s,Vlt}^{*slope} V_{l,t} \qquad K_s^{**} = K_{s,Vlt}^{**int} + K_{s,Vlt}^{**slope} V_{l,t} \tag{2.18}$$

where $K_{s,Vlt}^{*int} = 0.44 + 0.055C/D$, $K_{s,Vlt}^{*slope} = -0.041$, $\left(\partial x^*/\partial z\right) = -0.436$, $K_s^{**} = K_s^* + 0.29$, and $\left(\partial x^{**}/\partial z\right) = \left(\partial x^*/\partial z\right) - 0.20$. This regression of the centrifuge data was performed assuming a linear variation of the trough shape parameters $\left(\partial x^*/\partial z; \partial x^{**}/\partial z; K_{s,Vlt}^{*slope}; K_{s,Vlt}^{**slope}; K_{s,Vlt}^{*int}; K_{s,Vlt}^{**int}\right)$ with tunnel volume loss and C/D ratio. Therefore, this approach would not allow the extrapolation of the set of equations to higher C/D ratios because they do not account for the transition between shallow to deep tunnels.

Zhou (2014) carried out centrifuge tests in sands with varying relative density ($I_d = 0.5$, 0.7, 0.9) for a given tunnel size and depth ($C/D = 2.0$) to examine the effect of the soil relative density. The dataset presented by Zhou (2014) shows negligible differences in the curve shape parameters for centrifuge tests in sands at 50% and 70% relative density. At low $V_{l,t}$ values, the settlement trough in dense sand were wider than in loose and medium sands. However the differences in shape decreased with $V_{l,t}$ resulting in K^* and K^{**} in dense sands being smaller than in medium and loose sand at high $V_{l,t}$ values. Therefore, the conclusion that i decreases with I_d, reported by Zhou et al. (2014), may be misleading at high volume losses and further works are necessary to fully understand the effects of I_d.

Finally, to define the settlement trough magnitude in sandy soil, it is necessary to define the relationship between $V_{l,s}$ and $V_{l,t}$. This relationship depends on the distribution and magnitude of the volumetric strains; therefore, it is also a function of z/z_t. Marshall et al. (2012) measured $V_{l,s}$ and $V_{l,t}$ during centrifuge tests (see Figure 2.11). Interestingly, the centrifuge experiment data show that the overall soil is contracting ($V_{l,s} > V_{l,t}$) for most practical values of tunnel volume loss even for a dense silica sand, except for shallow tunnels or at higher values of tunnel volume loss when the overall soil is dilating ($V_{l,s} < V_{l,t}$). In the case of dense sands, the soil underwent a contraction at low values of $V_{l,t}$ because of the distribution within the soil of shear strains: low shear strains (and associated volumetric contraction) were measured in most of the soil whereas high shear strains (associated with volumetric dilation) were concentrated in a limited zone at the tunnel shoulders. At high $V_{l,t}$, the region of soil around the tunnel crown was characterised by high shear strains, resulting in dilative strains of the soil mass for incremental volume losses (i.e. the first derivative of the $V_{l,s} - V_{l,t}$ curve at the surface is lower than the 1:1 line). Zhou (2014) presented data that agree with the framework proposed by Marshall et al. (2012). Furthermore, it was proved that the looser the soil i) the higher $V_{l,s}$ (because of soil volumetric behaviour) and ii) the higher $V_{l,t}$ at which the change from overall soil contraction to dilation occurs.

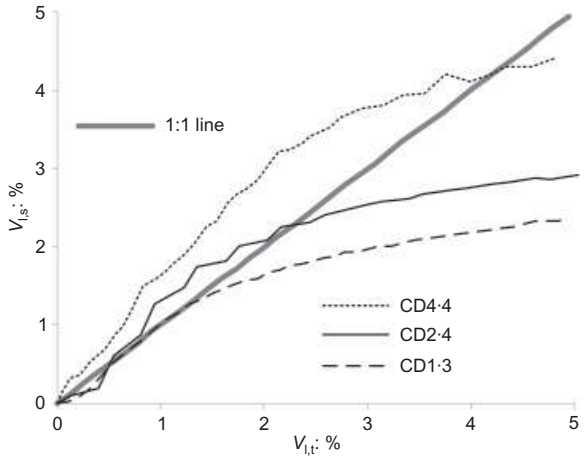

Fig. 2.11 $V_{l,s}$ vs $V_{l,t}$ at the surface for dense sands [Marshall et al. (2012)].

By regression of the data, Marshall et al. (2012) proposed the following empirical relation for the experimental soil volume loss at the surface ($z = 0$)

$$V_{l,s} = \left(C/D\right)^{\beta} \left(c_a - c_b \exp\left[- \left(\frac{V_{l,t} + c_c}{c_d} \right)^2 \right] \right) \qquad [\%] \tag{2.19}$$

where $V_{l,t}$ is in percentage and the coefficients depend on the type of sandy soil and its relative density. For dry silica sand with $I_d = 0.9$, they proposed $c_a = 2.0$, $c_b = 3.7$, $c_c = 2.8$, $c_d = 3.6$, and $\beta = 0.5$. To account for the variability of soil density, Zhou (2014) proposed the following expression for the term β.

$$\beta = 1.75 - 1.5 I_d \tag{2.20}$$

2.1.3.3 Transverse horizontal movements

Although tunnelling-induced settlements represent the primary source of damage, there are specific scenarios in which horizontal greenfield movements can increase the risk of damages for structures and services. Despite this, their understanding is partial, especially for sandy soils.

In the past, the first estimation of horizontal movements in clays was suggested by O'Reilly and New (1982). They correlated, at a given location (x, z), horizontal ground movements, u_x, to the local ground settlement, u_z, assuming that the trough width parameter K is constant with depth and that displacement vectors are oriented towards the axis of the tunnel. These assumptions resulted in

$$u_x = \frac{x}{z_t - z} u_z \tag{2.21}$$

Based on the constant volume condition and the variation of K with depth z described by Equation (2.21), Taylor (1995b) proposed to estimate the horizontal displacements with

$$u_x = \frac{x}{\left(1 + 0.175/0.325\right) z_t} u_z \tag{2.22}$$

which is associated with a displacement vectors directed towards the tunnel centreline at a depth of $0.175z_0/0.325$ below the tunnel axis. The predictions of this equation agreed with centrifuge tests in clays (Grant and Taylor, 2000). Interestingly, Equation (2.22) results in a significant reduction of horizontal displacements with respect to Equation (2.21).

For tunnels in sands, Attewell and Yeates (1984) proposed the following generalisation of Equation (2.22):

$$u_x = \frac{nx}{z_t - z} u_z \tag{2.23}$$

stating that $n = 1.0$ is applicable to cohesive soils whereas they suggested to assume $n < 1.0$ in granular soil (implying that displacement vectors point to a location below the tunnel axis). Marshall (2009) analysed data from a centrifuge test in dry sands; he showed, although a representative value of n is between 0.91 and 0.46 (which compare well with Equation (2.22)) this empirical approach was not able to accurately describe the spatial variability of the horizontal displacements.

2.1.4 Closed-form analytical and semi-analytical solutions for ground movement prediction

Empirical relationships have been extensively used for tunnelling problems due to their reliability and simplicity. However, they do not provide a fully satisfactory framework for the prediction of the overall deformation pattern (i.e. both vertical and horizontal movements), which is of great interest for tunnel-pile and tunnel-structure interaction analyses. The following presents a background of simple closed-form analytical and semi-analytical solutions, often used in research and practice, which aim to provide a consistent deformation pattern and overcome some limitations of empirical methods.

Because the far-field ground movements (i.e. at some distance from the tunnel periphery) are mostly depending on the tunnel ground loss distribution rather than the details of the complex excavation sequence taking place at the tunnel, several closed-form solutions have been developed controlling the deformations of the tunnel periphery. In general, as shown in Figure 2.12, there are three components of tunnel deformation: uniform convergence, distortion (ovalization) and vertical translation, which is a geometric concept only. In this thesis, the tunnel deformations are assumed positive in the sense shown in Figure 2.12. Note that, in the analytical solution, the tunnel volume loss is related to the convergence parameter ε as:

$$V_{l,t} = \frac{\Delta V}{V_0} \times 100 \approx \frac{2\pi R u_\varepsilon}{\pi R^2} \times 100 = 2\varepsilon \times 100 \tag{2.24}$$

whereas the ovalization mechanism is not associated with tunnel ground loss.

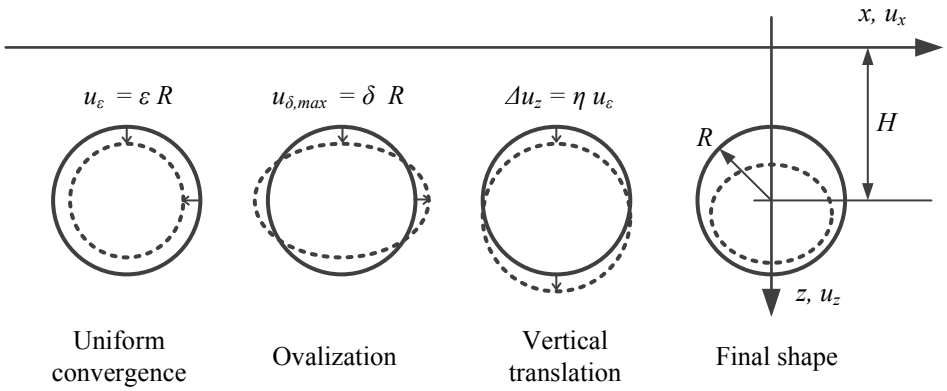

Fig. 2.12 Tunnel deformation components [González and Sagaseta (2001)].

2.1.4.1 Elastic solution for deep tunnels

For deep tunnels, it is legitimate to neglect the influence of the free surface and study the problem of a cavity excavation within an infinite medium. The problem of evaluating the displacements due to the excavation of a circular tunnel within an infinite isotropic elastic medium (G, ν) was first solved by Kirsch (1898) for uneven initial stresses σ'_{v0} and $\sigma'_{h0} = K_0\sigma'_{v0}$, where σ'_{v0} and σ'_{h0} are, respectively, the initial vertical and horizontal effective stress and K_0 is the coefficient of earth pressures at rest. However, in its original work, the solution was given for the case of stresses acting on a medium with a pre-existing hole, whereas the tunnelling problem is described by the excavation of a cavity in a pre-stressed medium (Pender, 1980). Simulating the tunnel excavation by relieving normal and tangential stresses at the tunnel border, Pender (1980) found the ground displacement field in polar coordinates.

The initial in-plane stress state at the tunnel springline can be decomposed into volumetric (p_0) and deviatoric (q_0) total stress components, respectively

$$\begin{aligned} p_0 &= \sigma'_{v0}\frac{1+K_0}{2} + p_w \\ q_0 &= \sigma'_{v0}\frac{1-K_0}{2} \end{aligned} \tag{2.25}$$

where p_w is the pore pressure. Within an infinite space, changes in the volumetric stress produce a uniform convergence of the tunnel periphery, u_ε, and changes in the deviatoric stress induce an ovalization, $u_{\delta,max}$, as shown in Figure 2.12. As illustrated in Figure 2.12, these displacement may be normalised by the tunnel radius, R, to define the tunnel deformation components

$$\begin{aligned} \varepsilon &= \frac{u_\varepsilon}{R} \\ \delta &= \frac{u_{\delta,max}}{R} \end{aligned} \tag{2.26}$$

where ε is the unit uniform radial contraction and δ is the unit cavity ovalization. It is possible to show that the cavity ovalization is not associated with tunnel volumetric changes.

As displayed by Pinto and Whittle (2014), if third order terms $O(1/r^3)$ are neglected because the displacements of interest are in the far field from the tunnel, the displacement field resulting from stress relief at the circular tunnel periphery in a pre-stressed medium can be written as follows

$$\begin{aligned} u_x &= -\varepsilon \frac{xR^2}{x^2+z^2} + \delta \frac{4R^2(1-\nu)}{3-4\nu} \frac{x\left(x^2 - \dfrac{\nu}{1-\nu} z^2\right)}{\left(x^2+z^2\right)^2} \\ u_z &= \varepsilon \frac{zR^2}{x^2+z^2} - \delta \frac{4R^2(1-\nu)}{3-4\nu} \frac{z\left(\dfrac{\nu}{1-\nu} x^2 - z^2\right)}{\left(x^2+z^2\right)^2} \end{aligned} \tag{2.27}$$

where ν is the elastic Poisson's ratio. The tunnel deformation components ε and δ are related to the soil state parameters and stress relief as

$$\begin{aligned} \varepsilon &= \frac{p_0 - p_i}{2G} \\ \delta &= \frac{q_0}{2G}(3-4\nu) \end{aligned} \tag{2.28}$$

where p_i is the inner supporting pressure due to grouting and/or the lining action. It is interesting to define a further parameter, the relative distortion of a deep cavity ρ, equal to

$$\rho = \frac{\delta}{\varepsilon} \tag{2.29}$$

that in the case of a deep tunnel in elastic soil is

$$\rho = \frac{1-K_0}{1+K_0+2r_u} \frac{3-4\nu}{1-p_r} \tag{2.30}$$

where $r_u = p_w/\sigma'_{v0}$ and $p_r = p_i/p_0$. Note that Equations (2.28) and (2.30) display the physical significance of the parameters for convergence, ε, and ovalization, δ, and their relations with the soil elastic parameters and initial stresses for deep tunnels. Nevertheless, these deformation components, in subsequent sections, are considered as input parameters regardless of their origin when this solution is extended to shallow tunnels influenced by the surface.

2.1.4.2 Elastic solutions for shallow tunnels

The superposition of singularities method A number of studies have investigated the application of the superposition of singularities method to the problem of tunnelling-induced ground displacements in a half-space. Its first application was proposed by Sagaseta (1987) to evaluate soil movements in undrained conditions. The author assumed that a shallow void of radius a (whose area represents the tunnel volume loss, $\Delta V = \pi a^2$) and located within a half-space at depth H is originated and filled by the surrounding soil on the assumptions of incompressible ($\nu = 0.5$) linear isotropic elastic behaviour. As described by Sagaseta (1987), the method involves three steps as shown in Figure 2.13: 1) the strains due to volume loss are computed by

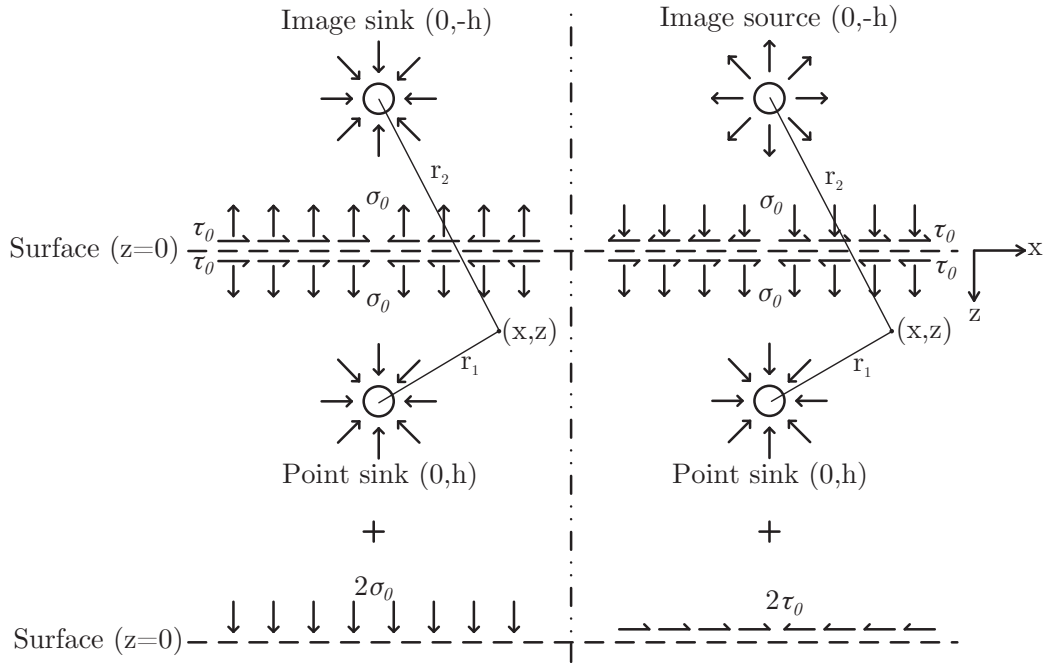

Fig. 2.13 The superposition of the singularities method: (left) virtual source, (right) virtual sink [Sagaseta (1987)].

making use of a sink placed into an infinite medium; 2) to balance normal or shear stresses at the soil surface, either a virtual source or a sink are introduced as a mirror image of the shallow void with respect to the ground surface; 3) finally, it is necessary to evaluate the residual shear or normal stresses at the surface and remove them with the introduction of an equivalent and opposite system of forces. This is carried out by integration of the known solutions for point loads (using Cerruti's solution for horizontal stresses and Boussinesq's solution for vertical stresses). The final displacement field within the half-space is then given by the summation of the displacements from steps 1, 2, and 3. The solution provided by Sagaseta (1987) adopted the virtual source technique.

In plane-strain condition, Sagaseta (1987) indicated that the final displacement field is given by

$$\begin{aligned} u_x &= -\frac{a^2}{2}\left(\frac{x}{r_1^2}-\frac{x}{r_2^2}\right)-a^2\frac{x}{r_2^2}\left(1-2\frac{z(z+H)}{r_2^2}\right) \\ u_z &= -\frac{a^2}{2}\left(\frac{z-H}{r_1^2}-\frac{z+h}{r_2^2}\right)+a^2\frac{z}{r_2^2}\left(1-2\frac{x^2}{r_2^2}\right) \end{aligned} \tag{2.31}$$

where u_x and u_z are, respectively, the total horizontal and vertical displacements at point (x,z), $r_1=\sqrt{x^2+(z-H)^2}$, and $r_2=\sqrt{x^2+(z+H)^2}$. At the surface ($z=0$), Equation (2.31) results in

$$\begin{aligned} u_{x,o} &= -a^2\frac{x}{x^2+H^2} \\ u_{z,o} &= a^2\frac{H}{x^2+H^2} \end{aligned} \tag{2.32}$$

As discuss by Sagaseta (1987), despite a consistent deformation pattern around the tunnel, this method leads to an overestimation of the horizontal and vertical settlements in the far field, thus the settlement trough is wider than expected.

Verruijt and Booker (1996) used Equation (2.27) as the singularity solution for the superposition of the singularities method, which is the approximate elastic solution for a deep tunnel in an infinite space (Verruijt and Booker, 1998). In this way, they were able to take into account the ground compressibility (through the Poisson's ratio) and the ovalization deformation mechanism. It is worth noting that the Verruijt and Booker (1996) input deformation parameters, ε and δ, do not induce perfect uniform contraction and ovalization of the tunnel in the half-space as they would in the full-space due to the surface influence. For instance, non-uniform deformations occur around the tunnel cavity due to ε and both ε and δ induce a tunnel downward movement. This vertical displacement decreases with the increase in H because the tunnel tends to behave as in the infinite space. According to the results shown by Pinto and Whittle (2006), the ratio $\Delta u_z/\varepsilon$ is approximately within the range 0.2-0.4 for $\nu = 0.5$ and $R/H = 0.2-0.4$.

The Verruijt and Booker (1996) solution is obtained by superposition of i) the full-space elastic solution for a deep tunnel and its virtual mirror sink image and ii) the Boussinesq-type problem solution to balance the residual normal stresses at the surface due to the previous contribution. The overall ground displacement is given by the summation of Equations (2.33) and (2.34). The singularity and its image result in the following

$$\begin{aligned} u_x &= -\varepsilon R^2\left(\frac{x}{r_1^2}+\frac{x}{r_2^2}\right)+\delta R^2\left(\frac{x\left(x^2-kz_1^2\right)}{r_1^4}-\frac{x\left(x^2-kz_2^2\right)}{r_2^4}\right) \\ u_z &= -\varepsilon R^2\left(\frac{z_1}{r_1^2}+\frac{z_2}{r_2^2}\right)+\delta R^2\left(\frac{z_1\left(kx^2-z_1^2\right)}{r_1^4}-\frac{z_2\left(kx^2-z_2^2\right)}{r_2^4}\right) \end{aligned} \tag{2.33}$$

whereas the following displacement field was obtained by imposing a free-stress boundary condition at the ground surface

$$\begin{aligned} u_x &= -\frac{2\varepsilon R^2 x}{m}\left(\frac{1}{r_2^2}-\frac{2mzz_2}{r_2^4}\right)-\frac{4\delta R^2 xH}{m+1}\left(\frac{z_2}{r_2^4}-\frac{mz\left(x^2-3z_2^2\right)}{r_2^6}\right) \\ u_z &= \frac{2\varepsilon R^2}{m}\left(\frac{(m+1)z_2}{r_2^2}-\frac{mz\left(x^2-z_2^2\right)}{r_2^4}\right)-2\delta R^2 H\left(\frac{x^2-z_2^2}{r_2^4}+\frac{m}{m+1}\frac{2z_2z\left(3x^2-z_2^2\right)}{r_2^6}\right) \end{aligned} \tag{2.34}$$

where H is the depth of the tunnel axis, $z_1 = z-H$, $z_2 = z+H$, $r_1 = \sqrt{x^2+(z-H)^2}$, $r_2 = \sqrt{x^2+(z+H)^2}$, $k = \nu/(1-\nu)$, and $m = 1/(1-2\nu)$. Note that ε and δ are considered as input parameter regardless of the soil and tunnel parameters; therefore their values are generally obtained by back-analysis and curve-fitting of field measurements. Interestingly, the integration

of the settlement trough at the surface

$$u_{z,0} = 2\varepsilon R^2 \frac{m+1}{m} \frac{H}{x^2+h^2} - 2\delta R^2 \frac{h\left(x^2-H^2\right)}{\left(x^2+H^2\right)^2} \tag{2.35}$$

results in a surface soil volume loss (volume per meter of the surface settlement) equal to

$$V_s = 4\left(1-\nu\right)\varepsilon\pi R^2 \tag{2.36}$$

Equation (2.35) highlights that the shape of the settlement trough due to contraction is independent of ν whereas the shape is influenced by the tunnel ovalization. On the other hand, Equation (2.36) displays that V_s is not dependent on tunnel ovalization (δ) and that V_s at the surface increases with a decrease in ν from 0.5. The latter observation is compatible with field data showing that consolidation settlement increases with time and develops uniformly compared to undrained settlements. The main limitation of the approaches proposed by Sagaseta (1987) and Verruijt and Booker (1996) is that the solutions over-predict the width of the surface settlement trough significantly, with wider troughs and larger horizontal movements than observed values (Loganathan and Poulos, 1998).

González and Sagaseta (2001) modified the Verruijt and Booker (1996) elastic solution for an incompressible medium ($\nu = 0.5$) to account for the effect of soil dilation. They introduced an additional term, α, based on the fact that, in a non-elastic medium, the displacements attenuate with a power law of the distance within the plastic zone, $O(1/r^{\alpha})$ with $\alpha \geq 1$. The equations from González and Sagaseta (2001) for horizontal (u_x) and vertical (u_z) displacements are:

$$\begin{aligned}\frac{u_x}{2\varepsilon R\left(\frac{R}{H}\right)^{2\alpha-1}} = &-\frac{x'}{2r'^{2\alpha}_1}\left(1-\rho\frac{x'^2-z'^2_1}{r'^2_1}\right) - \frac{x'}{2r'^{2\alpha}_2}\left(1-\rho\frac{x'^2-z'^2_2}{r'^2_2}\right) \\ &+\frac{4x'z'}{2r'^{2\alpha}_2}\left(\frac{z'_2}{r'^2_2}-\rho\frac{x'^2-3z'^2_2}{r'^4_2}\right)\end{aligned} \tag{2.37}$$

$$\begin{aligned}\frac{u_z}{2\varepsilon R\left(\frac{R}{H}\right)^{2\alpha-1}} = &-\frac{z'_1}{2r'^{2\alpha}_1}\left(1-\rho\frac{x'^2-z'^2_1}{r'^2_1}\right) + \frac{z'_2}{2r'^{2\alpha}_2}\left(1+\rho\frac{x'^2-z'^2_2}{r'^2_2}\right) \\ &-\frac{1}{2r'^{2\alpha}_2}\left(2\left(z'+\rho\right)\frac{x'^2-z'^2_2}{r'^2_2}+4\rho z'z'_2\frac{3x'^2-z'^2_2}{r'^4_2}\right)\end{aligned} \tag{2.38}$$

the prime ($'$) denotes that the variables are normalised by the tunnel depth, H, other geometrical parameters are defined in Figure 2.12. The compressibility parameter α should be assumed equal to the mean value within the soil, considering that $\alpha = 1$ in the elastic condition.

Exact solution Recent developments in the field of the complex variable method resulted in several publications investigating the exact solution of ground movements induced by ground loss, ovalization and buoyancy (due to the self-weight of the removed soil) in the elastic half-space. Verruijt (1997) studied the problem of the uniform convergence of the tunnel boundary, which induces a downward displacement of the tunnel; Strack and Verruijt (2002), Strack (2002) and Verruijt and Strack (2008) studied the buoyancy effect showing that the surface settlement trough is smaller in magnitude and narrower than in the case of ground loss only. Overall, in his review paper, Pinto et al. (2014) proved that the solution derived by superposition of singularity solutions is able to provide a good approximation of the exact one in the case of ground loss and tunnel ovalization (especially for $C/D > 2$). However, the solutions based on the superposition of the singularities method disregards the buoyancy effects (Klar, 2006).

Other solutions An alternative elastic solution was proposed by Park (2004) for the estimation of ground deformations due to tunnels in clay. The author suggested studying the undrained movements due to a tunnel applying the elastic solution of Timoshenko and Goodier (1970) to the case of a circular tunnel within an infinite space. The deep and shallow tunnel cases were studied considering different vertical and horizontal stress distribution within the elastic infinite space. The basic solutions were obtained from relieving the normal and tangential stresses at the tunnel border. The final displacement fields were obtained by imposing prescribed displacement boundary conditions at the tunnel opening: several oval-shaped tunnel deformation conditions (i.e. ground loss distributions) were implemented. However, to improve the predictions of his solutions, Park (2004) proposed to envelope the two distinct solutions for deep and shallow tunnels, obtained starting from a different initial stress state, which is a remarkable inconsistency for an elastic approach (Pinto and Whittle, 2006).

2.1.4.3 Semi-analytical solutions

Close-form semi-analytical solutions have been developed by applying a correcting term to displacement deformation patterns obtained for elastic solutions to improve their predictions. Because of their efficiency, they have been widely implemented in numerical and analytical studies of tunnel-structure interaction.

Loganathan and Poulos (1998) proposed a semi-analytical solution to evaluate undrained movements. Their formula is based on Equations (2.33) and (2.34), the elastic solution of Verruijt and Booker (1996), for an ovalization term $\delta = 0$. By substituting the parameter ε of the elastic solution provided by Verruijt and Booker (1996) with the modified equivalent ground loss parameter

$$\varepsilon_{x,z} = \varepsilon_0 \exp\left[-\left(\frac{1.38x^2}{(H+R)^2} + \frac{0.69z^2}{H^2}\right)\right] \tag{2.39}$$

where $\varepsilon_0 = V_{l,t}/100$ is the equivalent ground loss parameter, the authors derived the following expressions for vertical, u_z, and horizontal, u_x, displacements

$$\begin{aligned} u_z &= \varepsilon_{x,z} R^2 \left(-\frac{z-H}{x^2+(z-H)^2} + \frac{(3-4\nu)(z+H)}{x^2+(z+H)^2} - \frac{2z\left(x^2-(z+H)^2\right)}{\left(x^2+(z+H)^2\right)^2} \right) \\ u_x &= -\varepsilon_{x,z} x R^2 \left(\frac{1}{x^2+(H-z)^2} + \frac{3-4\nu}{x^2+(H+z)^2} - \frac{4z(z+H)}{\left(x^2+(z+H)^2\right)^2} \right) \end{aligned} \tag{2.40}$$

where R is the tunnel radius, H is the depth to the tunnel axis, x is the distance from the tunnel centreline, z is depth and ν is the Poisson's ratio of the soil. Note that the modified equivalent ground loss parameter may be written as

$$\begin{aligned} \varepsilon_{x,z} &= \xi \varepsilon \\ \xi &= 2\exp\left[-\left(\frac{1.38x^2}{(H+R)^2} + \frac{0.69z^2}{H^2} \right) \right] \end{aligned} \tag{2.41}$$

Therefore, Loganathan and Poulos (1998) modified the elastic displacement field proposed by Verruijt and Booker (1996), u^{el}, by introducing a corrective term, ξ, such that the semi-analytical displacement field is $u^{sa} = \xi u^{el}$.

Loganathan and Poulos (1998) theorise the use of $\varepsilon_{x,z}$ to allow for oval-shaped radial ground movements (i.e. oval-shaped ground loss distribution) around the tunnel to overcome the drawbacks of the elastic solution, which adopts a uniform radial ground loss. Unfortunately, Loganathan and Poulos (1998) failed to recognise that the ground loss shape predicted by Verruijt and Booker (1996) for $\delta = 0$ is not uniform due to the influence of the surface. Therefore, as pointed out by Pinto and Whittle (2006), Loganathan's formula is mainly the outcome of a calibration process with the boundary conditions of the corrective term ξ chosen to account for field observations and centrifuge model tests outcomes. This solution was shown to agree with several field measurements of ground movements because the corrective term was conveniently chosen.

Loganathan and Poulos (1998) related the equivalent ground loss parameter, ε_0, (i.e. the tunnel volume loss, $V_{l,t}$) to the gap parameter, g, introduced by Rowe and Kack (1983), which represents the equivalent 2D ground loss considering the 3D nature of the tunnel excavation.

$$\varepsilon_0 = \frac{\pi\left(\frac{2R+g}{2}\right)^2 - \pi R^2}{\pi R^2} \tag{2.42}$$

The aim of using g is to account for the effects of tunnelling methods, shield, lining geometry, 3D elasto-plastic ground deformation and quality of workmanship during the assessment of the tunnel ground loss. The gap parameter can be estimated by means of the procedures proposed by Lee et al. (1992), once the details of the support system and soils are provided, and is defined as follows:

$$g = G_p + U_{3D} + \omega, \tag{2.43}$$

where G_p is the physical gap that represents the geometric clearance between the outer skin of the shield and the lining, which is the sum of twice the thickness of the tailpiece plus the clearance required for erection of the lining, U_{3D} is the equivalent 3D elasto-plastic deformation at the tunnel face and ω is the value that takes into account the quality of workmanship.

Loganathan et al. (2001) extended the semi-analytical approach to the case of tunnelling within sandy grounds introducing an additional parameter in the equation of modified equivalent ground loss parameter $\varepsilon_{x,z}$ as follows

$$\varepsilon_{x,z} = \varepsilon_0 \exp\left[-\left(\frac{1.38x^2}{(H\cot\beta + R)^2} + \frac{0.69z^2}{H^2}\right)\right] \tag{2.44}$$

Assuming that the zone of influence in sands is narrower than in clays, the authors suggested the use of the limit angle $\beta = 45° + \phi'/2$, where ϕ' is the angle of shearing resistance. Chi et al. (2001) carried out a back-analysis of tunnelling-induced ground movements from the Taipei Rapid Transit construction, adopting Equations (2.40) and (2.44), to investigate the value of the angle β. Furthermore, they introduced a factor of backfill grouting α to define a novel gap parameter, g, for EPB shield tunnelling. To sum up their back-analyses, they obtained that the limit angle, β, is approximately 45° for tunnelling in clayey soils whereas it ranges from 40° to 60° for sands; they proposed to assume, respectively, an average β value of 45° for clays and 49° for sands in the case of tunnelling in the silty clay and silty sand of Taipei basin with earth pressure balance (EPB) shield machine. Despite the attempt to highlight some differences in clays and sands, Equation (2.40) does not consider that the deformation pattern in sandy soils is highly dependent on $V_{l,t}$ and C/D. Furthermore, the settlement trough may be wider in sands than in clays for low volume loss and relatively deep tunnels, as displayed by Marshall et al. (2012).

Park (2005) proposed an alternative semi-analytical formula for undrained movements. Similar to Loganathan and Poulos (1998), he adopted the closed-form analytical solution of Verruijt and Booker (1996) with the ovalization term $\delta = 0$. To induce an oval-shaped tunnel ground loss distribution, he proposed the use of the following modified equivalent ground loss parameter

$$\begin{aligned} \varepsilon_{x,z} &= \xi\varepsilon \\ \xi &= 1 - \frac{z-H}{\sqrt{x^2 + (z-H)^2}} \end{aligned} \tag{2.45}$$

The corrective term, ξ, was obtained by considering that ε in Verruijt and Booker (1996) corresponds to a uniform contraction and imposing that the tunnel periphery deforms according to an oval-shaped distortion. Note that this solution is also based on the erroneous interpretation of the Verruijt and Booker (1996) solution because Park (2005) assumed that only a uniform radial displacement is associated with ε, which is not correct. In terms of performance, Park (2005) predicts a wide settlement trough in comparison with field measurements in uniform clay, similar to Verruijt's solution, because the correction ξ of Park (2005) tends to unity in the tunnel far field (i.e. the greater the distance from the tunnel the more $\varepsilon_{x,z}$ tends to ε). Evidently, the Loganathan's semi-empirical solution calibrated on experimental data proved to be more efficient than Park's formula based on a theoretical observation.

Elasto-plastic solution Mair and Taylor (1993) adopted a linear elastic-perfectly plastic ground model and axisymmetric (spherically symmetric) conditions ahead of an advancing tunnel (along the tunnel axis) to predict the ground deformations around tunnels in clays. Therefore, the movements are radial in a spherically symmetric sense at the tunnel heading and in an axisymmetric sense further back from the heading. They showed that field measurements are reasonably consistent with the outcomes of their method. It is also assumed that the tunnel is circular, of diameter D, and that the lining is installed at a distance P behind the face.

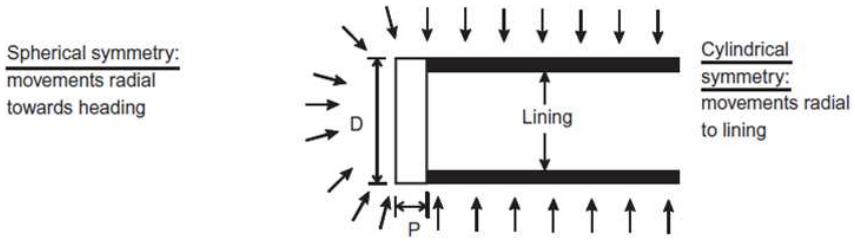

Fig. 2.14 Idealisation of a tunnel heading [Mair and Taylor (1993)].

The radial ground movements in a plane-strain tunnelling condition are well schematised by means of a fully unloaded cylindrical contracting cavity and the displacement expression presented by the authors is

$$\frac{\delta}{a} = \frac{s_u}{2G}\left(\frac{a}{r}\right)\exp(N^* - 1) \tag{2.46}$$

where δ is the radial movement at radius r, a is the inner radius of the tunnel, N^* is the stability ratio ($N^* = \sigma_0/s_u$), σ_0 is the initial total stress at the cavity boundary, s_u is the undrained shear strength, and G is elastic shear modulus. An approximate evaluation of the soil movements ahead of the tunnel face was proposed by the authors by making use of a fully unloaded spherical cavity as follows

$$\frac{\delta}{a} = \frac{s_u}{3G}\left(\frac{a}{r}\right)^2\exp(0.75N^* - 1) \tag{2.47}$$

In the case of deep-tunnelling without internal temporary support, the value σ_0 could be approximated with the vertical stress at the level of the tunnel axis. Thus, the value of N^* corresponds to the stability ratio, N, shown by Equation (2.1).

2.2 Tunnelling effects on pile foundations

The development of urban areas has resulted in an increased demand for underground construction. The increasing number of case studies testifies that, in recent years, tunnelling near to piled structures and infrastructure has become more common. For instance, Mair (1993) reported the horizontal and vertical displacements during the excavation of a new escalator tunnel from the basement of a piled building in London. Takahashi et al. (2004) reported on the construction of the Higashi-Sinagawa tunnel section of the Rinkai Railway, Tokyo. Jacobsz et al. (2005) reported on the effects of the CTRL tunnel construction on piled bridges. Teparaksa et al. (2006) presented settlements for timber piled three and four storey structures and a pre-cast concrete piled bridge subjected to the construction of a new flood diversion tunnel. Photayanuvat et al. (2006) and Phienwej et al. (2006) analysed the construction of the First Bangkok Subway Line, where instrumentation for monitoring of ground movements induced by the excavation was an important component of the construction works to avoid damages to existing buildings.

In general, the construction of new tunnels in the proximity of deep foundations raises concerns related to pile failure and associated structural damage (in both the superstructures and the foundation). Additionally, because of uncertainties related to excavation-induced effects on piles, significant project costs are committed to structural protection measures according to a conservative approach. To reduce uncertainties in the design of tunnel route/depth and the provision of preventative actions, such as compensation grouting, it is required to achieve an understanding of the global soil-pile-structure interaction and the way it may affect/damage the superstructure. The first step towards the global understanding is the study of the response of piles and pile groups to tunnelling when the effects of protective measures or other construction activities are not present.

The following presents an overview of the main studies that address the problem with field, experimental, and analytical research; these provide good insights into the main interaction phenomena. However, it is worth noting that the problem of tunnel-pile foundations interaction has also been investigated with complex 3D numerical modelling (Cheng et al., 2007; Lee and Jacobsz, 2006; Mroueh and Shahrour, 2002; Pang et al., 2005), and that further recent advancements have been made (Jongpradist et al., 2013; Lee, 2012; Yoo, 2013).

2.2.1 Piles

Pile performance to withstand a vertical load, P, is evaluated in terms of bearing capacity and stiffness. It is generally desirable to have a pile with both high capacity and stiffness so that the design load results in acceptable settlement. A schematic of pile bearing capacity is shown in Figure 2.15. The total bearing capacity (Q) consists of two parts: base capacity (Q_{tip}) and shaft frictional capacity (Q_s). The average base resistance pressure (q_b) is given by the ratio Q_{tip} to the area of the pile cross-section (A_p), and the average shaft friction ($\bar{\tau}_s$) equals Q_s divided by

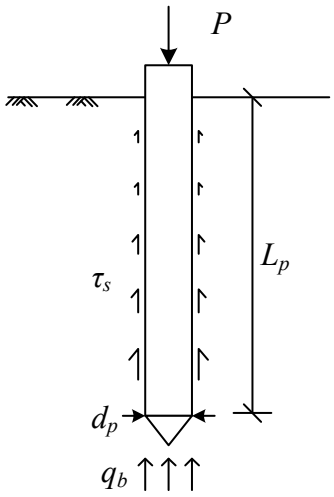

Fig. 2.15 Schematic of pile bearing capacity.

the shaft surface area (A_s).

$$Q = Q_{tip} + Q_s = q_b \times A_p + \int_0^{L_p} \tau_s \pi d_p dz = q_b \times A_p + \bar{\tau}_s \times A_s \tag{2.48}$$

It is widely known that the pile installation method has a significant impact on the stress regime of the pile/surrounding soil and subsequently on the pile load-settlement curve. In the following, piles are distinguished between displacement (driven and jacked) and non-displacement (bored) piles because their response to tunnelling is highly influenced by the different distribution of pile load between the pile shaft and base. Non-displacement piles withstand the pile service load mainly through shaft friction since the displacements needed to mobilise base capacity do not occur. Displacement piles have their base capacity partially mobilised by the installation process, with residual pressures locked in at the base and negative shaft friction along the shaft. This work does not aim to investigate the differences occurring because of installation technique (for instance between jacked or driven piles).

2.2.2 Field trials

A full-scale trial was performed on piles at the Second Heinenoordtunnel project for the assessment of effects due to the construction of the new North-South metro line in Amsterdam (Kaalberg et al., 2005), where most buildings are founded on old timber piles. The pilot tests were conducted in strata consisting of a layer of 4m of soft clay underlain by fine sand. To reproduce similar geotechnical conditions, wooden and concrete piles were driven within 2m diameter pre-installed clay columns to simulate the 10-13m of soft clay in Amsterdam so that the ratio between bearing capacity and shaft friction was reasonably reproduced. The final pile configuration was equivalent to the end-bearing piles founded within the sand layer. On the other hand, Selemetas (2005) investigated the pile response to tunnelling in London Clay, planned as part of the Channel Tunnel Rail Link (CTRL) project in the UK. Two twin 8.15m diameter

tunnels were bored using Earth Pressure Balance (EPB) shields with tail-skin grouting. The field trial involved the installation, loading and monitoring of four piles and the comparison with greenfield ground settlements. The driven-cast-in-situ piles were embedded at different depth: two of the piles were end-bearing in the Terrace Gravels (8.5m long) and the other two were friction piles with their toes in London Clay (13m long). One of each type of pile was located directly above the centreline of one of the tunnels while the other two piles were located at an offset of 9m from the same tunnel. The piles were loaded with a load corresponding to half of their ultimate capacity to compare the results with the work of Kaalberg et al. (2005).

The most relevant outcomes of the field trials were obtained by comparing pile and ground settlements. Kaalberg et al. (2005) and Selemetas (2005) suggested three zones where pile head settlements may be larger than (zone A), equal to (zone B) or smaller than (zone C) the greenfield surface settlements (see Figure 2.16). In general, piles with their tips within the area of major settlements above the tunnel settle more than the surface greenfield settlement trough; piles outside this area settle less than surface greenfield levels. These also agree qualitatively with experimental results obtained with centrifuge testing (Jacobsz et al., 2004; Marshall and Mair, 2011), which are illustrated in the following.

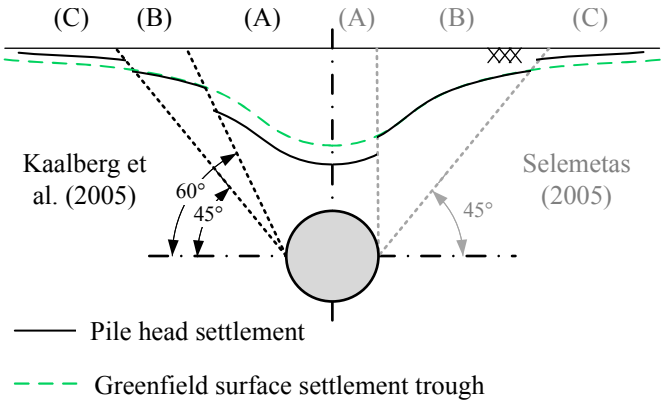

Fig. 2.16 Proposed relationships between pile head and greenfield surface settlements depending on pile tip location.

However, despite the general agreement, a comparison of studies available in the literature carried out by Dias and Bezuijen (2015) demonstrated that the relationship between pile head and greenfield surface settlements is not a unique function of the relative tunnel-pile tip position; it also depends on working loads, tunnel volume loss, and distribution of working load between pile base and shaft. This should impact previously proposed relationships between pile and greenfield surface settlements, which is described as a function of the pile tip location with respect to the tunnel. As shown in Figure 2.17, Dias and Bezuijen (2015) indicated that the regions A-B-C defining the relative pile/surface settlements do not capture the full complexity of the problem. The authors suggested an upper limit of the normalised pile head settlement depending on the normalised horizontal pile offset to the tunnel centreline, displayed in Figure 2.17(b). However, use of this upper limit would lead to an over-conservative assessment of tunnelling-induced deformation in piled buildings.

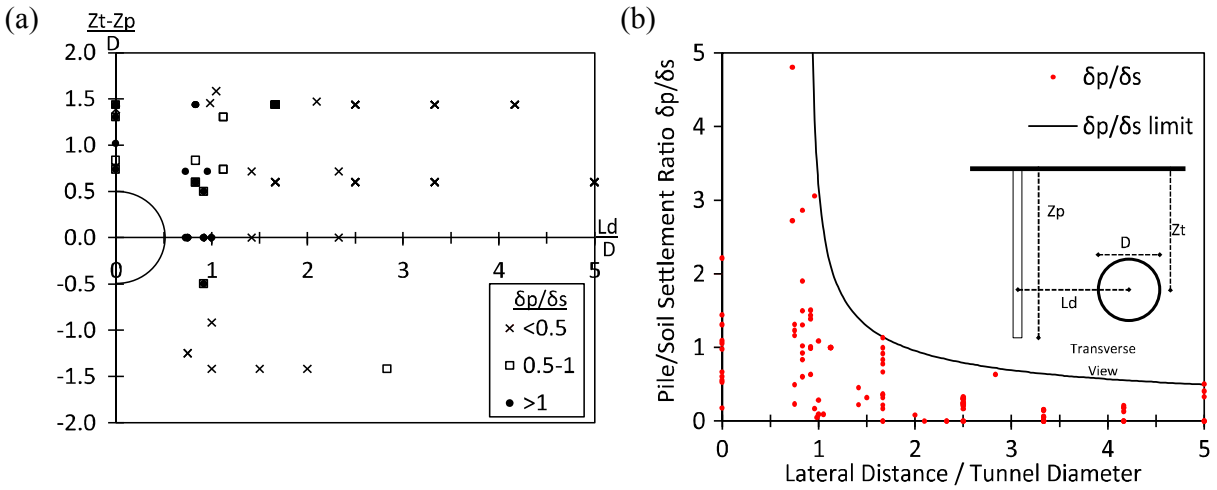

Fig. 2.17 Analysis of pile settlement data: (a) ratio between the pile (δp) and the ground surface settlements (δs) with respect to the pile tip position; (b) upper envelope of measured $\delta p/\delta s$ at different normalised lateral distances [Dias and Bezuijen (2015)].

2.2.3 Physical and centrifuge studies

2.2.3.1 Physical modelling

Lee and Bassett (2007) developed a testing equipment to perform 1g model experiments of tunnelling near to piles whose outcomes were validated against FEM analysis. In particular, they used multi-sized aluminium rods regarded as the frictional granular material in plane-strain condition. In order to replicate the numerical mesh size, the aluminium rods were variable in size: smaller diameter rods were used close to the row of piles and the tunnel, whereas larger diameter rods were located close to the boundaries. Moreover solid aluminium alloy plates were adopted to represent a row of closely spaced piles. The outcomes of physical and numerical modelling were used to identify pile-tunnel influence zones , which were larger that the regions previously proposed by centrifuge modelling and field trials (Jacobsz et al., 2004; Kaalberg et al., 2005; Selemetas, 2005). However, considering the approximations resulting from plane-strain problem and 1g stress conditions, their findings could be considered in qualitative accordance with previous researches.

2.2.3.2 Centrifuge modelling: non-displacement single piles and pile group in clay

Loganathan et al. (2000) performed a series of three centrifuge tests to investigate the effects of tunnelling in undrained condition on a single pile and 2×2 pile group foundations in pre-consolidated kaolin clay. As shown in Figure 2.18, the depth of the tunnel was varied, whereas the pile base depth was held constant (tunnel depth lower, equal to and greater than pile embedment depth). The piles were jacked into the clay prior the spin up and loaded to a service load corresponding to 50% of the estimated ultimate load (i.e pile safety factor $SF = 2$) reproducing the response of non-displacement piles. They were instrumented with strain gauges to evaluate axial and bending forces; pile displacements were also measured.

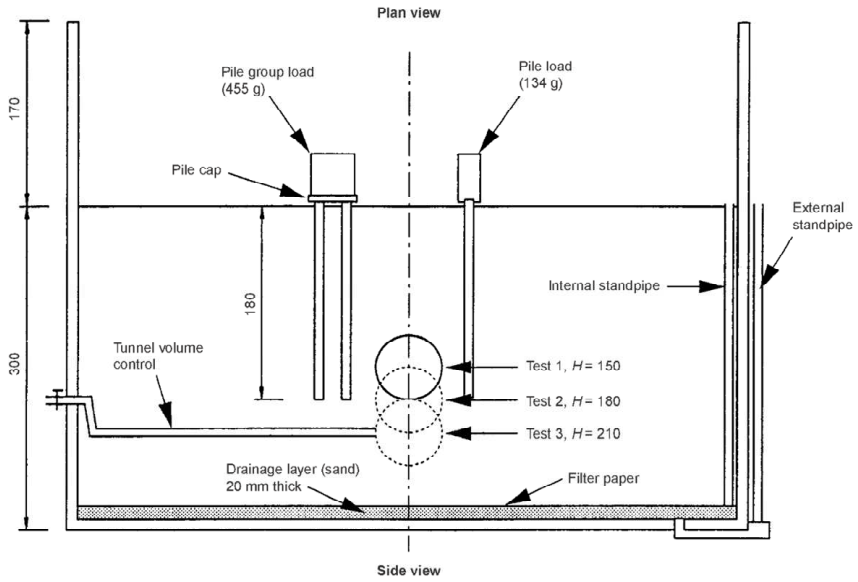

Fig. 2.18 Configuration of the centrifuge model [Loganathan et al. (2000)].

Overall, their investigation pointed out the major interaction mechanisms between a new tunnel and pile foundations: the group effect is beneficial because it decreases forces and settlements induced in the piles; tunnelling adjacent to piles is critical for the transverse response of the foundation both in terms of pile deflections and bending moments; tunnelling beneath piles results in remarkable settlements. Finally, the authors highlighted a linear relationship between ground volume loss and maximum bending moment (within the range of $V_{l,t}$ measured in practice) underlining the usefulness of elastic tunnel-pile interaction analysis.

Williamson (2014) performed a series of centrifuge tests of tunnelling beneath non-displacement piles in stiff clay with a constant service load. Part of the results were discussed by Mair and Williamson (2014). The test plan investigated the effects of pile horizontal offset to the tunnel centreline, pile load condition and soil stiffness/strength. The trends of the pile settlements confirmed previous research showing that piles directly above and adjacent to the tunnel settle, respectively, more and less than the greenfield surface settlement trough. Additionally, there was a remarkable influence of the external head load on pile displacements: the higher the pile head load the greater the pile settlement due to a given volume loss. Regarding pile failure, it should not be expected, even at high tunnel volume loss, for non-displacement piles in clays. This is due to the tunnelling-induced soil degradation at the pile shaft and base being balanced by additional pile settlements relative to the soil (that mobilise positive shaft friction). Finally, in the case of stiff clays, the effects of the relative pile-soil stiffness were negligible and the variation in the axial force distribution along the pile axis with volume loss was small.

2.2.3.3 Centrifuge modelling: displacement single piles in dry dense sand

Jacobsz (2002) and Jacobsz et al. (2004) investigated, with centrifuge tests, the problem of tunnelling beneath single displacement piles installed in dense dry sands with different horizontal

offsets with respect to the tunnel centreline. This installation method results in end-bearing piles and a local increase in the soil stiffness around the pile.

Jacobsz (2002) identified the tunnel-pile interaction mechanism in the case of an end-bearing pile located above the tunnel. Tunnelling results in the reduction of the stress level within the soil, associated with strength loss of the soil beneath the pile base; this results in, subsequently, the reduction in pile base loads and increase in shaft friction. Initially, at small tunnel volume loss, small pile settlements allow mobilising the required additional shaft friction; when the maximum shaft capacity is reached, further volume loss results in large pile displacements to guarantee equilibrium between pile capacity and applied external load.

Analysing the series of tests where the pile location was varied, the authors defined influence zones where one may expect large pile displacements at a volume loss of 1.5% (displayed in Figure 2.19), where large displacements correspond to settlements greater than 20mm at prototype scale (0.022 pile diameter). Furthermore, they partitioned the area above the tunnel in four influence zones (A, B, C, and D) to qualitatively describe the ratio of pile head settlement to greenfield surface movement depending on the location of the base of a pile, as subsequently done by Kaalberg et al. (2005) and Selemetas (2005), and to describe the effects of tunnelling on shaft and base capacity. A summary of the experimental observations made by Jacobsz (2002) on the influence zones follows.

- Zone A:
  - Pile settlement greater than surface soil settlement.
  - Base loads reduced rapidly from 0 to 1.5% volume loss, after which base load remained relatively constant as pile settlement accelerated rapidly.
  - Full shaft friction mobilised during pile settlement of less than 1% of the pile diameter, after which it remained relatively constant.
- Zone B:
  - Pile settlement greater than surface soil settlement.
  - Base load reduction occurred at a similar rate as Zone A.
  - Shaft friction mobilised quickly with tunnel volume loss. Unlike Zone A, shaft loads continued to rise gradually, likely associated with an increase in normal stress on the pile shaft resulting from high shear strains and soil dilation.
- Zone C:
  - Pile settlement similar to surface soil movements.
  - Base loads reduced more gradually than Zones A and B.
  - Shaft friction initially negative; afterwards, the base load reduced at a lower rate than in Zones A and B without ever fully mobilising the total shaft friction.

- Zone D:
  - Pile settlement less than the surface soil settlement.
  - Base load increased slightly due to negative skin friction but remained relatively constant after about 1.5% volume loss.
  - Shaft friction negative with very small changes in load distribution occurring.

Furthermore, it was claimed by Jacobsz et al. (2004) that horizontal stress changes resulting from the tunnel volume loss process do not significantly increase the shaft friction capacity of piles located directly above a tunnel; on the contrary, the dilatation in the shearing zone propagating from the tunnel shoulder to the surface increases the shaft friction capacity (Jacobsz et al., 2004).

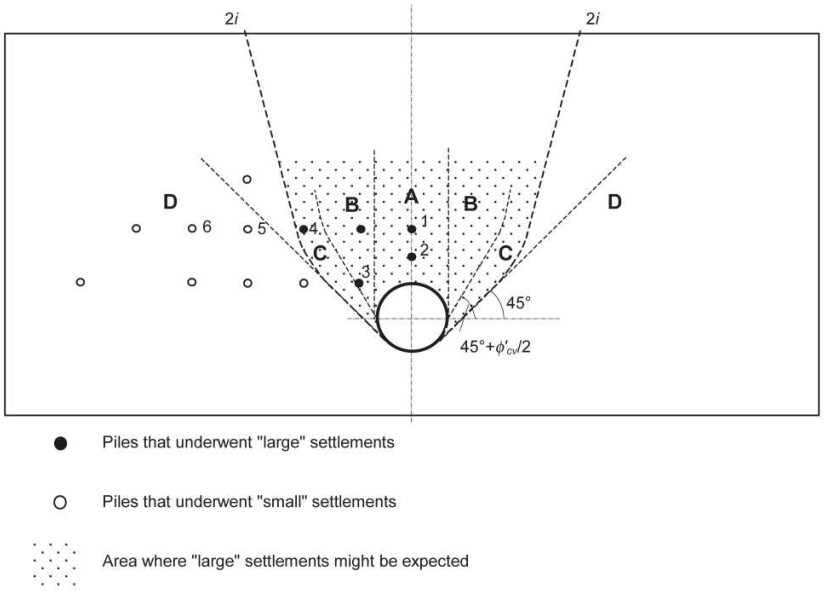

Fig. 2.19 Influence zone around a tunnel [Jacobsz et al. (2004)].

Overall, the work of Jacobsz (2002) illustrated that the evaluation of the pile reserve in shaft capacity and the load distribution between shaft and base are required to assess the effects of tunnelling. The critical volume loss (associated with pile failure) is a function of the location of the pile base within the zone of influence and shear bands, the length of the pile shaft on which friction can be mobilised, the roughness of the shaft and the amount of shaft capacity mobilised prior to tunnelling. Consequently, tunnel-pile interaction is considerably different for displacement and non-displacement piles.

2.2.3.4 Centrifuge modelling: displacement pile groups in dry dense sand

Analysing the results of two centrifuge tests, Marshall (2009) and Marshall and Mair (2011) evaluated the main aspects of tunnelling beneath displacement pile group in dense sands, with applied constant head loads during tunnelling. To provide detailed information, the experiments were conducted measuring, during the pile jacking and the tunnel volume loss, pile settlements

and soil strains at the Perspex window. Two aluminium piles with semi-circular cross-section were jacked a distance of 2 pile diameter into silica sand against a Perspex window (assumed to be a frictionless plane of symmetry). The installation took place after the spin-up procedure to replicate realistic ground conditions around the piles. Prior to volume loss modelling, the driving force was reduced to a lower service load giving a safety factor $SF = 1.6$. The layout of the tests was related to the influence zones identified by Jacobsz et al. (2004). The first test consisted of a pile immediately above the tunnel centerline and another pile at an offset of 2.1 tunnel diameters, whereas the second test had two offset piles at a distance of approximately 1 tunnel diameter from the tunnel.

The displacement distribution at the pile tip during jacking consisted in outwards displacements from the tips, which agrees with a cavity expansion mechanism altering considerably the soil state around the pile, as shown by Figure 2.20(a). As a consequence, pile and ground displacements resulting from tunnel-soil-pile interaction differ from greenfield movement distributions. The comparison of pile and greenfield settlements, shown in Figure 2.20(b), highlights that, at low tunnel volume loss, piles showed negligible settlements with respect to the greenfield case up to the critical volume loss, when a brittle pile failure mechanism took place. This tunnel-pile-soil behaviour was probably due to the dense soil state that allowed for soil dilation. The authors suggested that for displacement piles (with the installation process affecting the ground state) the greenfield movements should not be used as input for analytical tunnel-soil-pile interaction analysis, whereas this approach may be realistic for non-displacement piles. Additionally, Marshall and Mair (2011) outlined a linear relationship between the volume loss at pile failure and the square of the normalised tunnel-pile distance (see Figure 2.20(c)) which would confirm the applicability of the cylindrical cavity contraction theory to study the failure of end-bearing piles. This chart may provide some guidance, however it should be noted that the critical tunnel volume loss for driven piles is probably affected by the soil density prior to tunnel installation as well as the pile loading condition (i.e. the initial safety factor).

In general, the results of this series of tests confirmed the interaction mechanisms proposed by Jacobsz et al. (2004), which are based on the decrease in base capacity due to volume loss, and agreed with the influence zones defined by the authors. In addition, it was confirmed that, at the pile failure, large pile settlements compensate any tunnelling-induced loss in confining pressure at the pile tip to re-establish the equilibrium condition (pile load equal to bearing capacity); in this condition a zone of soil displacing uniformly from the tip towards the sides of the tunnel was measured. This zone was surrounded by bands of dilating soil at high shear strains.

2.2.3.5 Centrifuge modelling: non-displacement single piles in sandy ground

Lee and Chiang (2007) provided in-depth analysis of tunnel-bored pile interaction in sandy ground based on a series of centrifuge tests in saturated sand. Instrumented axial and bending piles subjected to constant axial loads with different factors of safety were installed during the preparation of the sand bed: the piles were placed either side of the tunnel and they were not

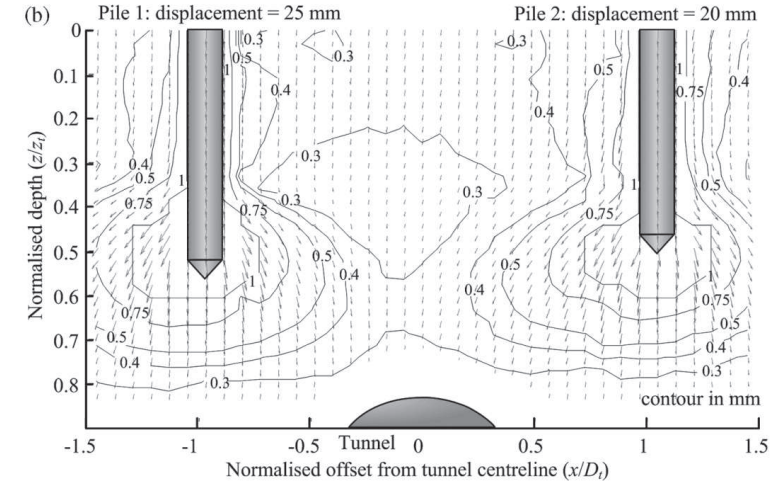

(a)

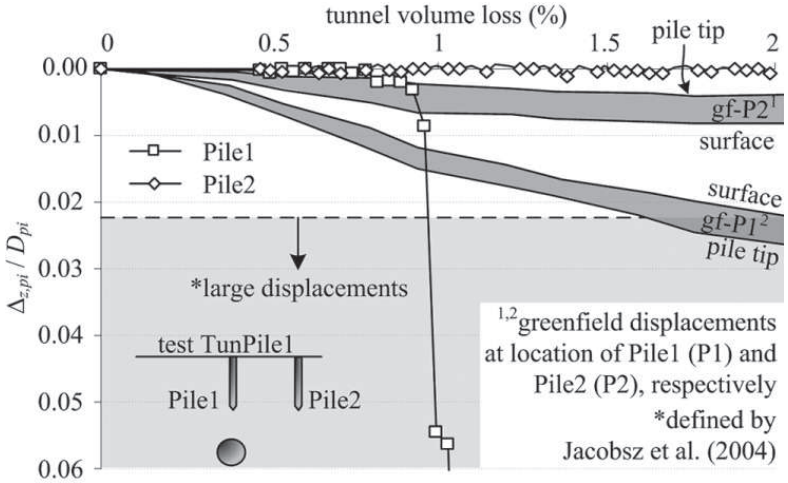

(b)

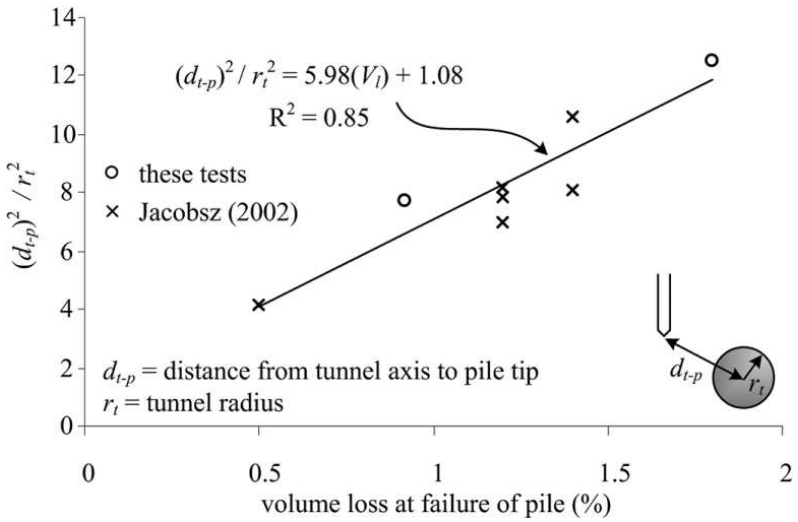

(c)

Fig. 2.20 Centrifuge modelling of tunnelling beneath jacked piles: (a) jacking displacement patterns; (b) pile and greenfield settlements; (c) volume loss at pile failure [Marshall and Mair (2011)].

driven after spin-up to replicate the response of bored piles. The tunnels were embedded at depths with various cover-to-diameter ratios.

The measurements of pile settlements and forces indicated that only the tunnel-pile depth ratio influences the bending moment distribution, but both the pile-tunnel depth ratio and the working load on the pile determine the axial force profile along the pile. Interestingly, the more the pile is loaded (i.e. the lower the initial SF), the more the pile is expected to settle. Furthermore, the authors identified the main causes of pile settlements: loss of skin friction for tunnelling adjacent to piles (compensated by the mobilised base capacity) and the reduction of end bearing capacity during tunnelling at the pile base depth. Although the piles were not driven, these mechanisms are consistent with the work of Jacobsz (2002). To sum up, the author represented the qualitative variation of axial load and skin friction with the sketches shown in Figure 2.21.

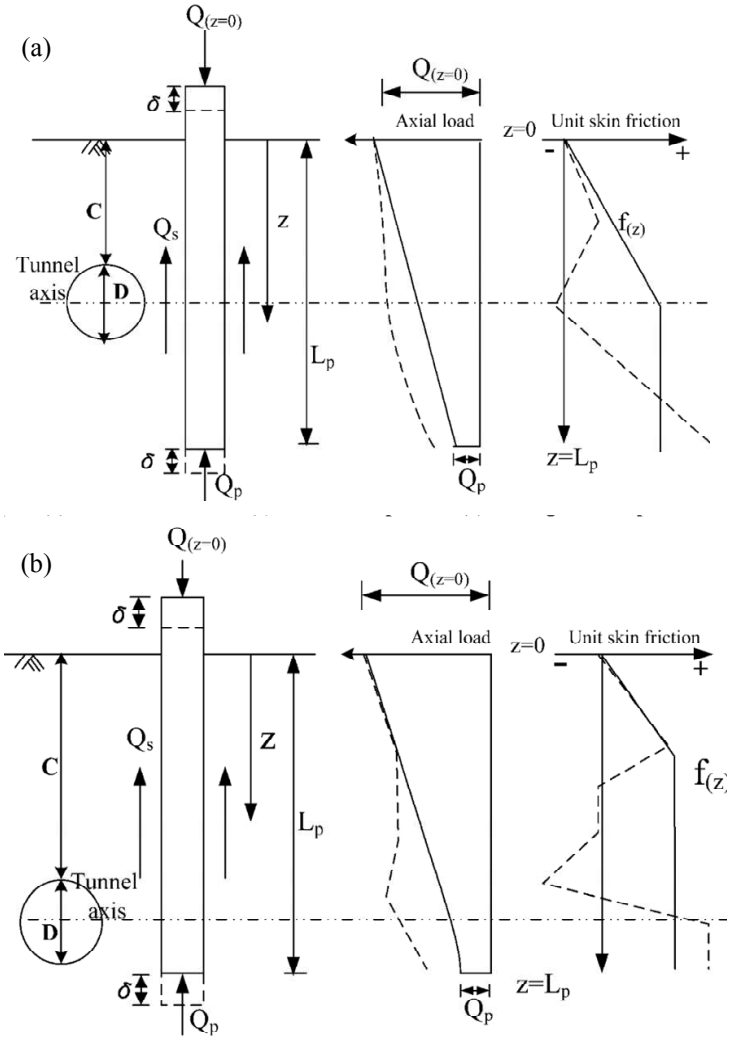

Fig. 2.21 Load transfer mechanism and skin friction profile at the tunnel collapse state for (a) $L_p/z_t > 1.0$ and (b) $L_p/z_t = 1.0$ [Lee and Chiang (2007)].

2.2.4 Analytical studies

Despite the non linear behaviour of the soil and the complex mechanisms that rule the interactions, analytical solutions have been developed for the estimation of the effects of tunnelling on piled foundations. The fundamental simplifying assumptions concerning the soil modelling, soil-pile interactions, tunnelling-induced movements and pile installation effects are illustrated in this section to obtain a better understanding of the problem.

2.2.4.1 Cavity expansion/contraction method

Cavity expansion theory was first applied by Poulos and Deng (2004) to evaluate the loss of pile geotechnical capacity due to tunnelling (i.e. loss of shaft friction and end bearing capacity). The researchers coupled a 2D elastic, cylindrical cavity contraction analysis and standard bearing capacity factors. Although the radial displacement pattern around the tunnel is oval-shaped rather than uniform (Loganathan and Poulos, 1998), the stress change predicted by the proposed method agreed with 2D FEM benchmark analyses. The authors carried out several parametric studies that pointed out a dependence between the loss of geotechnical capacity and the distance between the pile tip and the tunnel, which agrees with Marshall and Mair (2011). It is possible to note a significant loss of bearing capacity within the critical zone defined by Jacobsz (2002), up to 90% when the pile tip is close to the tunnel, whereas the expected reduction is limited to a maximum of 30% for tunnelling adjacent to the pile.

An elasto-plastic analysis method was presented by Marshall (2012) to estimate the safe distance between end-bearing displacement piles and tunnels based on an expected failure tunnel volume loss. Note that both the methods proposed by Poulos and Deng (2004) and Marshall (2012) do not provide information on tunnelling-induced displacements; their methods aim to provide insights on the pile residual bearing capacity. The ground was modelled as an elastic-perfectly plastic material using the Mohr-Coulomb failure criterion (to account for the dilation effects) and a modified shear modulus of the soil was used to account for the effect of pile installation. The analytical solution is based on the combination of spherical and cylindrical cavity expansion/contraction methods, although the superposition of spherical and cylindrical stress changes would not be strictly compatible with the plastic constitutive law. This method was, subsequently, revised by Marshall and Haji (2015) to improve the formulation of the modified soil stiffness and to include the effects of pile shaft capacity degradation with volume loss.

To summarise, the analytical method of Marshall and Haji (2015) consists of the following 4 stages. [a] For displacement piles, where pile installation has a remarkable effect on the ground, it is necessary to replicate the pile installation. A spherical cavity expansion analysis is used to evaluate the limiting cavity pressure and the change in ground stress around the pile due to its installation; furthermore, a procedure to account for the effect of pile installation on soil stiffness is included. [b] The end-bearing and shaft capacity of the pile is evaluated following the methods of Randolph et al. (1994). [c] A cylindrical cavity contraction analysis is used to evaluate the effect of tunnel volume loss (cavity contraction) on the stresses within the ground.

[d] The reduction in pile end-bearing and shaft capacity is evaluated based on the altered stress conditions within the ground (due to [c]) at the tip and the shaft of the pile.

A pile capacity reduction factor $R_{Q,S}$ which accounts for the effect of the tunnel contraction on both pile end-bearing and shaft capacities was defined by Marshall and Haji (2015) as

$$R_{Q,S}\left[V_{l,t}\right] = \frac{Q_{Vlt}}{Q_0} = \frac{q_{b,Vlt}d_p + 4\bar{\tau}_{s,Vlt}L_p}{q_{b,0}d_p + 4\bar{\tau}_{s,0}L_p} \tag{2.49}$$

where Q is the pile bearing capacity, q_b is the end-bearing capacity pressure of the pile; $\bar{\tau}_{S,Vlt}$ is the average shear stress along the pile shaft, and the subscripts 0 and V_{lt} indicate the initial and post tunnel volume loss values, respectively. The value of $R_{Q,S}$ at pile failure was investigated and compared against centrifuge test data for tunnelling beneath jacked piles in dense sand (dataset from Jacobsz (2002) and Marshall (2009)). The authors suggested that $R_{Q,s} = 0.85$ corresponds conservatively to a critical value of tunnel volume loss, $V_{l,t}^f$, associate with pile failure and potentially large displacements. Therefore, a safety pile-tunnel distance could be evaluated considering $R_{Q,s} = 0.85$ if the service load is approximately 50-60% of the maximum jacking force. However, this approach neglects the importance of the initial pile safety factor and would lead to the same value of $V_{l,t}^f$ in the case of different service loads, P.

A modified approach is currently being investigated by the author. If the definition of initial safety factor, $SF_0 = Q_0/P$, and residual safety factor after ground loss, $SF_{Vlt} = Q_{Vlt}/P$, are introduced as the ratio between the pile bearing capacity, Q, and the service load, P, the residual safety factor can be computed as

$$SF_{Vlt} = R_{Q,S} \times SF_0 \tag{2.50}$$

By definition, pile failure due to the critical volume loss is associated with $SF_{Vlt} = 1$. Therefore, considering Equation (2.50), the reduction factor at failure, $R_{Q,S}^f$, is equal to the inverse of SF_0. This definition of the limit value of $R_{Q,S}^f$ would agree with the data plotted in Figure 2.22 ($R_{Q,S}^f = 1/SF_0 = 0.6 - 0.75$ for this dataset) providing a criterion to account for the pile load P in the pile failure mechanism. Future work will explore this approach with cavity expansion/contraction methods.

2.2.4.2 Two-stage analysis method (TSAM)

Soil-structure interaction systems are characteristically complex due to the effects of interfaces, soil non-linearity, and plasticity. However, many useful tools for tunnel-pile interaction analysis have been developed using the elastic framework which are based on a two-stage procedure: (1) the greenfield soil displacements caused by tunnel excavation are estimated analytically or empirically, through closed-form expressions, or numerically using software based on the finite element (FE) or finite difference (FD) methods; (2) the analysis of the full system, including soil, foundation and superstructure, is carried out considering the foundation subjected to a system of external loads that would, in the absence of the included structure, reproduce the greenfield soil movements. Two-staged analyses of tunnel-pile interaction problems have incorporated

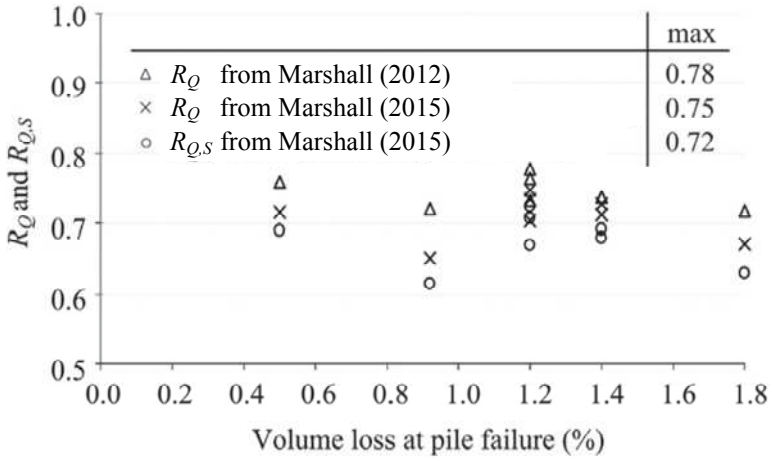

Fig. 2.22 Comparison of reduction factor predicted by Marshall (2012) and Marshall and Haji (2015) [Marshall and Haji (2015)].

continuum or Winkler-based analyses in order to study tunnel-single pile and tunnel-pile group interactions. However, most of the works in this section considered the problem of tunnelling adjacent to piles.

Boundary element elastic methods Several authors used a boundary element method (BEM) to analyse pile group response to tunnelling (Figure 2.23). Chen et al. (1999) studied lateral and axial responses of single piles due to greenfield soil movements estimated with the solution of Loganathan and Poulos (1998). The second stage of the analysis was performed with a BEM that models the pile as an elastic beam with uncoupled vertical and later behaviour and the surrounding soil as an elastic continuum. The model accounts for local soil failure imposing a limit to the maximum lateral and shaft pile-soil stresses. A parametric study of tunnel-single pile interaction was carried out confirming that the pile response to tunnelling depends on the pile tip location with respect to the tunnel horizontal and vertical axes. The authors suggested using the tunnel-single pile interaction analysis as a conservative upper bound approach.

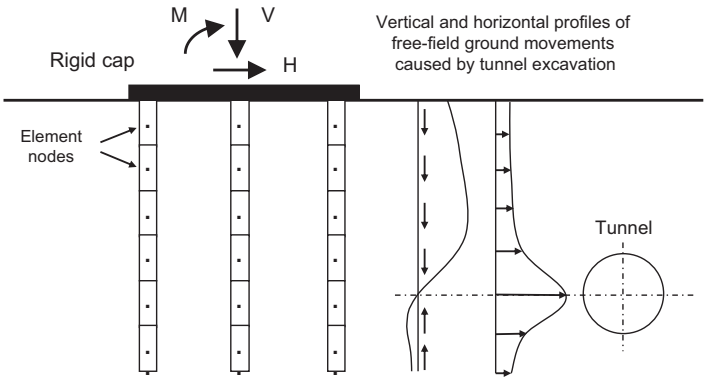

Fig. 2.23 BEM schematisation of the problem [Basile (2014)].

Loganathan et al. (2001) and Xu and Poulos (2001) analysed single piles and pile groups. They used the 3D elastic BEM proposed by Xu and Poulos (2000) for pile-soil interaction

with fully coupled axial, lateral and torsional behaviour of the pile and no slippage or soil plastic behaviour at the pile-soil interface. The basic assumption of a rigid cap that is not in contact with the ground was introduced to study pile groups. 2×2 pile groups were analysed to evaluate the effects of pile length and horizontal distance from the tunnel. As reported by Loganathan et al. (2001), remarkable pile settlements and lateral displacements were shown by the piles with the tip at the tunnel axis level, whereas negative skin friction and additional bending moments characterised piles with their base at the invert depth. The authors confirmed that the qualitative response of piles equally positioned with respect to the tunnel does not differ if isolated or in a pile group; however, the group effect is beneficial, resulting in a reduction in the tunnelling-induced forces.

Basile (2014) extended previous works on BEMs to include the non-linear and plastic soil behaviour at the soil-pile interface. The author limited the maximum normal and tangential stress at the pile–soil interfaces (shaft and base) and implemented a soil stiffness degradation curve with the pile–soil interface stress according to a hyperbolic stress-strain law. The comparison of this BEM model outcomes with previously published results was satisfactory. It was confirmed that the group effect is beneficial because it decreases foundation displacements and internal pile forces compared to isolated piles. Furthermore, the work of Basile (2014) indicated that soil non-linearity leads to a remarkable reduction of axial forces within the piles at high volume loss.

Winkler-based methods Several researchers considered a beam on a Winkler elastic foundation to study the problem of tunnel-pile group interaction, confirming the beneficial effects of pile-soil-pile interaction. Kitiyodom et al. (2005) adopted a previously published FEM computer programme PRAB (Piled Raft Analysis with Batter piles) to study the considered problem, implementing as free-field input the tunnelling-induced movements predicted by Loganathan and Poulos (1998). The problem consists of a piled flexible raft and the ground modelled with a plate, elastic beams and interactive springs. The interactions between structural members (pile-soil-pile, pile-soil-raft and raft-soil-raft interactions) were modelled based on Mindlin's solutions for both vertical and lateral forces, whereas the integral method was adopted for the definition of the springs stiffness and to consider the interaction between the nodes of the same pile. This was necessary to improve the estimation of pile internal forces, in particular axial forces. Kitiyodom et al. (2005) demonstrated that this method allows for the prediction of the excavation-induced deformations and load distributions of piled raft foundations by comparing their analyses to the output of BEMs.

Huang et al. (2009) proposed to solve the problem of tunnel-pile group interaction with the use of a fully elastic Winkler-based model implemented with a FDM (finite difference method) with no gap and slippage at the soil-pile interface. Firstly, at the second stage, the problem of tunnel-single pile interaction is solved with the theory of a beam on a Winkler elastic foundation. Secondly, the difference in displacement between the greenfield and the single pile displacement field is computed and propagated to the other piles, resulting in additional forces to the receiver pile, to account for the shielding effect within a pile group. Note that the shielding

displacements (i.e. the pile-pile interaction) are propagated using a logarithmic attenuation function and Mindlin's solution in the vertical and horizontal solution, respectively. Finally, the response of a pile group due to tunnelling is obtained by the superposition of the tunnel-single pile and pile-pile interaction contributions. In terms of displacements, the results agree with the work of Loganathan et al. (2001) and Xu and Poulos (2001), which show that the group effect is beneficial, despite an underestimation of the induced axial loads along the pile axes.

Zhang et al. (2011a,b) and Zhang et al. (2013) improved the Winkler-based soil model to account for soil non-linearities, linear elastic unloading and reloading curves and pile-soil interface characteristics following the FDM approach used by Huang et al. (2009). These works aimed to evaluate the influence of working loads on the pile-tunnel interaction. When considering the response of a pile group, to account for the pile-pile interaction, it was assumed that only the elastic contribution of the tunnel-single pile interaction propagates to other piles (with a logarithmic attenuation function), whereas the plastic behaviour is limited at the pile shaft (attenuation function is null). The pile-pile interaction was numerically implemented with an iterative process to consider that each propagated displacement from the source to the receiver pile would result in an attenuated displacement for the source element. This is a drawback of adopting a FDM rather than a FEM to implement the model. In general, these works showed that an increase in the existing working loads results in an increase of excavation-induced pile settlements and a decrease of axial forces within the piles. These conclusions agree with BEM model analyses carried out by Basile (2014) and the experimental outcomes of Lee and Chiang (2007).

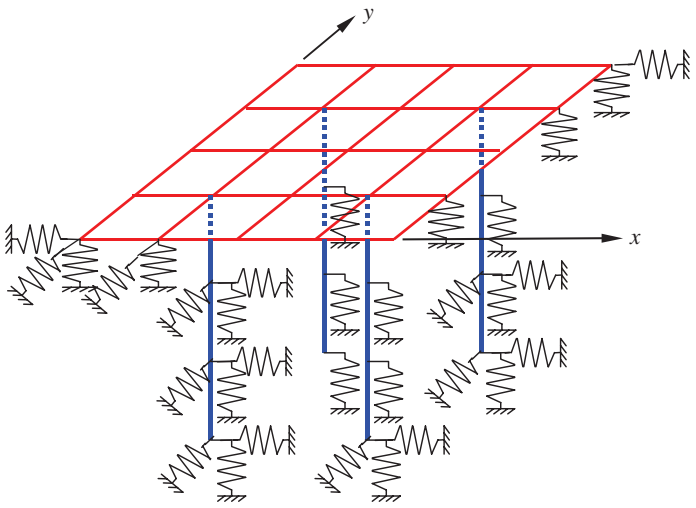

Fig. 2.24 Plate-beam-spring model of a piled raft for soil-structure interaction analysis [Kitiyodom et al. (2005)].

2.2.4.3 Simplified methods used in practice

In practice, simplified tools are used to assess the effects of tunnelling on piles (Devriendt and Williamson, 2011). Engineers typically evaluate the tunnelling-induced deformations empirically,

assuming that pile heads settle according to a subsurface greenfield settlement profile. The depth of the selected settlement trough is usually taken at some distance between the surface and the pile tip in order to account for the piles being dragged down by subsurface soil movements . The pile head, pile toe and 2/3 from the pile head are often used in practice to account for the pile load redistribution between shaft and base. For instance, this method proposed was by Crossrail for analysis of its effect on nearby structures (Williamson, 2014). However, in this way, the influence of the building on the global interaction is neglected.

Alternatively, the neutral axis method may be used. Adopting greenfield settlements and an analytical solution with elastic-perfectly plastic pile-soil interface, this approach assumes that the pile head settlement is equal to the settlement at the neutral axis depth, where the shaft friction changes from negative to positive. As discussed by Devriendt and Williamson (2011), the neutral axis method cannot be applied when the pile is compressed along the entire embedment depth (for instance, piles with their tip outside the tunnel influence area).

2.3 Tunnelling effects on structures

This section reviews previous research on tunnel-structure interaction (TSI) and its effects on the superstructure with shallow foundations. Thus far, most studies have considered the case of tunnel construction beneath buildings with shallow foundations, and it has been recognised that the building stiffness should be taken into account in the assessment of tunnel-structure interaction since it generally tends to decrease the structural distortions and risk of damage with respect to the greenfield case. On the other hand, few researchers have considered the case of tunnelling near to piled structures.

2.3.1 Deformation parameters

Tunnel excavation causes ground movements at the foundation level that result in structural damage. Vertical and horizontal differential movements result in load redistributions and strains within the superstructure, which may lead to local cracks and loss of bearing capacity of the structural elements. Additionally, it is necessary to account for the overall building settlement and tilt that pose a threat to serviceability limit states and building-service connections.

In general, the main deformation parameters in hogging and sagging zones, illustrated in Figure 2.25, were listed by Burland et al. (1977) as follows

- the settlement, S;
- the differential settlement, ΔS, is the difference in settlement between two points;
- the rotation, δ, is the change in gradient of a straight line connecting two points;
- the relative deflection , Δ, defined with respect to a line connecting two points is the maximum distance between the settlement curve and the straight line;
- the deflection ratio, $DR = \Delta/B$, is the ratio between the relative deflection between two points and their horizontal distance;
- the tilt ω is the rigid body rotation of the entire structure or part of it;
- the angular distortion (or relative rotation), β, is the rotation of the straight line connecting two points relative to their tilt.

2.3.2 Empirical approaches: limit values of deformations

In practice, limit values of the deformation parameters, which have been proposed after surveys of damaged buildings, are often used by engineers. For instance, Skempton and MacDonald (1956) indicated that angular distortions, β, lower than 1/500 should prevent cracking of structures and that a more severe limit of 1/1000 should be adopted for sensitive brick structures, whereas β should not exceed 1/150 to avoid structural damage of facades. Further limits of safe β

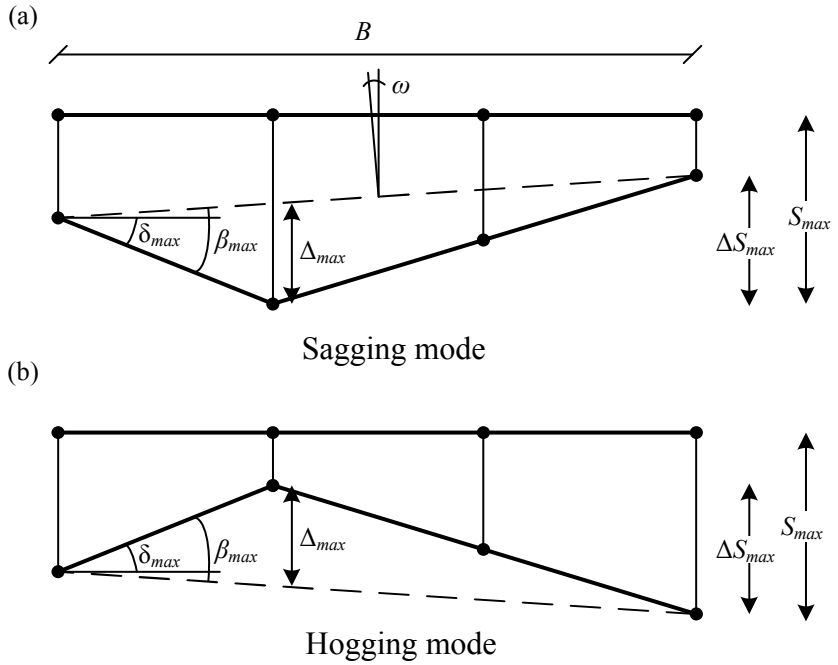

Fig. 2.25 Definition of the deformation parameter in (a) sagging and (b) hogging.

values were suggested by Bjerrum (1963). This approach, based on acceptable limit values for the deformation parameters, has been extended to new construction by the Eurocode 7, which accounts for the structural typology and the deformation mode (sagging deformations are less prone to cause damages than hogging deformations).

2.3.3 Semi-empirical approach: limiting tensile strain method

Despite the reliability of the previous simple empirical criteria, they do not allow consideration of the deformation mechanisms of the structure, accounting for structural details, and assessing the risk of damage with a closed-form solution. For this purpose, the limiting tensile strain method is often adopted in tunnelling engineering. The standard procedure for preliminary risk assessment of surface structures to tunnelling-induced movements was defined by Mair et al. (1996) considering the framework provided by Burland et al. (1977) and Boscardin and Cording (1989). The limiting tensile strain method and its background are illustrated in the following.

By idealising the structure as a linear, elastic, weightless, simply supported beam, Burland et al. (1977) proposed to estimate the maximum bending strain, ε_b, and diagonal strain, ε_d, induced by a given deflection ratio, DR, in the case of a purely hogging or sagging deformation mode as follows

$$\varepsilon_b = \frac{1}{\left(\frac{B}{12t} + \frac{3EI}{2tBHG}\right)} DR \tag{2.51}$$

$$\varepsilon_d = \frac{1}{\left(1 + \frac{HB^2G}{18EI}\right)} DR \tag{2.52}$$

where H is the height of the building, B is the building length in hogging or sagging, E and G are, respectively, the Young's modulus and shear modulus, I is the moment of inertia of the idealised beam, and t is the maximum distance between the neutral axis and the edge of the beam in tension. The authors suggested to assume the neutral axis should be located at the middle and bottom of the beam in the hogging and sagging zone, respectively, to empirically account for the higher potential for damage associated with the hogging deformations. Both the beam idealisation and the qualitative crack distribution due to shearing and bending are represented in Figure 2.26.

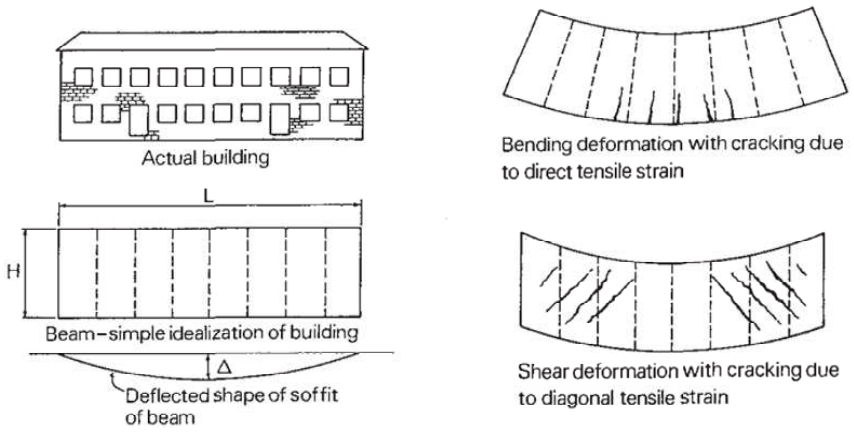

Fig. 2.26 Simple beam idealisation (left) and cracking in bending and in shearing (right) [Burland et al. (1977)].

Because horizontal strains may be induced in the structures by ground movements, Mair et al. (1996) suggested to account for the horizontal building strain, ε_h, using an average value computed along the building portion undergoing hogging or sagging. As reported by Mair et al. (1996), the combination of shearing, bending and horizontal deformations leads to the following total maximum bending strain, ε_{bt}, and diagonal strain, ε_{dt}, if Poisson's ratio is equal to 0.3.

$$\varepsilon_{bt} = \varepsilon_b + \varepsilon_h \tag{2.53}$$

$$\varepsilon_{dt} = 0.35\varepsilon_h + \sqrt{(0.65\varepsilon_h)^2 + \varepsilon_d^2} \tag{2.54}$$

To identify the start of serviceability loss, Burland et al. (1977) firstly used the concept of "limiting tensile strain", ε_{lim}, which allows engineers to identify with elastic beam analysis (considering the structure properties) the state corresponding to the onset of visible cracks. To measure the degree of damage, Burland et al. (1977), and at a later stage Boscardin and Cording (1989), adopted a classification based on "ease of repair" of the visible damage. This classification provides five categories, ranging from negligible (category 0) to severe damage (category 5), with an associated description of the cracks. These categories were correlated to a range of limiting tensile strains by Boscardin and Cording (1989) (see Table 2.1). As highlighted by Mair et al. (1996), an important threshold is the transition from category 2 to category 3, with the latter category often associated with relevant tunnelling-induced damage.

Table 2.1 Damage classification system proposed by Boscardin and Cording (1989) and Burland and Wroth (1974) [Giardina (2013)].

Category of damage	Damage class	Description of typical damage and ease of repair	Approx. crack width (mm)	Limit. tensile strain levels
Aesthetic damage	Negligible	Hairline cracks of less than about 0.1 mm width.	up to 0.1 mm	0 - 0.05
	Very slight	Fine cracks which can easily be treated during normal decoration. Perhaps isolated slight fracturing in building. Cracks in external brickwork visible on close inspection.	up to 1 mm	0.05 – 0.075
	Slight	Cracks easily filled. Redecoration probably required. Several slight fractures showing inside of building. Cracks are visible externally and some repainting may be required externally to ensure water tightness. Doors and windows may stick slightly.	up to 5 mm	0.075 – 0.15
Functional damage, affecting serviceability	Moderate	The cracks require some opening up and can be patched by a mason. Recurrent cracks can be masked by suitable linings. Repainting of external brickwork and possibly a small amount of brickwork to be replaced. Doors and windows sticking. Service pipes may fracture. Weather-tightness often impaired.	5 to 15 mm or a number of cracks > 3 mm	0.15 – 0.3
	Severe	Extensive repair work involving breaking out and replacing sections of walls, especially over doors and windows. Windows and door frames distorted, floors sloping noticeably. Walls leaning or bulging noticeably, some loss of bearing in beams. Service pipes disrupted.	15 to 25 mm, but also depends on number of cracks	> 0.3
Structural damage, affecting stability	Very severe	This requires a major repair involving partial or complete rebuilding. Beams loose bearing, walls lean badly and require shoring. Windows broken with distortion. Danger of instability.	usually > 25 mm, but depends on number of cracks	> 0.3

A procedure for preliminary risk assessment of surface structures to tunnelling-induced movements was proposed by Mair et al. (1996) based on the assumptions of plane-strain conditions, the building-foundation system represented as an equivalent linear elastic beam, and that the building is divided into two independent structures in the hogging and sagging zones. Note that the authors adopted the deflection ratio, DR, rather than the angular distortion, β, because β requires the assessment of the building tilt, which is difficult to estimate. The Mair et al. (1996) procedure consists of the following steps.

1. Greenfield surface movements are calculated; only if the settlement trough affecting the building exceeds 10mm magnitude, it is necessary to proceed to step 2. The authors assumed the empirical method based on Gaussian curves to predict horizontal and vertical movements; however, a generic approach may be implemented.

2. The beam is constrained to displace as the greenfield movements and the resulting maximum tensile strains in the hogging and sagging zones are calculated with Equations (2.53) and (2.54) as $\varepsilon_{max} = max(\varepsilon_{bt}, \varepsilon_{dt})$. Subsequently, the damage assessment in hogging and/or sagging is performed by comparing maximum building tensile strain ε_{max} with the limiting tensile strain ε_{lim} and relating it to the expected damage level with the table in Table 2.1.

3. Step 2 leads to a conservative assessment because it neglects the structural stiffness (i.e. the building exhibits a fully-flexible behaviour). If the structure is associated with category 3 or higher of expected damage, a detailed evaluation of the building deformations (accounting for the soil-structure interaction, 3D geometries of structure and tunnels) should be carried out, which may result in a decrease of the damage category.

Further details to account for the soil-structure interaction (structural stiffness and self-weight) in the risk assessment are provided in the following section.

2.3.4 The effects of soil-structure interaction and the modification factor approach

The building modification factor approach was introduced by Potts and Addenbrooke (1997) to relate building deformations (maximum deflection ratio, DR, and maximum horizontal strain, ε_h) caused by adjacent excavation and tunnelling activities to surface greenfield soil movements accounting for the structural stiffness. For the sake of simplicity, a building that spans hogging and sagging zones is commonly considered as two independent structures. The deflection ratio modification factor, M^{DR}, is calculated by dividing the building sagging and hogging deflection ratio resulting from tunnel construction $\left(DR_{sag,Bldg}; DR_{hog,Bldg}\right)$ by the deflection ratio of the greenfield settlement trough $\left(DR_{sag,GF}; DR_{hog,GF}\right)$, as shown in Figure 2.27.

$$M^{DR,sag} = \frac{DR_{sag,Bldg}}{DR_{sag,GF}} \quad || \quad M^{DR,hog} = \frac{DR_{hog,Bldg}}{DR_{hog,GF}} \quad [-] \tag{2.55}$$

The modification factors for the maximum tensile and compressive horizontal strains, $M^{\varepsilon h,t}$ and $M^{\varepsilon h,c}$, are given by the ratio between the maximum building strains $\left(\varepsilon_{h,t,Bldg}; \varepsilon_{h,c,Bldg}\right)$ and the maximum greenfield horizontal strains at the building location $\left(\varepsilon_{h,t,GF}; \varepsilon_{h,c,GF}\right)$.

$$M^{\varepsilon h,t} = \frac{\varepsilon_{h,t,Bldg}}{\varepsilon_{h,t,GF}} \quad || \quad M^{\varepsilon h,c} = \frac{\varepsilon_{h,c,Bldg}}{\varepsilon_{h,c,GF}} \quad [-] \tag{2.56}$$

2.3.4.1 Simple beam and plate structures

Several relative stiffness factors (i.e. the stiffness of the structure in relation to that of the soil) have been proposed to assess the contribution of structural stiffness in reducing the damage induced by greenfield ground movements. The use of relative stiffness factors was proposed

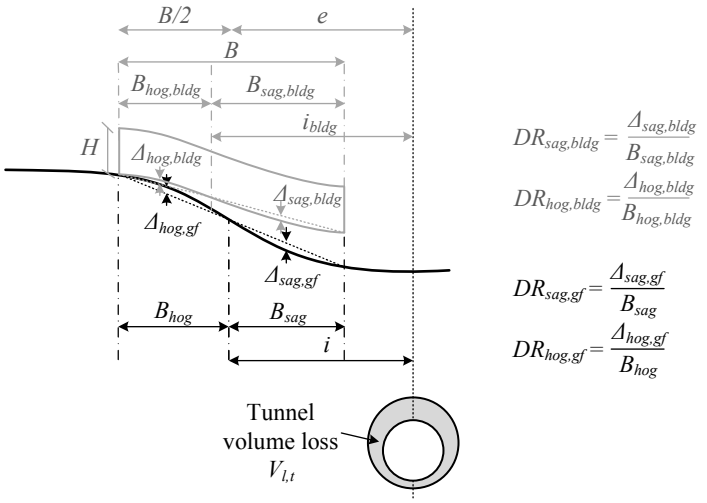

Fig. 2.27 Definition of relative deflection, Δ, and deflection ratio, *DR*, in sagging and hogging of the greenfield settlement curve and a surface building in the case of tunnelling.

by Potts and Addenbrooke (1997) and later modified to a dimensionless form by Franzius et al. (2006). These authors carried out parametric finite element analyses of building deformations caused by tunnelling and showed that the resulting building deflection is mostly dependent on relative bending stiffness, whereas final building axial strains depend on relative axial stiffness. They summarised their results in design charts in which reduction factors are related to the appropriate relative stiffness, depending on deformation zone (sagging, hogging) and the ratio e/B, where eccentricity e is the horizontal distance from the tunnel centreline to the centre of the building with width B in the transverse direction (illustrated in Figure 2.27). The dimensionless forms of the relative bending stiffness, ρ^*_{mod}, and the relative axial stiffness, α^*_{mod}, are given by

$$\rho^*_{mod} = \frac{EI}{E_s z_t B^2 L} \quad || \quad \alpha^*_{mod} = \frac{EA}{E_s B L} \quad [-] \tag{2.57}$$

where EI and EA are the bending and axial stiffness of the superstructure (in kN m^2 and kN), respectively, E_s is the soil Young's modulus that may be estimated as the secant stiffness of the soil at an axial strain of 0.01% and at a depth of $z = z_t/2$, z_t is the tunnel axis depth, and L is the longitudinal length of the building (in the direction of the tunnel axis).

To generalise the design charts suggested by Franzius et al. (2006) and reduce the level of scatter, Farrell (2010) and Goh and Mair (2011) proposed the following dimensionless expressions for the relative bending stiffness in sagging and hogging zones:

$$\rho_{sag} = \frac{EI}{E_s B^3_{sag} L} = \frac{(EI)^*}{E_s B^3_{sag}} \quad || \quad \rho_{hog} = \frac{EI}{E_s B^3_{hog} L} = \frac{(EI)^*}{E_s B^3_{hog}} \quad [-] \tag{2.58}$$

where $(EI)^*$ is the bending stiffness of the building per running metre (in kN m^2/m run), and B_{sag}, B_{hog} are the lengths of the building in the sagging and hogging zones based on the greenfield settlement trough (i.e. for a fully flexible building). Because of the use of B_{sag} and B_{hog}, these formulas account indirectly for the tunnel-building eccentricity. The authors suggested that a

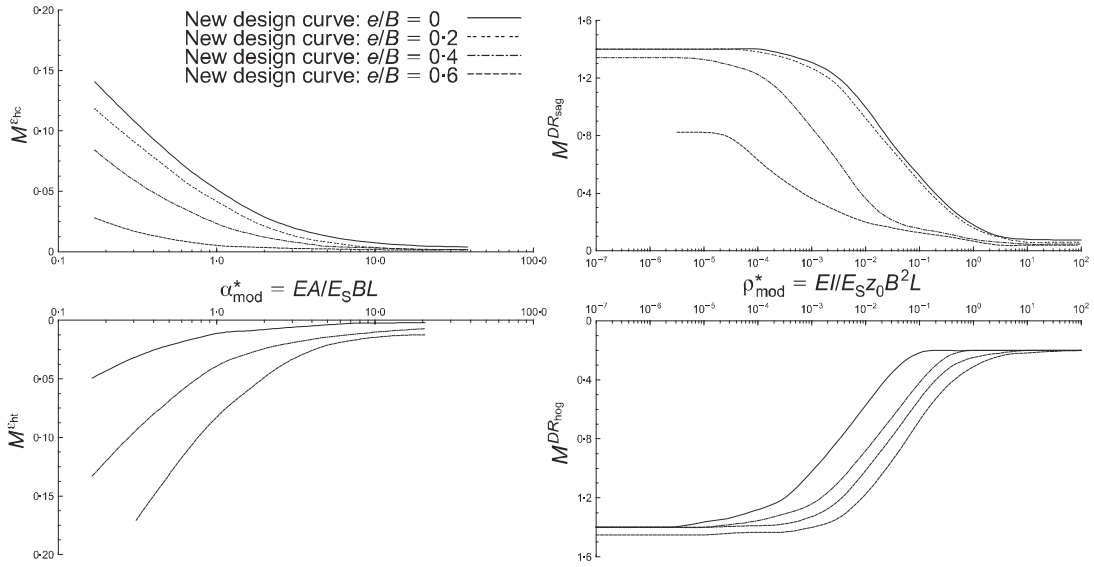

Fig. 2.28 Design curves for M^{DR} and $M^{\varepsilon h}$ adopting the modified relative stiffnesses ρ^*_{mod} and α^*_{mod} [Franzius et al., 2006].

representative value for soil stiffness could be based on a weighted average of the elastic modulus of the soil above the tunnel at a level of strain that is representative of the tunnelling scenario. The soil and building stiffnesses are difficult parameters to evaluate accurately, however a reasonable assessment of the modification factors only requires determination of relative stiffness within an order of magnitude because of the semi-logarithmic scale of design charts (Mair, 2013). This definition of relative bending stiffness permitted Mair (2013) to describe, with narrow envelopes, data of M^{DR} obtained for tunnelling and deep excavations from finite element analyses (Franzius et al., 2006; Potts and Addenbrooke, 1997), centrifuge modelling (Farrell, 2010; Farrell et al., 2014) and field studies available in the literature (see Figure 2.29). The narrow envelope proves the efficiency of Equation (2.58) in taking into account the effects of tunnel eccentricity e/B on building deformations through the use of B_{sag} and B_{hog}.

2.3.4.2 Deflection ratio for framed buildings

For framed structures, several authors have discussed the possibility of simplifying the interaction analysis by considering an equivalent simple beam or plate. To estimate the bending stiffness of the equivalent beam, Potts and Addenbrooke (1997) suggested the use of the parallel axis theorem, whereas Mair and Taylor (2001), neglecting the stiffening effect of shear walls, connections, and columns, indicated that the equivalent bending stiffness should be the algebraic sum of all floor slabs. Although the use of the parallel axis theorem with the corrections proposed by Dimmock and Mair (2008) may be appropriate for masonry buildings, both approaches are not adequate in the case of framed structures (Goh and Mair, 2014). In particular, the use of the parallel axis theorem in Equation (2.59) and the algebraic sum in Equation (2.60) provide an overestimation

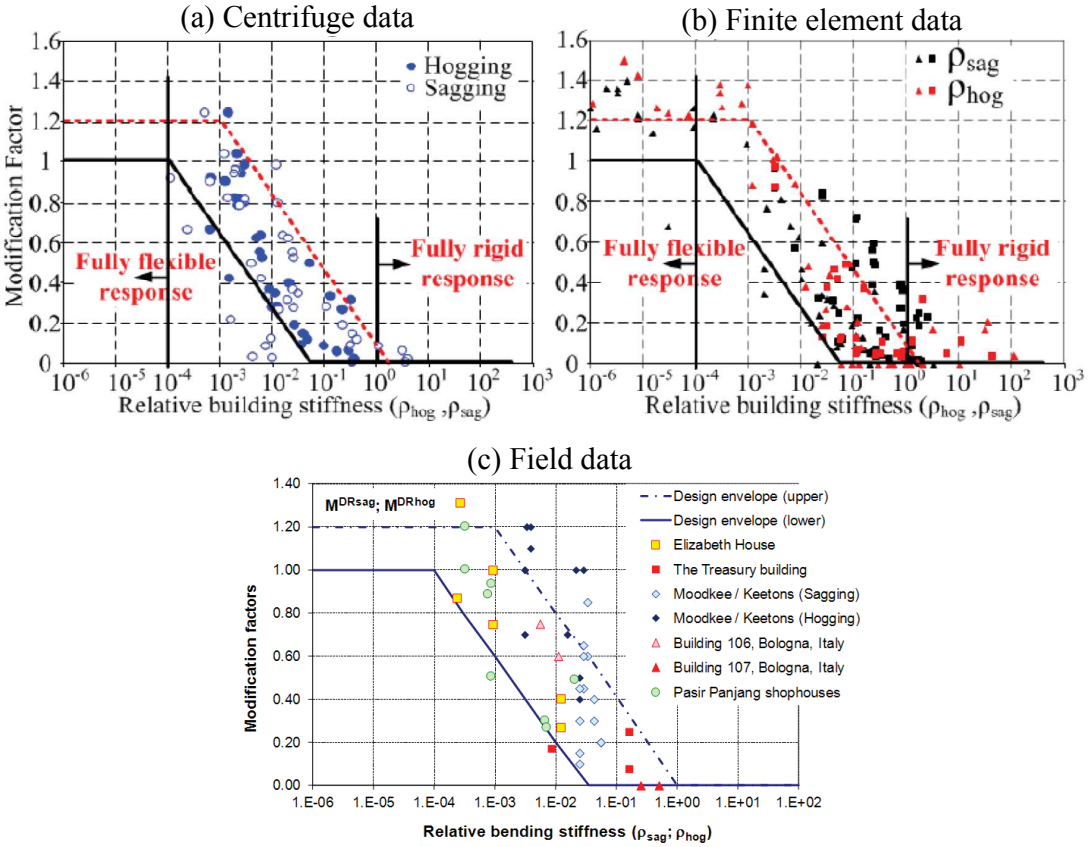

Fig. 2.29 Centrifuge, numerical and field data of deflection ratio modification factor versus relative building stiffness defined in Equation (2.58) [Mair (2013)].

and underestimation of the overall structural stiffness, respectively.

$$EI_{eq} = \sum E\left(I + Ad_{ax}^2\right)_{i-thfloor} \tag{2.59}$$

$$EI_{eq} = \sum (EI)_{i-thfloor} \tag{2.60}$$

where d_{ax} is the vertical distance between the neutral axis of the beam at the i^{th} floor and the neutral axis of the entire frame.

In the case of frame structures, it is necessary to correctly account for the stiffening contribution of columns to the beam flexural stiffnesses. If bays have an approximately equal length, Goh and Mair (2014) showed that this effect may be estimated with the following column stiffening factor, obtained from the structural analysis of a frame deflecting in a sagging deformation mode:

$$\begin{aligned} C_{sag} &= \left[1 + \left(\frac{B_{sag}}{l}\right)^2 \left(\frac{K_{LC} + K_{UC}}{K_{LC} + K_{UC} + K_b}\right)\right] \\ C_{hog} &= \left[1 + \left(\frac{B_{hog}}{l}\right)^2 \left(\frac{K_{LC} + K_{UC}}{K_{LC} + K_{UC} + K_b}\right)\right] \end{aligned} \tag{2.61}$$

where l is the span length of each beam bay, h is the storey height, $K_{LC} = (EI/h)_{LC}$ is the average stiffness of the lower column, $K_{UC} = (EI/h)_{UC}$ is the average stiffness of the upper column, and

$K_b = (EI/l)_b$ is the average stiffness of the beam line. From Goh and Mair (2014), the equivalent bending stiffness of the frame structure is given by

$$EI_{eq,sag} = \sum \left(C_{sag} \times EI\right)_{floors} \;||\; EI_{eq,hog} = \sum \left(C_{hog} \times EI\right)_{floors} \tag{2.62}$$

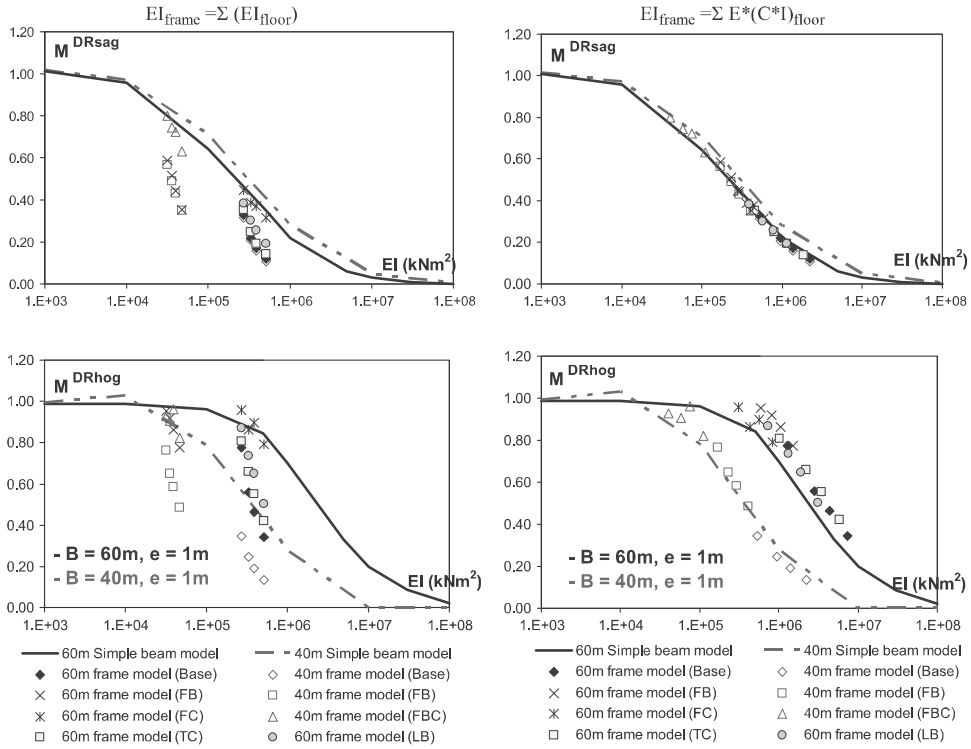

Fig. 2.30 Comparison between beams and framed building deflection modification factors in hogging and sagging zones [Goh and Mair, 2014].

It is important to note that C depends on the number of spans in the hogging or sagging zones, B_{sag}/l or B_{hog}/l; the coefficient C increases with the number of spans because of the contribution of additional columns to the stiffness of the beams. With reference to deflection ratio modification factors, the effectiveness of Equation (2.62) was shown for framed structures subjected to deep excavation-induced movements. However, further investigation is needed for the case of tunnelling.

2.3.4.3 Horizontal strains in framed buildings

For the case of deep excavation, Goh and Mair (2014) derived a stiffness parameter that is able to approximately quantify the contribution of the frame with shallow foundations to the reduction of horizontal strains compared to greenfield soil movements. The reaction of the structure at the ground level to horizontal strains was conservatively estimated considering a simple portal frame with a single bay on two pin-supports displayed in Figure 2.31(a). The frame stiffness factor α_f was defined by imposing a unit differential horizontal displacement Δ between the pin-supports

and calculating the external horizontal reaction force H

$$\alpha_f = \frac{H}{\Delta} = \frac{3K_bK_c}{h^2(2K_b+3K_c)} \qquad [\mathrm{KN/m}] \tag{2.63}$$

This stiffness parameter is a function of $K_c = EI_c/h$ and $K_b = EI_b/l$, where h is the column height, EI_c and EI_b are the bending stiffness of the column and the first-floor beam, respectively. This stiffness parameter, α_f, is not dimensionless. As recognised by Goh and Mair (2014), a single portal neglects the influences of additional storeys, variable bay length, and the presence of structural infill walls with bearing capacity. Equation (2.63) was used by Goh and Mair (2014) to define a reasonable upper bound for α_f; Figure 2.31(b) shows the comparison of outcomes of the parametric study with the upper envelope.

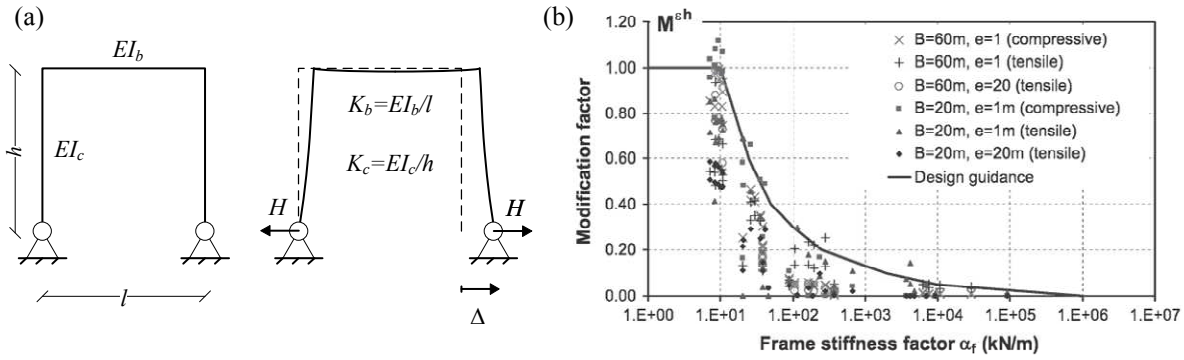

Fig. 2.31 (a) Simple portal static scheme; (b) $M^{\varepsilon h}$ against α_f for frames on individual footings near to deep excavations [Goh and Mair, 2014].

2.3.4.4 The effects of structural self-weight

If the limiting tensile strain method defined by Mair et al. (1996) is combined with the modification factors proposed by Franzius et al. (2006) and Farrell (2010), the effect of the structural self-weight is neglected. Recent research has highlighted that the effect of the building self-weight on the tunnelling-induced damage due to soil-structure interaction is not conservative. To study the impact of the building self-weight on tunnelling-induced distortions, Franzius et al. (2004) performed a parametric numerical analysis. Their work demonstrated that the magnitude of the building deformations increases with the increase in the self-weight; on the other hand, this variation was found secondary with respect to the influence of the relative soil-structure stiffness. Therefore, it was concluded that the use of the upper bounds defined by Potts and Addenbrooke (1997) is acceptable for realistic values of building self-weight.

At a later stage, Giardina et al. (2015) pointed out that the problem is influenced by the formation of a gap between the soil and the structure, which was measured during centrifuge testing by Farrell et al. (2014), and that the outcomes of Franzius et al. (2004) were probably affected by the implementation of a tie condition at the soil-structure interface. Giardina et al. (2015) allowed for the development of this gap in their numerical models and the simulations suggested that the building weight influence on the building distortions may be remarkable

and decreases with the increase in relative soil-structure stiffness. They suggested the use of the normalised relative soil-structure stiffness in sagging and hogging, $\rho_{norm,sag}$ and $\rho_{norm,hog}$, defined as the ratio between ρ_{sag} and ρ_{hog} (defined by Equation (2.58)) and the ratio σ/σ_1, where σ is the total bearing pressure acting at the building foundations and σ_1 is the bearing pressure produced by one typical storey of the same building (if the building weight is directly proportional to the number of storeys, σ/σ_1 is the number of storeys).

$$\rho_{norm,sag} = \frac{\rho_{sag}}{\frac{\sigma}{\sigma_1}} \quad || \quad \rho_{norm,hog} = \frac{\rho_{hog}}{\frac{\sigma}{\sigma_1}} \quad [-] \tag{2.64}$$

As displayed by Figures 2.32, the use of the normalised relative stiffness defined by Equation (2.64) results in a linear trend of M^{DR} with relative stiffness, removing the dependency on the structure self-weight. Additionally, it was shown by Giardina et al. (2015) that Equation (2.64) is compatible with the use of the upper and lower envelopes proposed by Mair (2013).

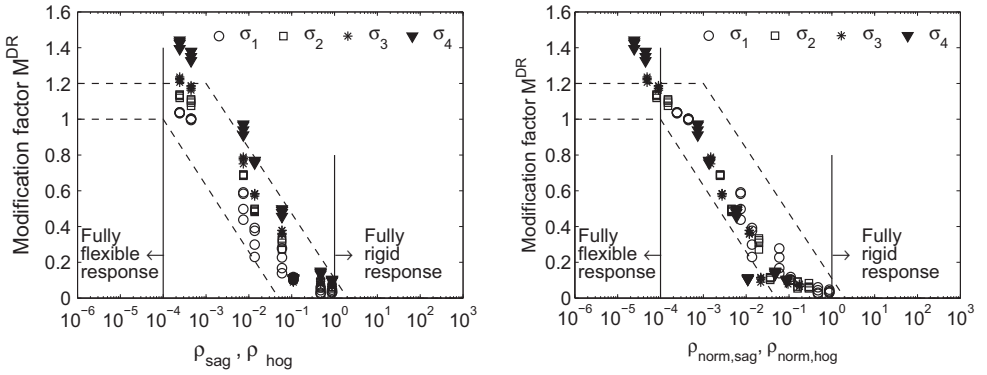

(a) modification factor vs relative stiffness, numerical results (Giardina et al, 2015)

(b) modification factor vs normalised stiffness, numerical results (Giardina et al, 2015)

Fig. 2.32 M^{DR} vs ρ_{norm} with the envelopes proposed by Mair (2013) [Giardina et al. (2015)].

2.3.4.5 The effects of structural configuration

Goh and Mair (2014) highlighted the importance of structural configuration in the global interaction based on an extensive set of numerical analyses which evaluated the response of framed buildings to deep excavations. Fargnoli et al. (2015) suggested that the use of an equivalent plate and beam model for the superstructure may lead to an erroneous evaluation of the structural response to tunnelling-induced movements. The work of Losacco et al. (2014) suggested that, in order to obtain satisfactory results, more advanced simplified structural models of the building, rather than a simple beam/plate, could be incorporated into the global interaction analysis. In general, it is not fully understood the influence of the structural configuration on the building distortion for a given relative soil-structure stiffness in the case of tunnelling.

2.3.5 The effects of deep foundations

For tunnelling beneath buildings on piled foundations, there are a limited number of case studies and research projects that have investigated the global interaction. Therefore, there is a lack of information and guidance available for the risk assessment of piled-buildings.

Goh and Mair (2012) and Goh and Mair (2014) illustrated the monitoring results obtained during the excavation of twin tunnels along Pasir Panjang Road in Singapore. The tunnels were located beneath two 2-storey reinforced concrete framed buildings founded on individual footings supported by short timber piles, as shown in Figure 2.33(a). At the ground floor, some of the columns were not connected by tie-beams; this allowed for differential displacements between the footings due to ground movements. Greenfield and building settlements are shown in Figure 2.33(b) for the shop house A32. Both buildings exhibited a fully-flexible response to the excavation of the first tunnel with a relatively narrow settlement trough ($K \approx 0.35$) due to the fact that piles were influenced by the narrow subsurface settlements of the sand deposit at the pile base. Note that the buildings were entirely in the hogging zone with respect to this tunnel. On the other hand, the buildings had a semi-rigid response to the second excavation with the buildings both in hogging and sagging zones. This was probably due to the decreased transverse widths B_{sag} and B_{hog} that resulted in a higher relative stiffness of the buildings. This case study displayed that the action of framed structures may reduce the building distortions and that tunnel-pile interaction may result in narrower settlement troughs of buildings.

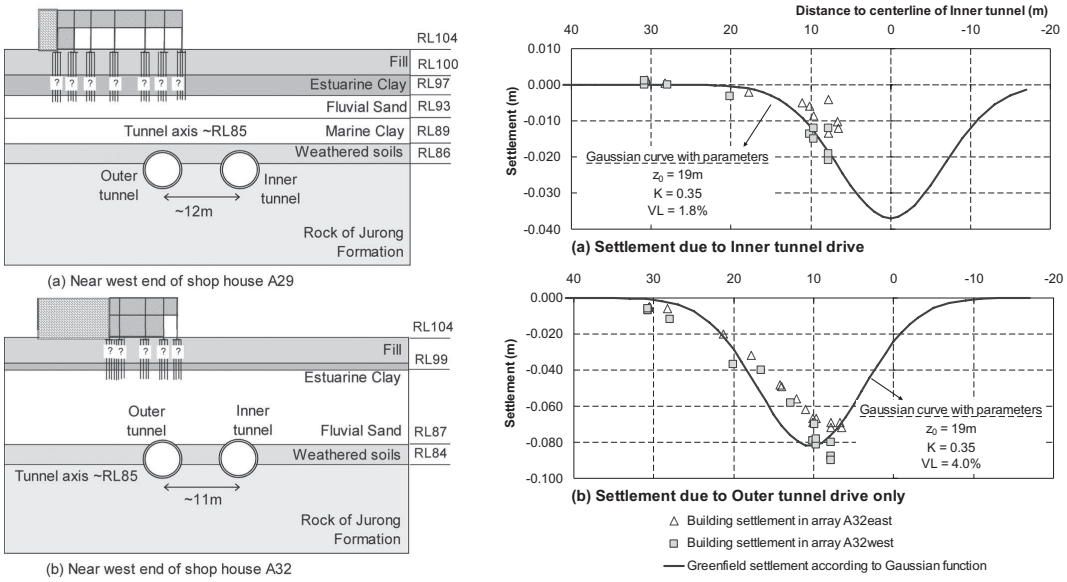

(a) (b)

Fig. 2.33 (a) Cross-sections of the shop houses and soil profiles; (b) greenfield and building settlement at both east end and west end of shop house A32 [Goh and Mair (2012)].

Williamson (2014) and Mair and Williamson (2014) reported field measurements of two Crossrail tunnelling projects, a case of twin running tunnels and a case of station tunnels, where the tunnel crowns were close to the pile tip level of piled buildings. In both cases, the

building response to tunnelling was fully-flexible with little differences between the building and greenfield settlement troughs. Williamson (2014) concluded that the global tunnel-piled building interaction was not fully understood for these cases because of multiple phenomena playing significant roles (e.g. tunnel-single pile interaction, soil-pile cap interaction, concrete cracking, pile factor of safety and pile-pile interaction).

2.4 Conclusions

A good understanding of the relationship between tunnel construction and resulting greenfield ground deformations has been reached through empirical approaches, especially in clays. On the other hand, the displacement field induced by the ground loss in sands should be described with more accuracy accounting for the interrelated effects of tunnel volume loss, depth, and soil relative density. Additionally, engineers need solutions to assess tunnelling-induced movements in soft ground that can be used as inputs for soil-pile interaction analyses (in particular tunnel-pile interaction requires a consistent deformation pattern around the tunnel because of the influence of both horizontal and vertical soil movements).

Researchers have investigated the effects of tunnelling on pile foundations with experiments, either in the laboratory or in the field, or analytically, agreeing on some general observations. The response of piles to tunnelling-induced movements is generally very sensitive to the relative pile tip-tunnel location, the installation method of the piles, pile safety factor, and the load distribution between base and shaft. Several zones of influence above the tunnel, where large pile settlement may occur, were defined. Several authors proposed to conservatively evaluate pile group behaviour considering the tunnel-single pile interaction because of the beneficial group effect in the case of tunnelling; however neglecting the group response and the load-redistribution due to a cap may mislead the analysis. In general, as indicated by Mair and Williamson (2014), past studies have focused predominately on tunnelling adjacent to piles, for which the induced building distortions are expected to be minimal. In these cases, tunnelling mainly causes lateral bending in piles rather than settlements along the pile axis. In contrast, tunnelling beneath piles induces vertical pile movements, which leads to structural deformations. Therefore, pile settlements represent the major concern for tunnelling considering the way in which they affect buildings. Finally, recent works have focused their attention on the pile failure mechanism. However, despite initial works underling a high potential for pile failure, recently it has been shown that failure is not a primary concern in clays and should be better investigated in sands to consider the pile safety factor.

Tunnelling in urban areas is potentially associated with a low to medium risk of damage for the buildings (for instance cracking of inner walls, fracture of service pipes, danger of instability, etc.) that may compromise the serviceability and ultimate limit state requirements. Engineers need tools to carry out risk assessments and to evaluate the impact of tunnelling-induced damages on the overall costs of the project. A good understanding of tunnel-building interaction has been achieved for shallow foundations. Preliminary risk assessment methods for building damage caused by tunnelling were proposed that are able to predict, with reasonable simplicity and reliability, the induced structural deformations, accounting for the tunnel location, building geometries, self-weight and stiffness. On the other hand, previous studies on tunnel-pile interaction (TPI) indicate that piles with their tips directly above the tunnel (i.e. within a horizontal offset of one tunnel radius from the tunnel axis) are likely to settle more than the surface, whereas piles outside this area generally settle less than the surface. This causes a

narrowing of the pile head settlement profile with respect to the greenfield surface settlement trough, leading to an increased potential for building damage. However, if the influence of the building on the global tunnel-pile-structure interaction (TPSI) is neglected and tunnelling-induced deformations in buildings are assessed using a TPI analysis (i.e. assuming that the building follows the settlement curve obtained from a tunnel-pile or tunnel-pile group analysis), the resulting risk assessment is overly conservative in the case of relatively stiff structures, as illustrated by a case study reported by Goh and Mair (2014). Therefore, considering that limited research has been performed on the global TPSI, the combination of previous works on TPI and TSI is necessary to achieve a better representation of the TPSI. Ideally, the effects of piles should be implemented in the procedures used in practice to assess tunnelling-induced deformations as deflection ratio and horizontal strains of the superstructure.

Chapter 3

Experimental methods, equipment and testing plan

The design of the experimental equipment and the development of an innovative real-time hybrid model is an important part of this research. This chapter illustrates the experimental methods and equipment used for the investigation of tunnelling-induced greenfield soil movements and the response of piles and piled structures to tunnelling. Note that the centrifuge model for greenfield tunnelling was developed by Zhou et al. (2014), which contains further details.

This chapter is structured as follows. Firstly, Section 3.1 introduces geotechnical centrifuge modelling and its principles and Section 3.2 illustrates the components of the centrifuge package. Then, Section 3.3 provides details of the development of an innovative coupled numerical-centrifuge modelling technique (i.e. hybrid model) and an overview of the tests performed to evaluate the system performance. Finally, Section 3.4, Section 3.5 and Section 3.6 describe the three series of centrifuge tests for greenfield tunnelling, tunnelling beneath pile foundations and tunnelling beneath piled structures, respectively. In the following, both the model dimensions and results are reported in model scale.

3.1 Geotechnical centrifuge modelling

This section briefly introduces the use of centrifuge modelling for geotechnical and soil-structure interaction problems; furthermore, the known scale and boundary effects, which are relevant to this research, are discussed.

3.1.1 Geotechnical centrifuge

The University of Nottingham geotechnical centrifuge manufactured by Thomas Broadbent & Sons Ltd (Ellis et al., 2006), which is a medium-sized 2m radius beam centrifuge with one swinging cradle and 50g-tonne capability, was used for this research (see Figure 3.1).

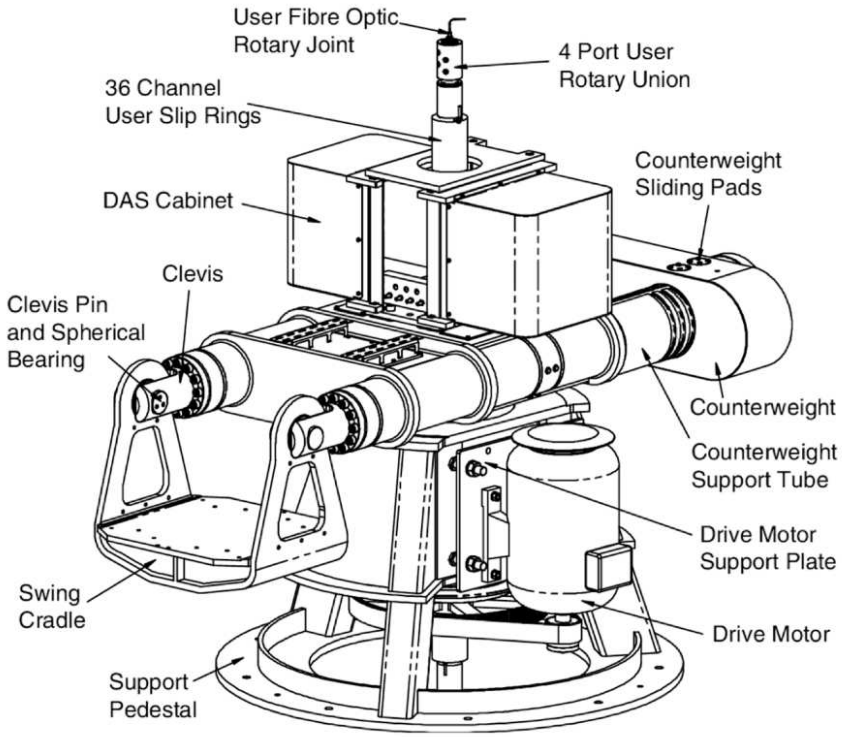

Fig. 3.1 University of Nottingham 50g-tonne, 2m radius, geotechnical centrifuge [Ellis et al. (2006)].

3.1.2 Centrifuge principles

In geotechnical engineering, the understanding of the behaviour of soils and their interactions with structures is often achieved with the use of experimental testing and measurements obtained by monitoring and field data. Regarding experimental testing, full-scale trials, which result in sparse localised measurements, are rarely undertaken because of the costs and difficulties in evaluating complex site conditions. On the other hand, experimental testing of reduced scale models of actual prototype scenarios is commonly undertaken in engineering because it provides a method of conducting experiments in a well controlled laboratory environment. In particular, in

geotechnical engineering, centrifuge technology allows testing of small scale models at elevated gravity to reproduce full-scale soil stresses. The full-scale stress condition is essential due to the non-linear behaviour of the soil, which depends on the current stress conditions and the soil's stress history. Though it has limitations due to scale effects, boundary conditions and modelling simplifications, centrifuge testing can provide high quality data for the study of many problems in geomechanics and offers an efficient and cost-effective way to study geotechnical problems compared to full-scale testing.

The basic principle of centrifuge testing is that it reproduces the full-scale stresses within a model scaled down in dimension by a scale factor N by applying a centrifuge gravity field N times greater than earth's gravity, g. This is achieved by the centrifuge spinning inducing a centrifugal acceleration radially with respect to the axis of rotation. The scale factor is computed as the ratio between centrifugal acceleration, $a = \omega^2 r$, and the gravitational acceleration, $g = 9.81\text{ms}^{-2}$. The scale factor N corresponding to a is

$$N = \frac{\omega^2 R}{g}, \tag{3.1}$$

where ω is the rotation velocity and R the distance from the axis of rotation. Table 3.1 shows some of the scaling laws used to derive prototype-scale values from model-scale results.

Table 3.1 Centrifuge scaling laws [Taylor (1995a)].

Parameter	Units	Model Scale	Prototype Scale
Gravity	ms^{-2}	N	1
Length	m	1	N
Area	m^2	1	N^2
Volume	m^3	1	N^3
Force	$\text{N} = \text{kgms}^{-2}$	1	N^2
Density	kgm^{-3}	1	1
Stress	$\text{Pa} = \text{kgm}^{-1}\text{s}^{-2}$	1	1
Strain	–	1	1
Axial Stiffness - EA	N	1	N^2
Bending Stiffness - EI	Nm^2	1	N^4

Note that, within the model, the variation of the distance from the axis of rotation, R, results in a non-linear profile of the soil stress with depth. To minimise the error in stress between model and prototype, Taylor (1995a) suggested the use of the effective radius, R_e, equal to the distance between the centrifuge central axis and one-third the depth of the model.

$$R_e = R_t + \frac{h_m}{3}, \tag{3.2}$$

where R_t is the radius to the top of the model and h_m is the height of the model soil. Note that the use of R_e allows defining a unique scale factor, N, for the entire model. In this case, there is a correspondence in stress between model and prototype at two-thirds the model depth.

3.1.3 Scale and boundary effects in centrifuge modelling

Generally, the ground particle size is not scaled according to Table 3.1; therefore, scale errors are due to the relative size of the model structures to the average particle size of the soil. Boundary effects are due to the physical dimensions of the reduced-scale model. To ensure that the model reproduces realistically the behaviour of the equivalent prototype scenario, scale and boundary effects should be minimised. A comprehensive framework on scaling effects and boundary conditions was provided by Garnier et al. (2007). The aspects relevant to tunnels and piles are discussed in this section. To reduce the effects of scaling and boundary distances, it is necessary to respect the following recommendations:

- The centrifuge modelling of tunnelling in sands is mainly affected by particle size to tunnel diameter ratio. As reported in Marshall (2009), Kutter et al. (1994) conducted a series of centrifuge tests in which they looked at the collapse of sand into a de-pressurised cavity. Kutter et al. (1994) stated that grain size effects impacted tests with ratios of the diameter of the cavity to the average grain size, d_{50}, between 30 and 1000 and that the effects appeared to decrease after this ratio reached 350. Considering the effects of the soil dilation, Marshall (2009) suggested that scale effects are negligible for $D/d_{50} > 500$ at the collapse of the cavity, whereas this threshold ratio should be lower at the pre-collapse condition. Additionally, it is necessary to note that the frictional effect of the sidewall results in reduced tunnelling-induced settlements at the boundaries of the model.

- To correctly model the pile base capacity, the minimum ratio between the pile diameter to the average grain size, D_p/d_{50}, should be 20 (Bolton et al., 1999); furthermore, the boundary effects on the pile tip resistance are minimised if the ratio between the distance of the pile from the wall and the pile diameter, S/D_p, is greater than 10 diameters (Bolton et al., 1999).

- The correct centrifuge modelling of the pile shaft friction is not possible due to scaling errors. If the ratio D_p/d_{50} is lower than a critical value, reported as 100 by Garnier and König (1998) and 50 by Fioravante (2002), the peak shear strength at the pile shaft is affected by scaling and tend to be higher than the full-scale value. In general, the maximum shear strength depends on the normalised roughness, $R_n = R_{max}/d_{50}$, where R_{max} is the roughness of the pile shaft. R_n should be correctly reproduced in the centrifuge (Garnier et al., 2007). However, the peak shear strength is not affected by R_n for smooth interfaces ($R_n < 0.01$) and perfectly rough interfaces ($R_n > 0.1 - 1$) (Garnier and König, 1998). The normal stresses acting on the model pile shaft, and therefore the shear stress of the soil, is related to R_n: if the interface is smooth, there is not an increase in normal stress for

different pile diameters because a smooth interface causes the contraction of the soil at the interface, whereas a rough interface results in a band of soil dilation at the interface that is not scaled with N and results in increased normal stress (Garnier et al., 2007). Finally, the scaling effect concerning the displacement that mobilises the ultimate shear strength is not clear and does not scale with N (Garnier and König, 1998).

3.2 Experimental package

3.2.1 Set-up for modelling of greenfield tunnelling

The experimental package developed by Zhou et al. (2014) to model the greenfield tunnelling process in plane-strain conditions was used. The centrifuge package includes the centrifuge strong box, the soil, the model tunnel, and the tunnel volume control system. These components are described in the following sections.

3.2.1.1 Strong box

The strong box consisted of a stainless steel U-channel, a Perspex front wall and a back aluminium wall, which are displayed in Figures 3.3(a) and (b). The inside plan dimensions of the strong box are 640×260mm and the maximum height of soil within the box is 500mm. To avoid leakage, the stainless steel U-channel was bolted to the Perspex window and the aluminium back wall while rubber cords were placed between the Perspex window, U-channel and back wall.

The structural size of U-channel, front and back walls were designed to ensure plane-strain condition along the tunnel direction and minimise any disturbance of the lateral earth pressure. The front wall was made of 100mm thick Perspex so that ground movements could be measured using digital image analysis on a series of pictures taken during the test. A 100mm diameter and 20mm deep recess was cut into the inner face of the Perspex wall to accommodate one end of the model tunnel. It is important to report that the friction at the soil-Perspex interface reduces ground movement magnitude by 10%-15% without significant impact on the displacement distribution (i.e. the shape of the deformation pattern) (Marshall, 2009).

3.2.1.2 Soil

A dry silica sand known as Leighton Buzzard Fraction E, which has been used extensively for physical model testing in the UK, was adopted for testing. The sand has a typical average diameter $d_{50} = 0.122$mm, a specific gravity, G_s, of 2.65 and has the minimum and maximum void ratios, e_{min} and e_{max}, equal to 0.613 and 1.014, respectively. In the tests, the sand was poured to achieve a relative density, I_d, varying between 0.3 and 0.9. Table 3.2 provides the relationship between the relative density, I_d, and the dry soil density, ρ_s.

Table 3.2 The relative density and the density of soil.

I_d (%)	ρ_s (kg/m^3)
30	1399
50	1461
70	1529
90	1603

3.2.1.3 Model tunnel

Two model tunnels with different outside diameters (90mm and 40mm) were used during this research. Figure 3.2 illustrates the model tunnels. The model tunnels consist of a rigid inner cylinder sealed with a 1mm thick latex membrane and filled with water. Figures 3.3(a) and (b) show the model tunnel placed within the strong box and sketches the cross-section of the plane-strain model, respectively.

(a) (b)

Fig. 3.2 (a) 90mm diameter model tunnel, (b) 40mm diameter model tunnel and its fitting rings.

Despite the different inner shape, both model tunnels are based on the same modelling technique: the ground loss is modelled by water extraction. Because the tunnel membranes are fully-flexible and the structural lining is not modelled, the ground movements are due the equilibrium between the water and soil. Therefore, the shape of the inner cylinder should have no influence on the tunnel contraction. Furthermore, the tunnel longitudinal advancement is not modelled and tunnel volume loss, $V_{l,t}$, is an average value across the model tunnel.

The 90mm diameter model tunnel was designed and assembled by Zhou (2014) (Figure 3.2(a)). The tunnel consists of a hollow inner cylinder with enlarged ends covered by a latex sleeve sealed with O-rings, grease, and end plates. The gap between the inner cylinder and the latex sleeve is filled with water. The inner cylinder was designed with a downward eccentric shape to allow for the oval-shaped distribution of ground loss (Figure 3.3(h)). Loganathan and Poulos (1998), Marshall (2009) and Zhou (2014) confirmed a smaller tunnel contraction at the invert than those at the tunnel crown for shallow tunnels.

The 40mm diameter model tunnel was developed for this research and fitted within the available set-up with the use of new fitting rings (Figure 3.2(b)). The design of the outer diameter aimed to limit scale and boundary effects (discussed in Section 3.1.3), and provide acceptable digital image analysis performance for the measure of surface and subsurface ground movements, and give good control of the minimum incremental tunnel volume loss to be achieved with the available volume loss control system ($\Delta V_{l,tmin} \approx 0.05 - 0.1\%$). The model tunnel consisted of a concentric solid bar with enlarged ends covered by the latex sleeve. The tunnel was designed with a concentric cylinder rather than a downwards eccentric one because, due to the high relative

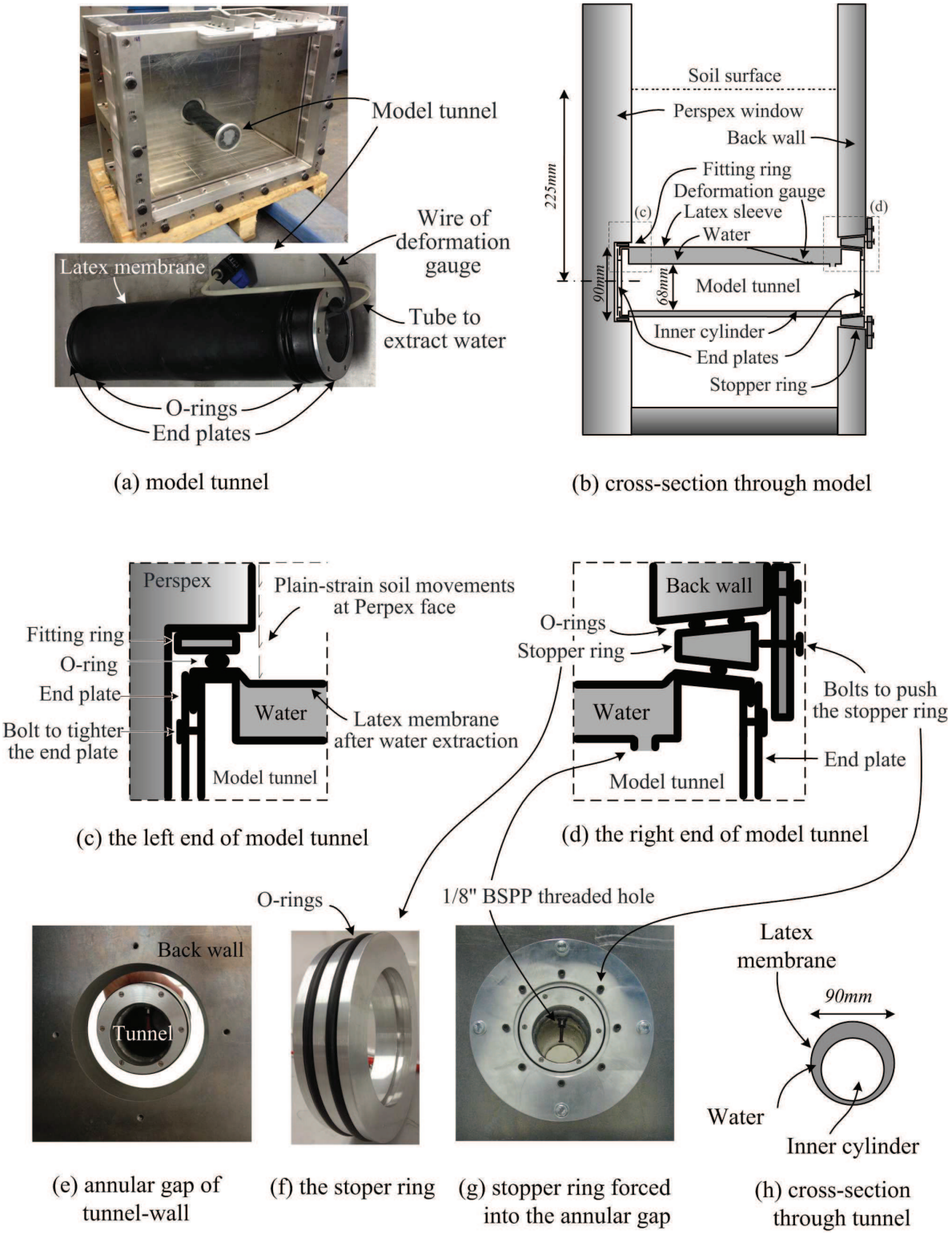

Fig. 3.3 The strong box, model tunnel and fitting rings [Zhou (2014)].

depth, the tunnel is most likely to experience a radial contraction. However, because the tunnel volume loss is due to water extraction, a concentric cylinder allows for both a radial and an oval-shaped contraction depending on the equilibrium condition between the soil and the model tunnel.

The diameters of the inner cylinders are, respectively, 68 and 18mm, thus providing more than 20% potential volume loss (dimensions shown in Figure 3.2). The ground loss was achieved by water extraction from the model tunnel with the volume control system described in Section 3.2.1.4. In this research, a maximum hydraulic pressure of approximately 350kPa was induced in-flight in the model tunnel . Therefore, the seal tests were conducted pressurising the water in the model tunnel to the maximum expected hydraulic pressure each time the model tunnel was assembled (e.g. for the replacement of the latex membrane).

To ensure a water and soil seal of the model tunnel and the strongbox, fitting rings were located at the ends of the tunnel. Although the size and shape of the fitting rings was adapted to the model tunnel diameter, the design configurations are similar for both model tunnels (the configuration adopted for the 90mm model tunnel is shown in Figure 3.3(f)). The front end of the model tunnel was forced within a fitting ring located at the recess of the Perspex. At the rear end, a trapezoidal ring was forced into the annular gap between the tunnel and the back wall (see Figure 3.3(g)). All the components (excluding the latex sleeve) were made of aluminium. Note that the latex membrane at the edges of the enlarged ends may provide a stiffening effect, which could affect the plane-strain condition at the Perspex. To minimise this disturbance, the enlarged ends of the tunnel cylinder were set slightly inside the recess of the Perspex and the back wall (as shown in Figures 3.3(c) and (d)).

3.2.1.4 Tunnel volume control system

Figure 3.4 illustrates the volume loss control system developed by Zhou et al. (2014) and its sketch. This system, bolted to a baseplate to avoid any misalignment problems, is composed of a constant-head standpipe, a Pore Pressure Transducer (PPT), a solenoid valve, a hydraulic cylinder with attached Linear Variable Differential Transducer (LVDT), an actuator and pipework connecting the system to the tunnel. Note that the system was adapted during this research to use a new L03 MecVel ball screw actuator (5kN/100mm stroke), which allowed for more accurate control of the tunnel volume loss than the previous system. The volume control system was used to achieve the following.

1. To compensate, during the centrifuge spin-up from $5g$ to Ng, the volume loss at the tunnel due to the compressibility of air trapped within the system. This was ensured by the solenoid valve connecting the model tunnel to the constant-head stand-pipe. The height of the overflow in the stand-pipe was set to provide a water pressure equal the estimated soil overburden pressure at the tunnel axis. Note that the connection between the tunnel and stand-pipe was closed by the solenoid valve during the spin-up to $5g$ to prevent a drop of the tunnel pressure.

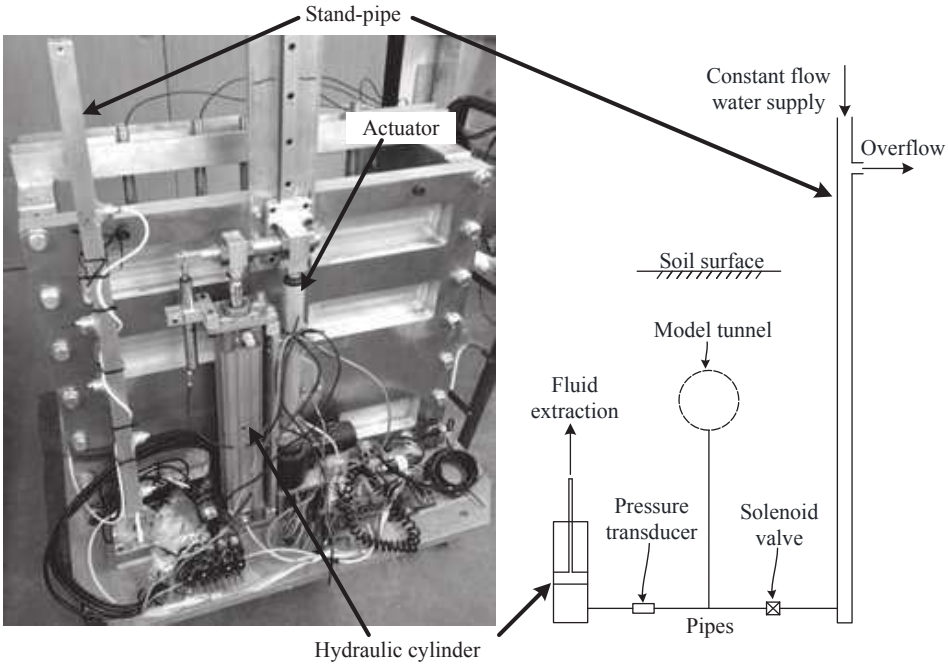

Fig. 3.4 Tunnel volume control system: (a) back view of the experimental package, (b) sketch of the volume control system [Zhou et al. (2014)].

2. To extract water from the tunnel during the test to replicate ground loss. When the target Ng-level was reached, the solenoid valve closed the connection between the stand-pipe to the model tunnel. Then, the water extraction from the tunnel was achieved by raising the actuator head connected to the hydraulic cylinder system.

3. To measure $V_{l,t}$ and tunnel pressure. The LVDT and the Pore Pressure Transducer (PPT) were used, respectively, to measure the relative displacement of the hydraulic piston, which is proportional to the extracted volume of the water (i.e. $V_{l,t}$), and the water pressure in the system.

3.2.2 Set-up for modelling of tunnelling beneath pile foundation

The set-up for greenfield tunnelling was modified to model tunnelling beneath piles. The equipment was developed to allow control of pile axial loads and measurement of the resulting pile settlements. The modification of this package required a model foundation (one transverse pile row), gantries, a loading system, and additional measurement systems. The designed experimental package, used as the physical set-up of the coupled centrifuge-numerical modelling tests in Section 3.3, is shown in Figure 3.5. Further details are provided in this section.

3.2.2.1 Model pile foundation and pile caps

For the test series (illustrated in Section 3.5) investigating tunnelling beneath a pile transverse row, a foundation consisting of either a single pile or four piles was used. During these tests,

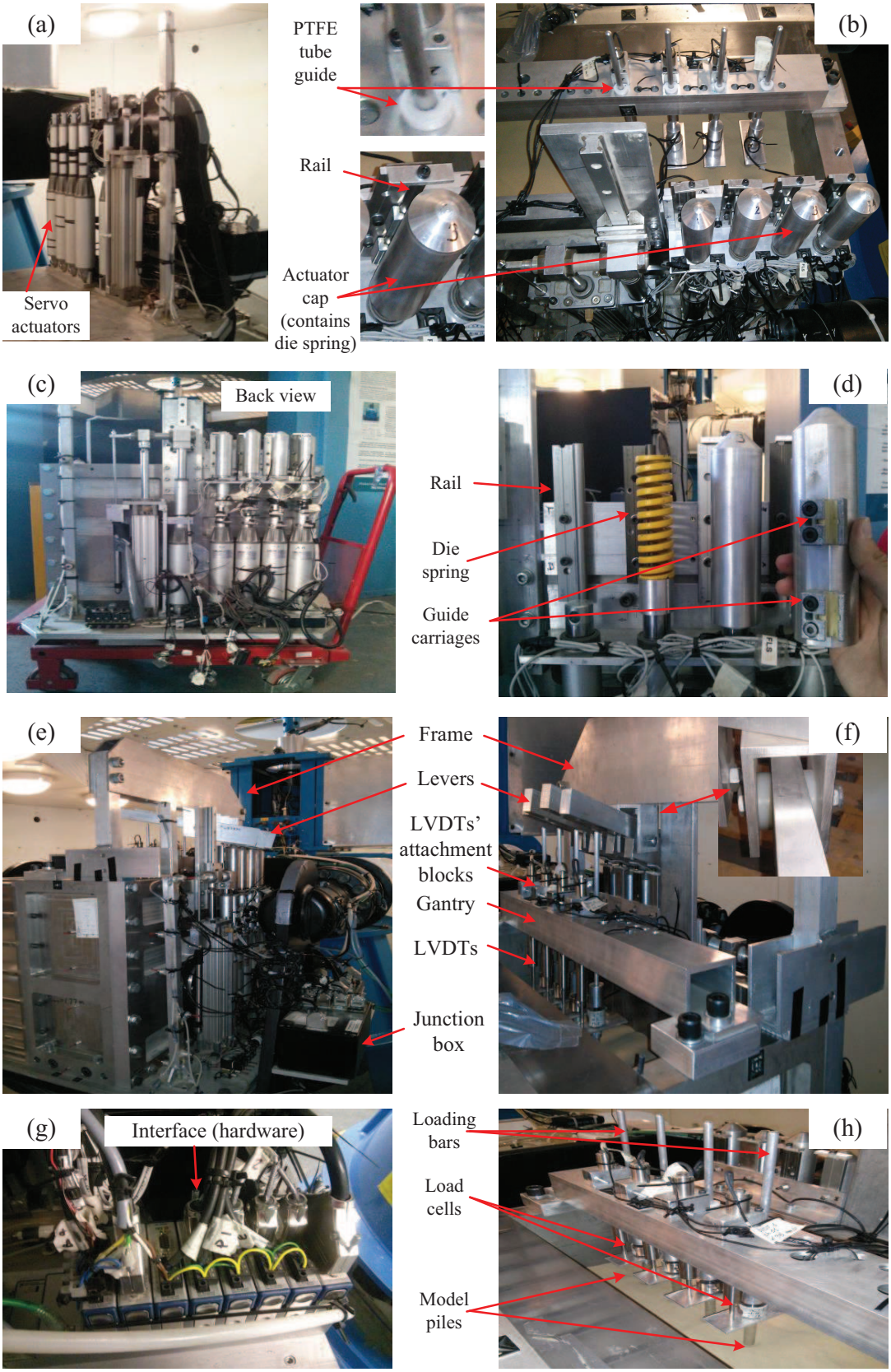

Fig. 3.5 (a) Four-axis servo actuator apparatus. (b) Details of the loading system. (c) Back view of the package. (d) Details of the actuator caps. (e) Back and (f) front views of the experimental equipment of the couple centrifuge-numerical model. (g) NI Ethernet RIO Expansion Chassis and modules for acquisition, relay triggering, motor control, and limit switch sensing. (h) View of the model pile foundation.

a load cell was installed in-line with the pile head to have a reliable measurement of the head load, which is a critical measurement for the coupling system (discussed later). The piles were full section, cylindrical aluminium rod. To reduce experimental complexity, the pile were not instrumented. The foundation and loading system, assembled in the package before spinning-up, are shown in Figure 3.5, whereas the details of the model pile and the pile cap are illustrated in Figure 3.6.

Four model piles were produced with a fully rough interface obtained by bonding sand to a 12 mm diameter aluminium alloy round bar, giving a final diameter, d_p, of 13 mm (the bending and axial stiffness values of the piles, in model scale, were 71.2Nm^2 and 7.9MN, respectively). This diameter was chosen to guarantee a realistic slenderness and a pile bearing capacity compatible with the loading system capability and accuracy. The model piles had a total length of 185mm and a 60° conical tip designed to ensure verticality throughout installation and test process; the top part of the pile was machined with a threaded hole to allow attachment of the pile cap. It was decided to adopt piles with a fully-rough interface to minimise errors due to centrifuge scale effects, which affect shear stress and mobilisation displacements (see Section 3.1.3). This design choice is further discussed in Section 3.5.5.

The pile cap was composed of two aluminium round junction bars, a load cell, a plate for the LVDT plunger, and a loading bar (see Figure 3.6). The junction bars were provided with threaded holes to attach the load cell and allow connection with the other elements. The lower junction bar had a threaded screw to connect the load cell to the pile head without eccentricities. A flat bar, onto which the plunger of the LVDT could rest to measure pile settlements, was machined with a clearance hole for the load cell extremity and glued to the top of the lower junction bar. The gap between the flat bar (for the LVDT plunger) and the load cell ensured the correct functioning of the load cell. The loading bar was machined from an 8mm round aluminium bar with a round top and a threaded end, which was screwed into the top junction bar. The material and the cross-section of the loading bar ensured the required stiffness and strength and minimised the self-weight. The vertical load was provided by the loading bar, which could be jacked/loaded at the top using the loading apparatus and the lever system. The load cell location (at the pile head) guaranteed an accurate measurement of the pile head load, which was not influenced by the loading system. Despite the fact that the pile caps and the loading bar were designed to minimise their self-weight, the applied load was given by the combination of the pile cap self-weight and the load provided by the loading apparatus; note that the pile cap self-weight resulted in the driving of the pile into the ground during the spin-up phase.

3.2.2.2 Loading apparatus and gantries

The control of the vertical loads at the pile head was achieved using a loading apparatus consisting of the following elements: actuators, die-springs, actuator caps and their vertical guide carriages and rails, a lever system, pile loading bars and their vertical guides within the gantry. Each pile was independently loaded via the lever system. The achievement of good performance from the load-control system (real-time interface and physical components) relied on the in-flight

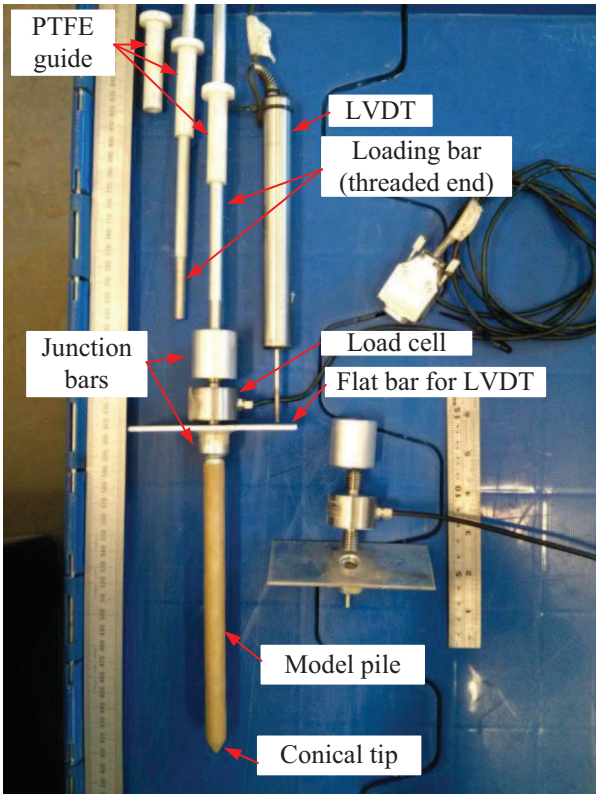

Fig. 3.6 The model pile and the pile cap.

efficiency of the loading apparatus. Despite the preliminary testing of the load-control system at 1g, the system apparatus capabilities in terms of maximum loads and accuracy were investigated during the preliminary centrifuge tests reported in Section 3.3. It should be noted that in-flight loss of loading capacity (due to misalignments) and geometrical restrictions (due to the pre-existing greenfield equipment) represented the greatest challenges for this design. If not stated otherwise, the material used was 6082T6 aluminium alloy.

The four-axis servo actuator apparatus capable of applying independent vertical pile loads is shown in Figure 3.5(a). Two elements were used to attach it to the strong box and avoid misalignments within the system: a) a T-shaped beam ($3''$ $W \times 3''$ $H \times 8$mm T) bolted to the actuator bottom ends and the base plate of the package, and b) an L-shaped bar ($3''$ $W \times 2''$ $H \times 1/4''$ T) bolted to the back-wall of the strong box; the latter element has four 36mm diameter clearance holes to accommodate the actuator bodies. Four L03 MecVel ballscrew actuators with 100mm stroke and 5kN capacity (at 1g) were used.

At the top end of each actuator was located an in-line heavy duty die-spring (32mm $D \times$ 16mm $d \times$ 102mm L, stiffness rate 155N/mm) inserted into a clearance hole by the actuator cap. An aluminium round block, with transverse dimension equal to the die spring external diameter, was placed between the actuator top end and the die spring. This block, at the bottom, and the actuator cap, at the top and laterally, confined the die spring. To minimise load eccentricities,

each actuator cap was machined from a 50mm diameter round bar with a round top end loading the lever beam. Threaded holes were drilled into the actuator cap to connect, using bolts, the cap to two linear guide carriages. For each actuator cap, the two linear guide carriages were used in-line with a single linear rail to limit the movement of the cap to the vertical direction and to balance any horizontal load raising from the lever inclination with the reaction forces of the rail. The four rails were bolted to two L-beams connected to the back wall of the strong box. The die springs were inserted to achieve good load-control accuracy and convergence. The die spring increase the system deformability; this allowed damping of the pile load-actuator displacement relationship while guaranteeing low convergence time (e.g. a spring with an excessively low stiffness rate would have increased the time necessary to apply a given incremental load). The actuator cap connected to a vertical rail was used to guarantee the correct functioning of the actuators, which are designed only to provide axial loads and are not able to resist horizontal forces at the top end piston. As a safety feature, a flat bar was bolted to the top of the rail. To summarise, in the implemented system, the loads from the actuators were transferred to the piles via a) the die springs and the actuator caps connected to vertical rails, b) the lever beam, and c) the pile loading bar.

The conceptual design of the system of levers and guides within the gantry was chosen to allow changing the pile location within the strong box with secondary modifications. The system was assembled with 4 lever flat bars ($3/4'' \; W \times 2.5'' \; H$) bolted to a U-channel ($1.5'' \; W \times 3'' \; H \times 1/4'' \; T$) connected to a frame, which was composed of a machined rectangular tube ($2'' \; W \times 6'' \; H \times 1/4'' \; T$) and two T-parts bolted to the strong box U-channel. The T-parts were obtained by welding a square bar ($1.5'' \; W \times 1.5'' \; H$) to a U-channel ($2'' \; W \times 3'' \; H \times 1/4'' \; T$) and, for sake of safety, a pinned connection was added. The pivot connection of each lever was realised with the use of a bolt, a deep groove ball bearing and two disks. A lock nut was used to prevent loosening of the bolt. Two frictionless PTFE disks were placed between the lever beam and the U-channel to fill the gap and prevent misalignments, whereas the deep groove ball bearing was installed in the middle of the lever to provide the pivot. The orientation of the beam in the horizontal plan was chosen to match the positions of the extremities of the levers to the four-axis servo actuator apparatus, on the rear side, and the pile loading bar connected to the pile caps, on the front side. The position of the pivot, closer to the actuator than the pile, allowed for an improved load-control accuracy (i.e. the ratio between actuator and pile forces is greater than unity) preventing problems due to the limited available actuator stroke. In particular, with the designed equipment, the piles could be driven approximately 50mm, which allowed for the in-flight pre-tunnelling pile installation, and approximately 25mm of potential tunnelling-induced settlements. Note that the lever was machined to reduce the beam cross-section on the side between the pivot and the pile foundation; in this way, the levers, due to their self-weight, rested on the actuators during the centrifuge tests allowing for the lever retraction and the complete unloading of the piles.

Figures 3.5(b) and (f) show the gantry used to hold the LVDTs and to provide vertical guides to the pile loading bars. The gantry consists of a $3'' \; W \times 2'' \; H \times 1/4'' \; T$ rectangular tube with

the extremities reduced to a flat bar. Multiple threaded and coaxial clearance holes (the latter on both top and bottom plates) were drilled, at a 75mm spacing, to allow the connection with the LVDTs and their attachment blocks. Furthermore, coaxial clearance holes at a 25mm spacing were machined to accommodate the pile loading bars, which were connected to the pile caps. Guides consisting of PTFE tubes were located in these clearance holes to ensure the verticality of the pile loading bar. In this way, bending moments were not transferred by the lever system to the pile cap, thereby preventing pile cap damage. These guides were machined from a PTFE 20mm diameter round bar, with inner and outer diameters providing, respectively, a tight fit with the pile loading bars and the coaxial clearance holes. These tubes were machined with an enlarged cap at the top to prevented the downwards movement of the guide. Although some friction between the guides and the loading bars may have been induced by misalignments and loading bar elastic bending, this friction did not affect the measured pile axial loads because the load cells were located at the pile heads.

The preliminary design of the lever system was carried out by means of the beam theory, whereas an Abaqus 3D FEM was developed to check stresses and stiffness (Figure 3.7). In general, the necessity to optimise the ratio between axial or bending stiffness, to minimise the lever system self-weight, and the geometrical limitations due to the existing facilities guided this design. Note that the final design, shown in Figure 3.5, slightly differs from the numerical model because several geometrical adjustments were adopted in the later stages. In the Abaqus model, the following geometric simplifications were introduced: the U strong box was only partially modelled introducing fixed constrains at the cuts; the top part of the U-channel and the M16 bolts screwed in it were modelled through a unique part; four levers were placed at the centre of the support beam spaced of 70mm; the contact surface between actuator head and lever beam was reproduced with a displacement boundary condition restraining the beam movement in the vertical direction, whereas the contact surface between the pile loading bar and the lever beam was modelled with a normal pressure distribution on a 4×4mm area at the bottom of each lever; the self-weight load of an LVDT and its support was replicated by means of a normal pressure on a 20×20mm surface and the presence of the holes in the gantry was neglected; channel and square beams of the T part were modelled as a unique part because of a welded connection.

A linear elastic isotropic behaviour was assigned to the materials (aluminium and steel) whereas the mesh optimisation was achieved by adopting wedge elements, imposing that the global seed size does not exceed 5mm and that mesh refinements in correspondence of holes (at least 16 elements for each edge). The pile load bearing capacity, the centrifuge scale factor and the actuator head displacement are indicated, respectively, as F, N and u. The investigated load combinations are: for the spin-up $F = 0$kN, $N = 80$, $u = -0.5$mm; for the Serviceability Limit State (SLS) $F = 2$kN, $N = 80$, $u = 0$mm; for the Ultimate Limit State (ULS) load: $F = 6$kN; $N = 80$, $u = 0$mm.

The results of the FEM analyses demonstrated the following. a) The spin-up simulation and the serviceability limit state analysis confirmed that the overall stiffness of the system is compatible with the mechanical parts and the desired degree of accuracy. Furthermore, the

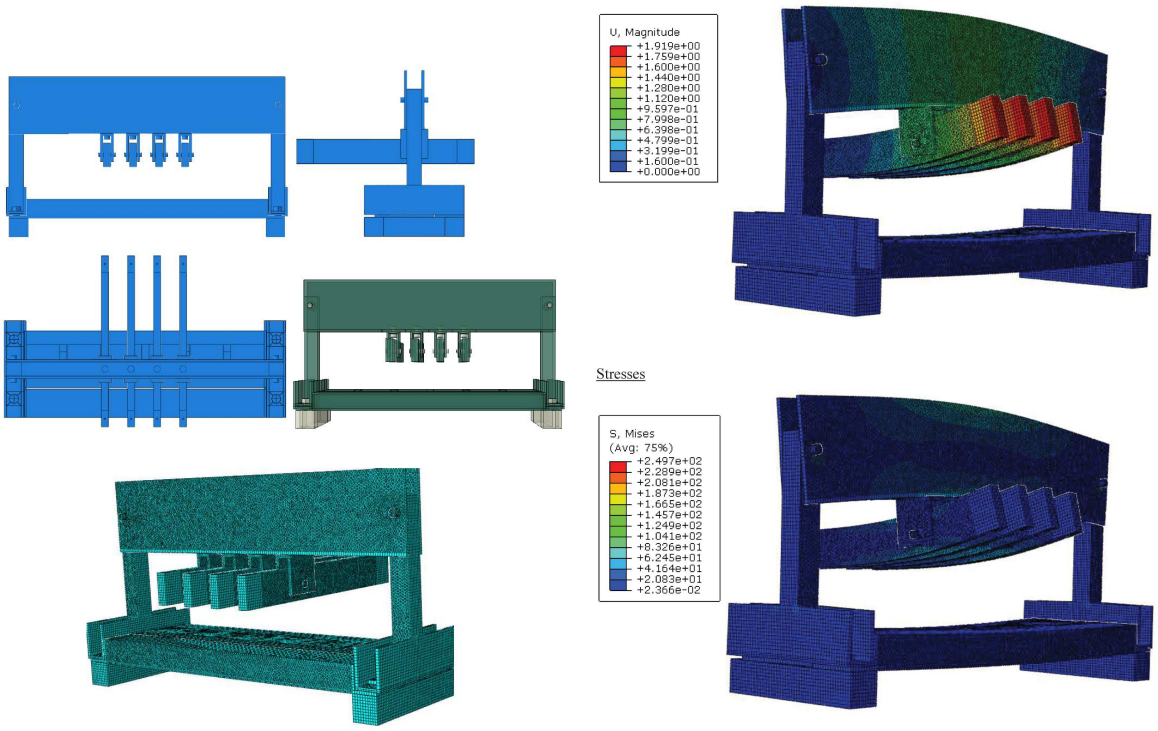

(a) (b)

Fig. 3.7 Abaqus model of the lever system and gantries: (a) geometric parts and mesh; (b) stresses and displacements at the Ultimate Limit State.

stress field depicts a fully elastic response of the system to moderate load. b) At the Ultimate Limit State, the displacements do not exceed 2mm and stresses do not indicate the risk a failure (Figure 3.7). In fact, the stresses are considerably lower than the yield value of 261 MPa (6082T6 aluminium alloy) in the model except at the lever beams at the boundary conditions modelling the tops of the loading bars and the actuators. Therefore, to minimise the stress concentration and the risk of locale failure, the top parts of the loading bars and actuator caps were designed with rounded surfaces.

3.2.3 Instrumentation and techniques for the measurement of displacements and forces

3.2.3.1 Digital image analysis

Digital image analysis was used to measure displacements at the at the Perspex window. In this research, the GeoPIV image-based measurement technique, developed by White et al. (2003), was used to measure i) surface and subsurface soil displacements in greenfield tests and ii) tunnelling-induced displacements of the piled plate during tunnel-pile-structure interaction tests. The GeoPIV method has proved to be a reliable tool for the measurement of displacement by previous applications (Marshall et al., 2012; Zhou, 2014). However, for the sake of validation,

the imaged-based data was compared with the vertical displacements of the piled plate measured by LVDTs at the middle of the strong box.

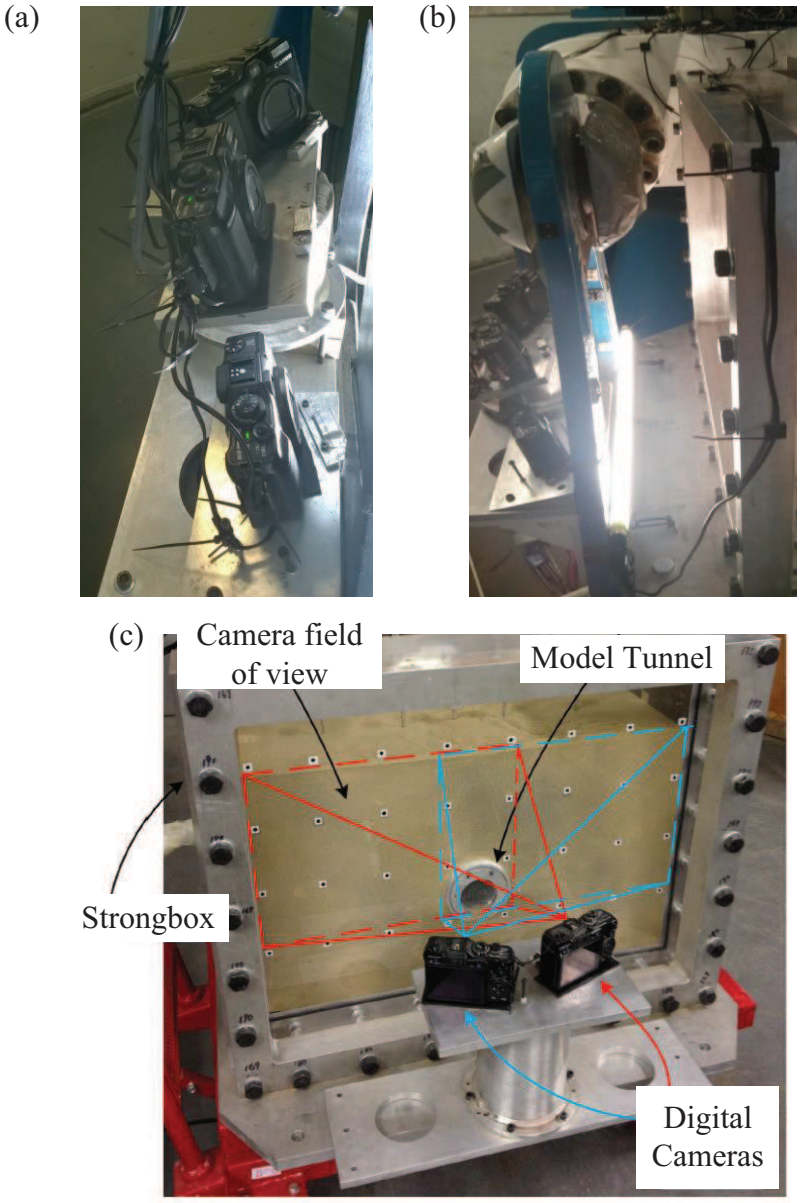

Fig. 3.8 (a) Digital camera set-up, (b) cameras, lights and strong box, (c) example of the camera fields of view.

The measurement process consists of taking a series of digital images at the Perspex wall throughout the tests and then analysing them with GeoPIV. Firstly, particle image velocimetry (PIV) is used to track the movement of pixel patches (soil or markers) through a series of images; subsequently, the reference system is transferred from pixels into spatial coordinates using close-range photogrammetry and the control markers painted on the inner face of the Perspex window. In this way, patch displacements are converted into distances with units of mm. Note that the coordinates of the control marker positions are needed. To accurately measure the location of the Perspex control points, the calibration process described in detail by Marshall (2009) and Zhou (2014) was adopted. To guarantee satisfactory performance of the GeoPIV

process, the zoom level of the lens was maximised with the necessary field of view, the texture of the soil was enhanced (when possible) by pouring a thin layer of dyed and un-dyed sand as the Perspex window, and the lighting of the Perspex window was set to achieve uniformity and avoid reflections within the camera field of view.

The centrifuge model includes two or three digital cameras located at the front of the centrifuge container, as shown in Figure 3.8(a). Canon PowerShot G10 14.7MP 28mm digital cameras were used. Two cameras were mounted on an aluminium frame. They were positioned to capture the soil above the model tunnel and at the tunnel springline or the piled plate deformations (the concept is illustrated in Figure 3.8(c)). Additionally, during some of the greenfield tests, the system was upgraded with a third camera, positioned on an aluminium support, and used to track soil movements beneath the tunnel invert. Each camera was secured to the frame with a bolt. An aluminium block was placed beneath the telescopic camera lenses of each camera to provide support and rubber mats were interposed between the aluminium support and the camera base and lenses to prevent in-flight stress concentrations. The cameras were positioned so that the field of views overlapped to allow merging of measurements. During a centrifuge test, the PSRemote software was used for the remote control of the cameras and synchronisation of image capture. Images were stored in the memory cards of the cameras. The software was installed in the computer mounted on the centrifuge, which was connected to the cameras by USB cables.

3.2.3.2 Linear Variable Differential Transducers (LVDTs)

In this research, Linear Variable Differential Transformers (LVDTs) were used to measure pile and piled plate settlements. The pile settlement measurement was performed with an LVDT located at each pile (Figure 3.5) (Solartron Metrology Displacement Sensor LVDT, S Series, $\pm$5V DC output, $\pm$25mm stroke). Five LVDTs were mounted on a gantry at the middle of the box to measure the settlements of the piled plate (Figure 3.17).

Figures 3.5(d) and (f) show the LVDT gantry used for investigating tunnelling beneath piles. Figure 3.17 shows the LVDT gantry, designed by Zhou (2014), that was used for the monitoring of the pile plate displacements. The gantry was made from a $2'' \; W \times 2'' \; H \times 1/4'' \; T$ U-frame. The gantry could secure five attachment blocks, each holding one LVDT. The material of the two gantries was 6082T6 aluminium alloy.

3.2.3.3 Load cells

It was important to achieve an accurate measurement of pile head loads during tunnelling beneath piles. In-line load-cells were used (Richmond Industries, 5kN capacity, nominal sensitivity 2.0mV/V). In general, sufficient sensitivity and acceptable peak-to-peak noise were ensured by these load-cells and the adopted data acquisition system (for details refer to Section 3.3.3). Load cells were mounted in-line with the pile axis at the pile cap as shown in Figures 3.5(d) and (f). Note that, prior to each centrifuge testing session, the load cells were loaded in steps to 1.5kN with the use of a calibration frame to check their performance.

In the case of the coupled centrifuge-numerical model, the measurement of the shared boundary conditions (loads and displacements) in the centrifuge model was essential to guarantee acceptable performance. Therefore, further information on the instrumentation and the measured peak-to-peak noise regarding the coupled centrifuge-numerical model are given in Section 3.3.3.

3.3 Development of a coupled centrifuge-numerical model to study soil-structure interaction problems

This section presents a method to study soil-structure interaction through the real-time coupling of the centrifuge and numerical modelling. This section provides a description of the design philosophy and the implementation of the system. Three applications were carried out: pile loading, tunnelling beneath piles with constant loads, and tunnelling beneath framed buildings (where the building characteristics affect the redistribution of loads on piles). Test results are presented to confirm the expected performance of the newly developed coupled centrifuge-numerical modelling (CCNM) system. The development presented here was also published within Franza et al. (2016b).

3.3.1 Background

The development of a coupled centrifuge-numerical model was an important part of this research. Accurate centrifuge modelling of soil-structure interaction (SSI) problems is notoriously difficult to achieve because of the difficulty of including realistic reduced scale models of structures. Conventional physical modelling methods tend to assume simplified/equivalent superstructures (i.e. rigid connections or beams) or constant loads from the superstructure. However, in this way, the super-structure contribution to the foundation response is not modelled properly and the effect of the modified response of the foundation on the behaviour of the soil is not accounted for.

To overcome these limitations, the real-time sub-structure testing approach described by Blakeborough et al. (2001) can be extended to centrifuge modelling. Real-time substructure testing consists of performing a full or large scale physical test on key elements of the domain (where non-linear or complex behaviour is expected), and coupling this experimental data in real time to a numerical model of the remaining domain. The coupling is based on the transfer of information (loads and displacements) at a shared boundary. Gaudin et al. (2012) successfully developed a hybrid centrifuge-numerical model to study the jack-up-footprint interaction problem. Real-time distributed substructure testing involving centrifuge facilities has also been applied in distributed grid testing networks, where testing is performed through experimental and numerical models (simulating the substructures) located at different test facilities (Madabhushi et al., 2010).

3.3.2 Methodology

The proposed global tunnel-structure analysis methodology is illustrated in Figure 3.9(a). The method couples experimental and numerical modelling tools to benefit from their respective strengths: the numerical model allows accurate simulation of the structure, whereas the tunnel-ground-foundation system is modelled with the centrifuge to accurately reproduce soil and soil-structure interaction behaviour. The coupling is achieved by means of a real-time data acquisition and load-control interface.

This method can be summarised in the following steps (see Figure 3.9(a) and (b) for the representation of the global and the decoupled domains). [1] In the centrifuge, using independent actuators, the model piles are driven or loaded to replicate an installation procedure and service loads P_0. After the initial pile loading, [2] the numerical model is run in parallel with the centrifuge model. Centrifuge and numerical models are coupled in real-time by the interface system that continuously a) adjusts the pile loads in the centrifuge, P, to the demand values P' ($\delta P = P' - P$), and b) retrieves the target loads P' from the numerical model. To compute the numerical demand value P', i) the incremental pile displacements, v, are measured in the centrifuge and passed to the numerical model; ii) the structural simulation is carried out to calculate the new pile loads, P'; iii) the modified loads, P', are passed back to the interface and the demand load for the centrifuge model is updated. The actions a) and b) are run independently by the interface at the maximum rate to achieve convergence of the CCNM (i.e. to match the boundary conditions at the interface). Note that the time necessary for the physical motion of the actuators and loading system inevitably results in a time lag for the convergence of the physical and numerical models. [3] An incremental tunnel volume loss, $\Delta V_{l,t}$, is induced in the model tunnel using an external volume control system. This volume loss causes settlement of the pile group, v. If the convergence of the coupled system is satisfied by the real-time interface through the process in step [2], it is possible to apply further $\Delta V_{l,t}$. To obtain an accurate coupling it is necessary to minimise: $\Delta V_{l,t}$, the computational time of the numerical analysis, and the load convergence time between P and P'. The vertical loads and settlements are the main parameters affecting tunnelling beneath piled foundations. Therefore, to minimise experimental complexity, the proposed tests only consider the vertical pile loads in the centrifuge.

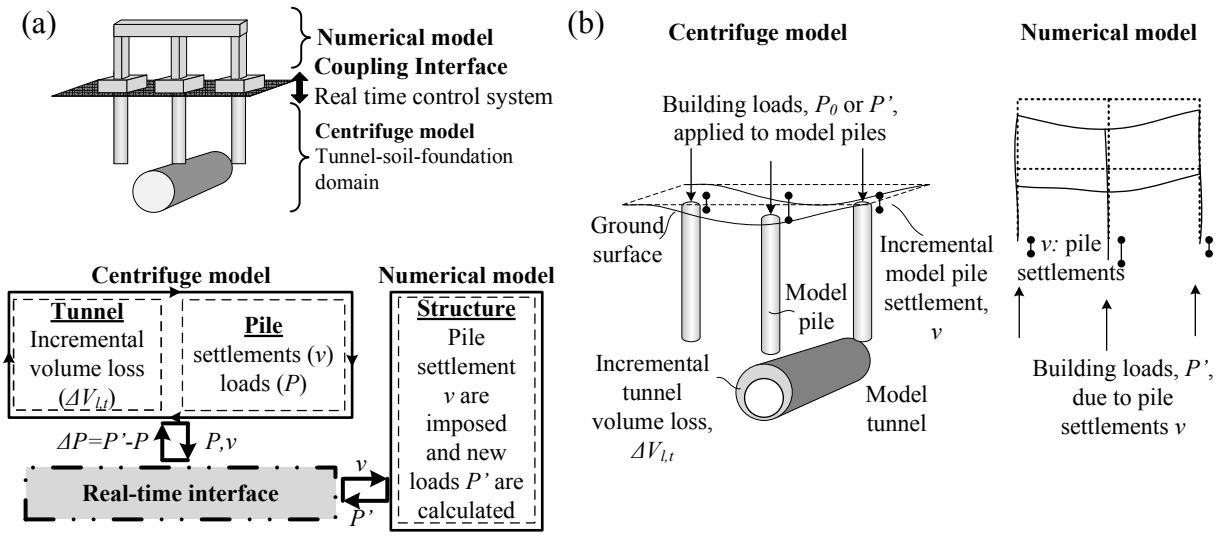

Fig. 3.9 Proposed coupled centrifuge-numerical model: (a) global domain and diagram of the coupling loop, (b) representation of the de-coupled geotechnical and structural domains.

3.3.3 Development of the experimental equipment, real-time interface, and numerical model

3.3.3.1 Centrifuge equipment

The experiment prototype illustrated in Figure 3.10(b) was simulated with the centrifuge model shown in Figure 3.10(a), as described in Section 3.2 , which comprised of the following components. [1] Tunnel: plane-strain tunnel model with 90mm diameter tunnel and tunnel volume control system. It was buried at 225mm depth (to tunnel axis). Dry silica sand (Leighton Buzzard Fraction E) was used. [2] Model foundation (one transverse pile row): 12 or 16mm diameter aluminium alloy round bar with a length of 185mm. Piles had a fully rough interface obtained by bonding sand to the outer surface. Final embedment depth was ≈ 150mm. Piles could be jacked into the ground in-flight to model the installation of displacement piles. [4] Loading system: four-axis servo actuator apparatus capable of applying independent vertical loads. Each pile was loaded via a lever system incorporating a 5kN/100mm stroke ball screw actuator. In-line load cells were used to measure pile head loads. [5] Pile settlement measurement: Linear Variable Differential Transformers (LVDTs) were mounted on each of the piles.

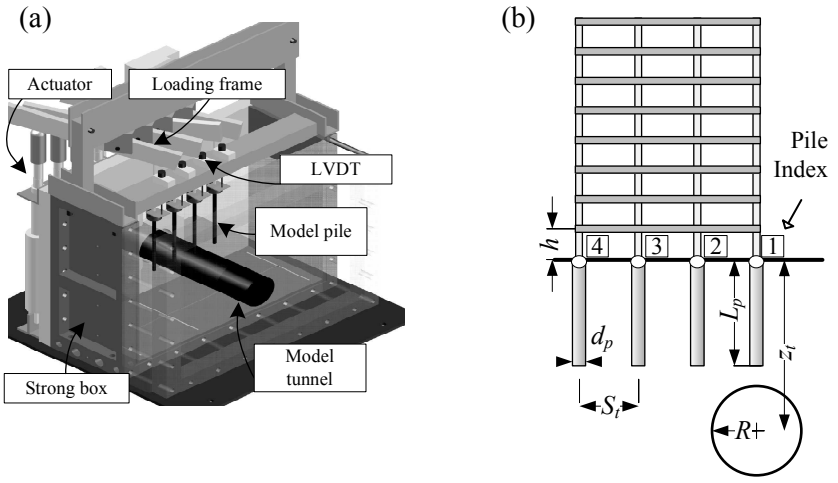

Fig. 3.10 (a) Drawing of the experimental equipment; (b) layout of the experiment prototype.

3.3.3.2 Real-time interfacing with control system

Coupling the output of the numerical models to the actuators requires the use of flexible and scalable hardware and reliable software integration. Actuator control and data acquisition tasks must be performed synchronously with the real-time numerical computations. Microcontrollers and embedded controllers have been used previously to achieve actuator control and data acquisition tasks. However, these systems do not provide a high level of flexibility, are difficult to integrate with other high-end acquisition systems, and require lengthy development (Monmasson et al., 2011). They are also not easy to reconfigure and are usually deployed after an extensive development process (Ullmann et al., 2004). An alternative implementation utilises Field Programmable Gate Array (FPGA) technology that consists of reconfigurable elements that give

the end user/developer full control of the controller at the hardware level (Monmasson et al., 2011). Their inherent ability to execute parallel programs makes them ideal for applications such as the real-time CCNM program that requires a low response time.

The real-time system is comprised of an FPGA controller (NI-9149) for scalable hardware integration, interchangeable modules, and a local PC that runs LabVIEW. The modules are required for acquisition (NI-9205); relay triggering (NI-9474); motor control (NI-9505); and limit switch sensing (NI-9403). Sensor signals are acquired and processed in the FPGA then transferred to a LabVIEW program on the local PC. The FPGA controller and its hardware components were mounted on the centrifuge platform adjacent to the centrifuge strong box to minimise the level of noise in the signals. The hardware was tested up to $\approx 100g$ without showing any performance issues.

The main processes that couple the two models are contained within two loops that are run independently and at different frequencies. One loop is executed in LabVIEW on the local PC and the other is run on the FPGA controller. The LabVIEW program on the PC loops at a fixed interval $\Delta t = 60$ms. This loop a) monitors changes to the user interface; b) gets new information from the FPGA on the centrifuge sensors; c) feeds the incremental pile settlements v to the numerical model which runs in a MATLAB script within LabVIEW; d) executes the structural analysis that computes new target loads; and e) transfers the new target loads to the FPGA. The local PC program also logs data and sends a signal to the FPGA at a given interval to indicate continued safe program operation.

The FPGA program, which loops at real-time frequency ($\approx$ 2ms), a) acquires data from the centrifuge instrumentation (4 load cells, 5 LVDTs and 12 limit switch sensors) and b) adjusts the pile loads in the centrifuge to the target values. The FPGA program carries out the action (b) by controlling the actuators based on communication with the PC and performing automatic load-control using a Proportional, Integral, Derivative (PID) algorithm. The program also transfers the system state to the local PC LabVIEW program and continuously maintains system safety by monitoring the limit switches and the "safe operation" signal from the PC.

The LabVIEW user interface provides the user with information about the sensors and adequate control of the actuators. Manual actuator extension or retraction can be executed by the FPGA motor controller when the user modifies manual controls. Alternatively, automatic load-control can be activated which initiates the PID force controller on the FPGA. Load targets for the automatic load-control can be specified by 1) the user on the LabVIEW control interface, or 2) set equal to the force targets obtained from the numerical model. These force targets are realised by the PID control algorithm. Manual tuning methods were used to determine gain settings for the PID control algorithm at $1g$ but were later fine-tuned for elevated gravity operations. The control system is illustrated in Figure 3.11(a), (b) and (c).

A watchdog timer in the FPGA was implemented as one safety precaution. Loss of communication with the PC for a time duration $t > 500$ms causes the watchdog to stop power to the motors. This prevents catastrophic actuator motion in the case of PC failure. Limit switches were also employed to prevent excessive actuator movement. Software limiting was adopted

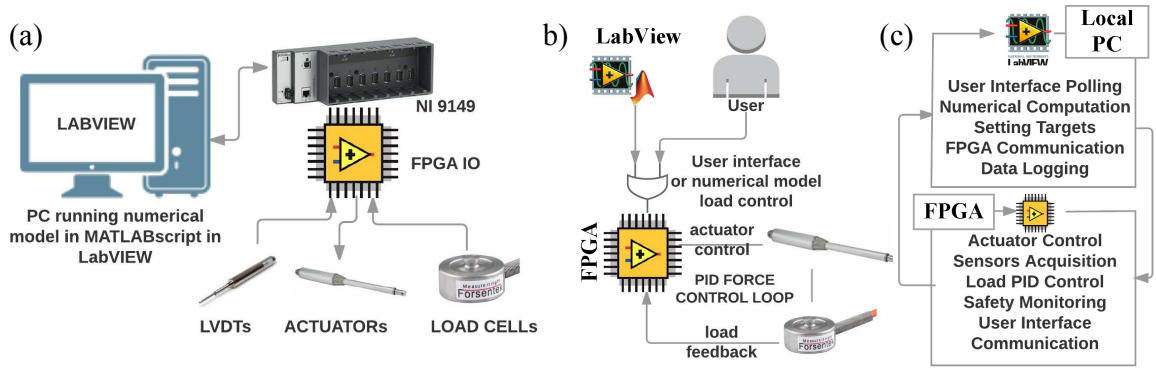

Fig. 3.11 (a) Components of Real-time control system; (b) load-control loop from user command and numerical model demand; (c) order of operations for LabVIEW on local PC and FPGA setups.

to halt unwanted motion and hardware limiting was implemented as an additional failsafe. A third level of safety was employed using data from the LVDTs to warn the user if any of the 4 actuators exceeded a pre-set movement threshold.

It was important to adopt effective signal filtering since scatter within measurements from the centrifuge model is amplified by the scale factors in the data passed to the numerical model (working at the prototype scale). In particular, filtering LVDTs was critical to avoid unrealistic target load fluctuations P' in the centrifuge model. For a given prototype structure of stiffness K, according to the centrifuge scaling laws, the target load at the model scale are $P' = K[N(U^r + U^e)]/N^2$, where U^r and U^e are, respectively, the model pile settlements and the error in the LVDT measurements due to the signal noise (both at the model scale). Target load fluctuations due to LDVT signal noise are $P'^e = KU^e/N$. Note that the stiffer the superstructure the more critical is this aspect.

The measurement system had peak-to-peak noise of 5mV which meant $\pm$0.0125mm noise on the 50mm LVDTs at the model scale. This would be equivalent to $\pm$0.75mm at prototype scale for a scale factor $N = 60$, which is not compatible with the structural analysis of realistic buildings. Signal filtering reduced this peak-to-peak noise to 0.3mV using a 4^{th} order Butterworth low-pass filter with 30Hz cut-off frequency implemented in the FPGA after the acquisition step. This resulted in the input for the numerical model being subjected to an acceptable fluctuation ($\pm$0.05mm at prototype scale). Clearly, minimisation of noise from the LVDTs has a beneficial effect on the CCNM performance; the minimum achievable range is determined by the hardware and adopted filtering. Definition of an acceptable noise level depends on the scaling factor N and the characteristics of the scenario and superstructure being studied, hence general criteria cannot be defined.

Minimal signal filtering was used for the load-control since high-frequency updates to the PID controller was required ($f = 1$kHz). As such, a low-pass filter with 1kHz cut-off frequency was applied to the load signals.

3.3.3.3 Numerical model system

In this research, a matrix structural analysis was adopted to calculate the pile load distribution, P', based on the pile head displacements, v. The simulation of the prototype framed structures was performed using the finite element method, which was implemented in MATLAB. The stiffness matrix of the rigidly connected elastic frame structure (fixed pillar-beam connections) was obtained using Euler-Bernoulli beam theory. The numerical model was designed with the assumption of hinged pile-superstructure connections to replicate the conditions in the centrifuge model (Figure 3.10(b)). The global interaction was assessed for the case of linear elastic frames. This aspect can be modified for for future research development.

The numerical model was implemented within the real-time interface as a component of the LabVIEW program using the MathScript node. Note that the time cost for calling and executing the function in the MathScript node was 35ms. Additional time ($\approx$ 20ms) was also required to complete the other tasks in the LabVIEW program. Therefore, the execution of the LabVIEW program, set to loop every $\Delta t = 60$ms, ensures a deterministic response of the CCNM. This frequency rate is considered satisfactory for the proposed tunnelling application.

3.3.4 Applications for preliminary testing of the system

For demonstration purposes, three applications were carried out in-flight. Note that the presented data were collected during preliminary tests aimed to validate the CCNM methodology. The tests were performed at $60g$ ($N = 60$); model dimensions and results are reported in model scale.

3.3.4.1 Pile axial loading

This experiment was performed using two model piles to verify the accuracy and the convergence time of the load-control system. Piles were located in positions 2 and 4 from Figure 3.10(b) and had, respectively, a diameter of 12 and 16mm to investigate the performance of the CCNM in the case of varying stiffness of the soil-pile system. Load was applied in steps of 50N, with minimum and maximum loads being 400N and 800N.

The demand loads, P', and the centrifuge load measured at the pile head, P, are shown against time in Figure 3.12(a) (large time interval) and (b) (detailed interval). The data show that the load-control system maintains the target load within 10N. For the specified load demand variation of 50N, the system reaches convergence ($\delta P = P' - P < 10N$) within $100 - 200$ms. For the tunnelling application, P' varies in steps considerably smaller than 50N due to the small increments of $V_{l,t}$; practical convergence time will, therefore, be less.

3.3.4.2 Tunnelling beneath piles

In the experiment, if the actuator position is not adjusted, pile settlements result in a decrease of pile loads. An experiment was performed for the case of tunnelling beneath piles with constant

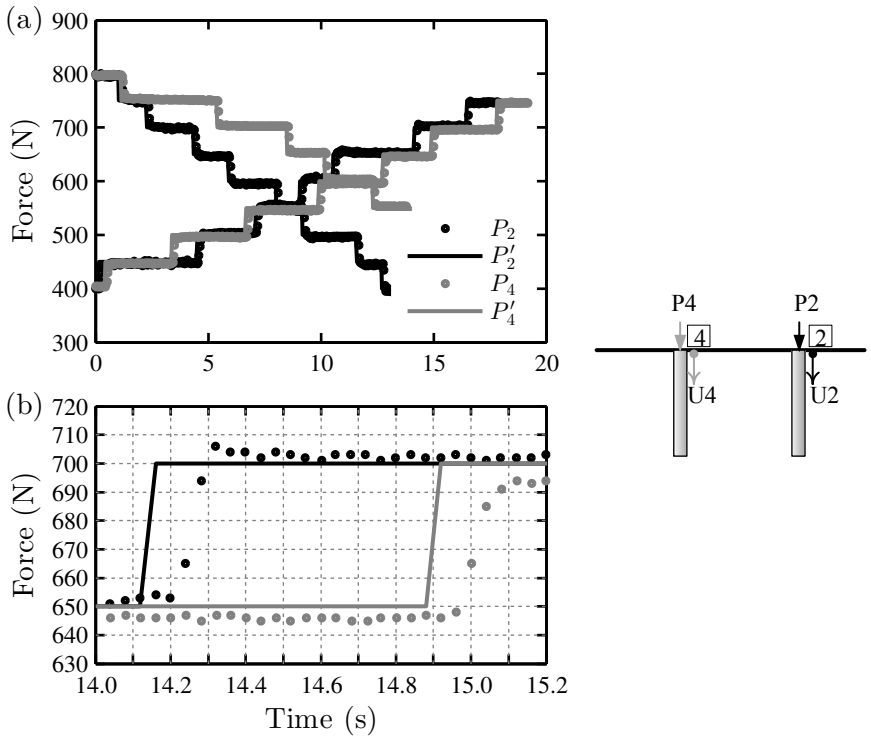

Fig. 3.12 Comparison of centrifuge and demand loads.

load demand to verify load-control capability. This testing procedure is equivalent to performing a more conventional centrifuge test where piles are loaded using independent masses.

Two model piles with a diameter of 12mm were located in positions 2 and 4 and a constant load demand, P', of 600N was specified after centrifuge spin-up. Thereafter, although CCNM tests of tunnelling beneath piles should be performed with discrete values of $\Delta V_{l,t}$, during this "performance" test a constant rate $\Delta V_{l,t}/s \approx 0.15\%$ was induced to investigate the capability of the system under more extreme conditions.

Figure 3.13 shows pile head settlements (U), vertical loads (P) and target forces (P') for the two piles. Note that as pile 2 undergoes a considerable rate of settlement ($U_2/s \approx 0.9$mm) for $V_{l,t} = 0.6 - 1.9\%$, the load-control system is able to maintain, within an acceptable tolerance, the target load. After $V_{l,t} \approx 1.9\%$, the system becomes unstable due to complete failure of pile 2. Overall, the results of this test illustrate the good performance of the load-control system.

3.3.4.3 Tunnelling beneath piled frames

Two tests (A and B) were performed for the case of tunnelling beneath piled framed buildings to verify the performance of the developed CCNM technique and to illustrate its potential. The flexibility of the framed building was varied: test A included a semi-flexible frame, whereas test B included a rigid frame. Frame B represents an upper limit of the practical stiffness of a framed building. Modelling of rigid buildings represents a challenge in these tests because of the LVDT signal noise amplification at the prototype scale, which for rigid buildings results in larger fluctuations of the target forces.

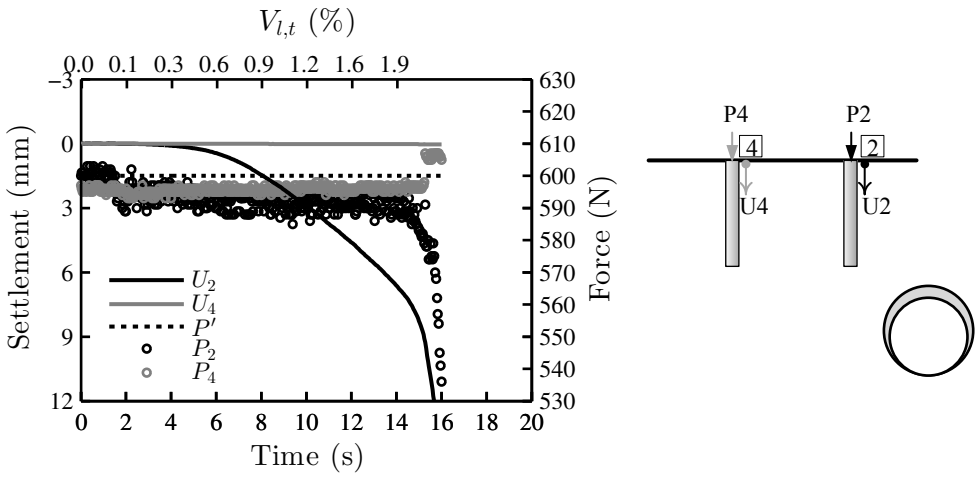

Fig. 3.13 Pile head settlements and load cell measurements during tunnelling beneath piles with a constant load demand.

During both tests, four model piles with a diameter of 12mm were located in positions 1 to 4. A structural service load demand, P'_0, of 500N was specified after centrifuge spin-up. Thereafter, to simulate tunnelling, discrete $\Delta V_{l,t}$ were induced in the centrifuge model. The resulting demand load is equal to the sum of the service load, P'_0, and the superstructure reactions, $\Delta P'$, due to incremental pile settlements, v (i.e. $P' = P'_0 + \Delta P'$). The geometry of the prototype frames is displayed in Figure 3.10(b). The 8 storey concrete buildings ($E = 30$GPa) had a storey height, h, and a span length, S_t, of 3 and 4.5m, respectively. The beams and columns of frame A had square cross-sections of 0.3×0.3m, whereas frame B had structural elements with square cross-sections of 0.7×0.7m.

The variation of head settlements (U) and model pile vertical loads (P) with $V_{l,t}$ during tests A and B are shown in Figure 3.14. The different response of the piled buildings to tunnelling in the two tests is evident, as illustrated by a qualitatively different distribution of loads and settlements in Figure 3.14(a) and (b). The fluctuation of model pile loads is greater in test B than test A due to signal noise amplification of LVDT measurements with the scale factor N which, as previously discussed, has a greater impact on the CCNM performance for more rigid structures. In general, the results of these two tests highlight the importance of accounting for the superstructure in the assessment of building/foundation response to underground excavations.

3.3.5 Summary

This section presented a method to study soil-structure interaction through a real-time load-controlled coupling of numerical and centrifuge modelling. A robust and versatile load-control system, which is based on a real-time interface able to actuate in the centrifuge (in-flight) user-defined load demands, has been developed to efficiently solve complex problems of motion control and load sequences in the centrifuge. The results of four preliminary tests illustrated system performance. This innovative modelling technique and loading apparatus provide a direct link between ground and structural engineering, enhancing centrifuge modelling potential

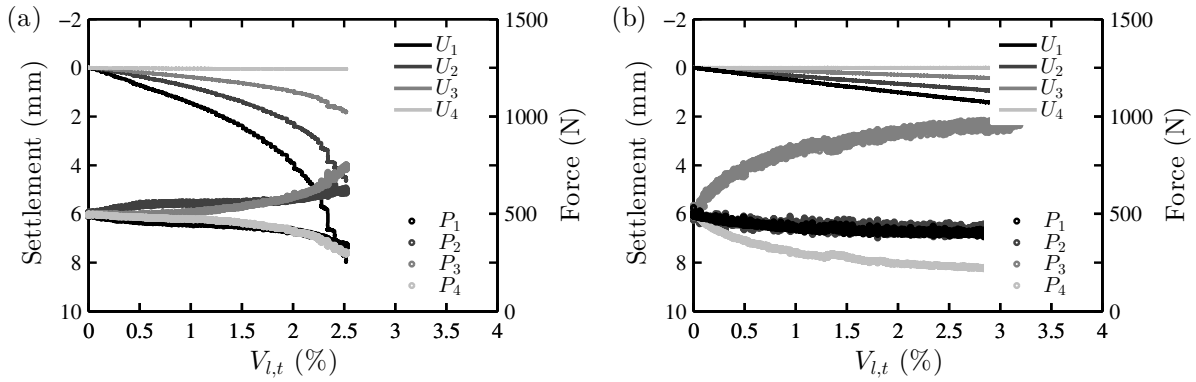

Fig. 3.14 Pile head settlements and pile loads in the case of tunnelling beneath (a) semi-flexible building in test A, and (b) rigid building in test B.

in studying global soil-structure interaction problems. Section 3.5 illustrates the various and complex construction scenarios of tunnelling beneath piled frames that were studied using this unique experimental equipment.

3.4 Centrifuge modelling of greenfield tunnelling

The greenfield centrifuge tests, labelled series 1, were performed in plane-strain condition to investigate the combined effect of soil density and tunnel relative depth on tunnelling-induced deformation patterns in sands.

3.4.1 Centrifuge package

The experimental package developed by Zhou et al. (2014) was adopted with model tunnel with either 40mm or 90mm diameter buried in dry silica sand at depth (to tunnel axis) varying between 165 and 270mm. The soil relative density was poured to achieve a target loose, medium-dense or dense density state corresponding to $I_d = 0.3, 0.5, 0.9$.

The tunnel volume control system comprising a constant-head standpipe, a solenoid valve, a linear actuator, a water-filled sealed cylinder and an LVDT was used. The tunnel volume loss process was conducted in increments up to a maximum value of 10%. Two or three digital cameras were used to take pictures of the soil at the front Perspex wall of the centrifuge container, which were processed with the GeoPIV image-based measurement technique. Note that the field of view of the soil was limited to one side of the tunnel with respect the centreline both above and beneath the tunnel when the 40mm diameter model tunnel was used. This allowed improvement of the measurement precision, which was a critical aspect of the experiment due to the small tunnel contraction movements (depending on $R \times V_{l,t}$).

3.4.2 Preparation of the model and test procedure

In the case of tunnelling in medium-dense and dense soil (i.e. $I_d = 0.5 - 0.9\%$), the adopted preparation method of the model is consistent with previous research (e.g. Marshall et al. (2012) and Zhou (2014)). The procedure consists of placing the Perspex face down, removing the back wall, and securing the model tunnel within the Perspex recess. A temporary wooden top was placed to prevent sands escaping from the open top. To prevent the deformation of the tunnel along the vertical direction due to the weight of the water, a temporary sleeve was placed around the 90mm diameter model tunnel above the sand level; this temporary sleeve was progressively retracted during the sand pouring to avoid disturbance of the sand sample. The temporary sleeve was not necessary for the 40mm diameter tunnel because the membrane stiffness was able to prevent the tunnel deformations. A thin layer of mixed dyed and un-dyed sand was poured onto the Perspex face to guarantee improved performance of the GeoPIV analysis. Then, sand pouring in line with the model tunnel was started. Sand was poured from a specific height with a controlled flow rate by a sand pourer to achieve good control of soil uniformity and sand density. Note that a calibration test for the target I_d was conducted prior to each model preparation to check the sand pourer set-up. At the completion of the pouring process, the sand was levelled and the back wall secured in place. The box was then slowly rotated to its upright position with care to avoid disturbing the sand sample. This procedure provides a uniform relative density of

the sand both above and beneath the tunnel. The final stages consisted of the movement and securing of the strong box on the aluminium base plate (containing the volume control system), the connection of the model tunnel with the volume loss control system, the movement of the model onto the centrifuge platform, the removal of the temporary wooden top, the mounting of the digital camera and their gantry, and the connection of the measurement sensors with the data acquisition system. The data acquisition system was operated by the software LabVIEW in the centrifuge control room.

The preparation of the loose soil sample ($I_d = 0.3$) was different. A loose sample prepared with the traditional technique described in the previous paragraph would have been disturbed by the process of tilting the model and lifting it onto the swing cradle of the centrifuge. Additionally, the aim of this research of investigating tunnelling beneath piled structures needed to be accomplished with a research plan based on numerous tests because of the lack of previous investigations. Therefore, a simplified test preparation procedure that achieved good repeatability of results was adopted in order to reduce the preparation time of loose samples. The loose sample preparation procedure can be summarised as follows. With the experimental package mounted on the centrifuge and fully connected to the data acquisition system, the un-dyed sand was removed up to the tunnel springline level and, then, manually poured to a relative density, I_d, of 30 $\pm$5%. The effect of soil inhomogeneity in the case of a loose sample was judged negligible. The effects of sand pouring only above the tunnel springline was considered secondary with respect to other factors because previous greenfield centrifuge tests showed that tunnel deformations are localised at the top half of the model tunnel (however, this aspect is less true for relatively deep tunnels). The acceptability of the test procedure was confirmed by test repeatability (in the case of pile loading tests and tunnelling beneath piled structures) and consistency of the greenfield deformation patterns measured with loose, medium-dense and dense sands (i.e. I_d varying between 0.3 and 0.9) for $C/D = 2$. These two aspects are discussed in Chapters 4 and 8.

The testing procedure is summarised as follows. [1] After the experimental package was mounted on the centrifuge, fully secured and connected to the data acquisition system, the package was spun up to 5g and the solenoid valve was opened to connect the model tunnel to the constant-head stand-pipe. [2] Then, the experimental package was spun up to Ng. Firstly, the 10g-level was reached and, afterwards, the reduced-scale model was spun up in stages of 10g. At each increment, the digital cameras took an image of the soil and the readings were checked to ensure model stability and safety. [3] At Ng, the solenoid valve was closed to isolate the model tunnel. [4] Then, the tunnel volume losses, $V_{l,t}$, was induced in increments until the maximum value of 10% volume loss was reached. Note that the ground loss was induced by water extraction through the relative displacement of the actuator in the volume loss control system. At each step, images of the soil were taken by the digital cameras. Furthermore, the PPT and LVDT readings were written down as a backup note. [5] When the volume loss process was terminated, the centrifuge was spun down.

3.4.3 Tested configurations

The performed greenfield tests, labelled as test series 1, are listed in Table 3.3; additionally, the table provides details of the centrifuge tests previously carried out by Marshall et al. (2012) (series M) and Zhou et al. (2014) (series Z), whose results are comparable with the experiments performed in this research because of the use of similar equipment. The centrifuge test data given by test series 1, M and Z are analysed together in Chapter 4. In the greenfield scenario, tests are labelled according to the C/D ratio and the soil relative density (i.e. test with C/D of 6.3 in a dense sand is referred to as CD63ID90).

Table 3.3 Summary of centrifuge tests for greenfield tunnelling (model scale dimensions).

Test series ‡	Name (# test)		D_t (m)	z_t (m) †	C/D (-)	I_d (%)	N (-)
1	CD13ID30	(1)	0.090	0.165 [13.2]	1.3	30	80
1	CD13ID50	(1)	0.090	0.165 [11.6]	1.3	50	70
M	CD13ID90	(1)	0.082	0.150 [11.3]	1.3	90	75
1	CD20ID30	(2)	0.090	0.225 [18.0]	2.0	30	80
Z	CD20ID50	(1)	0.090	0.225 [18.0]	2.0	50	80
Z	CD20ID70	(1)	0.090	0.225 [18.0]	2.0	70	80
Z	CD20ID90	(1)	0.090	0.225 [18.0]	2.0	90	80
1	CD25ID30	(1)	0.090	0.270 [21.6]	2.5	30	80
M	CD24ID90	(1)	0.062	0.182 [13.7]	2.4	90	75
1	CD45ID30	(1)	0.040	0.200 [16.0]	4.5	30	80
1	CD45ID50	(1)	0.040	0.200 [16.0]	4.5	50	80
M	CD44ID90	(1)	0.060	0.295 [11.8]	4.4	90	40
1	CD63ID30	(1)	0.040	0.270 [21.6]	6.3	30	80
1	CD63ID50	(1)	0.040	0.270 [21.6]	6.3	50	80
1	CD63ID90	(1)	0.040	0.270 [21.6]	6.3	90	80

† prototype scale dimension in square brackets
‡ M: Marshall et al. (2012); Z: Zhou et al. (2014)

3.4.4 Scale and boundary effects

Scale effects in centrifuge tests should always be evaluated. In the case of tunnelling, as discussed in Section 3.1.3, Kutter et al. (1994) and Marshall et al. (2012) suggested, respectively, that grain size impact on the test results decrease when $D/d_{50} > 350$ and that scale effects should be negligible for $D/d_{50} > 500$ in the collapse condition. For the test performed in this research (series 1), the model tunnel had a tunnel diameter D_t of 40 or 90mm. Thus, the ratio D/d_{50} is 327 and 738 and the investigated range of $V_{l,t}$ is within pre-collapse conditions. Therefore, although grain size effects may be present for the smaller model tunnel, they should have a minor influence on most results obtained at a pre-collapse state.

To assess the boundary effects, it is necessary to analyse the transversal geometry of the strong box and the settlement trough extension. Considering that a) the settlement trough extension is approximately equal to $2.5i$, b) the inflection point offset at the surface in sands for relatively deep tunnels is approximately $i = 0.7z_t$, and c) the horizontal distance between the tunnel centreline and the U-channel is 320mm, this indicates that the maximum tunnel depth that minimises boundary effects is $z_{t,max} = 320/(2.5 \times 0.7) = 182$mm. Therefore, the presence of boundary effects affecting surface ground movements was not avoidable for relatively deep tunnels when z_t was greater than 182mm. To partially overcome this issue, in Chapter 4, the study of the settlement trough width parameter, K and their variation with depth was performed with a least-square regression that analysed K as scattered points in the space $\left(V_{l,t}; z/z_t; K\right)$.

3.4.5 Limitations of the models and approximations

The experimental set-up was designed to guarantee, during spin-up, an inner tunnel pressure at the axis level equal to a theoretical vertical lithostatic value to minimise differential settlements between the tunnel and the soil. Because of the differences in the unit weight, ρg, and the coefficient of lateral earth pressure, K, of the soil and the tunnel (i.e. water), the tunnel pressure around the tunnel cannot match the lithostatic soil stress profile around the tunnel. This stress imbalance between the tunnel and the surrounding soil results in ground movements at the tunnel periphery (i.e. ovalization and buoyancy of the model tunnel) during the spin-up phase (Ritter et al., 2016; Zhou, 2014). Additionally, these ground movements may cause a variation of the soil relative density, I_d, due to soil densification (Zhou, 2014). Despite these limitations, this modelling technique has been widely used to study tunnelling-induced ground movements because of its reliability (water leaks can be easily detected and prevented) and efficiency in modelling small amounts of ground loss that allows for tunnel volume loss as small as 0.1%.

In general, when this technique is adopted for the tunnel volume loss, it is necessary to assess 1) the variation of soil relative density, 2) the effects of the approximate initial stress state within the soil surrounding the model tunnel on the studied model (as in the case of tunnel-pile interaction) and 3) the effects of the tunnelling-induced movements on damageable models of a structure included in the centrifuge package during spin-up.

3.5 Centrifuge modelling of tunnelling beneath pile foundations and building using CCNM

Test series 2 was carried out to study the response of pile foundations to tunnelling. It consists of 1 greenfield tunnelling, 3 pile loading tests, 12 tunnel-single pile interaction tests, and 8 tunnel-pile-structure interaction tests. Tests were performed at 60g. The real-time interface and load-control system developed to couple centrifuge and numerical modelling techniques was used to study the effects of the installation method (displacement vs. non-displacement piles) and load conditions (initial safety factor and load redistribution due to frame action) on tunnelling-induced settlements of pile foundations. The performed tests may be grouped in 4 sets depending on the objective of the test series:

- group A includes one greenfield test that was carried out to allow for the comparison;
- group B consists of three loading tests of a single non-displacement pile;
- group C investigated the response of isolated displacement and non-displacement piles to tunnelling. During each test, the settlement-ground loss curve was measured. Two different load levels (constant with tunnel ground loss) were investigated to assess the influence of the pile safety factor on the tunnel-pile interaction;
- group D modelled the response of piled frames to tunnelling, applying the CCNM technique. In this group, for a given self-weight of the superstructure, the tests were performed for displacement and non-displacement pile foundations subjected to the frame action of four different structures, whose stiffness resulted in a response to tunnelling varying from fully-flexible to rigid. The main objectives of this group of tests are a) the understanding of the effect of load redistribution among piles due to the superstructure action and b) the application of the CCNM system to a geotechnical problem. Furthermore, by comparing tests C and D for a fully-flexible frame, it is possible to study the group effect and the error induced by studying the global tunnel-piled structure interaction with a tunnel-single pile model using a constant pile head load condition throughout the ground loss process.

The experimental package is illustrated in Figure 3.10(a); the tested configurations of group B, C and D are sketched in Figure 3.15(a), (b) and (c), respectively. Further details on series 2 are provided in Table 3.4. The following section provides a description of the experimental equipment and the test procedure.

3.5.1 Centrifuge package

The components used for this test series are identical to those presented in Section 3.4 to model the greenfield tunnelling process with the addition of a pile foundation model, pile caps, and the load-control system illustrated in Sections 3.2 and 3.3. The equipment used is shown in Figure 3.5. In general, performing a variety of tests with a given experimental package was

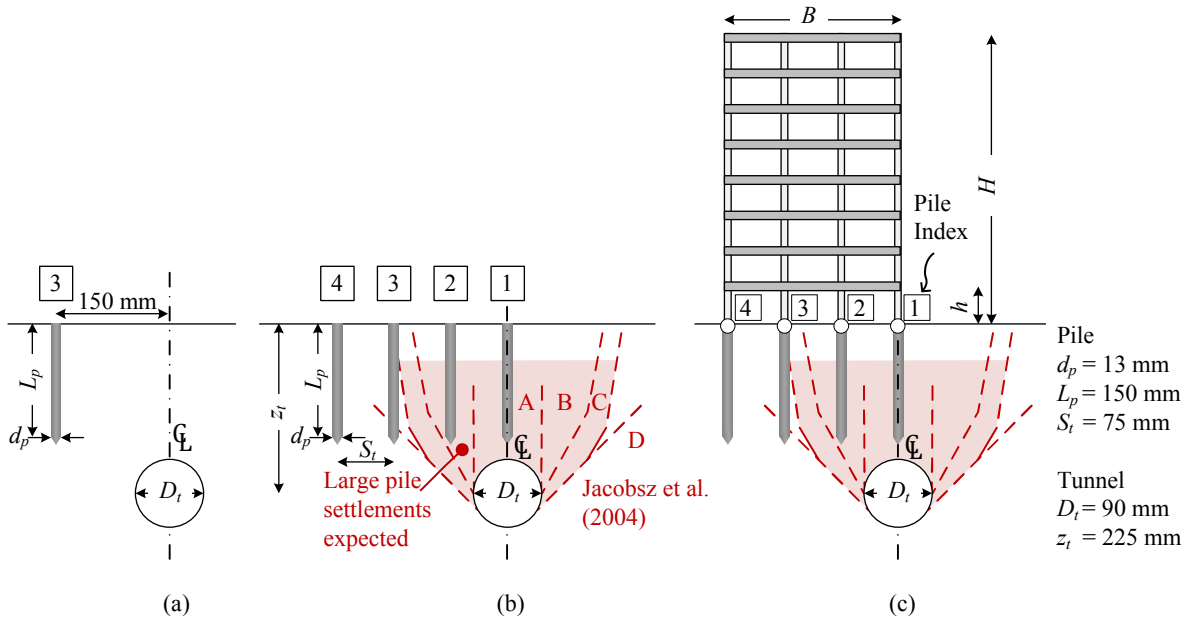

Fig. 3.15 Test layout (in model scale): (a) loading tests, (b) tunnelling beneath a single pile, and (c) tunnelling beneath a piled frame (the geotechnical domain is modelled in the centrifuge, whereas the frame is modelled numerically).

possible because the developed loading apparatus and real-time interface allow the in-flight actuation of user-defined load demands.

3.5.1.1 Tunnelling package

The experimental package developed by Zhou et al. (2014) to model the greenfield tunnelling process in plane-strain conditions was used. The 90mm diameter model tunnel buried at 225mm depth (at axis) was adopted to replicate a prototype 5.4m diameter tunnel with 13.5m of cover ($C/D = 2$). The tunnel volume loss process was conducted in-flight in small increments ($\Delta V_{l,t} \approx 0.02 - 0.04\%$ used to guarantee the convergence of the shared boundary conditions between the numerical and centrifuge models) up to either pile failure or $V_{l,tmax} = 10\%$.

3.5.1.2 Pile foundation, load-control system and instrumentation

The versatile load-control system and real-time interface illustrated in Section 3.3 was used. The experiments included the following components: a pile foundation consisting of either a single pile or four piles with a final diameter, d_p, of 13 mm; in-line load cells used to measure the pile head loads, P; Linear Variable Differential Transformers (LVDTs) used to measure the pile settlements U; a loading system able to drive the piles or to apply user-defined loads, P, at the pile heads through ball screw actuators and a lever system. The piles were located at the centre of the container with respect to the longitudinal tunnel direction. The experimental set-up allowed for high-frequency data acquisition of pile load and settlement during the tests (approximately every 40ms).

3.5.2 Preparation of the model and test procedure

This section describes the preparation of the model and the phases of the tests investigating the pile load capacity (series 2B) and the response of pile foundations to tunnelling (series 2C and D), whereas the greenfield test (series 2A) was prepared and carried out as described in Section 3.4. The preparation of the greenfield sample and details of the spin-up phase of test series 2 were provided in Section 3.4.2. The sand was placed by air pluviation to achieve a relative density, I_d, of 0.3 according to the simplified preparation methodology that achieved good repeatability of results and reduced the preparation time.

The procedure for tunnel-pile foundation interaction tests can be summarised as follows. [1] After sand pouring to achieve a loose sand sample ($I_d = 0.3$), the piles were installed prior to spin-up (at 1 g) by jacking to the final embedment depth L_p for non-displacement pile tests and $L_p - 2d_p$ for displacement pile tests (where the pile was driven $2d_p$ in-flight). [2] The model was spun-up to $60g$ (the connection between the model tunnel and the stand-pipe was closed at the target g-level). [3a] For displacement pile tests, the piles were jacked in-flight a distance of $2d_p$ and, subsequently, the pile head loads were reduced to the service initial value P_0; [3b] for non-displacement pile tests the service loads P_0 were directly applied to the piles. The jacking/loading of the piles was achieved using the pile caps and the loading apparatus. The value of the applied service load depended on the specified initial safety factor ($P_0 = Q_0/SF_0$, where Q_0 is the pre-tunnelling ultimate pile bearing capacity and SF_0 is the initial safety factor). In the case of a pile group, the sequence of pile jacking/loading was achieved by installing the piles one at a time, starting from the external pile and proceeding towards the centre of the strong box. [4] Then, if tunnelling beneath a piled frame was modelled, the LVDT readings of pile settlements were zeroed and, subsequently, the real-time interface coupling the centrifuge and the numerical model of the frame was activated. From this moment, the applied loads to the foundation, P, matched the numerical demand, P'. If the tested configuration included a single pile, the pile load demand, P', was maintained constant during the entire tunnelling process and set equal to the initial service load, P_0. [5] Increments of tunnel volume losses, $\Delta V_{l,t}$, were induced and the pile settlements were measured with the LVDTs. During pile loading tests, a pile was located with a horizontal offset from the tunnel centreline of 150mm; after steps 1 and 2, the pile was jacked while pile head reaction force and settlement were measured.

3.5.3 Tested configurations

This group of test is referred to as series 2; the performed tests are listed in Table 3.4, which provides details on pile load conditions, geometry and tested configurations (shown in Figure 3.15). The note column of Table 3.4 is used to describe the tests with TPI = tunnel-pile interaction, TPGI = tunnel-pile group interaction, TPSI = tunnel-pile structure interaction.

In this test series, the repeatability of results was verified by repeating the pile loading test three times with the same configuration. Further repeatability tests were carried out in test series 3 described in Section 3.6. In group 2C, piles in positions 1, 2, and 3 were tested (see Figure 3.15

for the position definition). Note that only the piles in positions 1 and 2 have their tips located within the influence zones defined by Jacobsz et al. (2004) where large pile settlements may be induced by tunnelling. Test group D investigated tunnelling beneath a transverse row of four piles (position 1-4) that was the foundation of a concrete frame modelled numerically. The 8 storey concrete frame ($E = 30$GPa) had a storey height, h, and a span length, S_t, of 3 and 4.5m, respectively. Four different superstructure where implemented; FR00 indicates a fully flexible frame (which does not provide reaction forces to base displacements); FR30, FR50 and FR70 indicate frames whose beam and column elements have square cross-sections of 0.3×0.3m, 0.5×0.5m, and 0.7×0.7m, respectively.

The tests are labelled as follows. The greenfield test is indicated as GF. The pile loading tests are named LP. The tunnel-single pile interaction tests are labelled according to installation method (N = non-displacement, D = displacement), pile position, and initial safety factor (for instance N2SF1.5 represents a non-displacement pile located in position 2 with an initial safety factor of 1.5). Finally, the tunnel-piled frame tests are named as the previous group except for the letter G, which stands for pile group, replacing the pile position number and the suffix FR, indicating the presence of the frame; for instance, NGSF2.0FR30 indicates a frame consisting of square cross-section elements of 0.3×0.3m and a foundation consisting of four non-displacement piles. The results of series 2 are illustrated in Chapter 7.

3.5.4 Scale and boundary effects

For the tunnelling problem, the scale effects were assessed in the Section 3.4.4. The ratio pile diameter to average grain size, d_{50}, was equal to 106; therefore, scale effects on peak shear strength and base capacity should be minimised (Bolton et al., 1999; Garnier et al., 2007). To reduce uncertanties caused by scale effects at the pile-soil interface, a perfectly rough interface was adopted (Garnier et al., 2007). In this test series, the minimum horizontal distance between the pile and the strong box wall was 10.5 pile diameters; therefore, the minimum distance of 10 pile diameters suggested by Bolton et al. (1999) to avoid boundary effects was respected.

3.5.5 Limitations of the models and approximations

The centrifuge model represents several approximations to reality. For displacement piles, the in-flight model pile jacking allows the creation of a realistic stress profile within the ground compared to the field installation of driven or jacked piles. For non-displacement piles, there is some degree of soil disturbance induced by the jacking process at 1g which tends to compact the soil rather than allowing the stress relief that would happen in the real case. However, the intention of this work is to compare the tunnel-pile interaction accounting for the main differences between displacement and non-displacement piles; that is the different distribution of pile load between the pile shaft and base. Non-displacement piles withstand the pile service load mainly through shaft friction since the displacements needed to mobilise base capacity do not occur. Displacement piles have their base capacity partially mobilised by the installation

Table 3.4 Summary, in model scale dimensions, of centrifuge experiments for test series 2 performed at 60g.

Test series	Label (# tests performed)		Pile type †	Pos. #	Offset x (mm)	Serv. Load P_0 (N)	Capacity‡ Q_0 (N)	SF_0 (-)	Note
2A	GF	(1)	-	-	-	-	-	-	GF
2B	LP	(3)	N	3	150	-	-	-	Loading
2C	N1SF1.5	(1)	N	1	0	493	740	1.5	TPI
2C	N1SF2.5	(1)	N	1	0	296	740	2.5	TPI
2C	D1SF1.5	(1)	D	1	0	667	1000	1.5	TPI
2C	D1SF2.5	(1)	D	1	0	400	1000	2.5	TPI
2C	N2SF1.5	(1)	N	2	75	493	740	1.5	TPI
2C	N2SF2.5	(1)	N	2	75	296	740	2.5	TPI
2C	D2SF1.5	(1)	D	2	75	667	1000	1.5	TPI
2C	D2SF2.5	(1)	D	2	75	400	1000	2.5	TPI
2C	N3SF1.5	(1)	N	3	150	493	740	1.5	TPI
2C	N3SF2.5	(1)	N	3	150	296	740	2.5	TPI
2C	D3SF1.5	(1)	D	3	150	667	1000	1.5	TPI
2C	D3SF2.5	(1)	D	3	150	400	1000	2.5	TPI
2D	NGSF1.5FR00	(1)	N	1-4	0-225	500	740	1.5	TPGI
2D	NGSF1.5FR30	(1)	N	1-4	0-225	500	740	1.5	TPSI
2D	NGSF1.5FR50	(1)	N	1-4	0-225	500	740	1.5	TPSI
2D	NGSF1.5FR70	(1)	N	1-4	0-225	500	740	1.5	TPSI
2D	DGSF2.0FR00	(1)	D	1-4	0-225	500	1000	2.0	TPGI
2D	DGSF2.0FR30	(1)	D	1-4	0-225	500	1000	2.0	TPSI
2D	DGSF2.0FR50	(1)	D	1-4	0-225	500	1000	2.0	TPSI
2D	DGSF2.0FR70	(1)	D	1-4	0-225	500	1000	2.0	TPSI

† N: non-displacement piles; D: displacement piles

‡ The reported values do not account for the influence of the pile offset

process, with residual pressures locked in at the base and negative shaft friction along the shaft. The adopted centrifuge testing procedure is able to capture these important differences. The differences related to jacking or driving piles are not considered.

Finally, it should be highlighted that an approximation was introduced in modelling the frame self-weight with a uniform distribution of initial service loads, P_0, during test group D. Initial service loads could have been assessed with a specific structural analysis of the frame (accounting for a detailed loading condition of the beams). However, considering the objectives of this test series (the evaluation of the effects of the pile offset, the pile safety factor, the load redistribution due to building stiffness) using a uniform P_0 simplifies the studied configurations and reduces the complexity of the prototype scenario so that it is possible to better isolate the influence of the building stiffness. Despite the approximation, the uniform P_0 distribution allows accounting for a building weight that is compatible with the pile group bearing capacity (i.e. $SF_0 = 1.5 - 2$). Extensive structural analysis of the building weight distribution and structural

loadings could be incorporated in the CCNM technique; this would be necessary for the study of structures with non-linear plastic behaviour.

3.6 Centrifuge modelling of tunnelling beneath piled buildings using an equivalent plate

Test series 3 investigating tunnelling beneath piled buildings was performed at 80g using the geotechnical centrifuge with a traditional approach (i.e. using a simplified reduced scale model of the structure). Four test groups were conducted:

- group A consists of a greenfield test used as a reference term for the analysis of the soil-structure interaction effects;
- group B is the loading test series carried out to characterise the pile load-settlement curve and the ultimate bearing capacity;
- groups C and D investigated the response of piled structures to tunnelling. In group C, the series of tests was performed with a superstructure of varying stiffness and self-weight, whereas, in group D, the weight of the building was kept constant while the plate stiffness was varied between tests. In this way, it was possible to isolate the contribution of the plate self-weight and the stiffness to the global interaction.

Figure 3.16(a) and (b) presents, respectively, a schematic of the pile loading test and the tunnelling cases, whereas pictures of the centrifuge model are displayed in Figure 3.17. Details of the tests are given in Tables 3.5 and 3.6.

3.6.1 Centrifuge package

To model tunnelling beneath a piled structure, the package described in Section 3.4 was used with the addition of the model structure; the pile loading tests were conducted with a set-up similar to the package adopted in Section 3.5 using a model pile with a different diameter.

3.6.1.1 Tunnelling package

The 90mm diameter model tunnel buried at 225mm depth (at axis) in dry silica sand was adopted to replicate a prototype 7.2m diameter tunnel with 14.4m of cover ($C/D = 2$). The tunnel volume loss process was conducted in 0.25% increments up to 5% and, subsequently, 0.5% increments up to 10%. Note that this set up does not allow modelling of the tunnel excavation progress in the longitudinal direction.

3.6.1.2 Piled structure and foundation model

Aluminium plate structures A piled building was modelled in the centrifuge using aluminium equivalent plates with varying stiffness supported by aluminium piles ($E = 70$GPa). The plates had a transverse width $B = 500$ mm and a length $L = 256$mm. Four different plate thicknesses, t, were used: 1.6, 3, 6 and 12.3 mm. A fully elastic response is expected for this type of

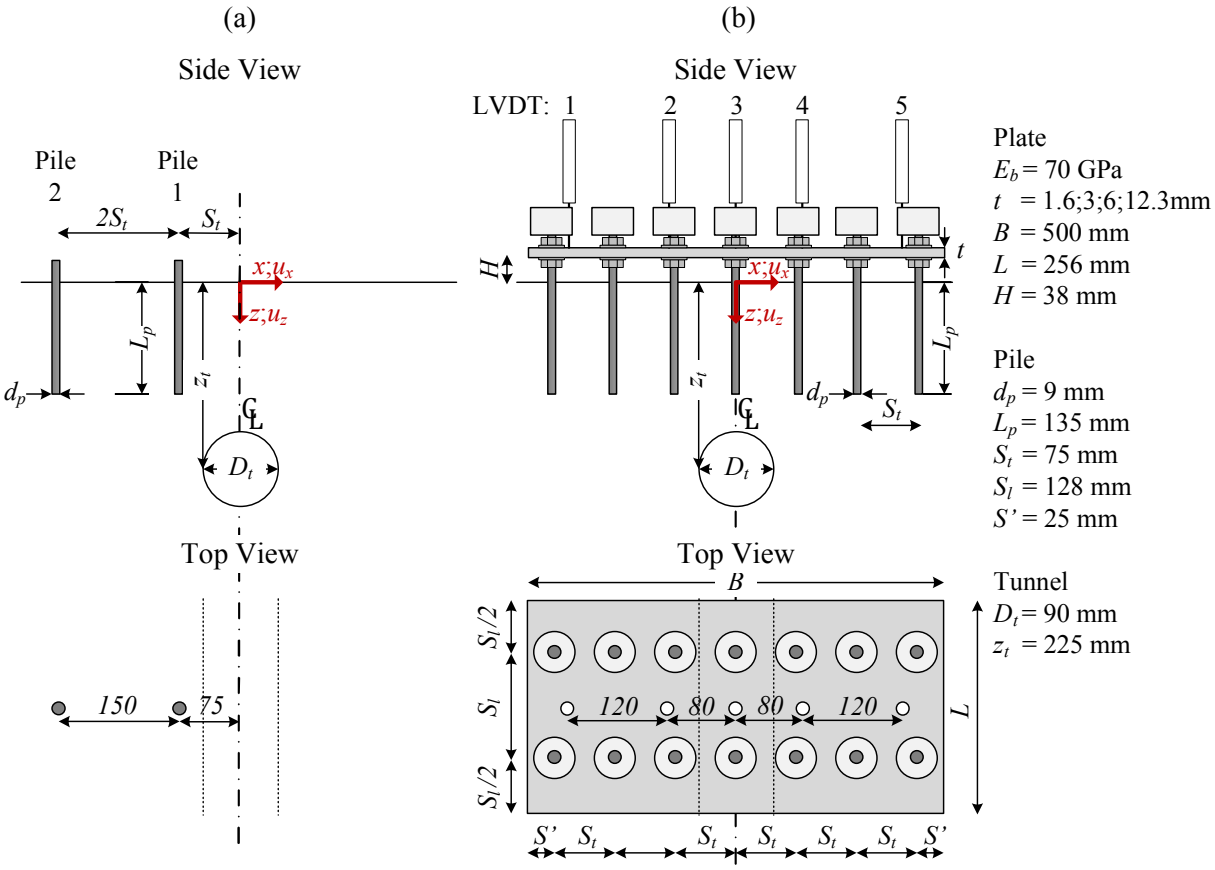

Fig. 3.16 Test layout (in model scale): (a) loading tests and (b) tunnelling beneath piled plate.

building model, whose axial and flexural stiffness at prototype scale is comparable with real case scenarios, such as the buildings monitored during the Jubilee Line Extension (Farrell et al., 2014; Giardina et al., 2015). Prototype axial and flexural stiffnesses are summarised in Table 3.5.

Table 3.5 Stiffness of the aluminium plates.

Test	Model Scale		Prototype			
	t	S_l	t	S_l	EI^*	EA^*
	(mm)	(mm)	(m)	(m)	(kNm^2/m)	(kN/m)
t1	1.6	128	0.13	10.24	1.2×10^4	9.0×10^6
t3	3	128	0.24	10.24	8.1×10^4	1.7×10^7
t6	6	128	0.48	10.24	6.5×10^5	3.4×10^7
t12	12.3	128	0.98	10.24	5.6×10^6	6.9×10^7

Pile foundations In the tests using the piled plate, the piled foundation consisted of two transverse pile rows of seven piles. Uninstrumented model piles consisted of 8mm diameter aluminium alloy full section round bar over a length of 220mm. Piles had a fully rough interface obtained by bonding fraction E sand to the outer surface. The final external pile diameter was 9mm and the embedment depth was 135mm, which correspond, respectively, to 0.72m and 10.8m at prototype scale. The pile tip was flat. The bending and axial stiffnesses of the model piles in

model scale were 14.1Nm^2 and 3.5MN, respectively. The additional pile length allowed for a gap between the plate and the soil, H, of 38mm as well as for a threaded pile top. Clearance holes were drilled into the plate in correspondence of each pile. These clearance holes, the threaded pile top, two bolts and washers were used to rigidly attach the piles to the plate (simulating fixed pile-foundation connections), as displayed in Figure 3.17.

In the pile loading tests, the loading apparatus and the instrumentation illustrated in Section 3.2.2.1 were used. The model pile used in this test series was also constructed out of 8mm diameter aluminium round bar with a total length of 175mm, a final external diameter of 9mm, a flat tip, and a machined top to allow the connection with the pile cap (load cell, the LVDT support plate and the loading bar).

Modelling building weight In group C (see Table 3.6), as a result of the varying plate thickness, the weight of the building also varied between tests. Although this impacts on results, it is not possible to separate the contribution of the self-weight and the stiffness with this modelling technique. Therefore, an additional series of tests, labelled group D, was performed locating additional masses on the pile heads, which would not result in the increase in the superstructure stiffness. The weight of the additional masses was chosen to achieve a given target total weight of the superstructure, as reported in Table 3.6. Thus, in the group D tests, the only varying parameter was the building stiffness. Comparison of group C and D tests performed with the same plate thickness illustrates the effects of building self-weight. Note that this additional weight was uniformly distributed between the pile heads; the error induced by this uniform redistribution was neglected. These masses were machined out of a round aluminium bar with a central threaded hole to allow connection with the threaded top of the piles. The sketch of the final configuration is shown in Figure 3.16(b), whereas pictures showing the additional masses are given in Figures 3.17(b) and (c).

3.6.1.3 Measuring devices and loading apparatus

During the tests of groups A, C and D, two digital cameras were used to take pictures of the soil (during test GF) and the plate at the front Perspex wall of the centrifuge container. During the tests, digital photos were taken at each $V_{l,t}$ increment. Plate settlements were also monitored with a row of five LVDTs located at a horizontal distance from the tunnel centreline of 0, $\pm$80 and $\pm$200mm (see Figures 3.16 and 3.17). Figure 3.17 shows the LVDT gantry, designed by Zhou (2014), that was used for the monitoring of the pile plate displacements. The gantry was made of $2''W \times 2''H \times 1/4''T$ aluminium U-frame (6082T6 aluminium alloy). The gantry, installed on the top of the strong box, could secure five attachment blocks that each held one LVDT.

During the pile loading tests (group B) the piles were attached to an in-line load cell and an LVDT for axial head load and settlement measurement. The loading apparatus and control system developed for the coupled centrifuge-numerical model, illustrated in Section 3.3, was used to apply axial loads and measure physical quantities.

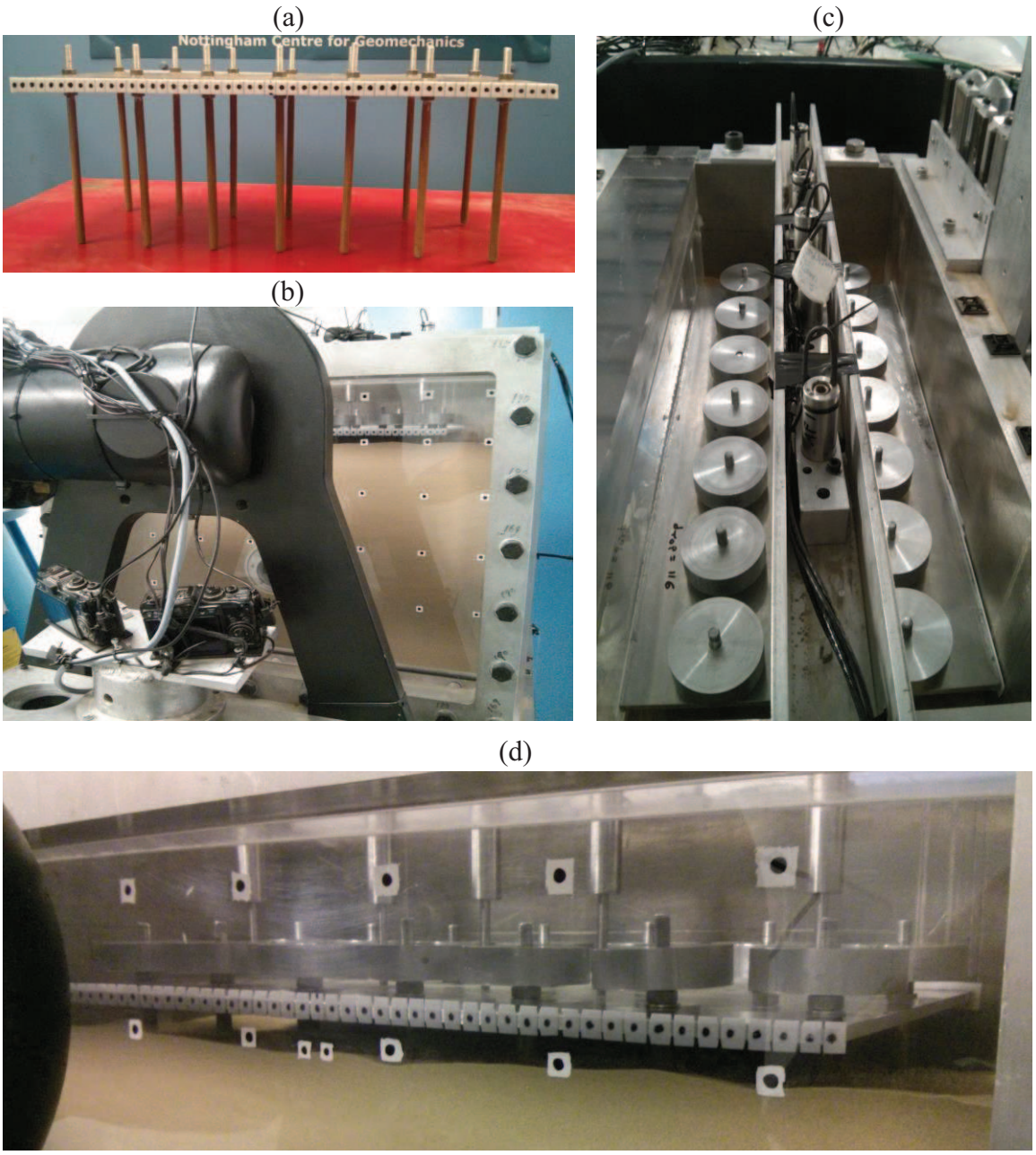

Fig. 3.17 (a) Model of the piled structure, (b) view of the centrifuge, digital cameras, and assembled model prior testing, (c) LVDT gantry and top view of the structure model with additional self-weights connected to the pile heads, (d) plate with additional self-weights.

3.6.2 Preparation of the model and test procedure

In this section, the model preparation and the test procedure for both pile loading and tunnelling beneath piled plate tests are detailed. Note that the preparation of the greenfield sample and details of the spin-up phase were provided in Section 3.4.2.

3.6.2.1 Tunnelling beneath piled plate

The test layout is shown in Figure 3.16(b). The procedure can be summarised as follows. [1] The sand was poured to a relative density, I_d, of 30 $\pm$5%, starting from the tunnel springline level. [2] The plate was installed prior to spin-up by jacking the plate-piled foundation to the design depth, which allowed for a gap between the soil and building. Therefore, the model replicated a piled foundation rather than a piled-raft foundation. The plate was placed centrally with respect to the tunnel centreline. Considering the aim of obtaining an overall loose soil sample without an entirely accurate control of I_d, the effects of driving the piled foundation at 1 g on I_d were neglected. [3] The model was spun-up to the level of 80g. [4] Once the target g-level was reached, the tunnelling process was modelled in-flight and plate deformations were measured with the GeoPIV technique as well as the LVDTs. [5] At the conclusion of the $V_{l,t}$ process, the centrifuge was spun down; the piled plate and the sand up to the tunnel depth z_t were removed and the model tunnel was filled back with the water extracted during phase [4].

3.6.2.2 Pile loading tests

The test layout is shown in Figure 3.16(a). The procedure can be summarised as follows. [1] After sand pouring, two piles were installed prior to spin-up (at 1g) by jacking to the final embedment depth L_p. The two piles were located at the longitudinal centre of the strong box with a transverse horizontal offset from the tunnel of 75 and 225 mm, respectively. Because the pile spacing is approximately 17 d_p, the foundation should respond to loading as isolated piles. [2] The model was spun up to 80g, [3] then the piles were jacked in-flight while pile head reaction force and settlement were measured to obtain the load-settlement curves. In this way, non-displacement piles were modelled.

3.6.3 Tested configurations

The detailed summary of the tests (testing configuration, test label, stiffness and self-weight of the plate) is given in Table 3.6. In the case of tunnelling beneath the piled structure, tests are labelled according to the plate thickness, self-weight (in the case of additional masses added at the pile heads) and repeated test indicator. For instance, the second test performed with a 6mm thick plate is referred to as t6.b and the unique test carried out with a 3mm thick plate and additional masses added to match the self-weight of the 12mm thick plate is labelled as t3.w12.

3.6.4 Scale and boundary effects

For the tunnelling problem, the scale effects were assessed in the Section 3.4.4. Scale effects were prevented by a ratio pile diameter to average grain size, d_{50}, equal to 73 (Bolton et al., 1999; Garnier and König, 1998). To reduce scale effects at the pile-soil interface a perfectly rough interface was adopted (Garnier and König, 1998). Bolton et al. (1999) suggested that minimum boundary effects on pile tip resistance are obtained for a ratio between the pile distance from the

Table 3.6 Summary of centrifuge test series 3 performed at 80g (model scale dimensions).

Test series	Name (# test)		Plate t (mm)	Plate mass (kg)	Pile extra mass (kg)	Total weight † (N)	Note
3A	GF	(1)	-	-	-	-	Greenfield
3B	SP	(3)	-	-	-	-	Pile loading
3C	t1	(1)	1.6	0.55	0	398	Plate
3C	t3	(3)	3	1.03	0	745	Plate
3C	t6	(3)	6	2.05	0	1491	Plate
3C	t12	(1)	12.3	4.21	0	3056	Plate
3D	t1.w12	(1)	1.6	0.55	0.26	3056	Plate + weights
3D	t3.w12	(1)	3	1.03	0.23	3056	Plate + weights
3D	t6.w12	(1)	6	2.05	0.15	3056	Plate + weights
† Self-weight computed considering the variation of N within the centrifuge model							

wall and the pile diameter greater than 10. In the set up shown in Figure 3.16(a), the minimum horizontal distance between the pile and the strong box wall is 10.5 pile diameters. In the set up shown in Figure 3.16(b), the distances between the vertical container walls and the piles were, respectively, 10.5 and 7.1 pile diameters in the transverse and longitudinal tunnel direction. Therefore, effects may be present but they should have a minor influence on the results because piles are jacked at 1 g and they are not driven in-flight (thus they are not end-bearing piles).

3.6.5 Limitations of the models and approximations

The first observation refers to the pile loading condition prior to ground loss. It is worth noting that the load application procedure differs between the pile loading tests (group B) and the tests modelling tunnelling beneath the piled plate (groups C and D). During the loading tests, the pile load was applied after the final g-level was reached; in the latter series the foundation load is due to the mass of the superstructure, thus the loads increased throughout the spin-up process. Furthermore, the load distribution within the pile group is the result of a soil-structure interaction phenomenon influenced by the superstructure stiffness and the pile response during spin-up. Therefore, prior to tunnel volume loss, the superstructure self-weight may not be uniformly distributed between the piles. Despite these uncertainties, a similar ultimate bearing capacity mechanism is expected from the non-displacement pile foundation in both types of tests.

Finally, it is important to stress that the model of tunnel-piled structure interaction did not satisfy the plane-strain condition. However, the longitudinal length L of the model building (256mm) was approximately equal to the strong box width (260mm) and the pile row spacing in the longitudinal direction, S_l, equal to 128mm (10.24m at prototype scale), was double the pile row distance from the building edges; therefore the Perspex wall and the back wall of the strong box approximately represent planes of symmetry. This means that the centrifuge tests modelled the behaviour of an infinitely long building in the longitudinal direction (limited in the model to

a portion corresponding to two pile rows) subjected to the ground movements due to plane-strain tunnel volume loss distribution (replicating the steady state condition obtained behind the tunnel face).

Chapter 4

Centrifuge study of greenfield tunnelling in sands

In engineering practice, tunnelling-induced ground movements are often described by empirical formulas. Past centrifuge studies have provided data on the variation of settlement distribution above relatively shallow tunnels in sands; recent research has proposed empirical relationships to predict the change in settlement trough shape that occurs in dense sands as tunnel volume loss increases at varying C/D ratios. There is, however, lack of comprehensive research that considers both the case of relatively shallow and deep tunnels for varying soil relative density.

To investigate the combined effect of the cover-to-diameter ratio, C/D, and the relative density, I_d, this chapter presents the outcomes of the centrifuge tests referred to as series 1, M and Z (Table 4.1). The centrifuge experimental set up and the scale effects for this research were described and analysed in Section 3.4. This series of plane-strain tunnelling centrifuge test was performed using a dry silica sand for a C/D varying between 1.3 and 6.3, thereby including relatively shallow and deep tunnels. The ground conditions were varied between 30% and 90% relative density to achieve a uniform loose ($I_d = 0.3$), medium-dense ($I_d = 0.5$ and 0.7) and dense sand ($I_d = 0.9$). Tests are labelled according to their C/D ratio and I_d (i.e. test with C/D of 6.3 and I_d of 0.9 is labelled CD6.3ID90). Note that test series 1 includes centrifuge test data from Marshall et al. (2012) and Zhou et al. (2014) performed with comparable soil and tunnel modelling technique. The experiments were carried out up to a maximum volume loss of the tunnel equal to 8-10%; therefore collapse conditions were not necessarily reached. Furthermore, to consider the value of volume loss generally achieved in practice most analyses in this chapter are limited to the volume loss range $V_{l,t} = 0-5\%$. In this thesis, $V_{l,t} = 1,2,3$, and 5% are referred to as low, medium, high, and extremely high volume losses, respectively.

This chapter is structured as follows. In Section 4.1, the ground reaction curves are analysed; then, the distributions of vertical and horizontal ground movements and strains around the tunnel are reported to clarify the main effects of C/D, for a given soil density, and I_d, for a given relative tunnel depth. Additionally, based on the measured displacements, strains and reaction curves, the influence of soil arching on tunnelling-induced ground movements is discussed. Section 4.2 presents an analysis of the settlement trough data. In Section 4.3, the empirical approach defined

Table 4.1 Summary of centrifuge tests for greenfield tunnelling in model scale dimensions.

Test series ‡	Name (# test)		D_t (m)	z_t (m) †	C/D (-)	I_d (%)	N (-)
1	CD13ID30	(1)	0.090	0.165 [13.2]	1.3	30	80
1	CD13ID50	(1)	0.090	0.165 [11.6]	1.3	50	70
M	CD13ID90	(1)	0.082	0.150 [11.3]	1.3	90	75
1	CD20ID30	(2)	0.090	0.225 [18.0]	2.0	30	80
Z	CD20ID50	(1)	0.090	0.225 [18.0]	2.0	50	80
Z	CD20ID70	(1)	0.090	0.225 [18.0]	2.0	70	80
Z	CD20ID90	(1)	0.090	0.225 [18.0]	2.0	90	80
1	CD25ID30	(1)	0.090	0.270 [21.6]	2.5	30	80
M	CD24ID90	(1)	0.062	0.182 [13.7]	2.4	90	75
1	CD45ID30	(1)	0.040	0.200 [16.0]	4.5	30	80
1	CD45ID50	(1)	0.040	0.200 [16.0]	4.5	50	80
M	CD44ID90	(1)	0.060	0.295 [11.8]	4.4	90	40
1	CD63ID30	(1)	0.040	0.270 [21.6]	6.3	30	80
1	CD63ID50	(1)	0.040	0.270 [21.6]	6.3	50	80
1	CD63ID90	(1)	0.040	0.270 [21.6]	6.3	90	80

† prototype scale dimension in square brackets
‡ M: Marshall et al. (2012); Z: Zhou et al. (2014)

by previous research is applied to the dataset and modified to improve predictions. Modified Gaussian curves are fitted to the settlement data in order to evaluate the characteristics of the settlement profiles, both at the surface and subsurface. It is displayed that the variation of the vertical settlement trough shape with C/D, I_d, and $V_{l,t}$ is a complex phenomenon and should be represented by non-linear trends. For instance, the results indicate a non-linear trend of settlement trough shape with C/D, which suggests a transition between shallow and deep tunnels within the investigated C/D range. Two new sets of equations based on logarithmic trends are proposed to attempt the estimation of the settlement trough shape and magnitude in relation to C/D, I_d, and $V_{l,t}$ (limited to 5%). Additionally, the relationship between tunnel and ground loss at varying normalised depth is analysed. The regression of the data resulted in an new empirical expression for the estimation of $V_{l,s}$ depending on $V_{l,t}$, C/D, and I_d. In conclusion, despite the additional complexity with respect to previous works, the proposed empirical approach cannot entirely capture the complexity of the problem. Finally, Section 4.4 reports a discussion on the impact of the tunnel modelling technique on resulting ground movements. All results are presented in model scale unless otherwise stated.

It is interesting to point out that this study does not account for the effects of the confining stress level on tunnelling-induced displacements because the tunnel cover is normalised by C/D (e.g. this formula would associate two tunnels with $D = 3,6$m and $C = 9,18$m, respectively, with the same $V_{l,s} - V_{l,t}$ curve, although the shear strains induced by the tunnel at greater depth would probably result in lower dilation). On the other hand, if the investigated problem is limited to

the investigated domain illustrated by Table 4.1 ($C/D < 6.3$ and prototype $z_t < 20$m), the effects of the stress level should be secondary. It would be interesting to consider the impact of the overburden stresses (by considering the centrifuge scale factor N as a variable of the problem); however, a systematic study is probably not possible because of the great number of possible test configurations.

It should be noted that the dataset reported in this chapter is also used in Chapter 5 and Chapter 8. These results may be useful for future research on the response of surface and buried structures to tunnelling in cohesionless soils. Part of this research was also published within Franza et al. (2016c) and Marshall and Franza (2016).

4.1 Centrifuge test results and analysis of displacement mechanisms

4.1.1 Assessment of spin-up and boundary effects

During the spin-up of the centrifuge model, ground movements at the tunnel periphery are induced by the stress imbalance between the tunnel and the surrounding soil (Ritter et al., 2016). This results in the ovalization and buoyancy of the model tunnel during the spin-up phase. In addition, there are boundary effects due to the soil undergoing increased stresses and the friction at the strongbox walls (Zhou, 2014). This results in soil densification and a variation of the soil relative density, ΔI_d. This phenomenon is a drawback of modelling a tunnel excavation with water extraction from a flexible membrane; these spin-up-induced ground movements should be taken into account for centrifuge modelling of soil-structure interaction if the model of the structure is damageable or affected by the stresses within the soil close to the tunnel (Ritter et al., 2016). On the other hand, their impact on greenfield tunnelling should be minimal. For test CD20ID50 (medium-dense sand), Zhou (2014) reported an average soil densification of $\Delta I_d \approx +1\%$ at the surface and a maximum $\Delta I_d \approx +5\%$ at the tunnel crown.

4.1.2 Ground reaction curves

The ground reaction curves (i.e. the variation of model tunnel pressure with tunnel volume loss) for the greenfield database are shown in Figure 4.1 and Figure 4.2. Data are presented in a normalised form. In Figure 4.1, the pressure σ_t is normalised as in Equation (4.1) to account for the variation of I_d during tests performed with different tunnel diameter, D_t, and to describe the magnitude of the pressure for different tunnel depths.

$$\sigma_{norm} = \frac{\sigma_t}{\rho g N D_t} \tag{4.1}$$

where ρ is the density of the soil, g is gravity (9.81 m/s^2), N is the centrifuge acceleration scale factor, and D_t is the model tunnel diameter. In Figure 4.2, σ_t is normalised by the initial tunnel pressure, $\sigma_{t,0}$, to evaluate the relative reduction of the initial loading due to the combined effects of I_d and C/D. Note that the reaction curve of test CD44ID90 was omitted because of an anomalous trend due to a problem with the pressure sensor.

Figure 4.1 shows that the reaction curve shape is significantly influenced by the soil relative density. [i] The lower the soil density, the higher the inner tunnel normalised pressure for a given C/D and $V_{l,t}$. [ii] Loose soils result in a gradual decline of σ_{norm} up to high volume losses ($\approx 10\%$), whereas dense soils induce a steep drop of the pressure within low-medium volume losses ($1-2\%$, depending on C/D) and the pressure stabilises afterwards (i.e. undergoes marginal variation due to further increments of $V_{l,t}$).

Figure 4.2 provides evidence that the minimum pressure occurs at different volume loss values depending on I_d and C/D: the greater C/D and/or the looser the soil, the higher the $V_{l,t}$

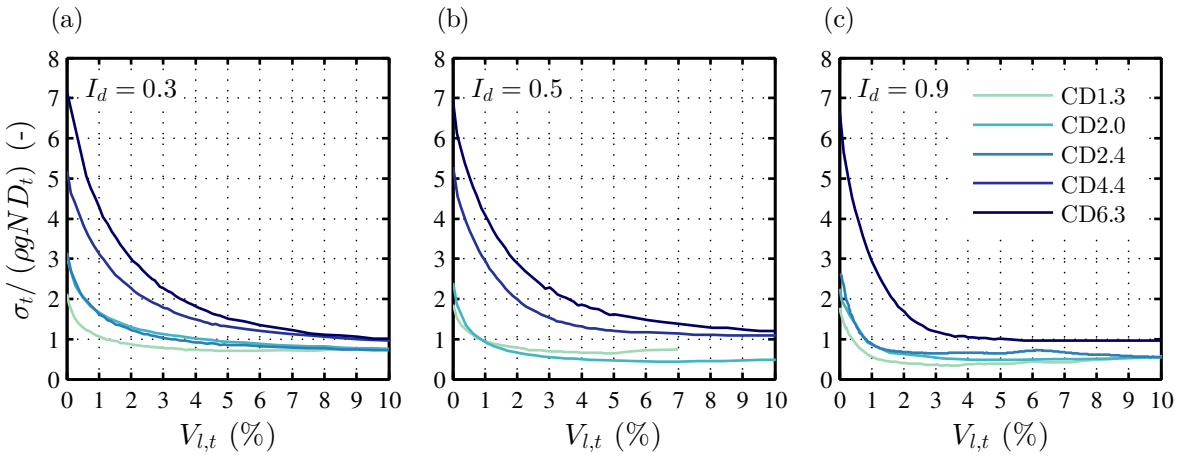

Fig. 4.1 Normalised tunnel pressure with volume loss.

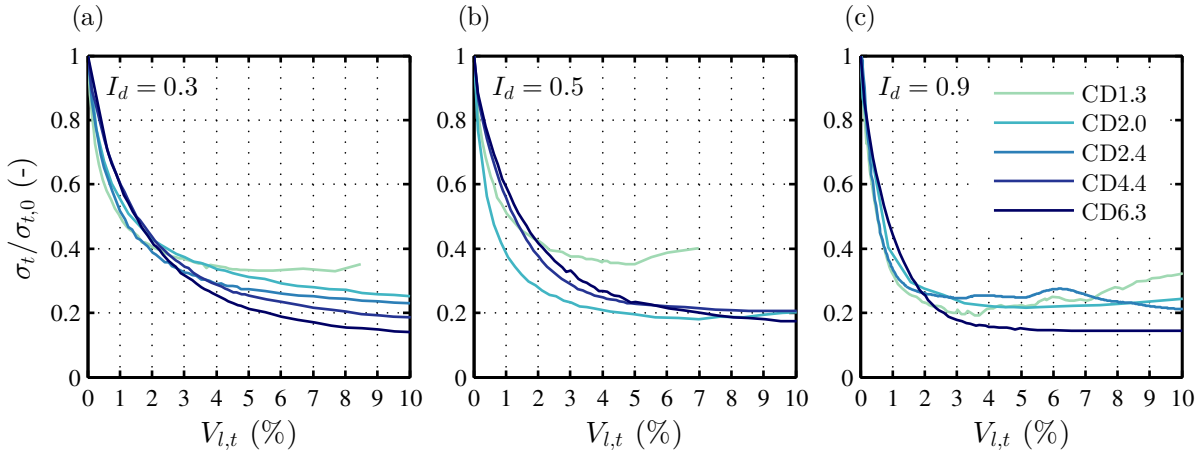

Fig. 4.2 Relative tunnel pressure reduction with volume loss.

corresponding to the minimum σ_t. Furthermore, the results display that the relative reduction of the loading $(1-\sigma_t/\sigma_{t,0})$ is higher at low-medium volume losses ($V_{l,t} < 2-3\%$) and lower at high volume losses ($V_{l,t} > 2-3\%$) for relatively shallow tunnels than deep tunnels. Finally, it is interesting to note that, for shallow tunnels ($C/D = 1.3$), the soil collapse, which results in an increase of σ_t, is initiated after 5% volume loss (see the loading recovery stage in the ground reaction curve displayed in Figure 2.6), whereas σ_t tends to stabilise in the cases with $C/D \geq 2.4$ within the investigated range of $V_{l,t}$. Note that the ultimate failure state of the soil was not reached at $V_{l,t} < 10\%$ for any of the test.

The reaction curves shown in Figures 4.1 and 4.2 are, at least partially, the consequence of the mobilisation of soil arching. Despite the fact that these results do not fully agree with the framework provided in Section 2.1.2.2 for centrifuge modelling of a trapdoor, the general trend of the reaction curves may be interpreted with the evolution mechanism of the arch. The results in Figures 4.1 and 4.2 confirm that minimum relative loadings ($\sigma_{t,min}/\sigma_{t,0}$) decrease with the increase of C/D and that $\sigma_{t,min}$ slightly decreases with the increase in I_d. On the other hand, it is not true that a higher arch efficiency, associated with the minimum loading $\sigma_{t,min}$, is mobilised at

a constant $V_{l,t}$ regardless of I_d and C/D. The relationship $V_{l,t} - \sigma_{t,min}$ would suggest that a higher $V_{l,t}$ is required to fully mobilise the arch (if the arch can form) for [i] relatively deep tunnels compared to shallow excavations and [ii] for looser soils. Additional evidence of the importance of soil arching during tunnelling in sands is provided in the following sections.

4.1.3 Tunnelling-induced displacement and strain mechanisms

In this section, tunnelling-induced soil movements and strains (derived from the measured displacements) are presented to isolate the contributions of tunnel relative depth and soil density on the displacement mechanisms. The objective of these analyses is not limited to the quantification of ground movements and strains depending on the state variables, which was previously carried out by Marshall (2009) and Zhou (2014); the main aim is to relate movements and strains to soil arching in order to illustrate the role of arching in tunnelling in sands.

4.1.3.1 Soil strains definition and calculation

Assuming plane-strain conditions, the engineering shear strain, γ, (corresponding to the diameter of the Mohr circle of strain) is defined as follows

$$\gamma = \sqrt{(\varepsilon_{xx} - \varepsilon_{zz})^2 + (2\varepsilon_{xz})^2} \tag{4.2}$$

where ε_{xz} and ε_{zz} are axial strains in the x and z directions, respectively, and ε_{xz} is the shear strain. Note that the term "shear strain" is used to refer to the engineering shear strains in this study.

The GeoPIV measurements of displacements were used to calculate strains. This computation was carried out by implementing the finite difference method (FDM) in a Matlab script (i.e. using the central difference for inner points of the grid and the single-sided difference values along the edges of the grid). The strain fields estimated with this method were compared with the data of Marshall (2009), obtained by importing the displacement fields in FLAC and exporting the strains provided by the software. The comparison was satisfactory considering that the calculation of strains from displacements measured with the GeoPIV technique is likely to be affected by significant errors because of the scatter in displacement measurements. Therefore, the FDM implemented in Matlab was preferred to guarantee the robustness of the analysis. Although use of a smoothing technique may decrease the level of noise in the data, it is likely that this process may average zones of localised strains, thereby compromising the analysis; therefore, smoothing of the data was not implemented in this work. In the following section, the influence of cover-to-diameter ratio on displacement mechanisms is considered. Finally, it should be noted that the analyses in Section 4.1.3 are limited to displacements and shear strains, whereas the effects of volumetric strain are discussed in Section 4.3.3, where the relationship between tunnel and soil ground losses is evaluated.

4.1.3.2 The effects of cover-to-diameter ratio

Figure 4.3 presents normalized vertical and horizontal displacement fields ($u_z/(V_{l,t} \times R)$ and $u_x/(V_{l,t} \times R)$) measured at $V_{l,t}$ equal to 1 and 3% for tests CD13ID90, CD24ID90, CD44ID90 and CD63ID90 in dense sands; Figure 4.4 plots normalised settlements and shear strains for the same tests and volume losses. To highlight the key aspects, the results were plotted with the following layout:

- Vertical settlements and spatial coordinates were normalised, respectively, by $V_{l,t}R$ and z_t to allow the comparison of the data at different $V_{l,t}$ by tunnels of different diameters. Normalisation was not necessary for strains that are dimensionless. The limits of the contours were maintained constant with tunnel volume loss to display the variation of the deformation pattern with tunnel contraction.

- Theoretically, the tunnelling problem should be symmetric with respect to the tunnel centreline; although experimental data may not be perfectly symmetric, the plots are limited to the first quadrant ($x \geq 0$ and $z \geq 0$).

- In the figures, the contour limits were set equal to $0-1$ and $0-0.15$ for movements in the vertical and horizontal directions, respectively, because of the different magnitude of the displacements induced in the two directions. The limits used for normalised settlements and strains were the same; the interval $\gamma = 0-1\%$ covers the range from small to large strains generally induced by tunnelling (Mair, 1993). In the case of $\gamma > 1\%$, a low residual soil stiffness should be excepted, which may be of interest for tunnel-structure interaction problems. Note that the range of $0-0.15$ for horizontal movements displays only movements towards the centreline (outwards movements were mostly due to scatter in the data).

- Measurements greater or lower than the contour thresholds were set equal to the closer limit value. In the regions where data were not available, the displacement values were set equal to zero (e.g. around the tunnel and at the side of the tunnel). For instance, during tests CD13ID90, CD44ID90 and CD63ID90 in Figure 4.3, soil movements were not measured close to the tunnel periphery. Because of this, the script used to compute strains may result in high strains at the boundaries of these regions with null values; therefore, these high strains are not physical measurements.

Figures 4.3 and 4.4 show that the lower C/D, the greater the magnitude of the normalised settlements and shear strains. Firstly, the settlements are analysed. Vertical displacements in the case of shallow tunnels are localised at the tunnel centreline, whereas vertical ground movements are highly spread out in the case of deep tunnels, resulting in wide settlement troughs and the decrease of the normalised settlement magnitude. In general, the deformation pattern becomes narrower with volume loss (i.e. are concentrated closer to the tunnel centreline). For the shallow tunnels (CD13ID90 and CD24ID90), low volume losses resulted in a chimney-like displacement

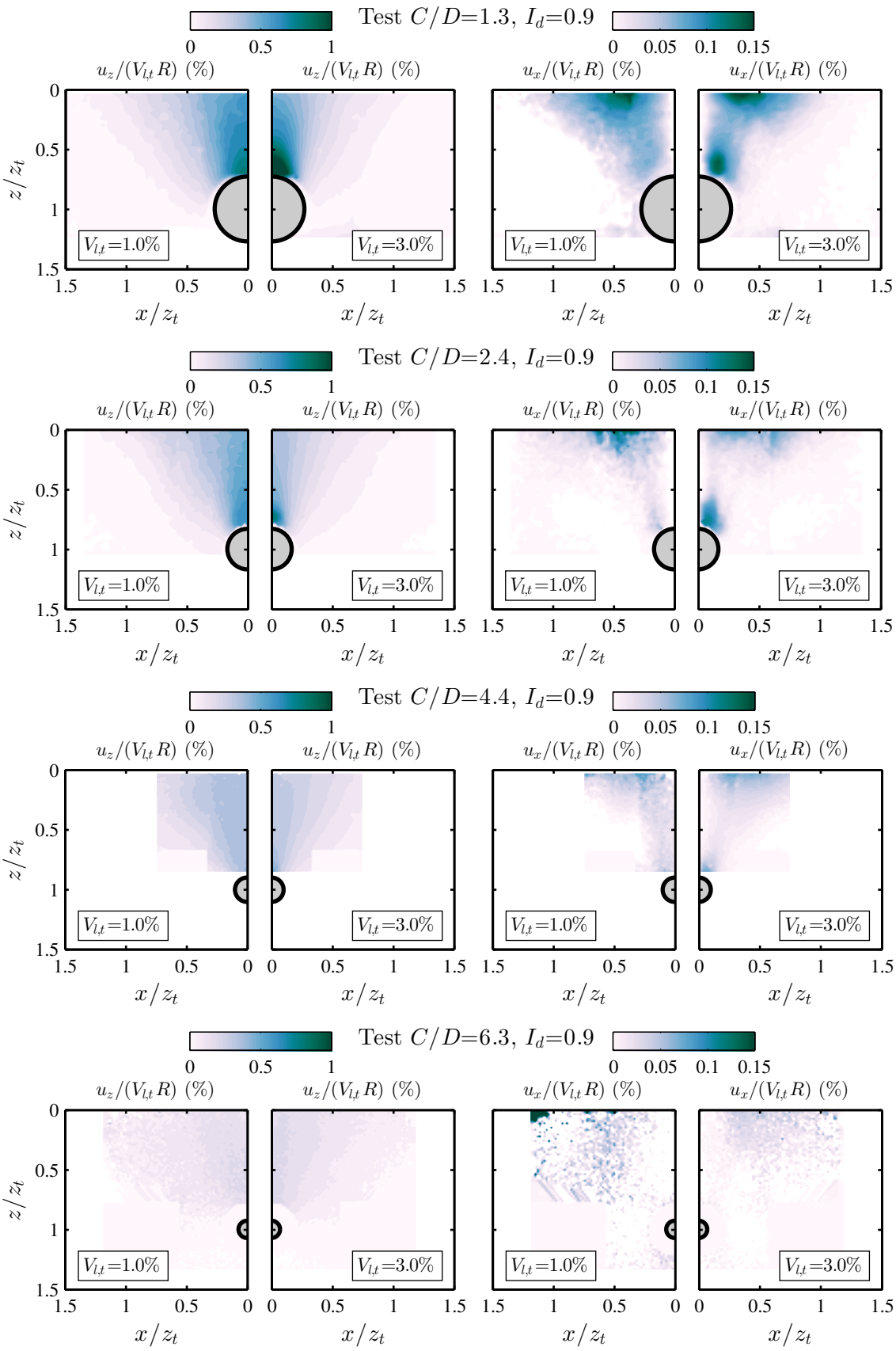

Fig. 4.3 Normalised vertical (left) and horizontal (right) displacement contours at $V_{l,t} = 1,3\%$ and $I_d = 0.9$ for varying C/D.

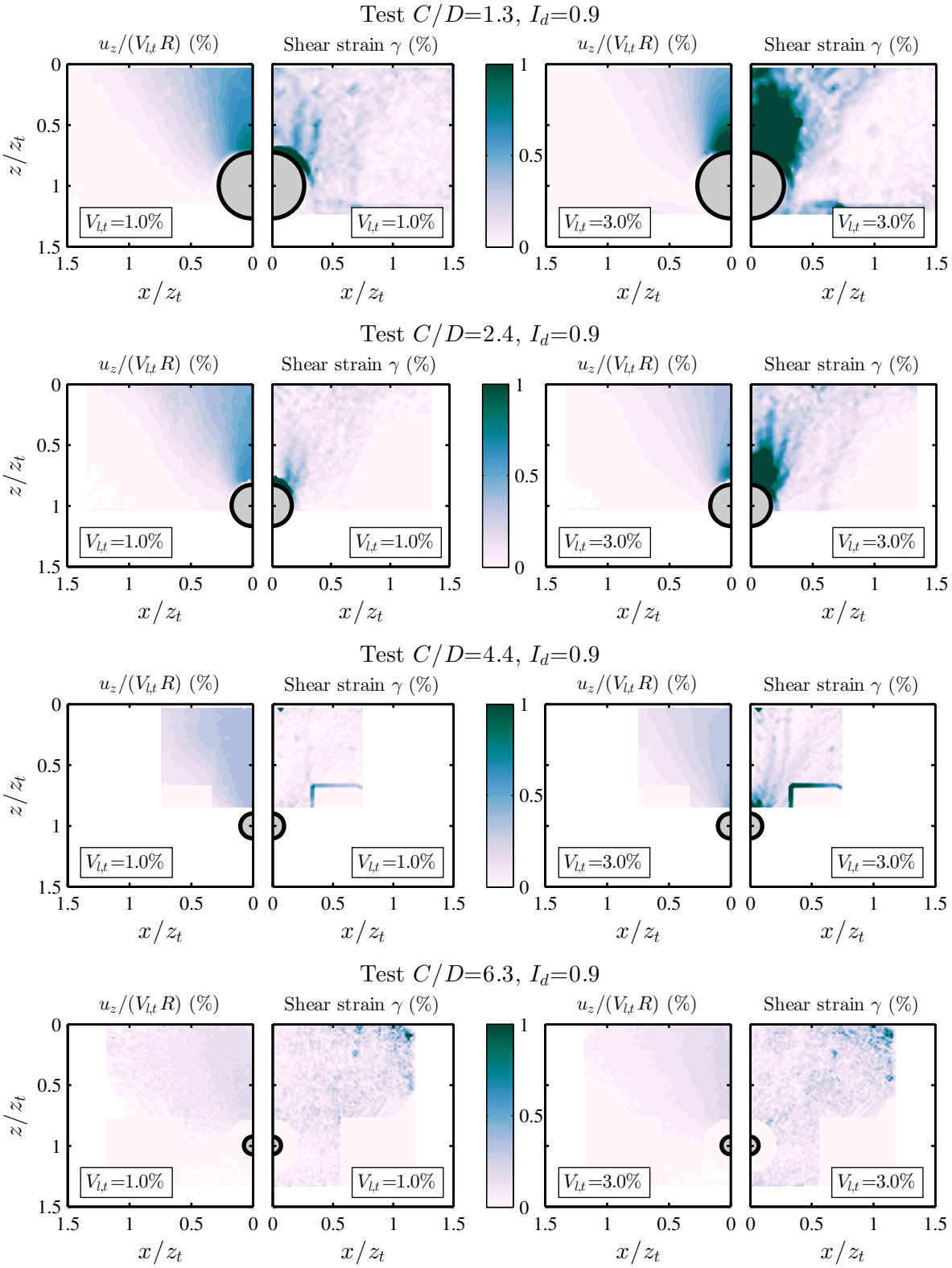

Fig. 4.4 Normalised settlement (left) and shear strain (right) contours at $V_{l,t} = 1,3\%$ and $I_d = 0.9$ for varying C/D.

field with soil movements that tend to propagate vertically from the tunnel; at high volume losses, the displacement mechanisms exhibit a local failure near the tunnel crown (with an associate concentration of displacements). For the deep tunnels (CD44ID90 and CD63ID90), it is not possible to identify the chimney-like mechanism, which was suggested for coarse soils by Cording (1991). Finally, it is important to report that, in both tests CD24ID90 and CD63ID90, soil movements measured below the tunnel springline depth were negligible across the range of volume losses considered.

The concentration of soil displacements at the tunnel crown may be related to soil arching (limiting the contours to a maximum $\gamma = 1\%$ allows defining the region of soil beneath the arch). From the comparison of $u_z/(V_{l,t} \times R)$ and γ of tests CD13ID90 and CD24ID90 in Figure 4.4, it is apparent that the response of the soil at the tunnel crown is in sharp contrast to the soil above, therefore defining a zone of arching. At low volume loss ($V_{l,t} = 1\%$), the bands of large shear strains above the tunnel shoulders correspond to the zones where arching is initiating. On the other hand, a generalised high level of shearing is measured both at the arch and the underlying soil at high volume loss ($V_{l,t} = 3\%$). In relatively deep tunnels (CD44ID90 and CD63ID90), the zone of major settlements at the tunnel crown can only be identified for $C/D = 4.4$ at high volume losses, whereas it is probably within the region where movements were not measured at the tunnel periphery for $C/D = 6.3$. The wide settlement mechanism of tests CD44ID90 and CD63ID90 is probably the results of the soil arching above the tunnel. The soil arch prevents the chimney-like settlement mechanism and allows for the "damping" of the tunnel ground loss that is spread over a wider region of soil; the response of the soil above the arch is probably close to elastic given low magnitude of shear strains.

Figure 4.3 also displays $u_x/(V_{l,t} \times R)$, which are generally affected by a higher level of scatter than $u_z/(V_{l,t} \times R)$. Comparison of results suggested that at $V_{l,t} = 1\%$, horizontal inwards ground movements are mostly induced at the surface and their magnitude decreases with normalised depth. On the other hand, there is evidence that subsurface horizontal ground movements arise at $V_{l,t} = 3\%$ (where there is a concentration of settlements at the tunnel crown due to soil arching) and the magnitude of normalised horizontal displacements decreases with volume loss.

From the data shown in Figures 4.3 and 4.4, a correlation was found between the vertical and horizontal tunnelling-induced soil movements as well as between the displacement mechanism, shear strain distribution and soil arching. These relationships are further investigated in a latter section to achieve an understanding of the role of soil density.

4.1.3.3 The effects of soil relative density

To evaluate the impact of soil relative density, all centrifuge tests with $C/D = 2.0$ (CD20ID30, CD20ID50, CD20ID70, CD20ID90) and $C/D \approx 2.5$ (CD25ID30, CD24ID90) were considered. Results are plotted in Figures 4.5, 4.6 and Figures 4.7, 4.8 for $C/D = 2.0$ and 2.5, respectively. To allow for the comparison, these figures have the same layouts and normalisations used in Figures 4.3 and 4.4. This dataset is particularly interesting because it illustrates effects of soil density on displacement mechanisms that have not been displayed by previous researches.

Figures 4.5 and 4.7 show the normalised displacement contours corresponding to low and high volume losses ($V_{l,t} = 1$ and 3%). In general, the figures display that greater tunnelling-induced movements should be expected in looser sands. Furthermore, for all six tests, the normalised settlements are concentrated mainly at the centreline at $z/z_t > 0.5$, whereas the results are characterised by a different vertical propagation between the depths $z/z_t = 0.5$ and $z/z_t = 0$ (from mid-depth towards the surface). The concentration of ground movements at the tunnel crown is limited to the area around the tunnel periphery for $I_d = 0.9$, whereas it includes a greater subsurface portion of ground for $I_d = 0.5, 0.7$. On the other hand, for a loose soil ($I_d = 0.3$), the settlement pattern appears as a purely chimney-like mechanism. Despite the slight attenuation of the normalised settlement magnitude with volume loss, the differences in the propagation of the settlements is qualitatively similar at low and high volume loss. In the following text, the variation of the displacement mechanism with I_d is further investigated by comparing settlements to the shear strain distributions.

Figures 4.6 and 4.8 plot normalised settlements and strains. Despite the scatter of the data, it is noticeable that the strain bands developing at $V_{l,t} = 1\%$ further develop at higher volume loss, delimiting the shearing region of soil with high strains at $V_{l,t} = 3\%$. The variation of shear strain distribution with soil density is discussed in the following list, which provides a framework that extends findings of previous research.

- In the case of dense sands (CD20ID90, CD24ID90), low volume losses initiate shear bands. These bands delimit the zone at the tunnel crown that undergoes a downwards movement as a block at high volume losses. At high volume loss, the soil arch becomes apparent, which reduces the tendency for tunnel volume loss to propagate to the surface. The zone of large shearing concentrated beneath the soil arch results in additional dilation that decreases the ratio $V_{l,s}/V_{l,t}$.

- For medium dense sands (CD20ID50, CD20ID70), the arching mechanism is similar to the dense sand tests and the arch is still able to fully mobilise. However, its size is greater than in the case of CD20ID90 because of the lower soil strength associated with $I_d = 0.5 - 0.7$, resulting in a greater region of soil experiencing large shear strains. Note that in test CD20ID50 at $V_{l,t} = 3\%$ the zone of large shearing is close to the surface, suggesting that the arch is close to failure.

- Interestingly, a chimney-like mechanism (tunnel ground loss propagates from the tunnel to the surface) with near-vertical shear bands at the tunnel shoulders is clear in loose sands (CD20ID30 and CD25ID30) both at $V_{l,t} = 1$ and 3%. Therefore, the resulting settlement field for $I_d = 0.3$ is qualitatively different than in the cases $I_d = 0.5 - 0.9$. This is due to the fact that, in the case of loose soil, the soil does not mobilise a close arch starting from the initial near-vertical shear bands. The shear bands simply increase in size between $V_{l,t} = 1$ and 3%. The soil above the tunnel moves downwards as a rigid body (there are no shear strains close to the tunnel centreline). Because the shear bands are not perfectly vertical, the soil above the tunnel is probably shearing as in a funnel mechanism.

Note that the plot of normalised settlements ($u_z/(V_{l,t} \times R)$) shows the wideness of the settlement field. Interestingly, the settlements in dense sand ($I_d = 0.9$) and $C/D = 2.0 - 2.5$ are wider than in medium dense sands ($I_d = 0.5 - 0.7$); whereas the vertical displacement mechanism for medium-dense sands is narrower than for loose soil ($I_d = 0.3$). This non-linear trend of the settlement width (confirmed by statistical regression of the dataset in Section 4.2) is consistent with the soil arching phenomenon. The tunnel ground loss propagates vertically between the tunnel and the soil beneath the arch, resulting in large movements and narrow settlement troughs; on the other hand, the ground loss spreads vertically and outwards above the soil arch, resulting in wider settlements troughs. The lower the density, the greater the soil arch size and the greater the amount of soil affected by the narrowing. However, if the soil arch cannot form (as for tests with $I_d = 0.3$), ground loss propagates from the tunnel towards the surface both vertically and laterally (also at the level of the shear bands that are not perfectly vertical).

The results in Figures 4.5 and 4.7 provide interesting insights on the distribution of horizontal movements. Figure 4.5 displays that, for medium-dense and dense soil ($I_d = 50 - 90\%$), normalised inwards movements decrease near the surface ($z/z_t < 0.25$) and increase above the tunnel crown with volume loss; this is similar to the mechanism illustrated in the previous discussion of Figure 4.3. On the other hand, in the case of $I_d = 0.3$, the distribution of normalised horizontal movements, both in terms of shape and magnitude, is not affected by $V_{l,t}$: inwards horizontal displacements do not attenuate with volume loss and they are mostly induced near to the surface. The differences in the distribution of horizontal movements between loose soils and medium-dense/dense soils can be related to the settlement mechanism. Subsurface inner horizontal displacements were measured simultaneously with the onset of the concentration of settlements at the tunnel crown. It can be concluded that subsurface horizontal movements develop with the localised failure of the soil at the tunnel crown; on the other hand, if the settlement mechanism has a chimney profile, subsurface horizontal displacements should be minimal. Therefore, horizontal displacements near the tunnel shoulders are significant only for shallow tunnels at high volume losses in dense sands.

4.1.3.4 Summary of displacement mechanisms and soil arching

The soil arching phenomenon probably plays a major role in the definition of tunnelling-induced displacement mechanisms. In particular, it can help to explain [i] the transition from a chimney-like displacement field to a wide displacement field with C/D, [ii] the narrowing of the displacement field with $V_{l,t}$, and [iii] the complex variation of settlements with soil density.

In general, ground movements due to tunnel ground loss tend to propagate vertically within the arching zone inducing narrow settlement troughs in this area. On the other hand, above the arch, ground movements propagate towards the surface, spreading in the horizontal direction, resulting in wide settlement troughs. In the case of deep tunnels, the soil arching is localized at the tunnel crown and the soil deformation pattern is wide overall. In the case of shallow tunnels, the arching affects a proportionally larger zone of soil above the tunnel, resulting in a chimney-like displacement field (i.e. narrow settlement troughs). With the increase of $V_{l,t}$, the

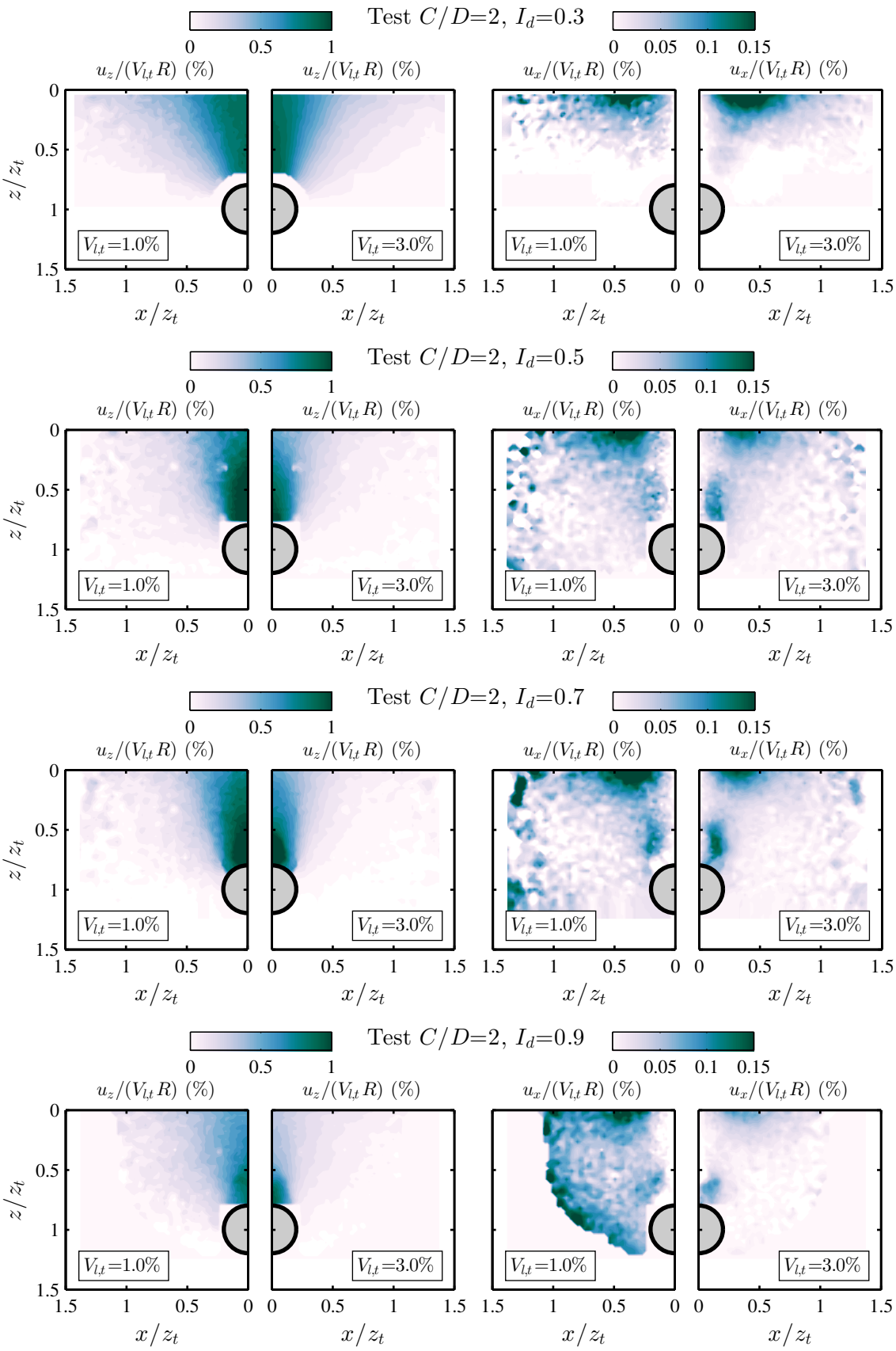

Fig. 4.5 Normalised vertical (left) and horizontal (right) displacement contours at $V_{l,t} = 1,3\%$ and $C/D = 2.0$ for varying I_d.

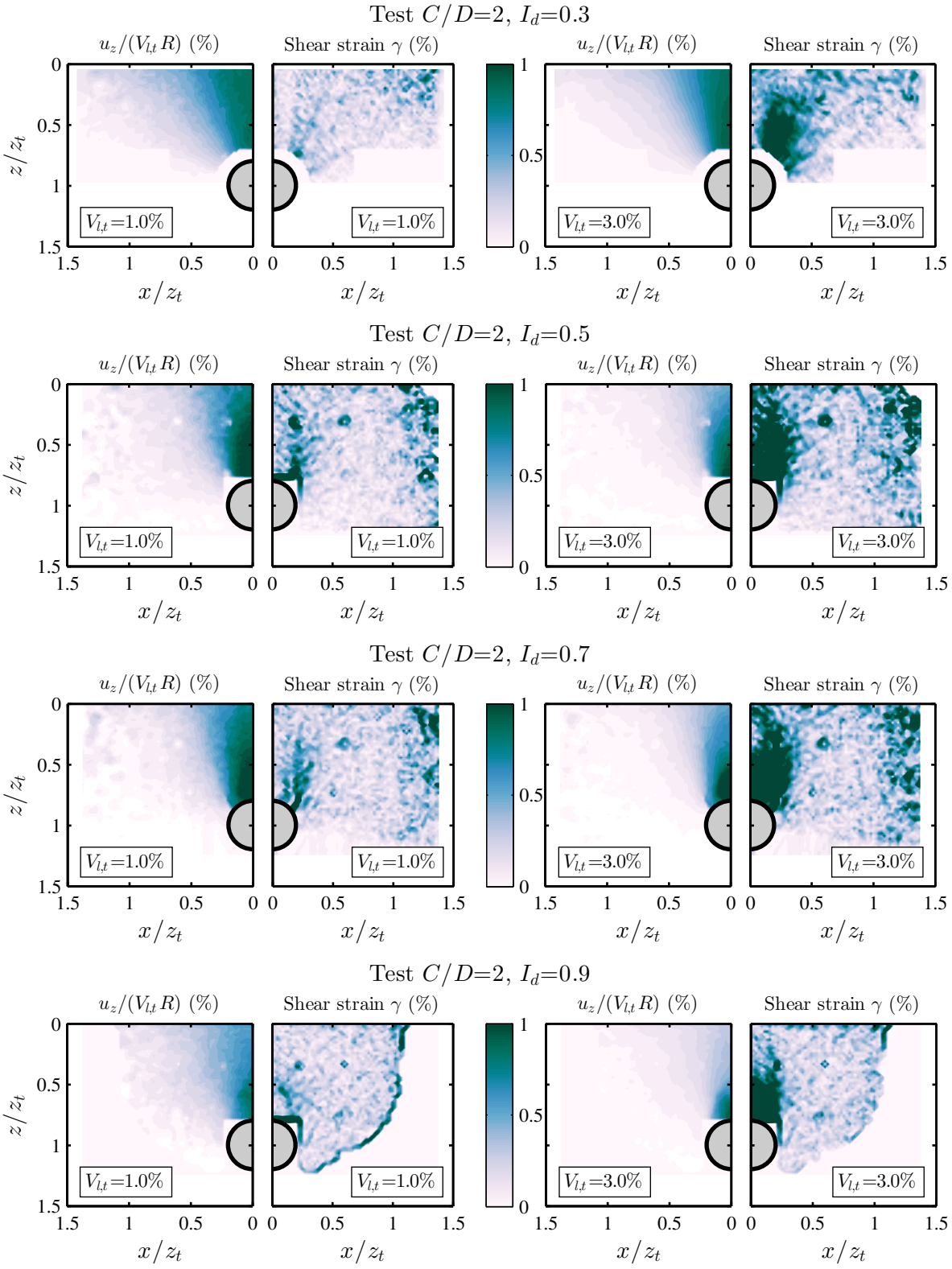

Fig. 4.6 Normalised settlement (left) and shear strain (right) displacement contours at $V_{l,t} = 1,3\%$ and $C/D = 2.0$ for varying I_d.

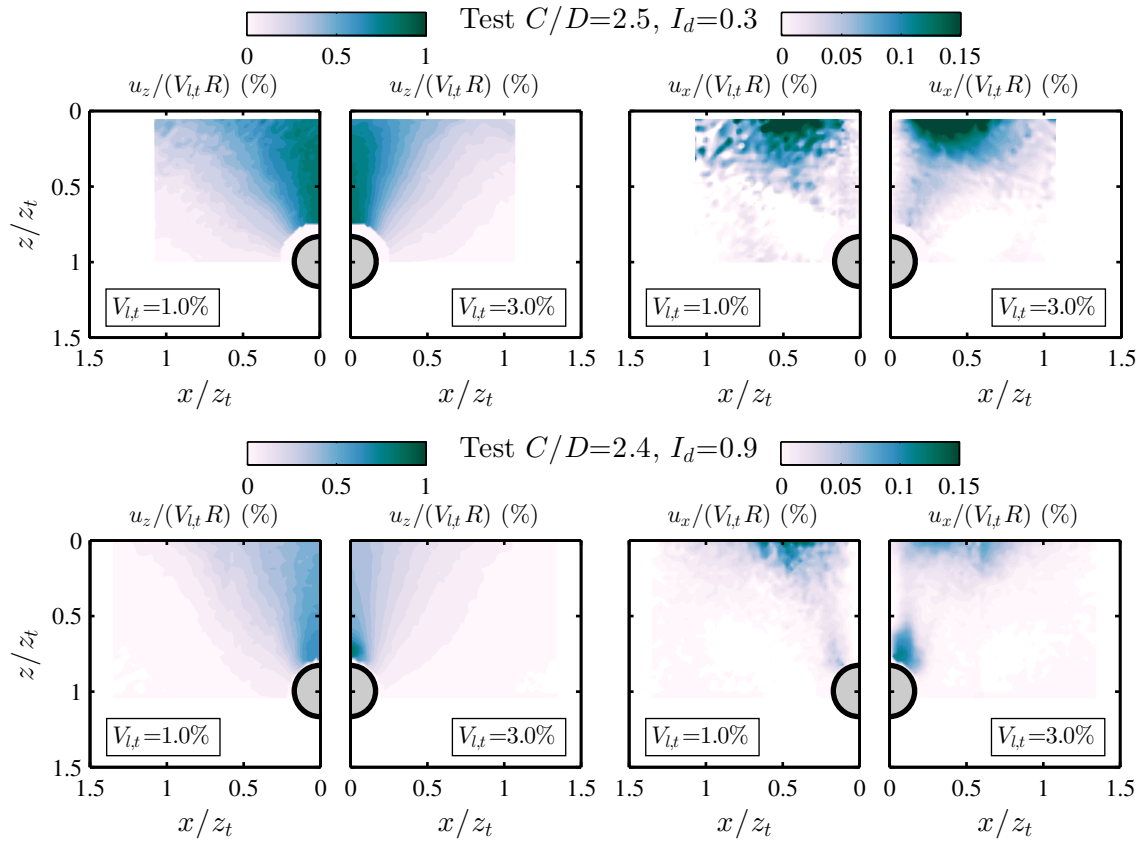

Fig. 4.7 Normalised vertical (left) and horizontal (right) displacement contours for $C/D \approx 2.5$ and varying I_d.

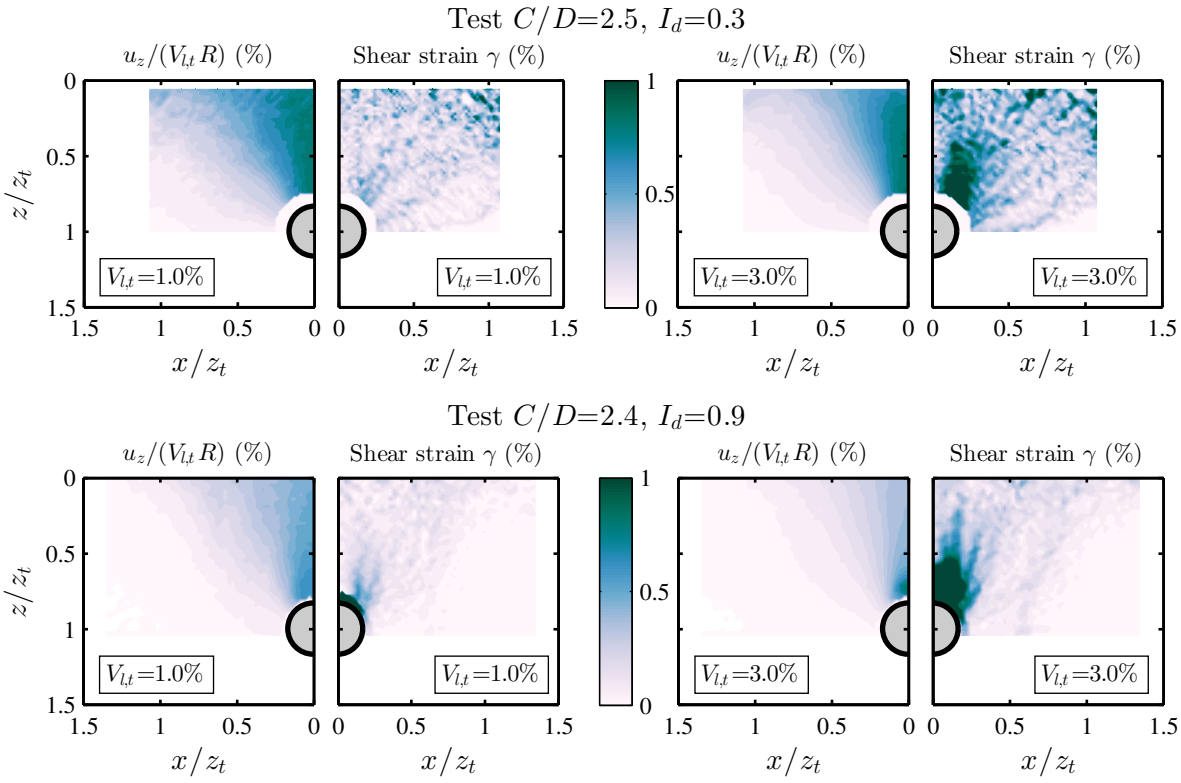

Fig. 4.8 Normalised settlement (left) and shear strain (right) displacement contours for $C/D \approx 2.5$ and varying I_d.

localised downwards movement of the soil between the tunnel crown and the arch as well as, probably, the evolution of the soil arch postulated by Iglesia et al. (2014) (displayed in Figure 2.7) results in the narrowing of the displacement field. The mechanisms highlighted in Section 4.1.3 are summarised in Figure 4.9.

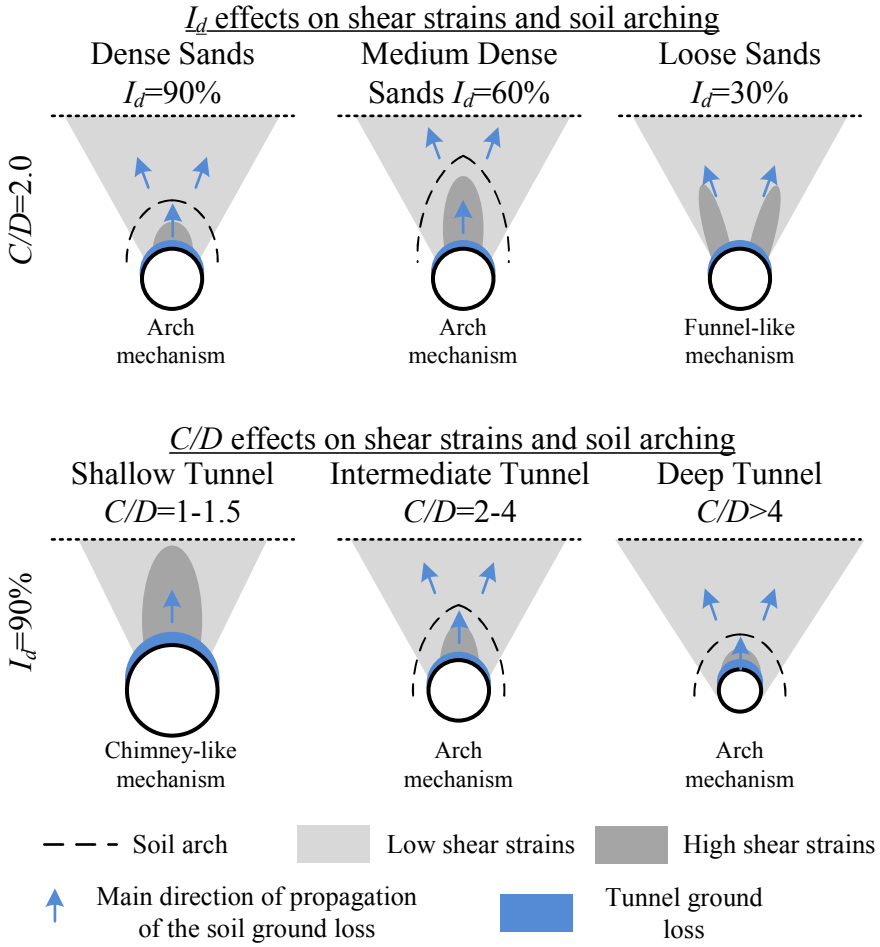

Fig. 4.9 Sketches of I_d and C/D effects on soil strains, arching mechanism and ground loss propagation.

4.2 Analysis of settlement troughs

This section aims to evaluate the shape of settlement troughs, which are associated with a greater potential for damage than horizontal movements. Previous research investigated the settlement profile with the analysis of parameters defining empirical settlement curves fitted to experimental and/or field data. As illustrated in Section 2.1.3.2, centrifuge transverse settlement troughs in sands should be interpolated with a modified Gaussian curve, reported in Equation (2.15), rather than a standard Gaussian curve in order to describe their full range of variability (Marshall et al., 2012; Vorster et al., 2005). The three degrees of freedom (dofs) of Equation (2.15) are the maximum settlement u_{max} and the horizontal offsets x^* and x^{**}, which are related to the trough width parameters K^* and K^{**} by Equation 2.16. In this section, the variation of maximum settlement and shape of the settlement curves with the main physical variables of the problem (z/z_t, $V_{l,t}$, C/D, and I_d) is assessed.

The GeoPIV data were curve-fitted in Matlab using a least squares regression technique. For instance, Figure 4.10 shows experimental data from test CD63ID90 for a relative depth, z/z_t, equal to 0 and 0.5; these data are curve-fitted with both Gaussian and modified Gaussian curves that are labelled in the legend as G and mG, respectively. Settlement troughs are shown to become narrower with depth. The goodness of fit is assessed with the coefficient of determination R^2. The modified Gaussian curve is able to provide a better fit to subsurface ground movements for test CD6.3. However, as also noted by Marshall et al. (2012), standard Gaussian curves are suitable for the interpolation of wide settlement troughs in sands, which are generally measured at the surface in the case of relatively deep tunnels. In the following sections, ground movements are curve-fitted with modified Gaussian curves because the cover-to-diameter ratio ranged between 1.3 and 6.3.

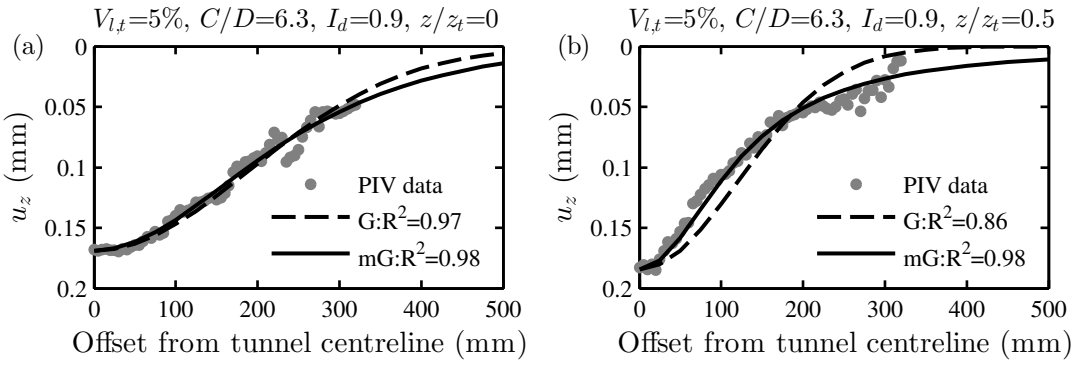

Fig. 4.10 Fitting curves to settlement data from test CD63ID90.

4.2.1 Maximum settlements

The maximum settlement is often used for a preliminary risk assessment (see Section 2.3.3); as a first approximation, the higher the maximum settlement, the higher the expected risk for damage. Therefore, the analysis of the maximum greenfield settlements of the centrifuge dataset

is interesting both for practical reasons and the understanding of phenomena associated with tunnelling.

The normalized maximum settlements, $u_{z,max}/R$, measured during test series 1 at $z/z_t = 0$ and 0.5 versus $V_{l,t}$ are plotted in Figure 4.11(a), (b), and (c), respectively, for $I_d = 0.3, 0.5, 0.9$. The displacement value was normalised to allow comparison of results obtained with model tunnels of different diameter.

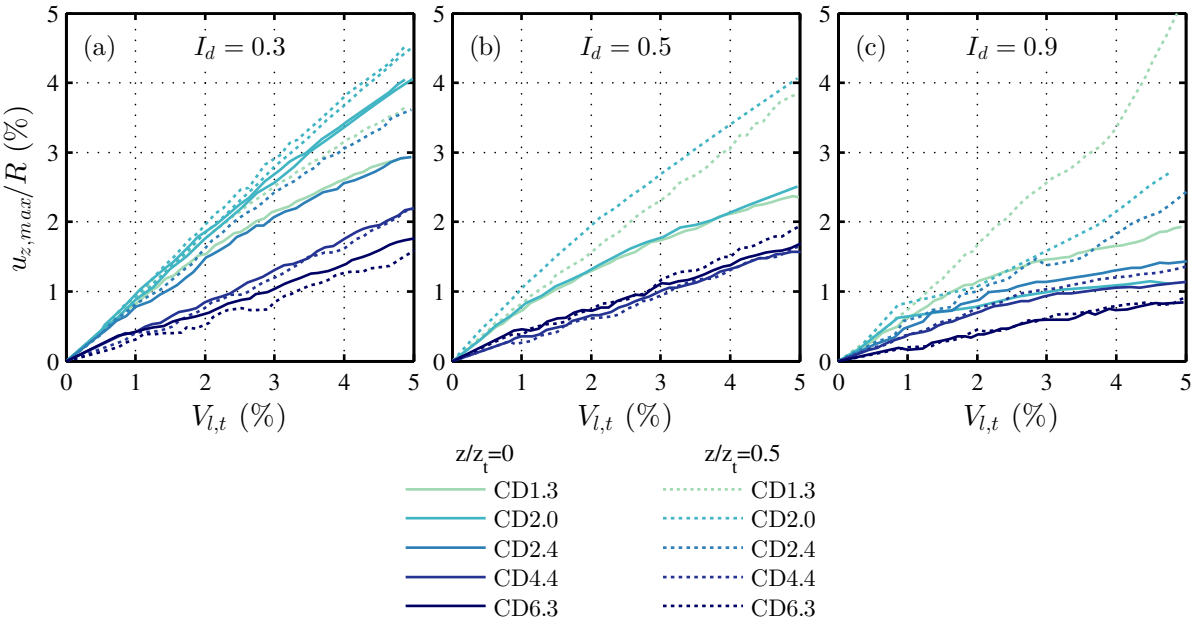

Fig. 4.11 Variation of the normalised maximum settlement with $V_{l,t}$.

The displayed results show that the value of $u_{z,max}/R$ generally increases with $V_{l,t}$, decreases with C/D, and reduces with I_d both at the surface and subsurface levels. Moreover, $u_{z,max}/R$ for shallow tunnels is lower at the surface than at the normalised depth $z/z_t = 0.5$, whereas this variation is negligible for deep tunnels ($C/D > 4$). On the other hand, note that $u_{z,max}/R$ is lower for $C/D = 1.3$ than $C/D = 2.0$ when $I_d = 0.3$. Secondly, it is interesting to highlight the variation of the normalised settlement with $V_{l,t}$. For loose sands ($I_d = 0.3$), the value $u_{z,max}/R$ varies approximately linearly within the entire range $V_{l,t} = 0 - 5\%$ both at the surface and subsurface, whereas the relationship $u_{z,max}/R - V_{l,t}$ is non-linear for dense sands ($I_d = 0.9$) with different trends observed at the surface and subsurface.

These phenomena are probably due to the combined effects of soil arching (associated with the settlement trough narrowing at depths close to the tunnel crown) and the dilative/contractive behaviour of the soil. For instance, the differences in the rate of variation with $V_{l,t}$ between loose and dense samples are probably due to the higher efficiency of the soil arch in dense sands than in loose sands, whereas $u_{z,max}/R$ being lower in CD13ID30 than in test CD20ID30 may be due to the absence of the soil arch for shallow tunnels in loose sand and the overall state of contraction of the soil. These insights on the influence of $V_{l,t}$, I_d and C/D on $u_{z,max}/R$ provide

useful indications for the preliminary design stage of tunnelling near to shallow and buried structures.

4.2.2 Settlement trough shape

Although a considerable amount of literature has been published on the settlement trough width in the case of tunnelling in sands, a systematic analysis investigating the impact of soil density at varying relative tunnel depth is missing. In this section, the correlation between the effects of cover-to-diameter ratio and soil density is studied.

4.2.2.1 The influence of cover-to-diameter ratio in dense sands

The influence of C/D on the settlement trough shape is assessed by plotting the normalised settlement troughs of tests CD24, CD44 and CD63 at $I_d = 0.9$ in Figure 4.12 for $V_{l,t} = 1,5\%$ and $z/z_t = 0,0.6$. These data, normalised by the maximum settlement at the tunnel centreline, are fitted with modified Gaussian curves. The higher the C/D, the higher the surface and subsurface settlement width. The level of scatter in the data of CD63 is relatively high due to the small tunnel diameter. Overall, Figure 4.12 suggests that the influence of C/D and $V_{l,t}$ on the settlement shape decreases with C/D magnitude, obtaining similar curves for the cases CD44 and CD63. These results suggest that C/D effects on greenfield ground movements may have a non-linear trend.

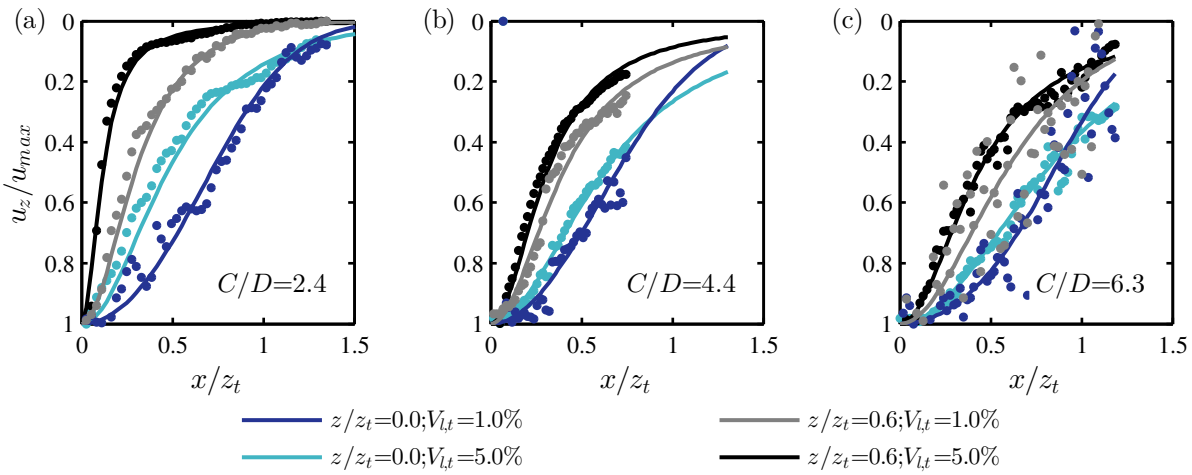

Fig. 4.12 Comparison of settlement trough curves for C/D 2.4, 4.4 and 6.3 ($I_d = 0.9$).

4.2.2.2 The influence of soil density for relatively shallow and deep tunnels

The influence of relative density on the shape of the settlements troughs is evaluated with tests CD20, CD45, and CD63 at $I_d = 0.3, 0.5, 0.9$. The normalised settlement curves for $C/D = 2.0$ and ≈ 4.5 are reported in Figure 4.13 with the same layout and legend of Figure 4.12 to allow for comparison. From the charts in Figures 4.13(a), (b) and (c), it can be seen that the

influence of the soil density on the settlement curve shape is marginal in the case of shallow tunnels ($C/D = 2.0$), whereas greater effects are induced in the case of relatively deep tunnels ($C/D \approx 4.5$) (see Figures 4.13(d), (e) and (f)). Furthermore, the plots confirm that greater volume losses are associated with narrower normalised curves. In general, the qualitative assessment of the normalised settlement curves in Figure 4.13 provides limited information; however, it is clear that the variation of settlement trough shape with C/D and I_d is a complex phenomenon.

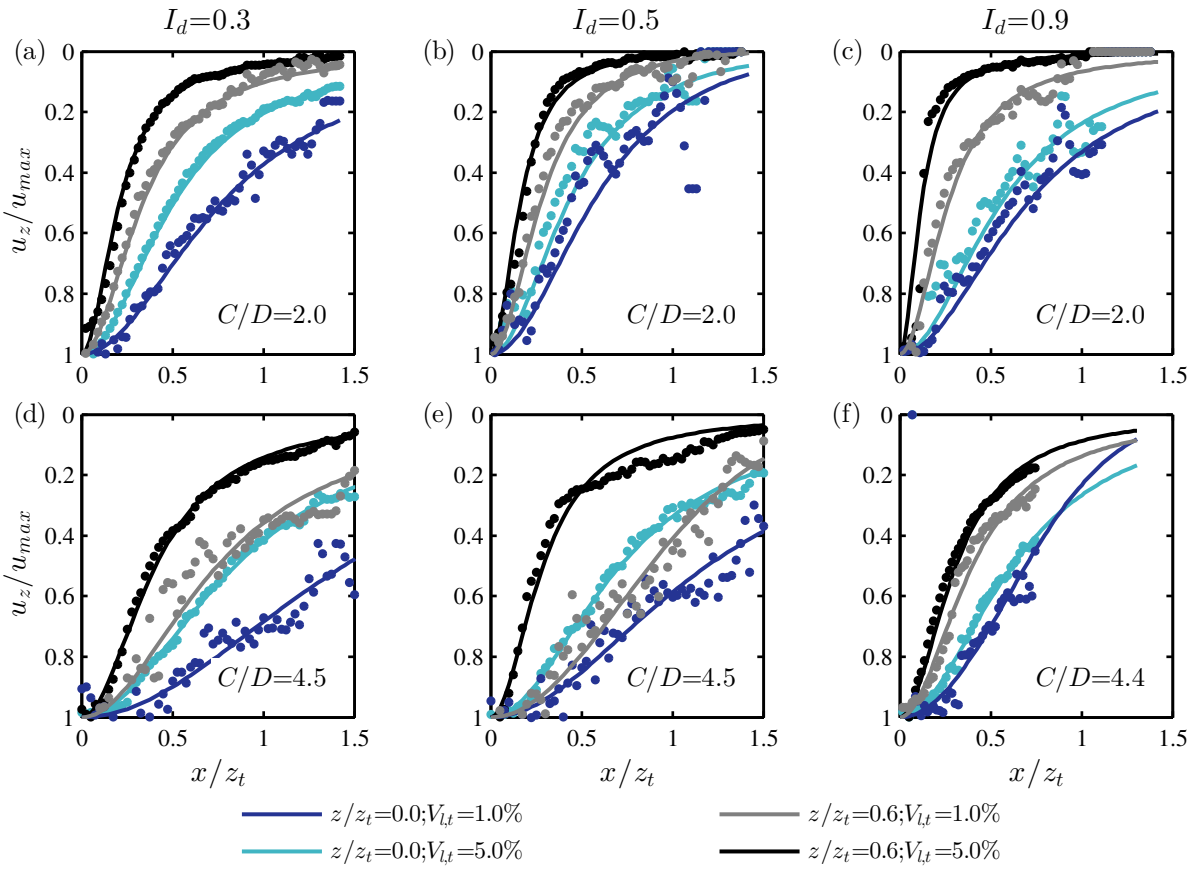

Fig. 4.13 Comparison of normalized settlement trough curves for $C/D = 2.0$ and ≈ 4.5 for different I_d.

The empirical formulas proposed by Marshall et al. (2012) (see Equation (4.3)) are based on the understanding of the dependency of $K_s^{*,**}$ and $x^{*,**}$ on the variables C/D, $V_{l,t}$ and z/z_t. In dense sands, the regression of parameters $K_s^{*,**}$ and $\partial x^{*,**}/\partial z$ was carried out by Marshall et al. (2012) on the assumption that they vary linearly with volume loss and depth, respectively; this assumption was supported by experimental evidence. On the other hand, there is minimal available information on $K_s^{*,**}$ and $x^{*,**}$ in the case of loose and medium-dense sands. Therefore, in the following, the effects of soil density on $K_s^{*,**}$ and $x^{*,*}$ are studied.

Firstly, K_s^* and K_s^{**} (i.e. the value of K^* and K^{**} at the surface) are plotted against $V_{l,t}$ for all tested configurations in Figure 4.14; solid and dashed lines are used, respectively, for K_s^* and K_s^{**}, whereas the darker the colour, the greater the soil density. The data confirm that the range of variability of settlement trough width with soil density is great for the cases of

high C/D and limited for relatively shallow excavations. Overall, the results in Figure 4.14 display non-linear distributions that are characterised by: [i] decreasing values of K_s^* and K_s^{**} with I_d and $V_{l,t}$, [ii] a gradual reduction of the decrease rate with $V_{l,t}$, [iii] the greater the C/D ratio, the higher the impact of I_d, with negligible effects of soil density for shallow tunnels ($C/D = 1.3$). On the other hand, it should be noted that tests for $C/D = 2.0$ do not fully agree with point [i] because K_s^* and K_s^{**} for $I_d = 0.5$ and 0.7 are lower than the values for a dense sand. When defining empirical formulas in Section 4.3, this complex trend for $C/D = 2.0$ is neglected because it results in limited variations of width parameters (compare Figure 4.14(b) and (d)). Furthermore, it is interesting to evaluate the shape of $K_s^* - V_{l,t}$ and $K_s^{**} - V_{l,t}$ relationships in Figure 4.14. The surface width parameters measured during tests with dense sands ($I_d = 0.9$) have an approximately constant rate of variation with tunnel volume loss, which supports the Marshall et al. (2012) assumption. On the other hand, the data for loose and medium-dense sands ($I_d = 0.3 - 0.5$) follow non-linear distributions.

Secondly, Figure 4.15 shows the profiles of offsets x^* and x^{**} with depth z for volume loss of $1, 2.5, 5\%$ and $C/D = 1.3, 2.0$. Note that both x and z axes are normalised by z_t. In general, the greater the value of x^* and x^{**}, the wider the settlement trough. The plotted data show that the relationship between the two offsets and depth is approximately linear at low volume losses, especially for the shallowest tunnel. However, with the increase in volume loss, the trend of the curves becomes non-linear. The non-linearity is due to a greater reduction with $V_{l,t}$ of the settlement trough width at $z/z_t > 0.2$ than at the surface. This mechanism is induced by the soil arching and the resulting concentration of settlements directly above the tunnel (see Figure 4.9). Considering these results, to improve their predictions, empirical methods should not impose the condition that $\partial x^*/\partial z$ and $\partial x^{**}/\partial z$ are constant. Furthermore, it is interesting to discuss the conclusion of Zhou et al. (2014) that suggested that the shape of the settlement trough is narrower in looser sands; according to data in Figure 4.15(d) and (e), the applicability of this conclusion is limited to the case of $C/D = 2.0$, $I_d = 0.5 - 0.9\%$, and $V_{l,t} \leq 1$.

To conclude, the outcomes presented in Figures 4.13, 4.14 and 4.15 provide important insights into the combined influence of tunnel relative depth and soil density on the settlement trough width. It was displayed that:

- the higher the cover-to-diameter ratio, the greater the effect of the density on the settlement trough width; in particular, this variation is negligible for relatively shallow tunnels, whereas the shape of the settlement trough is wider in looser sands for relatively deep tunnels;

- in loose and medium-dense sands, the trough shape parameters vary non-linearly with all the physical variables C/D, $V_{l,t}$ and z/z_t.

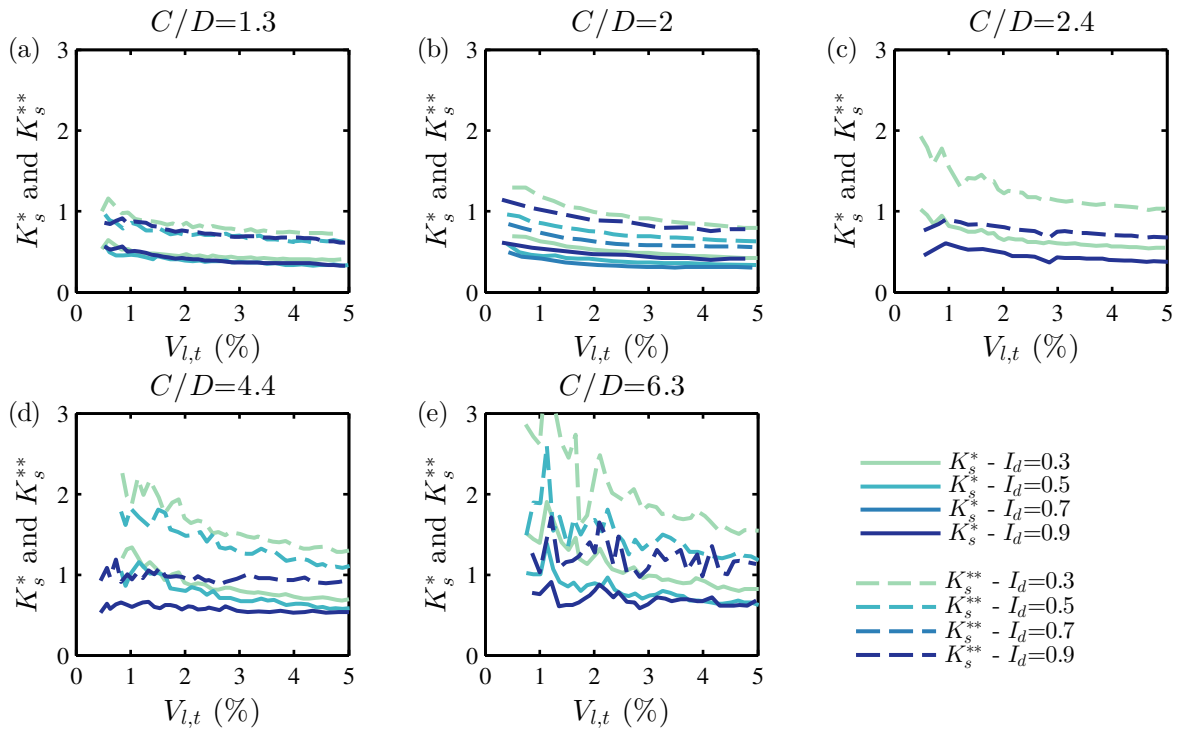

Fig. 4.14 Variation of K_s^* and K_s^{**} at varying I_d for $C/D = 1.3 - 6.3$.

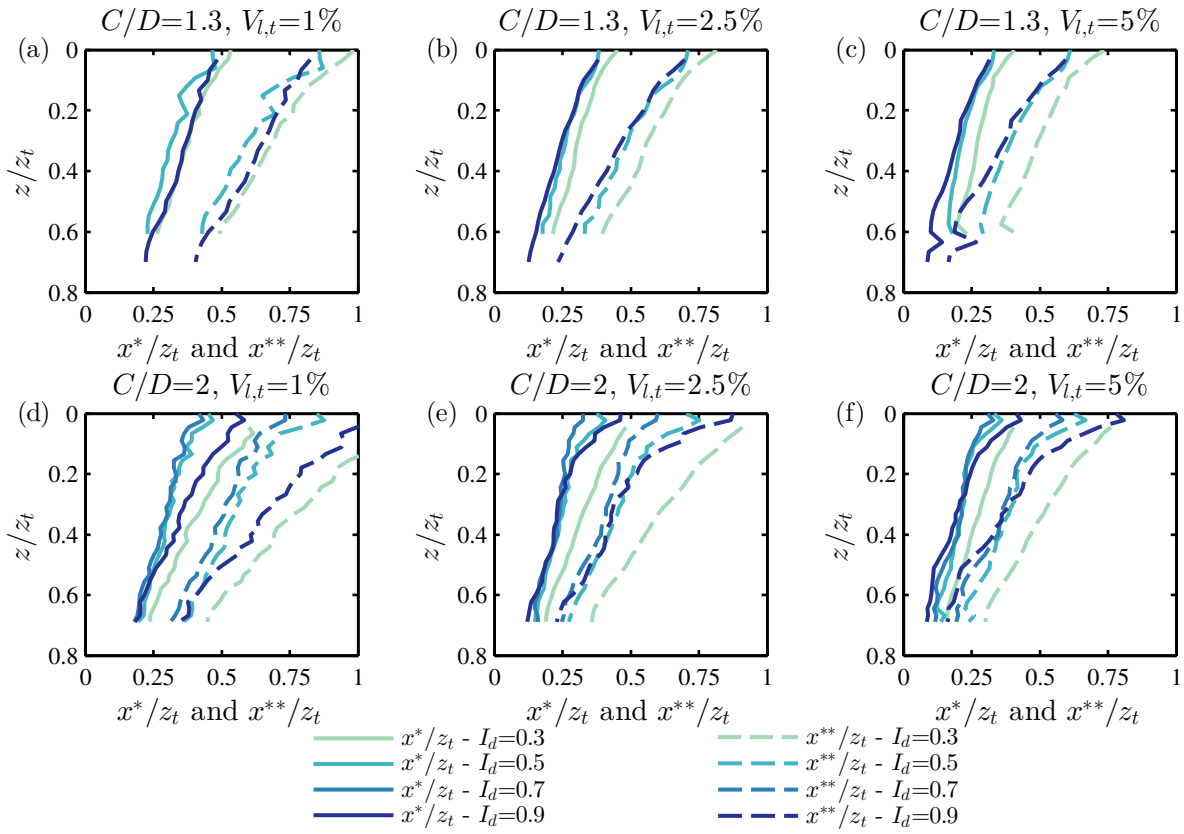

Fig. 4.15 Variation of x^* and x^{**} with z/z_t at varying I_d for $C/D = 1.3$ and 2.0.

4.3 Empirical formulas for settlement trough prediction

The modified Gaussian curves were fitted in Matlab to the experimental data collected using GeoPIV. First, in Section 4.3.1, Marshall et al. (2012) Equations (4.3) and (4.4) are used to characterise settlement trough shape parameters, K^* and K^{**}, in dense sand. The results in Section 4.2.2 indicate a non-linear trend of settlement trough shape with C/D in dense sand; to consider this, new relationships are proposed for the parameters of Equations (4.3) and (4.4). Then, the entire dataset of test series 1, M and Z (see Table 4.1) is considered in Section 4.3.2. A new approach to predict the surface and subsurface K^* and K^{**} is presented. This approach accounts for the non-linear trends of the settlement trough parameters with C/D, $V_{l,t}$ and z/z_t, implementing logarithmic equations; soil density is also considered. Finally, Section 4.3.3 analyses the ground volume loss relationship with tunnel volume loss.

4.3.1 A modified approach for width parameters in dense sand

In this section, the settlement data obtained in dense sand are analysed to investigate the effects of C/D and the transition from shallow to deep tunnels. The settlement trough data of centrifuge tests in dense sands (CD13ID90, CD20ID90, CD24ID90, CD44ID90, and CD63ID90) were interpolated with continuous modified Gaussian curves for $V_{l,t} = 0.5-5\%$ ($0.8-5\%$ for CD63ID90). Experimental values of K^* and K^{**}, which are a set of points corresponding to specific values of C/D, $V_{l,t}$ and z/z_t, were obtained. For each centrifuge test, K^* and K^{**} represent scattered points in the space $\left(V_{l,t}, z/z_t, K\right)$. K^* and K^{**} were curve-fitted with the surface described by Equations (2.17) and (2.18) proposed by Marshall et al. (2012), reported again here as Equations (4.3) and (4.4), obtaining scalar values of the trough shape parameters, which are plotted vs. C/D in Figure 4.16. Note that Equations (4.3) and (4.4) are based on the assumptions that x^* and x^{**} vary linearly with z as well as that K_s^* and K_s^{**} have a constant partial derivative with respect to the variable $V_{l,t}$; these approximations were shown to be satisfactory for tunnelling in dense sands by Marshall et al. (2012).

$$K^* = \frac{K_s^* + \left(\partial x^*/\partial z\right)\left(z/z_t\right)}{1 - z/z_t} \qquad K^{**} = \frac{K_s^{**} + \left(\partial x^{**}/\partial z\right)\left(z/z_t\right)}{1 - z/z_t} \tag{4.3}$$

$$K_s^* = K_{s,Vlt}^{*int} + K_{s,Vlt}^{*slope} V_{l,t} \qquad K_s^{**} = K_{s,Vlt}^{**int} + K_{s,Vlt}^{**slope} V_{l,t} \tag{4.4}$$

Results displayed in Figure 4.16 show that the variation of the vertical settlement trough shape with C/D ratio has a non-linear trend, probably due to a transition between shallow and deep tunnels. In clays, Jones (2010) has previously described the non-linear trend of K by means of a logarithmic curve. Therefore, the regression of the trough shape parameter coefficients with C/D was based on logarithmic formulas. This allows for a realistic extrapolation of these parameters in the case of C/D higher than the investigated range. The equations of the interpolating curves

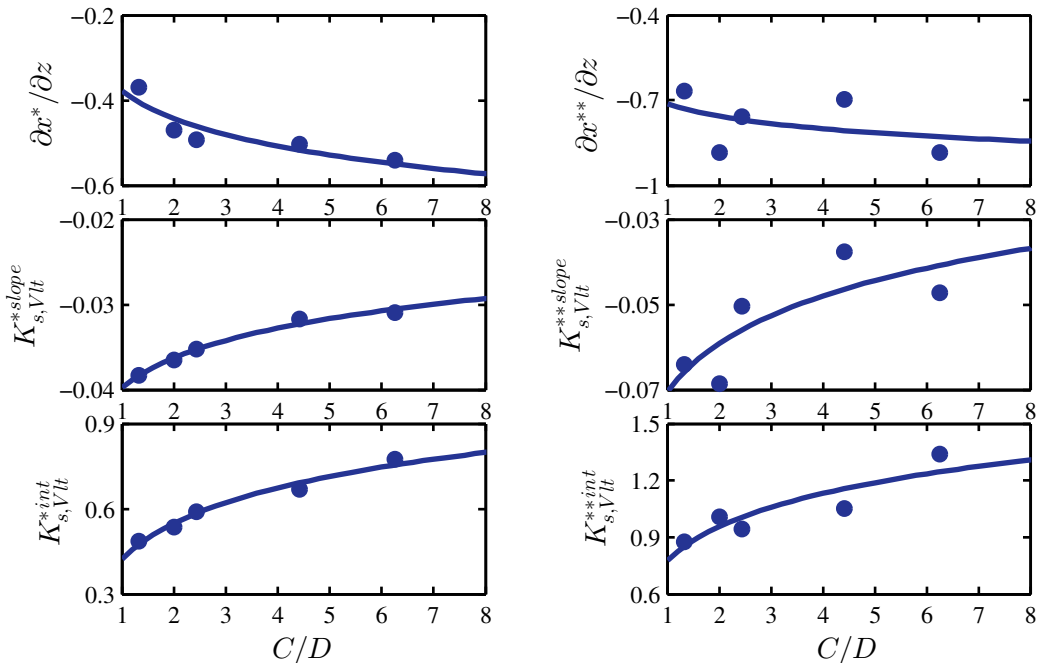

Fig. 4.16 Outcomes of the regression of settlement data in dense sands ($I_d = 90\%$) with Equations (4.3) and (4.4) (markers) and interpolation of the regression data with Equation (4.5) (solid lines).

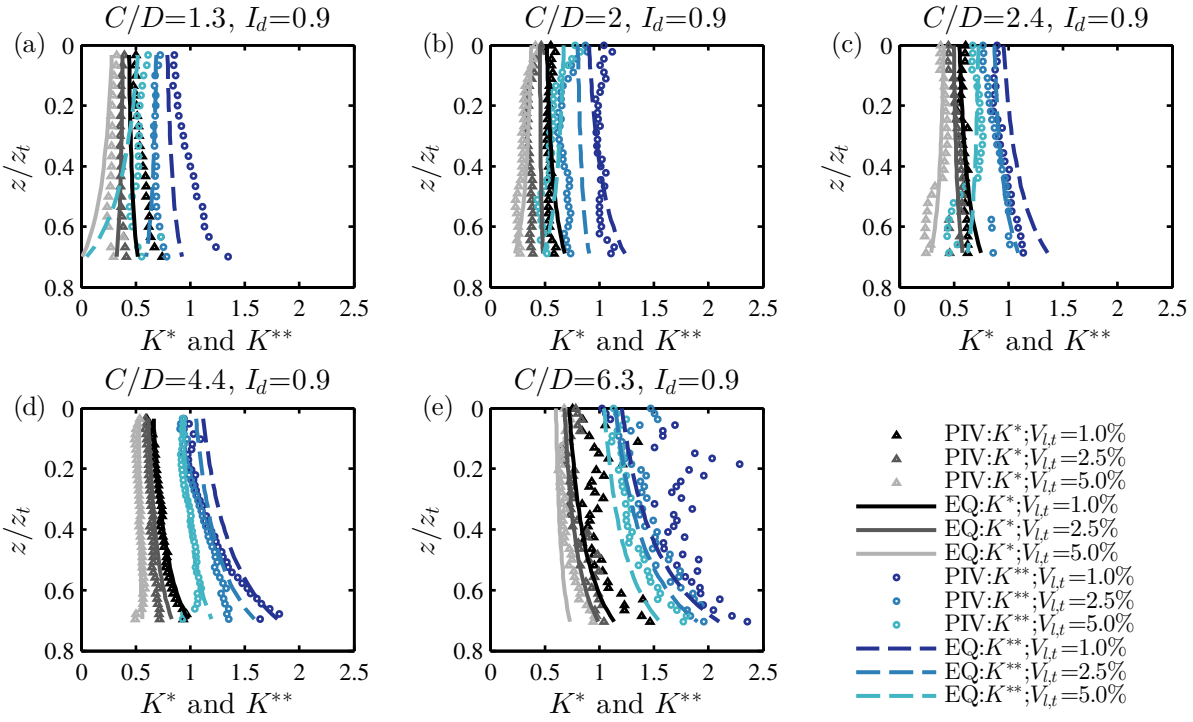

Fig. 4.17 Trough width parameters against depth: comparison between experimental data and predictions obtained using Equations (4.3), (4.4), and (4.5).

plotted in Figure 4.16 are reported in Equation (4.5).

$$\begin{aligned} \partial x^*/\partial z &= -0.094\ln\left[C/D\right]-0.378; & \partial x^{**}/\partial z &= -0.064\ln\left[C/D\right]-0.712 \\ K_{s,Vlt}^{*slope} &= 0.005\ln\left[C/D\right]-0.040; & K_{s,Vlt}^{**slope} &= 0.016\ln\left[C/D\right]-0.070 \\ K_{s,Vlt}^{*int} &= 0.180\ln\left[C/D\right]+0.424; & K_{s,Vlt}^{**int} &= 0.255\ln\left[C/D\right]+0.779 \end{aligned} \tag{4.5}$$

The predictions of Equations (4.3), (4.4), and (4.5) against the centrifuge measurements of K^* and K^{**} are plotted in Figure 4.17 for $V_{l,t} = 1, 2.5, 5\%$ and $z/z_t = 0-0.7$. These formulas compared well with most of the data used for their statistical regression, as shown in Figure 4.17. On the other hand, Figure 4.17(a) displays that a lower accuracy is achieved for the dataset CD13ID90, especially at high volume losses, because of a qualitatively different variation of the width parameters K^* and K^{**} with depth; this results in K^* and K^{**} significantly lower than the experimental values at the subsurface level and unrealistically close to a null value. It is interesting to highlight that similar results were obtained by the regression of Marshall et al. (2012) assuming a linear variation of the trough shape parameters. In the following Section 4.3.2, a different set of equations is presented, overcoming this drawback at low cover-to-diameter ratios.

4.3.2 A new approach for width parameters in sands

Despite the research in recent years on tunnelling in sands, empirical formulas to predict the settlement troughs accounting for the soil density are not available. This type of solution would be useful both to tunnel engineers and for the analysis of centrifuge test data of tunnel-structure interaction, which are often collected in dry silica sand. In this section, a new approach is proposed for the assessment of the settlement trough width as a function of I_d, C/D, $V_{l,t}$, and z/z_t. It is based on the regression of the entire dataset of tests (series 1, M, Z).

In this approach Equation (4.3) is adopted to describe K^* and K^{**}; however, to improve the approach performance the following formulas were assumed

$$\begin{aligned} K_s^* &= K_{s,Vlt}^{*int,ln} + K_{s,Vlt}^{*slope,ln}\ln\left[V_{l,t}+1\right]; & \frac{\partial x^*}{\partial z} &= \frac{M^*}{1+z/z_t}; \\ K_s^{**} &= K_{s,Vlt}^{**int,ln} + K_{s,Vlt}^{**slope,ln}\ln\left[V_{l,t}+1\right]; & \frac{\partial x^{**}}{\partial z} &= \frac{M^{**}}{1+z/z_t}; \end{aligned} \tag{4.6}$$

that account for the non-linear trends of x^*, x^{**}, K_s^*, and K_s^{**} shown in Section 4.2.2 with logarithmic functions. The partial derivatives of x^* and x^{**} were obtained assuming

$$\begin{aligned} x^* &= k_1^* + k_2^* \ln\left[1+\frac{z}{z_t}\right] \quad \rightarrow \quad \frac{\partial x^*}{\partial z} = \frac{k_2^*}{z_t\left(1+\frac{z}{z_t}\right)} = \frac{M^*}{\left(1+\frac{z}{z_t}\right)} \\ x^{**} &= k_1^{**} + k_2^{**} \ln\left[1+\frac{z}{z_t}\right] \quad \rightarrow \quad \frac{\partial x^{**}}{\partial z} = \frac{k_2^{**}}{z_t\left(1+\frac{z}{z_t}\right)} = \frac{M^{**}}{\left(1+\frac{z}{z_t}\right)} \end{aligned} \tag{4.7}$$

where k_1 and k_2 are functions not dependent on z. Note that Equations (4.3) and (4.6) are able to describe the relationships $K^* = K^*\left[V_{l,t}, z/z_t\right]$ and $K^{**} = K^{**}\left[V_{l,t}, z/z_t\right]$ with six coefficients (M^*; M^{**}; $K_{s,Vlt}^{*slope,ln}$; $K_{s,Vlt}^{**slope,ln}$; $K_{s,Vlt}^{*int,ln}$; $K_{s,Vlt}^{**int,ln}$) that are dependant on the remaining variables C/D and I_d. The regression of centrifuge data was performed as follows.

- For each test, the measured settlement troughs (for $V_{l,t} = 0.5-5\%$ if $C/D < 6.3$ and $V_{l,t} = 0.8-5\%$ if $C/D = 6.3$) were curve-fitted with modified Gaussian curves and their K^* and K^{**} were stored in memory with the associated values of I_d, C/D, $V_{l,t}$, and z/z_t.
- Subsequently, for each test, the data in the format $K^{*,**} = K^{*,**}\left[V_{l,t}, z/z_t\right]$ was interpolated with surface-type functions described by Equations (4.3) and (4.6); a vector consisting of six elements, corresponding to the surface coefficients, was obtained.
- At the end, a set of n values, which are a function of C/D and I_d, was obtained for each coefficient M^*; M^{**}; $K_{s,Vlt}^{*slope,ln}$; $K_{s,Vlt}^{**slope,ln}$; $K_{s,Vlt}^{*int,ln}$; $K_{s,Vlt}^{**int,ln}$, where n is the total number of tests.

The efficiency of the new approach (Equations (4.3), (4.6)) and the modified approach (Equations (4.3), (4.4)) is compared in Table 4.2, which reports the achieved coefficients of determination. Note that a good curve-fitting is associated with R^2 close to unity. Overall, the two sets of equations provided similar performance when interpolating the data of a given test. The advantages of adopting Equations (4.3) and (4.6) are illustrated in the latter part of this section.

The results of the regression detailed in the above bullet list that used Equations (4.3) and (4.6) are plotted in Figure 4.18 with markers. The charts report the coefficients of Equation (4.6) against the C/D ratio for varying soil density (I_d is plotted using different colours and marker-shapes). Based on the outcomes of Section 4.3.1, which illustrated a logarithmic reduction of the width parameter coefficients with C/D due to a transition from shallow to deep tunnels, it is possible to assume that

$$\kappa = g\left[I_d\right] \ln\left[C/D\right] - h\left[I_d\right] \tag{4.8}$$

where κ is used to indicate a generic coefficient M^*, M^{**}, $K_{s,Vlt}^{*slope,ln}$, $K_{s,Vlt}^{**slope,ln}$, $K_{s,Vlt}^{*int,ln}$, $K_{s,Vlt}^{**int,ln}$, and $g\left[I_d\right]$, $h\left[I_d\right]$ are functions of I_d. Considering that the settlement trough width decreases with soil density for relatively deep tunnels (see Section 4.2.2.2), for the sake of simplicity

Table 4.2 Coefficient of determination, R^2, achieved with modified and new approaches by curve-fitting data of each test.

C/D	I_d	$R^2_{K^*}$			$R^2_{K^{**}}$		
		Modified Approach	New Approach	Variation (%)	Mod. Approach	New Approach	Variation (%)
1.3	0.3	0.92	0.93	+1	0.91	0.93	+2
1.3	0.5	0.92	0.97	+5	0.92	0.97	+5
1.3	0.9	0.92	0.96	+4	0.94	0.96	+3
2.0	0.3	0.96	0.93	-2	0.96	0.95	-1
2.0	0.3	0.91	0.92	+2	0.89	0.93	+4
2.0	0.5	0.88	0.93	+6	0.89	0.95	+7
2.0	0.7	0.88	0.88	0	0.89	0.91	+2
2.0	0.9	0.94	0.96	+2	0.94	0.96	+2
2.5	0.3	0.83	0.90	+8	0.83	0.92	+8
2.4	0.9	0.69	0.40	-29	0.69	0.41	-28
4.5	0.3	0.90	0.93	+3	0.92	0.94	+3
4.5	0.5	0.90	0.93	+3	0.88	0.92	+4
4.4	0.9	0.92	0.86	-6	0.95	0.93	-2
6.3	0.3	0.92	0.93	+1	0.90	0.89	0
6.3	0.5	0.88	0.90	+2	0.90	0.91	+1
6.3	0.9	0.83	0.87	+4	0.85	0.84	-2

the interpolation of the markers in Figure 4.18 with Equation (4.8) was performed assuming a linear variation of the functions $g[I_d]$ and $h[I_d]$ with density. This resulted in the set of formulas in Equation (4.9). The logarithmic curves of the interpolating Equation (4.9) are plotted for comparison in Figure 4.18. Although this method does not account for the complex pattern of variation of the markers corresponding to $C/D = 2.0$, which is due to the variation of the arching mechanism with soil density, overall Equation (4.9) provides a good interpolation.

$$\begin{aligned}
M^* &= (+0.81I_d - 0.93)\ln[C/D] - 0.60I_d - 0.07 \\
M^{**} &= (+1.50I_d - 1.55)\ln[C/D] - 0.96I_d - 0.28 \\
K^{*slope,ln}_{s,Vlt} &= (+0.35I_d - 0.30)\ln[C/D] - 0.22I_d + 0.07 \\
K^{**slope,ln}_{s,Vlt} &= (+0.41I_d - 0.35)\ln[C/D] - 0.22I_d - 0.01 \\
K^{*int,ln}_{s,Vlt} &= (-0.84I_d + 0.95)\ln[C/D] + 0.45I_d + 0.07 \\
K^{**int,ln}_{s,Vlt} &= (-1.16I_d + 1.36)\ln[C/D] + 0.47I_d + 0.42
\end{aligned} \tag{4.9}$$

To validate Equations (4.3), (4.6), and (4.9) against the centrifuge measurements, the empirical predictions and the measured K^* and K^{**} values are plotted in Figure 4.19 for $V_{l,t} = 1, 2.5, 5\%$, $I_d = 0.3$ and 0.9 (loose and dense sands), and $z/z_t = 0 - 0.7$. Overall, the empirical predictions are shown to provide a satisfactory match with both benchmark K^* and K^{**}; additionally, it can be seen from results in Figure 4.19 that the proposed formulas are able describe the variation

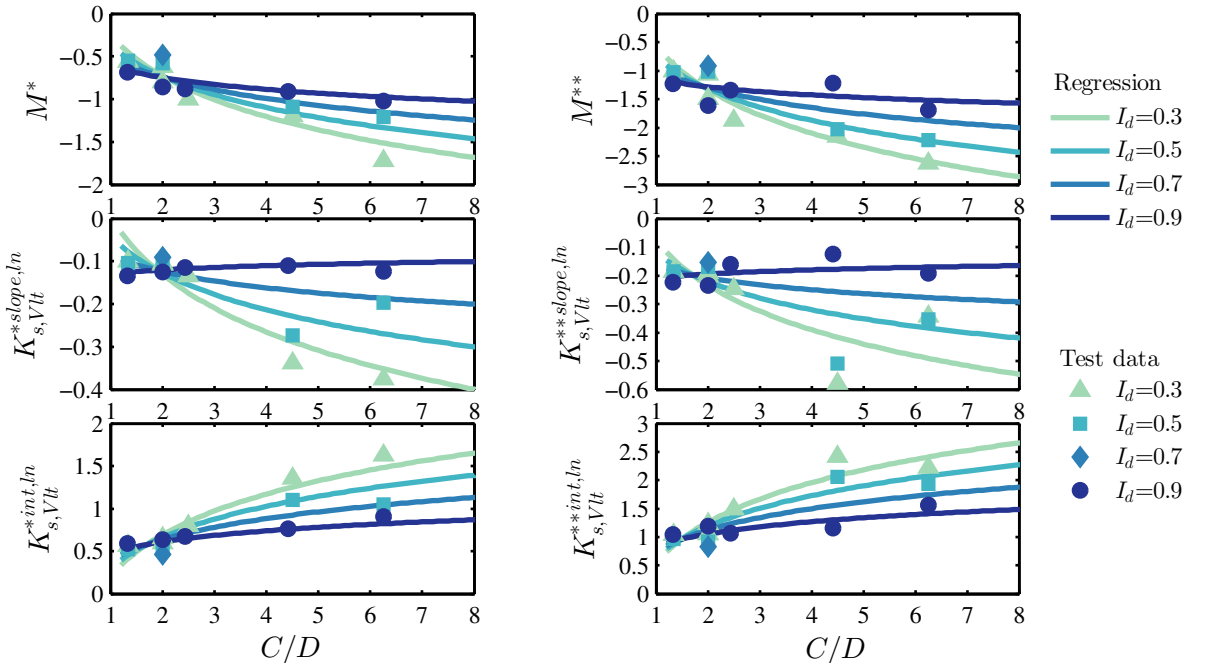

Fig. 4.18 Outcomes of settlement trough parameter regression using new approach for $I_d = 0.3, 0.5, 0.7, 0.9$.

of settlement trough width with soil density. Furthermore, there is a significant improvement in the prediction of subsurface K^* and K^{**} at $C/D = 1.3$ with the new approach, comparing Figures 4.17 and 4.19. Therefore, the main drawback at low cover-to-diameter ratios of the approach shown in Section 4.3.1 is overcome. It is possible that the improved performance may be due to the the assumption of logarithmic trends of the main variables, which takes into account the fact that [i] the process of soil stiffness degradation with strains is non-linear and [ii] the deeper the tunnel, the more the displacement mechanism should converge towards an elastic pattern. To conclude, Equations (4.3), (4.6), and (4.9) may be used to predict surface and subsurface settlement trough shape parameters in sands for loose, medium-dense and dense sands.

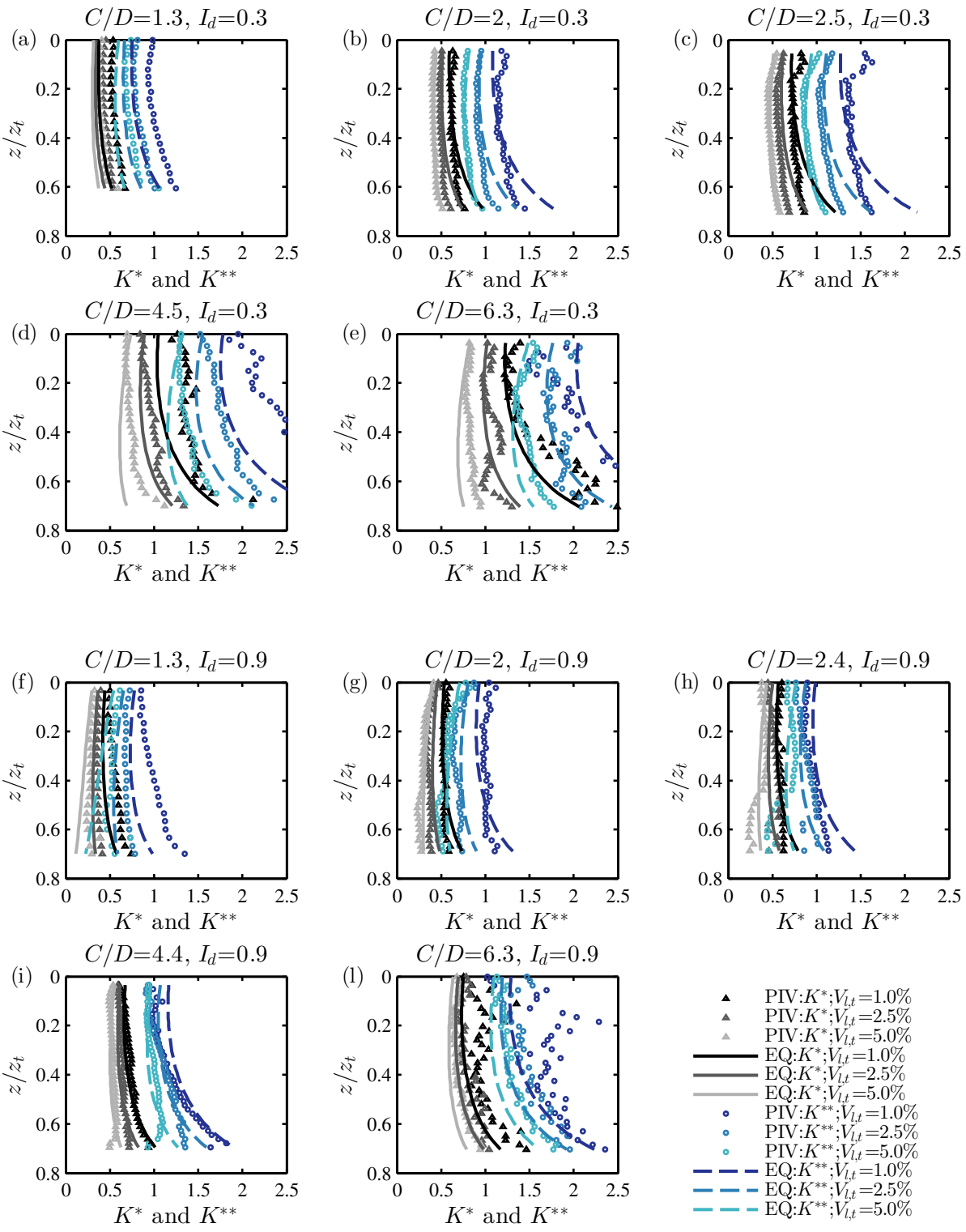

Fig. 4.19 K^* and K^{**} against depth for $I_d = 0.3$ and 0.9 compared with predictions using Equations (4.3), (4.6), and (4.9).

4.3.3 Relationship between soil and tunnel volume loss

In sands, soil and tunnel volume loss differ because of the contractive/dilative strains that occur. Therefore, it is important to be able to relate $V_{l,s}$, which is the normalised magnitude of the settlement trough, to $V_{l,t}$. If $V_{l,s}$, K^* and K^{**} are known, the modified Gaussian curve is fully defined.

The relationship between soil and tunnel volume loss was investigated by Marshall et al. (2012) and Zhou (2014). Note that these authors reported a reduction of soil movements at the front wall of approximately $10-15\%$ compared to the middle plane of the strongbox (i.e. $V_{l,s}$ from GeoPIV data are slightly underestimated). However, it is shown in the following that the variability of the relationship $V_{l,s}-V_{l,t}$ with soil density and cover-to-diameter ratio is greater than this rate of disturbance; therefore, in this section, the effects of the front wall friction are neglected .

Marshall et al. (2012) and Zhou (2014) illustrated that the relationship $V_{l,s}-V_{l,t}$ is highly affected by the volumetric strains induced by soil shearing. Interestingly, it was noticed that $V_{l,s}$ may be greater or lower than $V_{l,t}$ depending on $V_{l,t}$, C/D and volumetric-shear strain relationship (which is affected by both confining stresses and soil density) . In general, it was suggested that the ratio $V_{l,s}/V_{l,t}$ [i] increases with C/D, whereas [ii] it decreases with $V_{l,t}$ and I_d; these phenomena are, respectively, due to a lower shear strain level associated with high C/D, greater dilation in denser sands, and higher shear strains at high volume losses (the reasons for the impact of contractive/dilative soil behaviour on soil volume loss are sketched Figure 4.20).

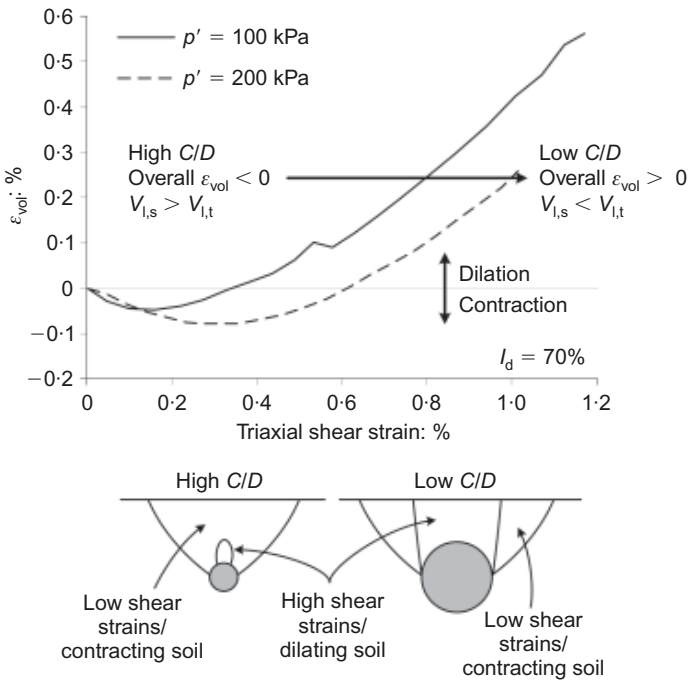

Fig. 4.20 Explanation of the reasons for contractive/dilative behaviour effects on soil volume loss [Marshall et al. (2012)].

This framework allows the interpretation of the full dataset of measured data, shown in Figure 4.21. In this figure, both the soil volume loss at $z/z_t = 0$ and 0.5 are reported, respectively, with solid and dashed lines. Note that $V_{l,s}$ greater and lower than $V_{l,t}$ are associated with an average cumulative contractive and dilative soil behaviour, respectively, over the entire tunnel ground loss process; a unit first derivative of these curves (i.e. curve parallel to 1:1 line) is associated with an incremental average volumetric strain equal to zero for the given volume loss increment $\Delta V_{l,t}$; a first derivative of the relationship $V_{l,s}/V_{l,t}$ greater/lower than unity is given by an average incremental contractive/dilative volumetric strain within the soil mass.

Results display good consistency and agreement with points [i] and [ii]. Additionally, $V_{l,s}$ is greater at $z/z_t = 0$ than at the subsurface level $z/z_t = 0.5$ for all the tests (except CD13ID90 at $V_{l,t} > 5$); this indicated that the overall soil behaviour within the range $z/z_t = 0 - 0.5$ is contractive regardless of the soil density because of low shear strains, whereas most dilation is concentrated at $z/z_t > 0.5$ (i.e. near the tunnel and the tunnel crown). For test CD13ID90 at $V_{l,t} > 5$, when the ultimate critical state is reached at the subsurface level (i.e. unit first derivative of $V_{l,s} - V_{l,t}$ at $z/z_t = 0.5$ and an increase of tunnel inner pressure shown in Figure 4.2), $V_{l,s}$ at $z/z_t = 0$ is lower than at $z/z_t = 0.5$ because of large strains within the entire ground mass (see Figure 4.4).

Finally, it should be noted that $V_{l,s} < V_{l,t}$ at high volume losses for the shallowest tunnels in loose sands (CD13ID30, CD20ID30, and CD25ID30), as displayed by the left plot of Figure 4.21. Considering that the shearing of loose soils should results in contractive strains (this was confirmed by GeoPIV assessment of strains for these tests), soil ground loss should not be lower than tunnel ground loss. It is likely that these outcomes are due to friction at the Perspex wall and unexpected phenomena very close to the model tunnel for large magnitudes of tunnel contraction. Overall, the results of the entire dataset are consistent for $V_{l,t} < 3\%$, which is the range of greatest interest to tunnel engineers.

Empirical formulas (Gaussian and modified Gaussian curves) for the prediction of tunnelling-induced settlement troughs in sands require a relationship as $V_{l,s} = f\left[V_{l,t}, z/z_t, C/D, I_d\right]$. To account for the effects of volumetric strains, Marshall et al. (2012) and Zhou (2014) proposed the use of Equation (2.19), which is an empirical formula to assess $V_{l,s} - V_{l,t}$ (limited to the dataset of test series M and Z). However, considering that the equation should have an intercept equal to zero (i.e. $V_{l,s} = 0$ for $V_{l,t} = 0$), Equation (2.19) can be manipulated to obtain

$$V_{l,s}^{exp} = (C/D)^{\beta} c_b \left(\exp\left[-\left(\frac{c_c}{c_d} \right)^2 \right] - \exp\left[-\left(\frac{V_{l,t} + c_c}{c_d} \right)^2 \right] \right) \quad \text{at} \quad z/z_t = 0 \qquad (4.10)$$

where the coefficients depend on the type of sandy soil and its relative density. For dry silica sand, they proposed β, $c_b = 3.7$, $c_c = 2.8$, and $c_d = 3.6$, whereas β is a linear function of relative density. Note that a coefficient was removed from Equation (4.10) by introducing the condition $V_{l,s} = 0$ for $V_{l,t} = 0$; furthermore, Equation (4.10) prevents inconsistencies resulting from the curve-fitting of data (e.g. $V_{l,s} > 0$ for $V_{l,t} = 0$).

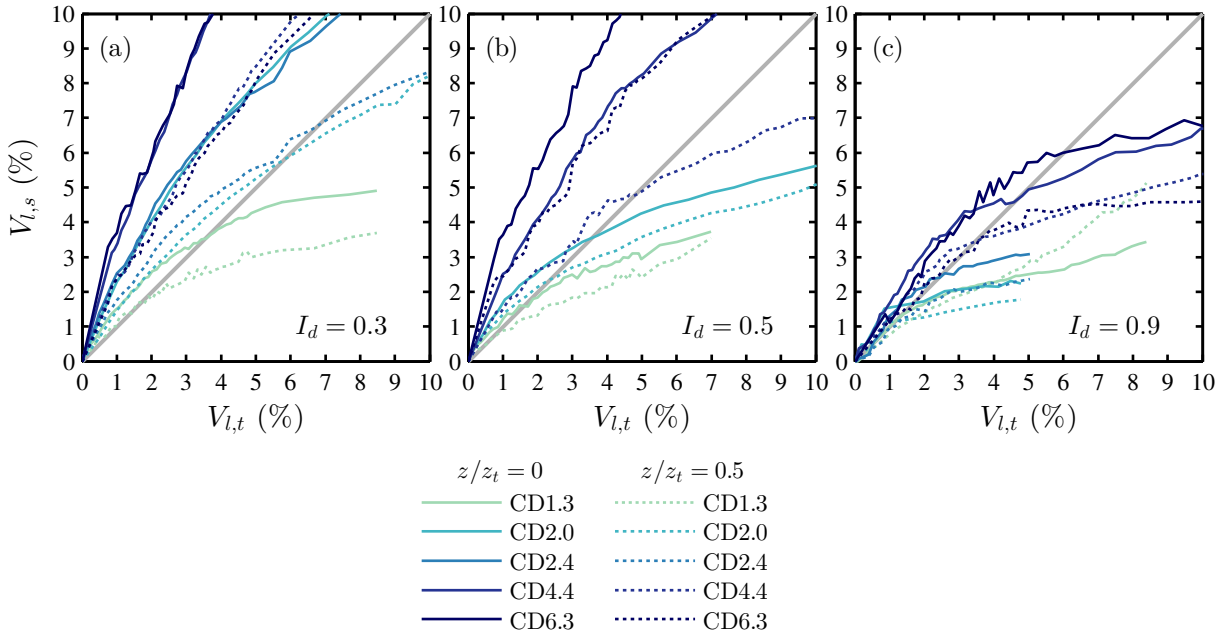

Fig. 4.21 $V_{l,s} - V_{l,t}$ for $z/z_t = 0$ and 0.5.

The approach defined by Equation (4.10) was extended to the entire dataset. Preliminary analyses displayed that, for loose samples, the description of the experimental $V_{l,s} - V_{l,t}$ curves required an additional coefficient, λ, for the volume loss. Therefore, the equation used for the curve-fitting of the experimental data is

$$V_{l,s}^{exp} = (C/D)^{\beta} c_b \left(\exp\left[-\left(\frac{c_c}{c_d} \right)^2 \right] - \exp\left[-\left(\frac{\lambda V_{l,t} + c_c}{c_d} \right)^2 \right] \right) \quad \text{at} \quad z/z_t = 0 \tag{4.11}$$

Because the soil used for test series 1, M and Z is dry silica sand, the value of coefficients c_b, c_c, and c_d were assumed as in Equation (4.10). The parameters λ and β were assumed to be polynomial curves of C/D and I_d. The regression of the dataset, which was limited to the range $V_{l,t} = 0 - 5\%$, resulted in the empirical Equation (4.12), accounting for both C/D and I_d. As displayed in Figure 4.22, the predicted $V_{l,s} - V_{l,t}$ values (markers) agree satisfactorily with experimental data (lines); furthermore, the regression of the dataset resulted in $R^2 = 0.98$.

$$V_{l,s}^{exp} = (C/D)^{\beta} 3.7 \left(\exp\left[-\left(\frac{2.8}{3.6} \right)^2 \right] - \exp\left[-\left(\frac{\lambda V_{l,t} + 2.8}{3.6} \right)^2 \right] \right) \quad \text{at} \quad z/z_t = 0$$
$$\beta = 2.81 - 1.99 I_d - 0.38 C/D + 0.12 I_d C/D + 0.035 (C/D)^2 \tag{4.12}$$
$$\lambda = 0.88 + 0.51 I_d - 0.12 C/D$$

It is interesting to point out that Equation (4.12) does not account for the effects of the confining stresses because the tunnel cover is normalised by C/D. Therefore, engineer judgements should be used before applying Equation (4.12) to real constructions.

Finally, in Appendix A, a set of equations is provided by Equation (A.13) to relate the degrees of freedom of the modified Gaussian curve defined in Equation (2.15) (α, i, u_{max}) to the parameters of the empirical method (K^*, K^{**}, $V_{l,s}$) proposed in Section A.1. Furthermore, Figure A.1-A.5 compare settlement troughs measured during centrifuge tests for $I_d = 0.3$ and 0.9 and empirical predictions obtained with Equation (A.13). Despite the scatter between experimental data and modified Gaussian curves, Equation (A.13) capture part of the complex behaviour of tunnelling-induced settlements in sands than was not described by previous research.

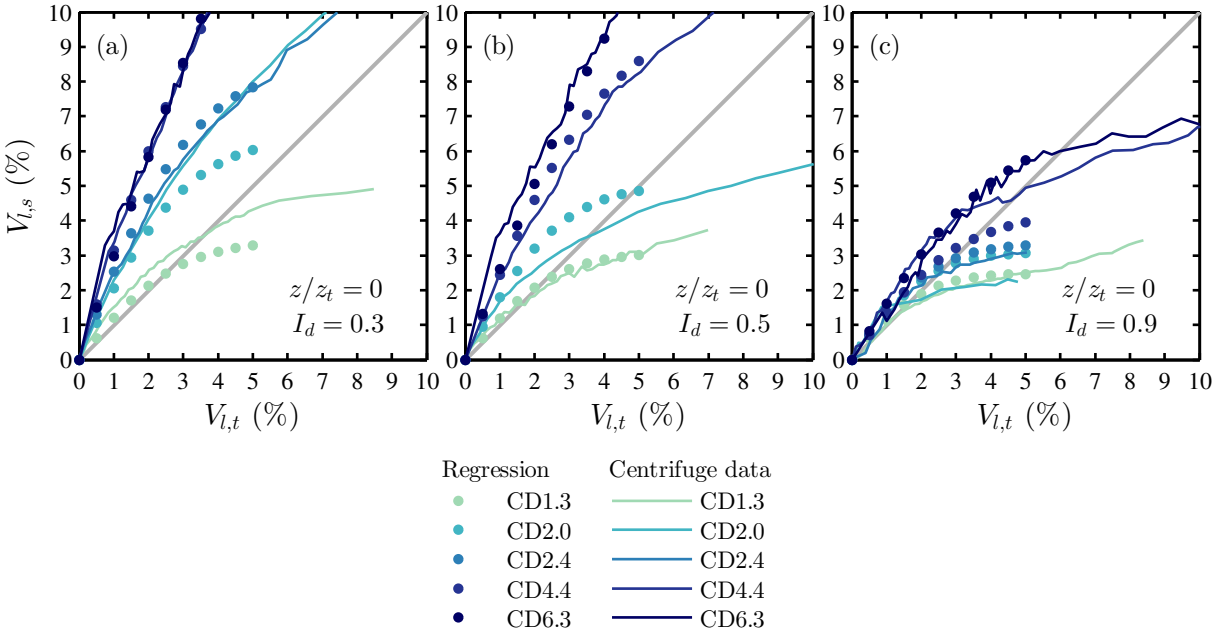

Fig. 4.22 Outcomes of the regression analysis of $V_{l,s} - V_{l,t}$ at $z/z_t = 0$.

4.4 Discussion of centrifuge modelling of tunnel volume loss

This discussion aims to look more closely at the impact of different tunnel modelling techniques during centrifuge tests on the greenfield ground movements. In particular, the data collected by Boonsiri and Takemura (2015), Marshall et al. (2012), Zhou et al. (2014) and this research, based on centrifuge experiments conducted using a dry, fine-grained silica sand, are compared to illustrate the differences in the results obtained with different model tunnels. The Boonsiri and Takemura (2015) experiment included a rigidly lined model tunnel that imposes a concentric deformation pattern to the tunnel periphery (resulting in a displacement control boundary condition); the model tunnel used by Marshall et al. (2012), Zhou et al. (2014) and this research consisted of a fluid-filled flexible latex membrane, with no strict imposition of the lining deformation pattern during tunnel volume loss (achieved by water extraction). In the latter

case, the equilibrium condition between the soil and the fluid-filled membrane controls the resulting shape of the tunnel lining at every stage of tunnel volume loss.

In their paper, Boonsiri and Takemura (2015) showed that the obtained greenfield data fits well to Moh et al. (1996) Equation (2.14), which was based on settlement data from a single tunnelling project in Taipei and, therefore, is not able to account for the effect of the range of influencing parameters; on the other hand, Marshall et al. (2012) Equations (2.17) and (2.18) did not provide a good prediction of the dataset presented by Boonsiri and Takemura (2015). It is worth investigating the possible reasons that could explain why the results of these two series of tests differ. The discussion focuses on the data obtained at a volume loss of 2% since, among the two values of volume loss considered by Boonsiri and Takemura (2015), this is the most applicable to realistic conditions (the other volume loss being 14% which is higher than reasonably expected).

Gaussian and modified Gaussian curves were fitted to the data provided by Boonsiri and Takemura (2015) for $C/D = 1.5$ and 2.5; all curve fitting was done using standard least-squares regression techniques within Matlab. In Figure 4.23(a), the resulting values of K and K^*, labelled "curve-fitting" in the chart, are compared with the data reported in their paper. The obtained values of K and K^* match reasonably well to the data provided by the authors (compare markers). The estimations of K^* based on Equations (2.17) and (2.18) suggested by Marshall et al. (2012) is also plotted. Interestingly, there is an acceptable agreement between the centrifuge outcomes and the equation prediction for the tunnel with $C/D = 2.5$, whereas the prediction of subsurface values is unsatisfactory for $C/D = 1.5$. As suggested by Boonsiri and Takemura (2015), these differences should be attributed to different boundary conditions at the tunnel resulting from the adopted modelling technique.

Given that the soil used in the two series of experiments was relatively similar, the data in Figure 4.23(a) would suggest that the boundary conditions of the mechanical tunnel are responsible for the wider settlement troughs above the tunnel compared to those obtained from the water-filled membrane, which were characterized by a localised narrow collapse at the tunnel crown for shallow tunnels in dense sand, as illustrated in Figure 4.3. The data in Figures 4.3 and 4.4 indicate that very little ground movement occurs at the sides of the tunnel if a concentric displacement pattern is not imposed on the tunnel lining. The impact of imposed displacements in these regions in the Boonsiri and Takemura (2015) tests must relate to the observation of wider settlement troughs, especially at depths nearer the tunnel. Moreover, Figure 4.23(a) illustrates that the profiles of K with depth measured by Boonsiri and Takemura (2015) are very similar at both C/D ratios (compare red and black markers). The profiles estimated according to Marshall et al. (2012) are noted to change in both shape and magnitude. Therefore, using a concentrically contracting tunnel appears to result in K distributions that are less affected by the C/D ratio than when the tunnel boundary condition causes volume loss deformations concentrated at the tunnel crown.

There are also some important similarities between the deformation patterns predicted by both tunnel modelling techniques. The two datasets suggest a similar consequence of the C/D

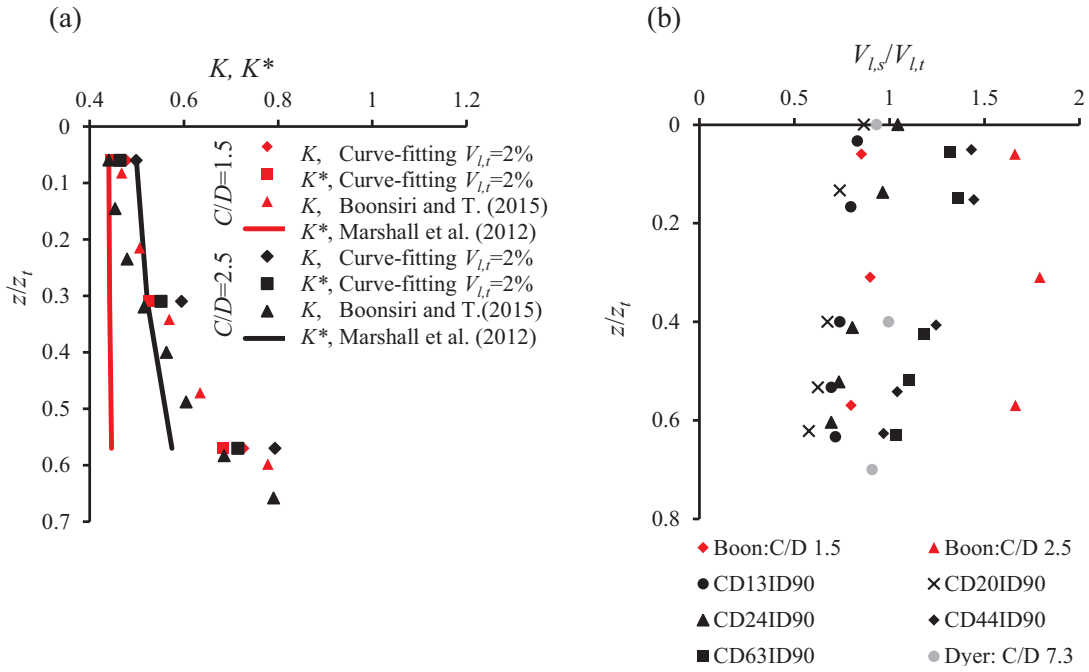

Fig. 4.23 (a) Variation of settlement width parameters with normalized depth; (b) Ratio between soil and tunnel volume loss with normalized depth at different values of C/D in dense sands.

ratio. Figure 4.4 shows the normalised vertical settlements ($u_z/(V_{l,t}R)$, which allows comparison of displacements between tests with different sized tunnels) for varying C/D ratios. This figure illustrates that the chimney-like mechanism suggested for coarse soils by Cording (1991) describes the deformation pattern induced by shallow tunnels ($C/D < 4$), whereas for tunnels with $C/D > 4$, the ground movements spread outwards from the tunnel without a zone of major settlement at the tunnel centreline. Boonsiri and Takemura (2015) suggest that the chimney-like mechanism is also more noticeable for $C/D = 1.5$ than for $C/D = 2.5$.

Finally, the ratio between the soil volume loss, $V_{l,s}$, and the tunnel volume loss, $V_{l,t}$, was computed for the settlement curves provided by Boonsiri and Takemura (2015) and is compared against other available data in Figure 4.23(b). This ratio would be equal to unity for tunnels in undrained, constant volume soils. In sands, the variation from unity of $V_{l,s}/V_{l,t}$ at a certain depth is due to the cumulative effect of the soil volumetric strains beneath that level. Thus, to fully understand the relationships in Figure 4.23(b), it is necessary to account for the volumetric strain distribution within the soil, which is related to the magnitude of shear strain and confining stress. The ratio $V_{l,s}/V_{l,t}$ is compared in Figure 4.23(b) with data obtained from Dyer et al. (1996), and centrifuge tests CD13ID90, CD20ID90, CD24ID90, CD44ID90, and CD63ID90. Both the results collected by Boonsiri and Takemura (2015) and the data used in this research illustrate an increase of $V_{l,s}/V_{l,t}$ with C/D for a given value of $V_{l,t}$. This phenomenon was explained qualitatively in Marshall et al. (2012); for a given tunnel diameter and tunnel volume loss, since the magnitude of shear strains in relatively shallow tunnels is greater than for deeper tunnels, the soil reaches a dilatant state at lower magnitudes of tunnel volume loss for relatively

shallow tunnels compared to deeper tunnels. However, the value of $V_{l,s}/V_{l,t}$ for the Boonsiri and Takemura (2015) test with $C/D = 2.5$ is quite high when compared with data for deeper tunnels ($C/D > 4$). This is probably due to the fact that the concentric displacement control tunnel modelling technique induces low-level shear strains in the soil around the tunnel, which cause contractive soil behaviour within an extended area around the tunnel. This is supported by the data in Figure 4.23(a), where the subsurface settlement curves obtained with the mechanical model tunnel are wider than those achieved with the water-filled membrane, confirming that a greater volume of soil undergoes shearing around the tunnel for the concentric displacement control tunnelling technique. The larger zone of soil affected by the uniform radial contraction of the mechanical tunnel would undergo lower levels of shearing than the more localised zone in the tests using the water-filled membrane. This results in larger values of $V_{l,s}/V_{l,t}$ for Boonsiri and Takemura (2015) both at the surface and subsurface. Furthermore, their ratio $V_{l,s}/V_{l,t}$ is fairly constant with depth, indicating that most of the contractive behaviour of the soil is localised at or below the level of the tunnel. On the other hand, the water-filled flexible lining model tunnel results in negligible strains at the tunnel invert and springline (illustrated in Figure 4.4), and the displacement mechanism is characterized by bands of high shear strains starting from the shoulders of the tunnel and developing towards the surface (Marshall et al., 2012). Similar strain distributions characterised by bands of high shear strains at the tunnel shoulder were suggested by Cording and Hansmire (1975) and Schuller and Schweiger (2002). This explains the decrease of $V_{l,s}/V_{l,t}$ with z/z_t for the data sets in Figure 4.23(b).

In general, it is not clear which boundary condition is more appropriate for the simulation of tunnelling in sands. However, previous researchers have suggested an oval-shaped (i.e. eccentric) tunnel volume loss distribution in clays resulting in small displacements at the tunnel springline and negligible displacements at the invert (Loganathan and Poulos, 1998). This oval-shaped mechanism was successfully implemented by Cheng et al. (2007) in a numerical model of tunnelling-induced movements based on a displacement controlled approach (i.e. displacement boundary conditions were imposed at the tunnel periphery). This displacement controlled approach has been applied in several papers regarding tunnel-structure interaction. Furthermore, the coefficient of lateral earth pressure, K, is generally lower in sands than in clays, which suggests that horizontal movements at the tunnel springline should be lower in sands than in clays. Therefore, inducing a uniform radial tunnel contraction (with equal contraction at the tunnel crown, springline and invert) may not be realistic. It would be interesting to evaluate the trend of settlement trough shape (i.e. K) and $V_{l,s}/V_{l,t}$ with the methodology adopted by Boonsiri and Takemura (2015) for $C/D > 2.5$ to further study the effects of differing tunnel modelling techniques.

4.5 Conclusions

Results showed that the displacement mechanism in sands is very complex, and the effects of relative tunnel depth and soil density on the problem are correlated. The following conclusions can be drawn.

- Modified Gaussian curves provided a better fit to the settlement data compared to Gaussian curves; the additional degree of freedom allows for an increased versatility necessary in the case of narrow settlement troughs. However, standard Gaussian curves may be representative of wide surface settlements induced by deep tunnels ($C/D > 4$).

- The ground reaction curves were measured during centrifuge tests. The relative reduction of the tunnel pressure ($1 - \sigma_t/\sigma_{t,0}$) increases with soil density; additionally, this relative reduction is higher at low-medium volume losses ($V_{l,t} < 2-3\%$) and lower at high volume losses ($V_{l,t} > 2-3\%$) for relatively shallow tunnels than deep tunnels. Finally, the greater C/D and/or the looser the soil, the higher the $V_{l,t}$ needed to fully mobilise the soil strength, corresponding to the minimum σ_t. This relationship is particularly influenced by the soil density.

- The vertical and horizontal displacement mechanisms are notably complex and correlated; it is demonstrated in this work that the displacement mechanisms are the consequences of the soil's capability for arching. Soil arching was studied by analysing the reaction curves, displacements, and strain distributions. A new framework for a qualitative soil arching assessment in the case of tunnelling was proposed.

- Maximum settlement at the tunnel centreline increases with $V_{l,t}$, decreases with C/D, and reduces with I_d both at the surface and subsurface levels. For shallow tunnels they are lower at the surface than at the normalised depth $z/z_t = 0.5$, whereas the scatter between the two depths is negligible for deep tunnels ($C/D > 4$). Note that the increment rate with $V_{l,t}$ is significantly non-linear in dense sands and approximately linear in loose sands.

- In general, the settlement field width increased with the increase in C/D ratio whereas it decreased with increase in $V_{l,t}$. However, the interpolation of settlement data with modified Gaussian curves indicated a non-linear trend of settlement trough shape parameters with C/D (the variation rate decreases with increase in tunnel depth), which suggests a transition between shallow and deep tunnels within the investigated range.

- The effect of soil density on settlement trough width is negligible for relatively shallow tunnels ($C/D = 1-1.5$), non-linear for intermediate tunnels ($C/D = 2-2.5$), and induced a significant widening of the settlements for deep tunnels ($C/D > 4$).

- Based on the Marshall et al. (2012) framework, a set of equations in which the coefficients have logarithmic trends with C/D was proposed to estimate settlement trough shape parameters in dense sands. Despite good performance for deep tunnels, the Marshall et al.

(2012) method may not be fully adequate for shallow tunnels ($C/D = 1.3$) at high volume loss.

- To overcome the drawback highlighted for the Marshall et al. (2012) method and to account for the influence of soil density, a new empirical method was defined to predict the width parameters of modified Gaussian curves; the proposed equations assume non-linear variations of the inflection point offsets with the physical parameters of the problem (C/D,I_d,$V_{l,t}$). Although the new set of equations does not capture the full complexity of the problem, it is able to describe the main variations in settlement trough width parameters.
- An empirical relationship between $V_{l,s}$ and $V_{l,t}$ at the surface was suggested.
- Compared to a fluid-filled flexible membrane, a rigid boundary model tunnel results in wider settlement troughs, which do not vary in shape considerably with changes in relative tunnel depth, and can result in higher ratios between the area of the settlement troughs and the tunnel ground loss. In general, the boundary conditions used to simulate tunnel ground loss have a significant impact on the settlement mechanism; rigid model tunnels with uniform contraction are not appropriate for a realistic modelling of tunnelling in sands.

The results of this chapter allow achieving a better understanding of tunnelling in sands, especially with respect to centrifuge modelling, which is often used to study the effects of tunnelling on buried infrastructure and buildings. In general, the outcomes of this research suggest that the problem of tunnelling in cohesionless soil is highly non-linear. Therefore, generalising the results of studies based on a few case studies or tests may lead to erroneous predictions.

Chapter 5

Analytical and semi-analytical prediction of ground movements due to tunnels in sands

Excavation of shallow tunnels in urban areas is becoming increasingly important. To prevent possible structural damage, it is necessary to assess the magnitude and distribution of tunnelling-induced ground movements. Analytical and semi-analytical solutions can provide an efficient way of evaluating ground displacements to be adopted in tunnel-soil-structure interaction analyses, especially when the horizontal ground displacements significantly affect the response of the system (e.g. tunnel-pile interaction analysis). Ground movements induced by the construction of bored tunnels in clay have been widely monitored and discussed; consequently, a good understanding of greenfield ground deformations has been achieved. Recently, several cases of tunnel construction in sands and coarse-grained soils have been documented (Fargnoli et al., 2013; Hsiung, 2011; van Jaarsveld et al., 1999). Although past studies have shown that the mechanism of tunnelling-induced ground displacements in sands is different to clay, there have been few analytical studies for tunnelling in sands. Therefore, this chapter proposes analytical and semi-analytical estimations of greenfield soil deformation patterns above shallow tunnels in sand.

The aims of this chapter are to assess the efficiency of an analytical closed-form solution available in the literature by comparing its predictions with geotechnical centrifuge experiment data and to develop a solution for tunnelling-induced ground movements in sandy soils that accounts for the effect of tunnel contraction on the resulting deformation pattern. As benchmark data, the plane-strain tunnelling centrifuge test data from Marshall et al. (2012) is used, which was performed using a dry dense (relative density of 90%) silica sand and provides detailed measurements of surface and sub-surface soil displacements. Three tests were reported, for cover-to-diameter ratios (C/D) of 1.3, 2.4, and 4.4; the data presented in this chapter focuses on the $C/D = 1.3$ and $C/D = 2.4$ tests.

The chapter consists of the following main sections. Section 5.1 compares the deformation parameters predicted with an analytical closed-form solution with centrifuge data to define the

input parameters on the basis of their physical meanings. The effects that tunnel size, depth and volume loss have on the tunnel deformation parameter are discussed. A set of equations for the model input parameters is proposed and results compared with centrifuge test outcomes. Section 5.2 provides a simple and efficient tool in the form of a semi-analytical solution based on the deformation patterns of the elastic analytical solution for incompressible soil and the back-analysis of the data of a single centrifuge test. Section 5.3 presents validation and assessment of the solution features, comparing the vertical and horizontal ground movements predicted by the analytical and semi-analytical formulas with centrifuge measurements. The outcomes illustrate that solutions developed by other researchers for clay may not be applicable in sands. Finally, Section 5.4 summarises the main findings.

The expressions illustrated in this chapter for the estimation of vertical and horizontal displacements may provide useful guidance to tunnel design engineers in the case of shallow tunnels in sands. In particular, they may be implemented as inputs of tunnel-soil-structure interaction analyses in sands for further research. Part of the results presented in this chapter were published within Franza and Marshall (2015a) and Franza and Marshall (2015b).

5.1 Investigation of the analytical deformation parameters

The general closed-form solution proposed by González and Sagaseta (2001), reported in Equations (2.37) and (2.38), is adopted in this work. In this type of solution, instead of attempting to accurately model the tunnel construction operations, the tunnel deformation parameters are used to reproduce their overall effects on the surrounding soil. González and Sagaseta (2001) includes two tunnel deformation parameters (ground loss, ovalization), illustrated in Figure 5.1, as well as soil volumetric compressibility. The compressibility term is used to describe the volumetric strain contribution to the ground settlements.

Previous researchers calibrated ground deformation parameters according to sparse field measurements. In this study, instead of performing a complex back-analysis of displacement data, the input parameters have been calibrated on the basis of their physical meaning and a qualitative assessment of the outcomes is made by comparison with experimental data. The results of the test series CD13ID90, CD24ID90, and CD44ID90 (see Table 4.1) are used to evaluate model input parameters.

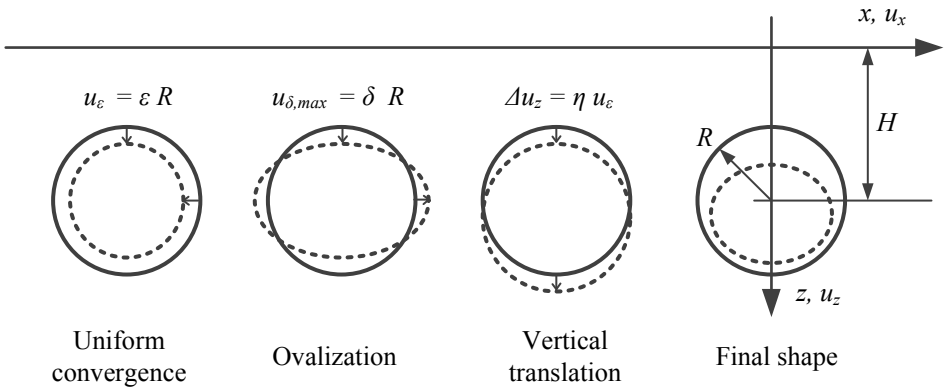

Fig. 5.1 Tunnel deformation components.

5.1.1 Ground loss, ovalization and compressibility

In tunnelling, ground loss describes the magnitude of settlement that occurs as a result of tunnel construction. It is described by means of the soil volume loss, $V_{l,s}$, that is defined as the ratio between the volume of the settlement trough per unit length of tunnel, V_s, (also referred to as ground loss) and the excavated area of the tunnel cross section, V_0. In experimental and analytical studies, the ground loss is modelled through the tunnel volume loss, $V_{l,t}$, which is the ratio between the over-excavated ground at the tunnel periphery, ΔV, and V_0.

In the analytical solutions provided by González and Sagaseta (2001), the tunnel volume loss magnitude is related to the uniform radial deformation parameter ε. Note that tunnel volume loss, $V_{l,t}$, was a controlled variable during the centrifuge tests, whereas it is an input parameter for analytical analysis. On the other hand, the tunnel ovalization mechanism is determined by the ovalization term, δ. As an alternative, the tunnel ovalization could be expressed using the relative distortion parameter ρ given by $\rho = \delta/\varepsilon$.

According to the three centrifuge results, the horizontal movements measured at the tunnel springline are negligible across the range of volume losses considered ($V_{l,t} = 0 - 5\%$), as displayed in Figure 5.2. This mechanism may differ slightly to some real tunnelling cases where a tunnel boring machine (TBM) with tail-skin grouting is incorporated; in these cases, horizontal displacements at the tunnel shoulders could be large and outwards (Dias and Kastner, 2013). In order to mimic the negligible horizontal movements at the springline in the analytical solution, the following ovalization term was assumed:

$$\rho = 1 \tag{5.1}$$

Volumetric strain within sandy soil varies due to the variation of shear strain experienced by the soil. The displacements at a given depth represent the cumulative effect of the soil beneath that level. This cumulative effect of volumetric strain determines the magnitude of the difference between $V_{l,s}$ at a given depth and the value of $V_{l,t}$. Surface displacements represent the cumulative effect of all volumetric strains occurring within the entire soil mass. In the analytical solution, the average soil volumetric strain contribution to the settlements is accounted for by the compressibility parameter α. Because α is an average value for the whole soil mass, it is sensible to estimate it from $V_s^{exp} = V_s^{an}$ at the soil surface, where the superscripts "exp" and "an" refer to experimental and analytical, respectively.

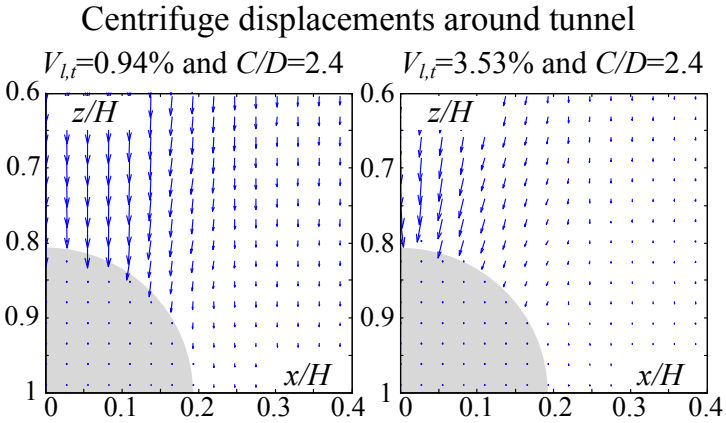

Fig. 5.2 Centrifuge test measurements of displacements near the tunnel.

By taking into account the definition of volume loss, Equation (2.19) proposed by Marshall et al. (2012) may be written as follows to obtain an empirical relation for the experimental soil ground loss at the surface

$$V_s^{exp} = \frac{\sqrt{C/D}}{100}\left(c_a - c_b \exp\left[-\left(\frac{200\varepsilon + c_c}{c_d}\right)^2\right]\right)\pi R^2 \tag{5.2}$$

where the coefficients depend on the type of sandy soil and its relative density. For dry silica sand with a relative density equal to 90%, they proposed $c_a = 2.0$, $c_b = 3.7$, $c_c = 2.8$, and $c_d = 3.6$.

The analytical soil ground loss was evaluated by integration of the ground settlement at the surface, resulting in:

$$V_s^{an} = 2\sqrt{\pi}\left((\alpha-1)\rho+\alpha\right)\varepsilon H^2\left(\frac{R}{H}\right)^{2\alpha}\frac{\Gamma[\alpha-0.5]}{\Gamma[\alpha+1]} \tag{5.3}$$

where Γ is the Euler gamma function. By replacing the ovalization term ρ in Equation (5.3) with that from Equation (5.1), the following is obtained:

$$V_s^{an} = 2\sqrt{\pi}\left(2\alpha-1\right)\varepsilon H^2\left(\frac{R}{H}\right)^{2\alpha}\frac{\Gamma[\alpha-0.5]}{\Gamma[\alpha+1]} \tag{5.4}$$

In order to provide a straightforward tool to engineers, Equation (5.4) has been approximated by Equation (5.5):

$$V_s^{an} = \left(c_1\exp\left[-c_2\alpha\right]\right)\varepsilon H^2\left(\frac{R}{H}\right)^{2\alpha} \tag{5.5}$$

with $c_1 = 9.0$ and $c_2 = 0.36$ (Figure 5.3). These coefficients are general and do not depend on the soil properties. The interpolation has been optimised for $\alpha = 0.9-1.3$ according to preliminary evaluation of Equations (2.19) and (5.3) using the data from the centrifuge experiments. Therefore, combining Equations (2.19) and (5.5), the approximate compressibility parameter in sandy soil could be estimated by

$$\bar{\alpha} = -\frac{\ln\left[\dfrac{V_s^{exp}}{c_1\varepsilon H^2}\right]}{c_2 - 2\ln\left[\dfrac{R}{H}\right]} \tag{5.6}$$

Marshall et al. (2012) reported centrifuge experiment data that showed that even for a dense silica sand, the soil underwent an overall contraction at low values of tunnel volume loss (based on the ratio of soil volume loss at the surface to tunnel volume loss). This is due to the shear strain distribution within the soil: low shear strains (and associated volumetric contraction) were measured in most of the soil whereas high shear strains (associated with volumetric dilation) were concentrated in a limited zone at the tunnel shoulders. Therefore the compressibility parameter could be lower than one (i.e. $\alpha < 1$) in sandy soils regardless of soil relative density.

5.1.2 Effects of deformation parameters

In this section the ground deformation patterns predicted by Equations (2.37), (2.38), (2.24), (5.1) and (5.6) are compared with the centrifuge results. Furthermore, the input parameter effects on the ground surface settlements are evaluated to provide some guidelines. Figure 5.4 shows that the input parameters estimated by Equations (2.24), (5.1) and (5.6) provide vertical and horizontal displacement fields compatible with the centrifuge results.

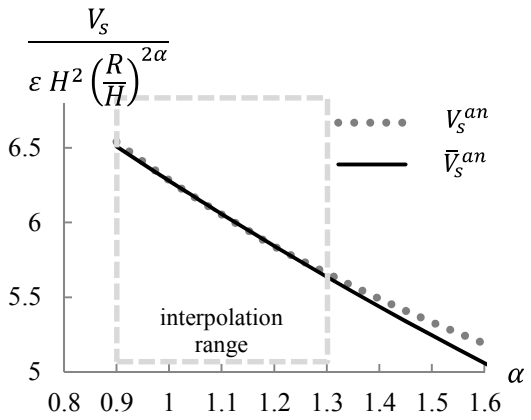

Fig. 5.3 Comparison between exact and approximate V_s.

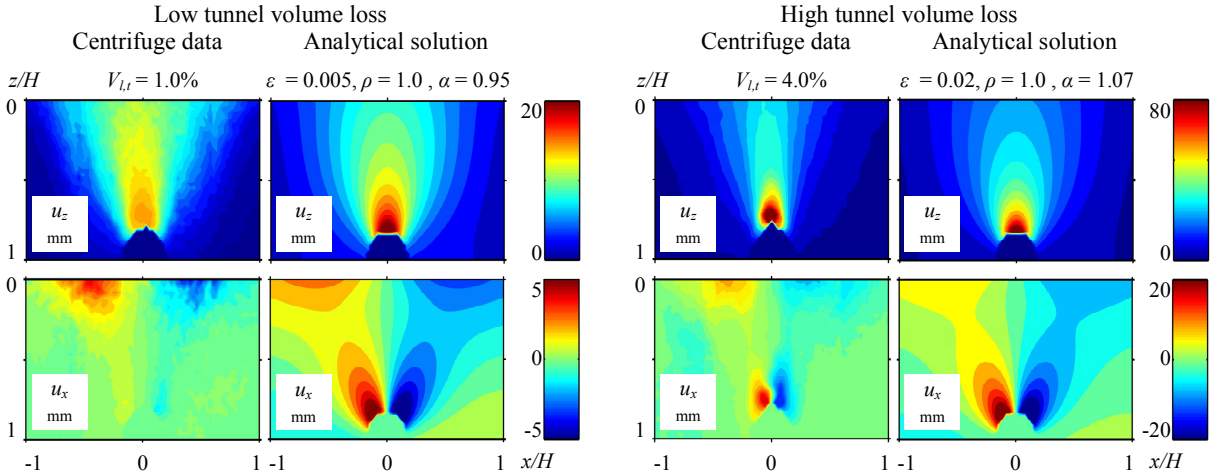

Fig. 5.4 Centrifuge and analytical deformation patterns.

Figure 5.5 displays an assessment of the variation of the relative contribution of the ovalization term and the compressibility parameter to the normalised surface settlement trough. Previous research calibrated the input parameters in order to obtain the best fit to sparse sets of field data, predominately at the ground surface. Using the empirically validated Gaussian curve as a reference for comparison, Figure 5.5(a) shows that a higher value of the ovalization term ($\rho = 2$) is required to obtain a good prediction of the expected narrow surface settlement trough. Likewise, in Figure 5.5(b) it is shown that a higher value of $\alpha = 2$ gives a better match to the Gaussian curves. However, using these higher values of α and ρ may not be realistic when considering their physical meaning, and do not provide good predictions of subsurface and horizontal ground movements when compared against the patterns measured in the centrifuge tests. In particular, a high value of ρ implies an outwards movement of the tunnel springlines, which was not observed in the centrifuge tests (see Figure 5.2); a value of $\rho = 1$ is more sensible considering the experimental data.

When subsurface and horizontal ground movements are used for tunnel-structure interaction analysis, it is necessary to assume a consistent soil deformation pattern. In this case, it is recommended to assume a unit value of relative distortion ($\rho = 1$) and a compressibility parameter

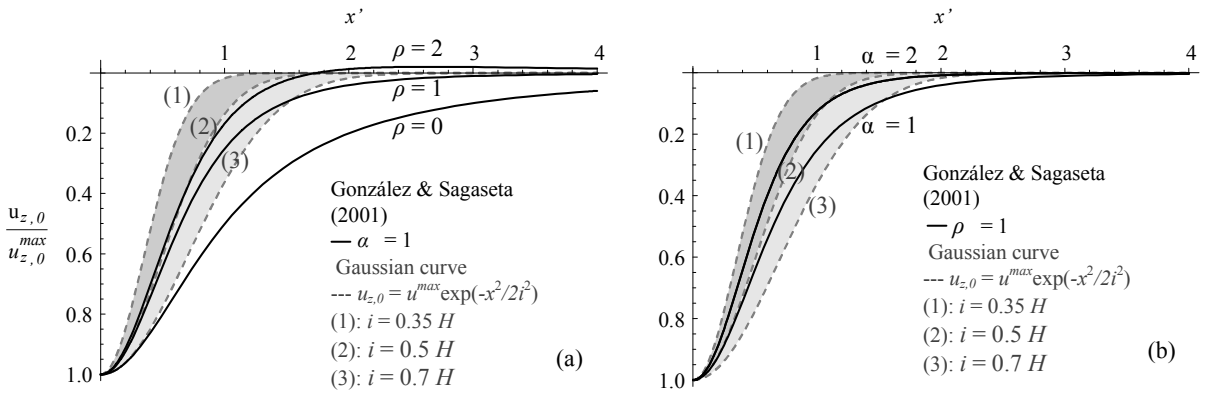

Fig. 5.5 Normalised analytical surface settlement trough: effects of (a) tunnel ovalization and (b) ground compressibility.

compatible with Equation (5.6) (i.e. $\alpha = 0.9 - 1.3$). With these input parameters, the comparison with the Gaussian curves in Figure 5.5 shows that the analytical surface settlement trough is too wide at high volume losses. In fact, according to Marshall et al. (2012), the distance from the centre line to the inflexion point, i, in sandy soils decreases with the tunnel volume loss from values of approximately $(0.5 - 0.7)H$ to $(0.35 - 0.5)H$ depending also on the relative tunnel depth (this range is represented in Figure 5.5 by the grey shaded areas).

5.2 Proposed semi-analytical solution

A new semi-analytical solution is proposed for the prediction of the tunnelling-induced ground movements in sandy soils to account for the effect of tunnel volume loss on the ground deformation pattern. The semi-analytical formula consists of modifying an elastic analytical solution for incompressible soil through a corrective term: the elastic solution allows modelling of the deformation pattern due to the tunnel deformation mechanism, whereas the corrective term aims to account for the effect of non-linear behaviour and volumetric strains on the resulting settlement trough shape. Note that this analysis is limited to one centrifuge test ($C/D = 2.4$ and $I_d = 0.9$); therefore, the equation validity is limited to dense sand and tunnels with C/D approximately equal to 2.4.

The elastic solution of Verruijt and Booker (1996) was modified as follows. 1) The case of elastic medium without volumetric strains is adopted (i.e. incompressible soil with $\nu = 0.5$) corresponding to González and Sagaseta (2001) solution for $\alpha = 1$. 2) The relationship $\delta = \varepsilon$ (i.e. $\rho = 1$) between the ovalization term and the uniform contraction was introduced to replicate the observed experimental tunnel deformation mechanism in the elastic solution (centrifuge test data indicates that the horizontal movements measured at the tunnel springline are negligible at low and high volume loss, as shown in Figure 5.2). 3) The elastic displacement pattern due to the above assumptions was corrected by means of the term ξ that considers the non-linear behaviour and volumetric strains of the soil. Considering assumptions 1), 2) and 3), the semi-analytical

solution for horizontal (u_x) and vertical (u_z) displacement at point (x,z) can be written as follows:

$$\begin{aligned}\frac{u_x}{2\xi\varepsilon R\left(\frac{R}{H}\right)} =& -\frac{x'}{2r'^2_1}\left(1-\frac{x'^2-z'^2_1}{r'^2_1}\right)-\frac{x'}{2r'^2_2}\left(1-\frac{x'^2-z'^2_2}{r'^2_2}\right)\\ &+\frac{4x'z'}{2r'^2_2}\left(\frac{z'_2}{r'^2_2}-\frac{x'^2-3z'^2_2}{r'^4_2}\right)\end{aligned} \tag{5.7}$$

$$\begin{aligned}\frac{u_z}{2\xi\varepsilon R\left(\frac{R}{H}\right)} =& -\frac{z'_1}{2r'^2_1}\left(1-\frac{x'^2-z'^2_1}{r'^2_1}\right)+\frac{z'_2}{2r'^2_2}\left(1+\frac{x'^2-z'^2_2}{r'^2_2}\right)\\ &-\frac{1}{2r'^2_2}\left(2z'\frac{x'^2-z'^2_2}{r'^2_2}+4z'z'_2\frac{3x'^2-z'^2_2}{r'^4_2}\right)\end{aligned} \tag{5.8}$$

where $z_1=z-H$, $z_2=z+H$, $r_1=\sqrt{x^2+(z-H)^2}$, $r_2=\sqrt{x^2+(z+H)^2}$, the prime denotes that the variables are scaled by the tunnel depth, H, (e.g. $x'=x/H$) and other geometrical parameters are defined in Figure 5.1.

5.2.0.1 Calibration of the corrective term

Because the corrective term, ξ, takes into account the difference between the analytical solution for an elastic incompressible medium and the experimental data, it should be a function of the variables affecting the non-linear behaviour and the volumetric strains of the soil. Thus, ξ should depend on the spatial coordinates (x,z), C/D, as well as soil and tunnel state variables I_d and $V_{l,t}$. However, in this chapter, the analysis for the semi-analytical approach is limited to one centrifuge test, where $C/D=2.4$ and $I_d=0.9$. Therefore only the spatial coordinates and the tunnel volume loss are the resulting variables in the following study of ξ. The calibration was performed considering the total ground movements. This approach is consistent with Equations (5.7) and (5.8): both horizontal and vertical displacements are proportional to $V_{l,t}=2\varepsilon\times 100$. To preliminarily investigate the corrective term spatial trend, the ratio between the total centrifuge and analytical elastic displacement fields u^{el} (resulting from Equations (5.7) and (5.8) with $\xi=1$) were plotted; this ratio is referred to as ξ^*. Because the unit elastic displacement field (i.e. u^{el} for $\xi=1$) is constant, ξ^* accounts for the experimental variation of the ground deformation pattern with $V_{l,t}$. Figure 5.6 shows the contours of the ratio ξ^* at low and high volume losses. It is evident that there is a variation of soil deformation pattern at different tunnel volume losses, which has never been directly implemented into any other closed-form or semi-analytical solution.

The structure of the corrective term ξ was defined in order to provide efficient curve fitting of the ratio ξ^*. The expression adopted is defined by Equation (5.9): it is composed of two three-dimensional Gaussian curves, is a function of the spatial coordinates x and z, and provides

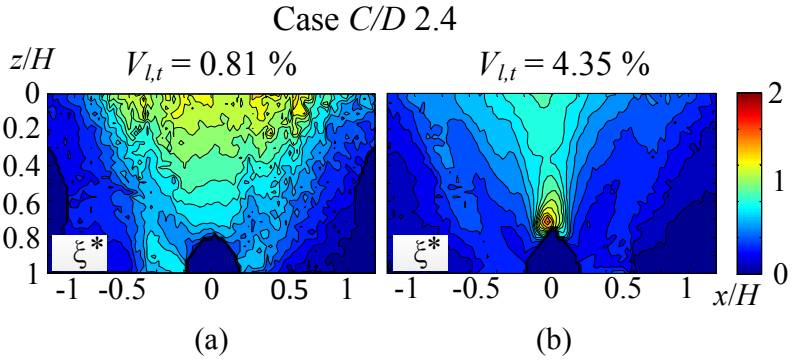

Fig. 5.6 Ratio ξ^* between total centrifuge and analytical displacements at (a) low and (b) high volume losses (Franza and Marshall, 2015b).

sufficient flexibility to reproduce the trends shown in Figure 5.6.

$$\xi = c_A \exp\left[-\left(c_1\left(\frac{z}{H}\right)^2 + c_2\left(\frac{x}{H}\right)^2\right)\right] + c_B \exp\left[-\left(c_3\left(\frac{z}{H} - c_4\right)^2 + c_3\left(\frac{x}{H}\right)^2\right)\right] \quad (5.9)$$

where the coefficient $c_A; c_B; c_1; c_2; c_3$ and c_4 depend on $V_{l,t}$. The first Gaussian function with coefficients c_A, c_1 and c_2 allows interpolating ξ^* at low volume losses (Figure 5.6(a)). c_A is the function amplitude whereas c_1 and c_2 are the attenuation factors respectively in the x and z directions. At higher volume losses, ξ^* exhibits an additional peak in the proximity of the tunnel crown (Figure 5.6(b)). To provide a good fit, an additional Gaussian function was introduced in ξ, which has its centre at $(0, c_4 H)$, amplitude c_B and attenuation factor c_3 in both spatial directions.

The results of the coefficient calibrations are summarised in Figure 5.7. At each $V_{l,t}$, the Gaussian curve coefficients were determined by curve fitting ξ^* with Equation (5.9) (using least-squares regression). Although based on nine data points within the range $V_{l,t} = 0 - 5\%$, the plot suggests a linear relationship between each coefficient and volume loss. Therefore, the final coefficient expressions reported in the following equations were determined by linear regression (i.e. $c_i = m_i V_{l,t} + q_i$ for the i^{th} coefficient).

$$\begin{aligned} c_A &= -0.147 V_{l,t} + 1.45; & c_B &= 0.156 V_{l,t}; \\ c_1 &= 1.20; & c_3 &= 13.43 V_{l,t}; \\ c_2 &= 0.040 V_{l,t} + 0.704; & c_4 &= 0.70. \end{aligned} \quad (5.10)$$

As displayed by Figure 5.7(a), the amplitude c_A of the first Gaussian surface decreases with volume loss due to the effect of soil dilation. The displacement attenuation in the z-direction, given by c_1, is constant close to the surface, where the correction term is not affected by the second Gaussian function. Finally, the trend shown by c_2 confirms that the width of the settlement trough in the x-direction decreases with tunnel volume loss (i.e. with the increase of the magnitude of displacements). On the other hand, Figure 5.7(b) illustrates the variation of the coefficients c_B, c_3 and c_4 of the second Gaussian function, whose effects are limited within

the depth $z = (0.5 - 1)H$. This function describes a localised zone of large displacements above the tunnel that increase with the tunnel contraction. Both the amplitude, c_B, and the attenuation factor, c_3, increase linearly with the volume loss, whereas the centre position is fixed (i.e. c_4 is constant).

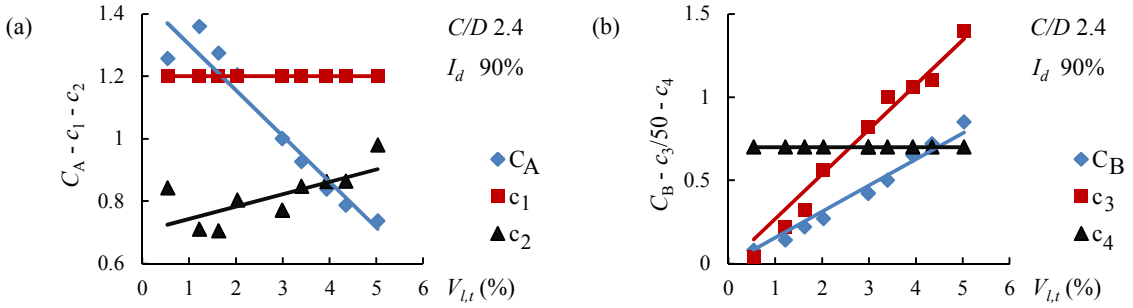

Fig. 5.7 Linear regression of the coefficients of Equation (5.9).

5.3 Ground movement prediction

5.3.1 Analytical method

In this section, the González and Sagaseta (2001) solution is applied to the centrifuge tests to evaluate its performance. The input parameters are selected by Equations (2.24), (5.1) and (5.6). The only resulting input ε is derived by the measured value of tunnel volume loss in the centrifuge tests.

Figure 5.8 shows a comparison between analytical predictions and centrifuge data of normalised displacements at two values of volume loss and at various depths within the ground for the cases $C/D = 1.3$ and $C/D = 2.4$. Because the analytical displacements are proportional to tunnel volume loss and radius, the ground movements were normalised by a multiple of this quantity ($4V_{l,t}R$ and $V_{l,t}R$, respectively, in the vertical and horizontal directions) to allow comparison of the unit settlement profiles on one plot with the same scale of normalised depth (z/H). The following observations can be made.

- The analytical vertical displacements are compatible with the centrifuge results; however the agreement tends to decrease at increased depth and volume loss.
- The analytical horizontal displacements do not agree with the centrifuge data, especially at low volume loss. In general, the surface movement magnitude is adequately replicated, though the analytical settlement profiles are wider than the experimental data. It should be emphasised that the distortion term was fixed at $\rho = 1$ to give a correct representation of the real displacements that occur near the tunnel springline.

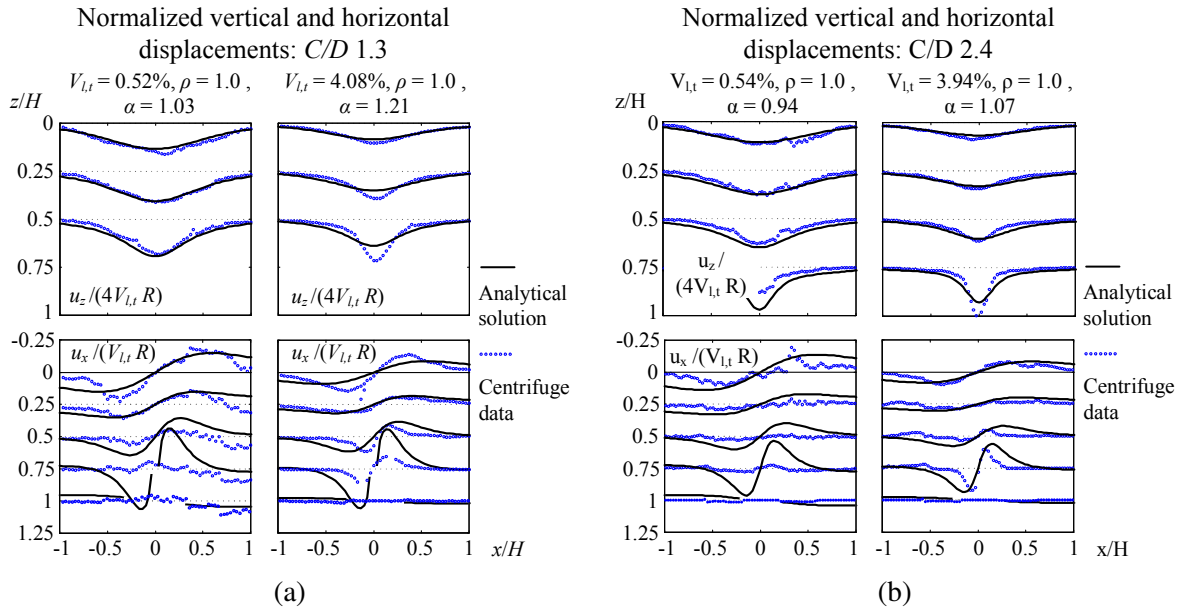

Fig. 5.8 Centrifuge and analytical displacements for (a) $C/D = 1.3$ and (b) $C/D = 2.4$.

5.3.2 Semi-analytical method

Firstly, for validation purposes, the proposed semi-analytical solution is compared to centrifuge measurements. Afterwards, it is compared with the displacements predicted by Loganathan and Poulos (1998), developed for clays in an undrained condition, to illustrate the main differences in the tunnelling-induced displacement fields in clays and sands.

The ground deformation patterns predicted by Equation (5.7), (5.8), (5.9) and (5.10) are compared with the centrifuge results in Figure 5.9. As expected, the semi-analytical predictions agree well with the centrifuge results, since the correction term calibration was based on the same benchmark data. The formula performs well in terms of overall vertical and surface horizontal movements. However, it performs less well for prediction of subsurface horizontal displacements at low volume loss, especially near the tunnel crown. This is probably due to the calibration that was based on the total movements and the fact that vertical movement magnitude is larger than horizontal. In general, the proposed method is able to describe the variability of the soil deformation pattern around tunnels in sands as it is affected by depth and tunnel volume loss.

Figure 5.10 shows a comparison between semi-analytical predictions of tunnelling induced movements in clays and sands at two values of volume loss in the case of $C/D = 2.4$. The movements in clays were estimated using Loganathan and Poulos (1998), whereas the displacement in sands was obtained using the proposed expressions. For comparison, the centrifuge results are included in the same figure. As previously done in Section 5.3.1, the movements were normalised. The following observations can be made.

- The deformation pattern in sands is significantly affected by the magnitude of the tunnel contraction (i.e. the settlement troughs are narrower at high volume loss), whereas the deformation pattern is constant with tunnel volume loss in clays.

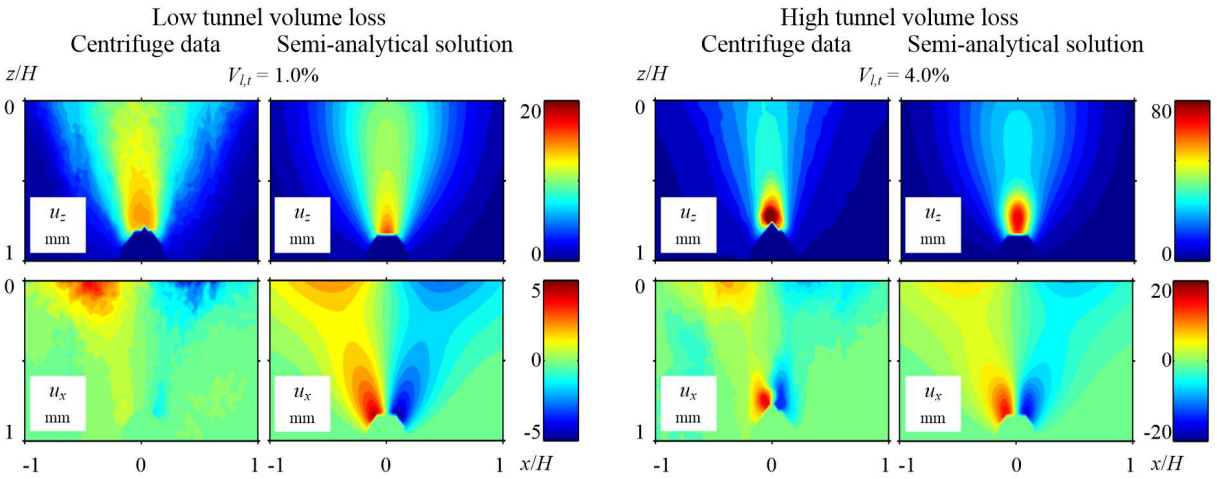

Fig. 5.9 Centrifuge and the semi-analytical deformation patterns.

- The vertical displacement fields in sands and clays differ; this is particularly true at high volume loss. The scatter is lower at the surface; however, the surface settlement troughs in sands are slightly narrower than in clays.
- Horizontal movement magnitude increases with depth in clays, whereas it decreases in sands; subsurface movements are wider in clays than in sands.
- At the springline, the ground exhibits limited inwards movements in sands. In clays, there are inwards horizontal movements due to an oval-shaped tunnel contraction. The results confirm a different ovalization mechanism of tunnels in fine and coarse soils.

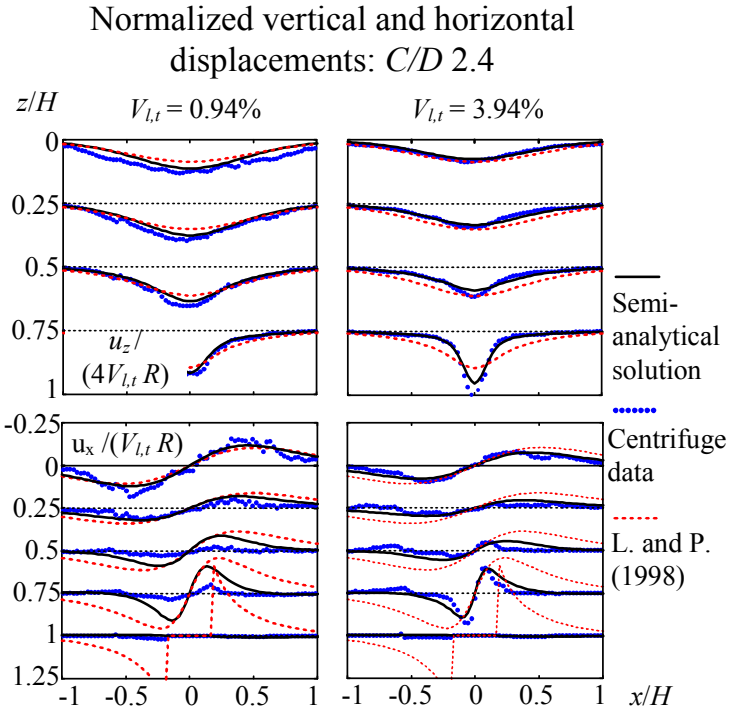

Fig. 5.10 Normalised horizontal and vertical displacements for $C/D = 2.4$.

5.4 Conclusions

In this chapter, the efficiency of the analytical closed-form solution provided by González and Sagaseta (2001) in estimating ground movements in sandy soil was assessed against centrifuge data. Furthermore, a semi-analytical solution based on the results of a centrifuge test was proposed. The main conclusions of this work are:

- The effect that tunnel relative depth and volume loss have on the analytical input parameters (ovalization and volumetric compressibility) was assessed; a set of equations was defined to relate their values to the tunnel volume loss.
- The predicted analytical soil deformation pattern is compatible with available centrifuge test results. Despite the acceptable prediction of surface vertical and horizontal movements, the analytical solution reveals poor prediction of subsurface displacements.
- For a given soil density and C/D ratio, the proposed semi-analytical formula is able to determine, with reasonable accuracy, the horizontal and vertical movements around tunnels in sands as they are affected by tunnel volume loss. With the use of a corrective term, the solution was able to replicate the narrowing of the settlement troughs with tunnel volume loss and a zone of localised large displacements at the tunnel crown.
- The differences in the deformation pattern of clay and sandy soil due to tunnelling were investigated: tunnel ovalization and tunnel volume loss lead to significant differences, particularly with regard to subsurface movements.

In general, results showed that the superposition of the singularities method with a mean compressibility parameter may not be fully adequate to assess tunnelling-induced ground movements in sands; this is due to the assumption of a mean compressibility parameter, which neglects the complex volumetric strain mechanism above tunnels in sands that depends on the tunnel volume loss magnitude. Because the analytical solution can predict a deformation pattern consistent with available centrifuge test results, semi-empirical solutions based on the use of a corrective term for the elastic displacement mechanism represent a useful tool for ground movement prediction.

With appropriate judgement, the proposed semi-analytical solution could be used as an input in soil-structure interaction analyses. For instance, because the accuracy of the proposed expressions is particularly satisfactory up to a depth equal to $0.5H$, they could provide useful guidance to assess the effect of tunnel construction on existing pipelines, which are generally buried at limited depth (between 1 and 5 m).

To conclude, further work is necessary to extend the semi-analytical solution to the centrifuge dataset provided in Chapter 4 and to improve its performances; in this way, it would be possible to account for the effects of the tunnel relative depth and soil relative density.

Chapter 6

A simplified elastic analysis of tunnel-piled structure interaction

The use of complex 3D numerical analyses, which are able to consider the non-linear behaviour of materials, structural configuration, the loading conditions, and the excavation sequence, is generally required for the final design stage of major projects or to obtain benchmark solutions to be used for research purposes. On the other hand, Winkler-based Two-Stage Analysis Methods (TSAMs) represent useful tools for preliminary design stages and simplified parametric studies.

TSAMs have been shown to be suitable for the analysis of tunnel-pile group interaction (see Section 2.2.4.2 of the literature review) whereas their application in the case of deformable piled superstructure has not been investigated. Recent studies have shown that the assumptions of soil linear-elasticity and perfect bonding between the soil and pile provide good predictions over the range of tunnel ground losses typically experienced in practice (i.e. $V_{l,t} = 0.5 - 1\%$), whereas non-linearity and plasticity play a more important role at higher volume losses (Basile, 2014; Zhang et al., 2011a, 2013). In addition, centrifuge tests have indicated a decrease of structural damage induced by tunnelling in elastic buildings with shallow foundations as tunnel volume loss increases because of the soil stiffness degradation (Farrell et al., 2014). Therefore, the complete tunnel-pile-structure interaction is investigated through a fully elastic Winkler-based Two-Stage Analysis Method (TSAM) that appears to be adequate to provide insight to the main interaction mechanisms as long as the tunnel ground loss is limited to low values not inducing pile failure.

In the first part of this chapter, the complete tunnel-pile-structure interaction is studied through a Winkler-based TSAM, focusing on structural displacements that result from the tunnel excavation. Since displacements are damage related quantities, their prediction can be used to evaluate building serviceability state. The TSAM method is able to capture the main interaction mechanisms and the effects of structural configuration on the global response of the system to tunnelling. In the second part of the chapter, effects of structure stiffness on the building deformations, both axial and flexural, are investigated, with emphasis on the role played by the piled foundations. Two simple design charts for evaluating the piled building deflection ratios and horizontal strains are proposed.

The author would like to acknowledge the contribution of Mr. T. K. Haji, a PhD candidate at the University of Nottingham, who developed the ABAQUS 3D models used for the validation of the TSAMs. The contents presented in this chapter were published within Franza et al. (2016a) and Franza et al. (2017).

6.1 Two-stage Winkler-based methods

This section presents details of the TSAMs used in this chapter. Two tunnel-pile-structure interaction (TPSI) approaches were adopted: a general method (Method G, referred to as TPSI-G) proposed by Kitiyodom et al. (2005), based on deformable interacting piles, and a simplified version (Method S, referred to as TPSI-S), based on the assumption of rigid isolated piles. The simplified Method S, described in Franza et al. (2016a), provides a relatively easy way to calculate tunnelling-induced settlements of piled buildings which may be useful when conducting preliminary risk assessments. A schematic representation of the two methods is shown in Figure 6.1.

The analysis is limited to two structural cases: either an elastic frame structure or a simple equivalent beam. The structures are supported by a foundation consisting of a row of uniformly spaced circular piles embedded vertically in an elastic homogeneous deposit. The foundation and structure are affected by displacements caused by the construction of a tunnel beneath the level of the pile tips. The structure is orthogonal to the longitudinal tunnel axis and is not in contact with the ground surface. Tunnelling induces vertical and lateral ground movements that cause displacements in the foundation-superstructure system. Note that this is not a plane strain problem because both the foundation and structure have a finite length in the tunnel longitudinal direction. It should be noted that the building weight was not considered in the paper because, under the assumptions of the proposed analysis method, the displacements induced by tunnelling and building self-weight would not affect each other.

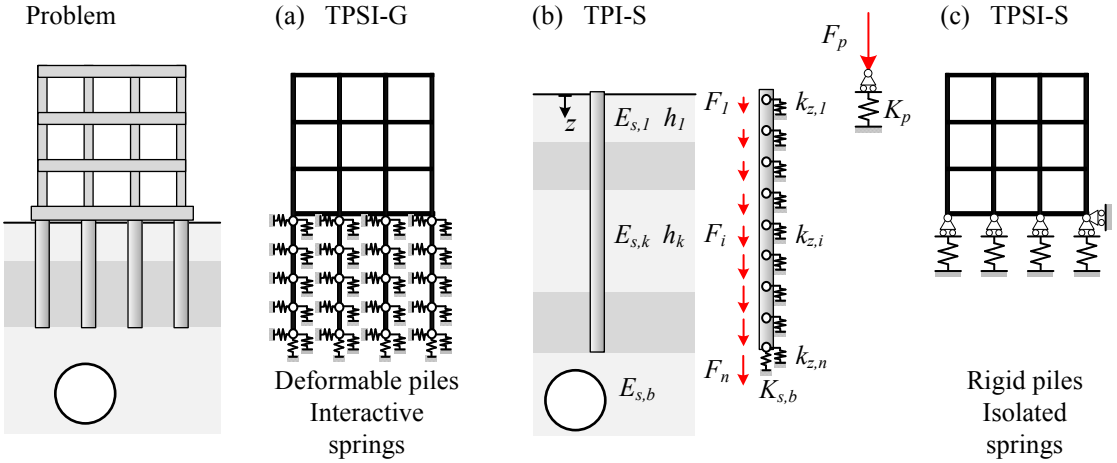

Fig. 6.1 Winkler model for tunnel-pile-structure interaction (TPSI): (a) deformable piles and interactive springs (method G); (b) single rigid pile (method S); (c) isolated rigid piles (method S).

6.1.1 Greenfield displacement input

The prediction of tunnelling-induced soil movements may be performed with empirical, finite element, or analytical methods. Empirical methods have been used extensively in practice for the

estimation of settlement trough shape because of their inherent simplicity. Empirical methods, however, do not provide reliable predictions of horizontal movements throughout the soil depth. On the other hand, finite element analyses generally require significant computational effort and detailed soil constitutive model input data that may not be available. Closed-form analytical and semi-analytical solutions have been successfully adopted in tunnel-soil-structure interaction analyses, especially when horizontal ground displacements are important (e.g. tunnel-pile interaction analyses), because they provide a consistent deformation pattern with depth. The closed-form expressions proposed by Loganathan and Poulos (1998), reported in Equations (2.39) and (2.40), for the prediction of vertical and horizontal greenfield tunnelling-induced displacements in clays were adopted for the analyses presented in this chapter. However, any greenfield displacement input could be used within the proposed method, thereby enhancing the versatility of the approach.

6.1.2 Soil springs

In this chapter, the soil-pile interaction problem is modelled through vertical and horizontal linear springs distributed along the pile shaft, and by means of a vertical spring placed at the pile base; slippage and gap formation are not allowed. Several methods are available in the literature for evaluating spring stiffness. For piles subjected to passive loads due to ground movements, Kitiyodom et al. (2005) demonstrated that the integral method is most suitable when the estimation of pile internal forces, in particular axial forces, is important. However, in this study, for the sake of simplicity, the horizontal and vertical soil spring stiffness were correlated to the elastic parameters of the soil with the expressions suggested by Vesic (1961) and Randolph and Wroth (1978). As shown by Mylonakis and Gazetas (1998) and Huang et al. (2009), these expressions allow for a good estimation of the displacements of floating piles induced by tunnelling and external loadings at the pile heads, which are of great importance for correctly describing tunnel-piled building interaction.

The assumed values of stiffness for vertical (k_z) and horizontal (k_x) shaft springs (per unit-length of pile) are given in Equation (6.1).

$$k_z = \frac{2\pi G_s}{\ln\left(\dfrac{2r_m}{d_p}\right)} \qquad || \qquad k_x = \frac{0.65E_s}{d_p\left(1-\nu_s^2\right)}\sqrt[12]{\frac{d_p^4 E_s}{E_p I_p}} \tag{6.1}$$

where G_s is the shear modulus of soil, E_s and ν_s are the Young's modulus and Poisson's ratio, respectively, of the soil at the pile shaft, r_m is an empirically determined distance beyond which the soil settlements become negligible, d_p is the pile diameter, L_p is the pile length, and E_pI_p is the flexural pile stiffness. In general, $r_m = \chi_1\chi_2 L_p\left(1-\nu_s\right)$ where χ_1 and χ_2 are empirical terms depending on soil inhomogeneity ($\chi_1\chi_2 = 2.5$ in the case of a homogeneous half-space) (Mylonakis and Gazetas, 1998; Randolph and Wroth, 1978). The stiffness of the vertical spring

$K^p_{s,b}$ at the pile base is evaluated with Equation (6.2) (Randolph and Wroth, 1979),

$$K^p_{s,b} = \frac{d_p E_{s,b}}{1 - \nu^2_{s,b}} \tag{6.2}$$

where $E_{s,b}$ and $\nu_{s,b}$ are the Young's modulus and Poisson's ratio, respectively, of the soil below the pile base.

6.1.3 General analysis method for tunnel-pile-structure interaction

The 'General Method' of tunnel-pile-structure interaction (TPSI) analysis (referred to as TPSI-G, refer to Figure 6.1) used in this chapter was achieved numerically by means of the finite element method (FEM) using a displacement-based approach. Using this method, when matrix condensation is conducted for the structure with respect to the pile head nodes, the remaining degrees of freedom (dofs) of the system are the generalised displacements of the pile element nodes (i.e. vertical and horizontal displacements, and rotations). Condensation of the problem allows reduction of the dofs (i.e. the computational effort of the analysis) while preserving the rigour of the approach. The equilibrium condition of the soil-pile-structure system is expressed by the following system of linear equations:

$$\left(\mathbf{C} + \mathbf{K}_s + \mathbf{K}_p\right) \mathbf{u}_p = \mathbf{f}_p \tag{6.3}$$

where $\left(\mathbf{C} + \mathbf{K}_s + \mathbf{K}_p\right)$ is the global stiffness of the piled structure system, $\mathbf{C}$ is the soil stiffness matrix, $\mathbf{K}_s$ is the condensed stiffness matrix of the structure, $\mathbf{K}_p$ is the stiffness matrix of the pile group, and $\mathbf{u}_p$ is the displacement vector of the piled foundation. Note that $\mathbf{f}_p = \mathbf{C}\mathbf{s}$ represents the external force vector acting on the piles due to vertical and lateral tunnelling-induced greenfield ground movements, where $\mathbf{s}$ is the vector of the tunnelling-induced greenfield movements. Equation (6.3) may be partitioned to highlight the dofs of the pile heads connected to the superstructure (subscript F) and of the embedded pile nodes (subscript E):

$$\left[\begin{bmatrix} \mathbf{C}_{FF} & \mathbf{C}_{FE} \\ \mathbf{C}_{EF} & \mathbf{C}_{EE} \end{bmatrix} + \begin{bmatrix} \mathbf{K}_{FF} & \mathbf{0} \\ \mathbf{0} & \mathbf{0} \end{bmatrix}_s + \begin{bmatrix} \mathbf{K}_{FF} & \mathbf{K}_{FE} \\ \mathbf{K}_{EF} & \mathbf{K}_{EE} \end{bmatrix}_p \right] \begin{bmatrix} \mathbf{u}_F \\ \mathbf{u}_E \end{bmatrix}_p = \begin{bmatrix} \mathbf{C}_{FF} & \mathbf{C}_{FE} \\ \mathbf{C}_{EF} & \mathbf{C}_{EE} \end{bmatrix} \begin{bmatrix} \mathbf{s}_F \\ \mathbf{s}_E \end{bmatrix} \tag{6.4}$$

Piles and superstructure elements are modelled as Euler-Bernoulli elastic beams. The soil stiffness matrix is defined as $\mathbf{C} = \mathbf{A}^{-1}$, where $\mathbf{A}$ is the soil flexibility matrix whose generic components A_{ij} describe soil displacement at node i of the pile induced by a unit force applied at node j. In this analysis, the interaction between nodes belonging to the same pile was neglected as well as the interaction between shaft and base nodes (i.e. pile base nodes only interact with each other). The diagonal terms of the flexibility matrix were determined starting from the

stiffness values obtained by Equations (6.1) and (6.2). In this chapter, the analyses were limited to the case of a homogeneous half-space, thus the off-diagonal non-zero terms, which represent pile-soil-pile interaction contributions, were obtained on the basis of Mindlin (1936) solutions for vertical and lateral forces at the pile shaft. Concerning displacements induced at a radial distance r by vertical forces at the pile base, the off-diagonal terms were obtained from the approximate attenuation function of soil settlements, $d_p/(\pi r)$, suggested by Randolph and Wroth (1979), which was derived from the solution of a punch on the surface of a half-space.

Once the equilibrium equation is solved with the inverse matrix method, the solution displacement vector, $\mathbf{u}_p$, is obtained. Then, the displacements and deformations of the entire superstructure can be computed by displacing the dofs of the pile heads connected to the superstructure by the sub-vector $\mathbf{u}_F$. Subsequently, superstructure internal forces and bending moments may be computed.

6.1.4 Simplified analysis method for tunnel-pile-structure interaction

The 'Simplified Method' for tunnel-pile-structure interaction analysis (referred to as TPSI-S) used in this chapter (1) assumes the piles to be rigid, (2) neglects the pile-soil-pile interaction, and (3) disregards the horizontal soil springs. Subsequently, this procedure only requires consideration of the vertical dofs of the piles. These simplifying assumptions reduce the global tunnel-pile-structure interaction analysis to that of a building on vertical springs which account for the soil deformability, subjected to a vertical system of forces induced by tunnelling (Figure 6.1(c)).

The schematic representation of the problem for a single pile case is shown in Figure 6.1(b). If each pile is discretised into $n+1$ nodes, it is possible to provide the following simple closed-form expressions for the stiffness of the equivalent pile-soil spring, K_p, and the resultant tunnelling-induced vertical force, F_p, at the p^{th} pile head.

$$\begin{aligned} K_p &= \sum_{i=1}^{n} k_z(z_i)\Delta z_i + K_{s,b}^p \\ F_p &= \sum_{i=1}^{n} s_z(z_i)k_z(z_i)\Delta z_i + s_z(L_p)K_{s,b}^p \end{aligned} \tag{6.5}$$

where Δz_i is the effective pile length corresponding to the i^{th} node, and s_z is the greenfield vertical soil movement induced by tunnel excavation at the p^{th} pile axis line.

If a piled structure is considered, the tunnel excavation induces a system of vertical forces at the pile head level. The equilibrium equation of the system is formulated by adding the contribution of soil stiffness to the condensed stiffness matrix of the structure. The equilibrium equation is

$$\left(\mathbf{K}_s + \mathbf{K}_g\right)\mathbf{u}_p = \mathbf{f}_p \tag{6.6}$$

where $\mathbf{K}_s$ is the condensed stiffness matrix of the structure, $\mathbf{K}_g$ is the stiffness matrix of the soil-pile group system, $\mathbf{u}_p$ is the displacement vector of the piled foundation, and $\mathbf{f}_p$ is the vector

of the tunnelling-induced forces. The condensed stiffness matrix of the structure is a full matrix, whereas the stiffness matrix of the pile-soil system is a diagonal matrix because the pile-soil-pile interaction is neglected. The non-zero diagonal terms of $K_{g,ii}$ and the terms of vector $f_{p,i}$ are obtained from Equation (6.5). Note that, because the problem is idealised as an elastic structure on independent vertical elastic springs, the superstructure should be restrained in the horizontal direction by an additional external constraint (see Figure 6.1(c)). Neglecting horizontal ground movements at the pile foundation is acceptable considering that tunnel construction generally induces negligible horizontal strains in structures with continuous foundation systems at the ground level (due to the relatively high axial stiffness of the building/foundation system) (Burland et al., 2004; Dimmock and Mair, 2008). However, this may not be the case for isolated piles or a foundation with a particularly low axial stiffness at the ground level (e.g. single columns supported by a single pile not connected at the ground floor level) (Goh and Mair, 2014). In these cases, particular attention should be paid in using the outcomes of the simplified Method S. In the analysis presented here, solution to Equation (6.6) was obtained with the inverse matrix method. Alternatively, a 3D numerical modelling software could be used. Although results presented here are limited to a simple pile row foundation, this analysis method can account for layered soil deposits and a generic structure with a variety of pile foundation configurations.

6.2 Model validation

This section demonstrates that the Winkler-based methods allow for a reliable assessment of piled building displacements due to tunnel construction. The efficacy of Methods G and S was investigated by comparing results against more rigorous 3D elastic FEM analyses performed using ABAQUS (Simulia, 2010). The influence of tunnel location, building configuration, as well as soil and structure stiffness were investigated. Although the analytical models allow implementation of multi-layered soil, all considered configurations correspond to vertical piles embedded in a homogeneous half-space. Results focus on the tunnelling-induced structural distortions at the foundation level (i.e. pile head movements). Pile head vertical and horizontal displacements are indicated as u_z^p and u_x^p, respectively, whereas rotations are given by φ^p. Tunnel-pile group interaction performed with free-pile head conditions (i.e. piles are not affected by a structure) are indicated with TPI; tunnel-pile-structure interaction analyses are denoted with TPSI. Figure 6.2 summarises the considered tunnel-pile-structure configurations and illustrates the adopted sign convention for displacements and rotations.

6.2.0.1 Numerical convergence

Before performing the validation analyses, a sensitivity study was performed to estimate the influence of pile finite element size on translations and rotations of the pile heads obtained with method G. Results showed that, for the considered frame case, the convergence was easily reached with an element size, Δh, smaller than 2.5 d_p (see Figure 6.3). In the model validation section, a

finite element size $\Delta h = 0.5$m was adopted. In later sections, when not stated, $\Delta h = 1.0$m was used because it resulted in a reliable and computationally efficient analysis.

6.2.1 Definition of analysis cases

Validation analyses were performed with for two structural/foundation models: 1) simple beams with a foundation comprising a row of either 5 or 11 piles, and 2) a framed structure with an 11 pile foundation, each of which was supported by a pile, and with no ground-level beam connecting the columns. The simple beam was given a stiffness that is representative of an equivalent foundation and superstructure system. Several relative soil-structure stiffness ratios, given by E_s/E, where E_s and E are the Young's modulus of the soil and superstructure, respectively, were investigated. The framed structure elements were given a Young's modulus of 30 GPa and realistic beam and columns cross-sections (as detailed in Figure 6.2). The pile spacing was fixed at 5m, hence the 5-pile building model had a width $B = 20$m, whereas the 11-pile foundation had a width $B = 50$m. The structures were located with their centre at a horizontal distance e from the tunnel centreline. Three different tunnel locations, $e = 0$, 15, or 25m, were considered. The tunnel volume loss, $V_{l,t}$, was assumed equal to 1% for all the performed analyses in this chapter. In this section, piles were assumed to be constrained through fixed connections to the superstructure. Both horizontal and vertical greenfield movements were considered except for the simple beam case, where only tunnelling-induced forces due to vertical greenfield movements were applied.

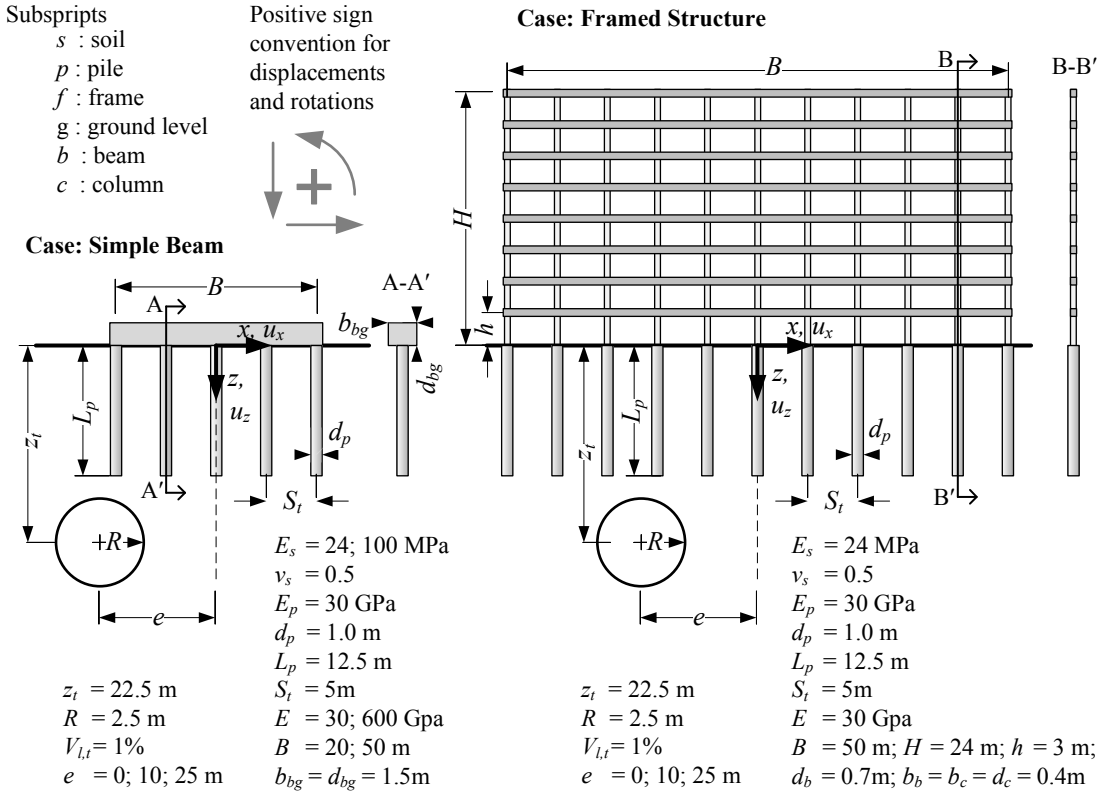

Fig. 6.2 Studied configurations for the validation.

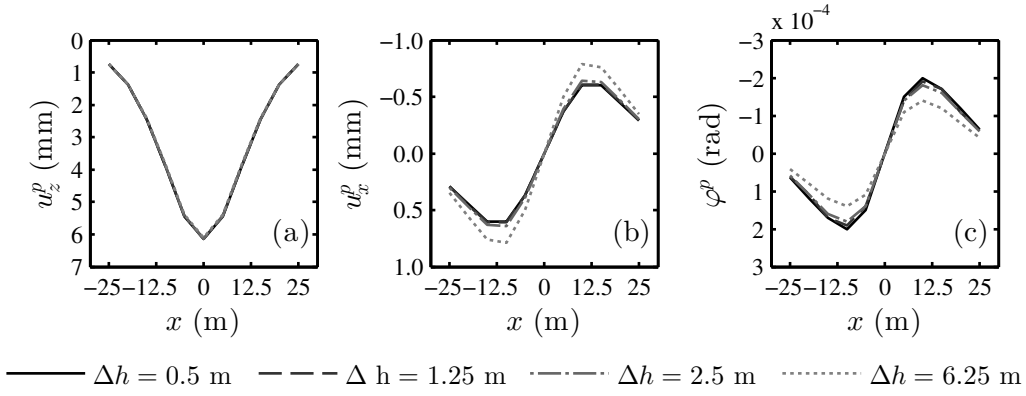

Fig. 6.3 Tunnelling-induced displacements of frame shown in Figure 6.2, obtained reducing the pile finite element size.

6.2.2 ABAQUS finite element models

The validation results were obtained with rigorous 3D elastic FEM analyses performed using ABAQUS. The model was composed of 3D structural bodies (beams and piles) as well as by a 3D soil mesh. Therefore, it correctly models the global interaction under the assumption of linear isotropic materials. The ABAQUS simulations modelled the soil and piles using 3D 8-node linear brick, reduced integration solid elements (C3D8R). The mixed analytical-numerical approach for soil-structure interaction analysis used by Klar and Marshall (2008) was adopted. This ensured that the input soil displacements due to tunnelling in the numerical model were consistent with those used in the Winkler-based model.

The mixed analytical-numerical analysis consists of two stages. In the first stage, all nodes of the soil model are forced to displace according to a chosen input for greenfield settlements and the reaction forces of the nodes (nodal forces required to produce the applied displacements) are recorded. In the second stage, the model is returned to its original condition (before deformation) and the selected structure is added to the model. The nodal reaction forces recorded in the previous stage are then applied to the model which includes the added structure. Any difference in soil displacements between the two stages of the model is due to the existence of the added structure (piles and superstructure). All other aspects of the ABAQUS model were consistent with the assumptions adopted in the Winkler-based model; tie connections at soil-pile interfaces, linear elastic isotropic materials, no contact between the soil and superstructure, and weightless materials. Furthermore, the model dimensions were set to ensure that boundary conditions did not affect results.

6.2.3 Validation test results

6.2.3.1 Simple beam model

A comparison of the ABAQUS and Winkler-based model results for the simple beam analyses are presented in Figure 6.4 for different values of soil and equivalent structure stiffness, as well

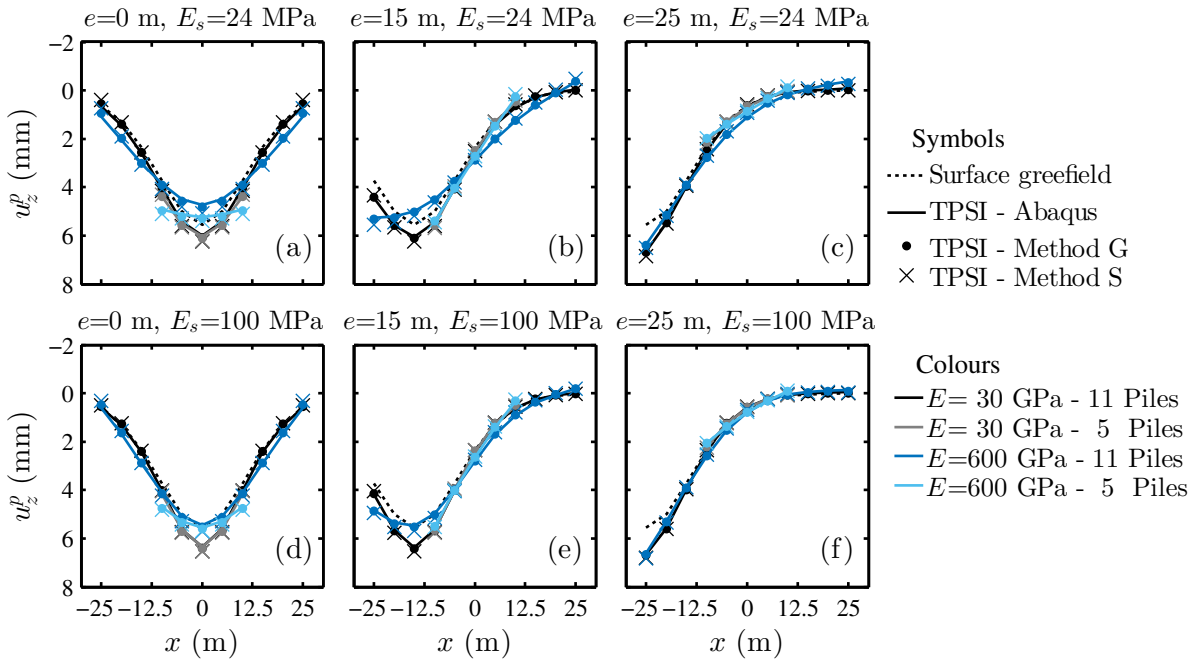

Fig. 6.4 Validation test results: simple beam models.

as building location. For comparison, greenfield ground movements (at the surface) are also plotted (see black dashed lines).

Figure 6.4 shows that the results obtained with method G match the ABAQUS results; method S gives a good and generally slightly conservative assessment of the tunnelling-induced deformation profile. The difference between the ABAQUS and Winkler model predictions was assessed using Δ_i (Equation (6.7)), which is the absolute value of the ratio between the difference in pile settlement estimation with the ABAQUS and the Winkler models and the maximum surface greenfield settlement of the pile group. Figure 6.5 shows that the accuracy is good for method G and acceptable for the simplified method S.

$$\Delta_i = \left| \frac{u_{p,z=0}^{Winkler} - u_{p,z=0}^{Abaqus}}{s_{z,z=0}^{max}} \right| \tag{6.7}$$

Particularly interesting is the settlement profile for the more flexible beam in Figure 6.4(a) and (d) ($E = 30$GPa and 11 pile foundation). The data show that piles with their tips above the tunnel (i.e. within a horizontal offset less than a tunnel radius, R, from the tunnel centreline) settle more than the greenfield ground surface, whereas piles with their tips outside this area settle by approximately the same amount as the greenfield surface, despite the presence of the superstructure. These results fit well with the defined influence zones relating pile response to surface greenfield displacements around a tunnel (see Figure 2.16).

The data illustrate that the superstructure stiffness tends to reduce the maximum relative deflection of the piled structure, where the relative deflection is the distance between the settlement curve and a segment connecting two points of the curve. For instance, in Figure 6.5(b), the

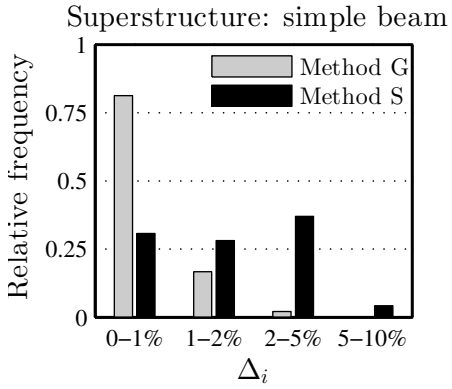

Fig. 6.5 Difference in pile settlement prediction, Δ_i, for simple beams.

settlement of the 5-pile building varies almost linearly with transverse distance, giving near-zero values of relative deflection. Moreover, as expected, the superstructure shows more flexible behaviour when the ratio between soil and structure Young's modulus and/or the ratio between structure width and tunnel depth is high.

6.2.3.2 Framed structure model

A framed structure with isolated ground level columns was chosen for the validation analysis in order to emphasise effects induced by horizontal translations and rotations of the pile heads. This provides further information on the effect of structural configuration to the overall response.

Figure 6.6 compares displacements and rotations of the frame structure model foundation from the Winkler-based and ABAQUS models; surface greenfield data are also included for comparison, when possible. Method S only accounts for the vertical dofs of piles; thus its use is only appropriate for the assessment of induced settlements. Displacements and rotations obtained from the tunnel-pile group interaction (TPI) analysis with a free-pile head condition are also provided in Figure 6.6 to highlight the effect of the frame. The data show good agreement between the ABAQUS results and both method G (u_z^p,u_x^p,φ^p) and method S (u_z^p) predictions. The tunnel-pile interaction analysis again highlights that the piles with their tips directly above the tunnel settle more than the greenfield surface settlements, whereas piles outside this area settle slightly less than the greenfield surface displacements. The reduction of vertical settlements due to the frame stiffness, in this case, is marginal. Furthermore, the shape of the structural settlement trough (i.e. curvature profile) is not altered by the framed building. Horizontal pile head displacements due to tunnel-pile interaction agree in magnitude and distribution with the greenfield values. Horizontal ground movements are transferred to the buildings by the piled foundation and, in the TPSI analysis, frame stiffness is able to reduce the magnitude compared to the TPI displacement curve. Furthermore, rotation distributions estimated in the case of TPI and TPSI differ. Interestingly, despite the connection condition of fixed pile heads, the TPSI pile head rotation distribution is qualitatively opposite to the first derivative of the frame settlement curve for $e = 0$. This aspect and additional influences of the structural configuration

are investigated further in the following section; the focus of this section was to illustrate how the results Winkler-based models compare against the more rigorous ABAQUS model results.

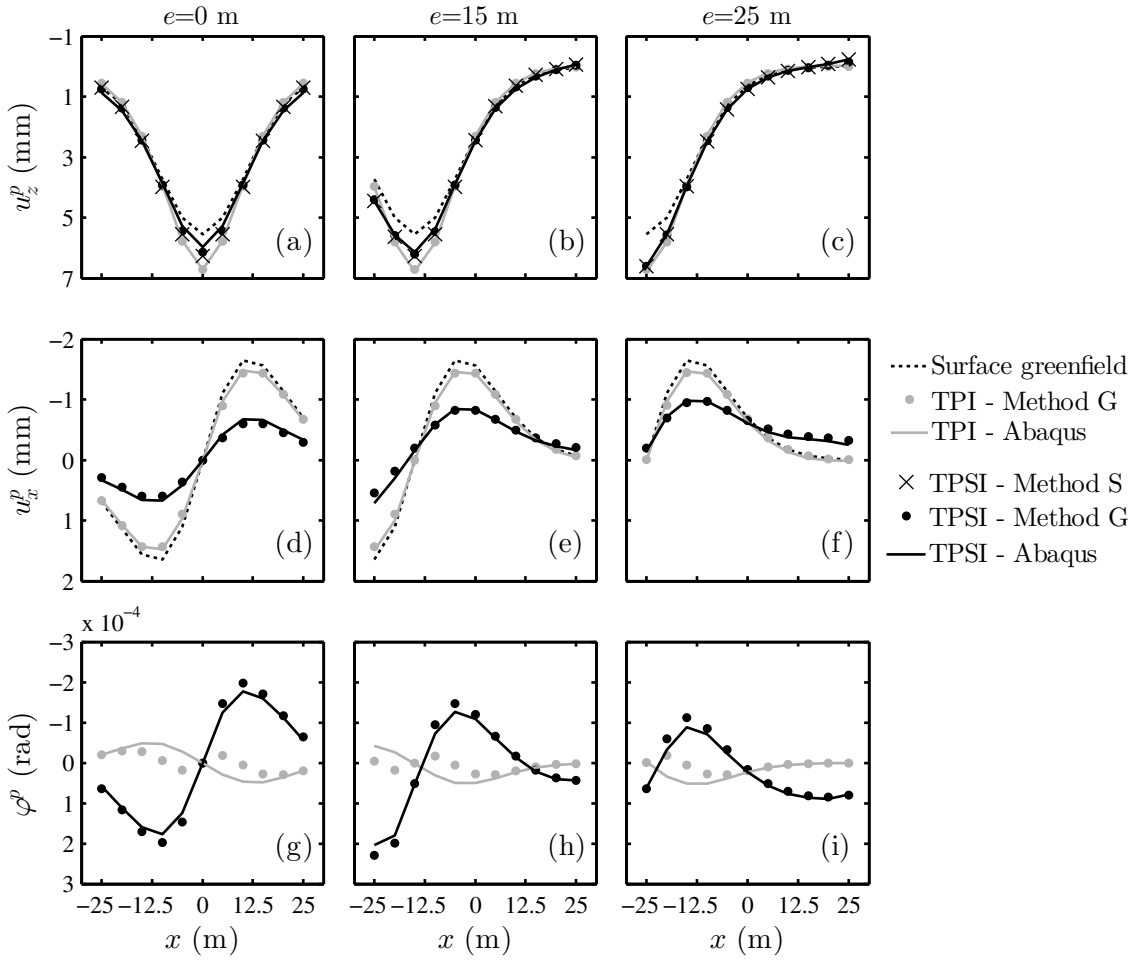

Fig. 6.6 Validation analysis outcomes: framed structure case.

6.3 Structural configuration and pile-structure connection

In this section, results from the 'General Method' of tunnel-pile-structure interaction analysis (TPSI-G) are used to evaluate the influence that structural configuration and pile-structure connection detail have on building displacements. Two building models were analysed: (1) a simple beam and (2) a frame. The parameters adopted for the analyses are summarised in Table 6.1 and results are presented in Figure 6.7. For comparison, greenfield displacements are also plotted. To allow for comparison of results, a unique geotechnical domain (i.e. tunnel, soil, and foundation properties) was assumed. In addition, the two building models were given properties such that maximum settlements obtained in the tunnel-pile-structure interaction analyses were equivalent (i.e. the two buildings models had a similar stiffness). Both fixed-head (FH) and hinged-head (HH) pile-structure connections were implemented. Note that pile head

rotations have no effect on building deformations and internal forces for hinged pile-structure connections.

Table 6.1 Model parameters - effect of structural configuration and pile-structure connection

Tunnel			Foundation and soil			Structure		Beam	Frame
z_t	(m)	20	E_s	(MPa)	24	E	(GPa)	30	30
R	(m)	3	ν_s	(−)	0.5	B	(m)	50	50
$V_{l,t}$	(%)	1	E_p	(GPa)	30	# storeys		/	15
e	(m)	0; 15; 25	d_p	(m)	0.5	h	(m)	/	3
			L_p	(m)	15	b_cxd_c	(m)	/	0.5x0.5
			S_t	(m)	5	b_bxd_b	(m)	/	0.5x0.8
			# piles		11	b_{bg}xd_{bg}	(m)	0.5x4	/

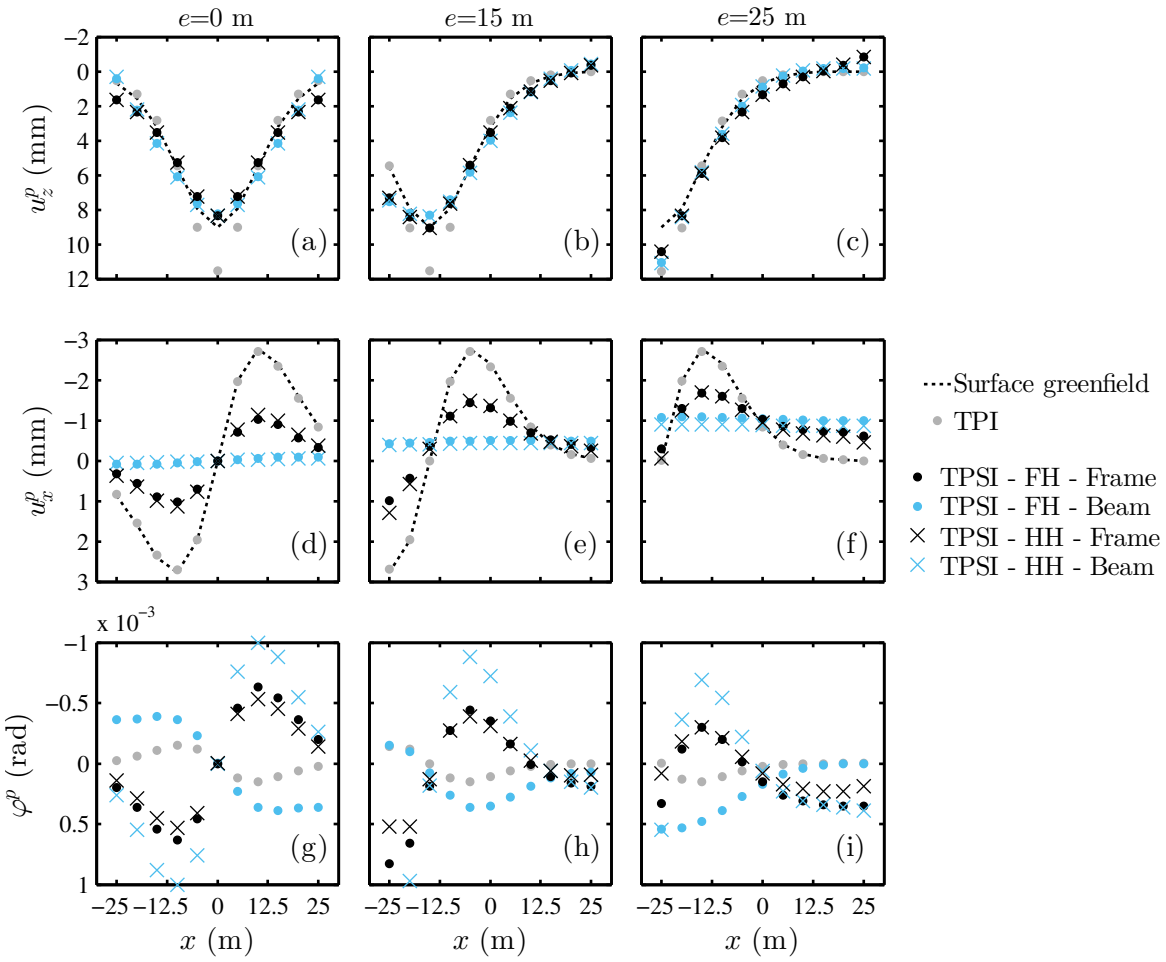

Fig. 6.7 Effect of structural configuration on tunnelling-induced distortions.

An important distinction between simple beams and framed buildings of similar stiffness is that, for the simple beams, the structural bending stiffness is concentrated at the ground level, whereas for frames, it is distributed over several storeys through the action of the columns.

This significantly affects pile head movements and rotations resulting from tunnel-pile-structure interaction.

As illustrated in Figure 6.7(a), (b) and (c), the shape of the framed building settlement curves is similar to that of the TPI curves (i.e. tunnel-pile interaction with no structure included). On the contrary, the stiffness of simple beams tends to have a more significant effect on the settlement curve shape and the resulting width of the building in the sagging and hogging zones, B_{sag} and B_{hog}, respectively. To illustrate the modification of B_{sag} and B_{hog}, the position of the inflection point of the settlement curves in Figure 6.7 are shown in Table 6.2. For the case $e = 0$, the inflection point offset (and therefore magnitude of B_{sag}) is increased, compared to the settlement curve resulting from TPI, more for the beam models than for the frame models. For the case of $e = 25$m, the settlement curve of the simple beam does not have an inflection point at all, indicating that the entire building is in hogging (i.e. $B_{hog} = B$).

Table 6.2 Horizontal offset to inflection point, x_i, of the settlement curves in Figure 6.7(a), (b) and (c).

Case	$e = 0$m	$e = 15$m	$e = 25$m
GF	$\pm$ 9.4	-5.6	-15.6
TPI	$\pm$ 6.2	-8.8	-17.2
TPSI-FH-Frame	$\pm$ 8.2	-7	-17.2; 15.2
TPSI-HH-Frame	$\pm$ 8.2	-7	-17.2; 15.2
TPSI-FH-Beam	$\pm$ 12	-3	-
TPSI-HH-Beam	$\pm$ 12	-3	-

The structural configuration also affects horizontal foundation movements at the surface. As shown by Figure 6.7(d), (e) and (f), the axial stiffness of the simple beam results in negligible horizontal pile head translations, whereas the framed structure is not able to prevent these movements. The horizontal movements obtained with the TPSI analysis is a reduced version of the displacements resulting from the TPI analysis. The frame resists differential pile head horizontal displacements through the bending stiffness of the base columns, which is less effective than the axial stiffness of horizontal structural elements connecting the pile heads in the beam analysis. Interestingly, the moderating effect of the structure on pile head horizontal translations induces an overall building shift towards the tunnel centreline.

Finally, the understanding of pile head rotations, φ^p, requires consideration of two aspects: 1) the degree of fixity of the pile heads, provided by the overall superstructure bending stiffness at the ground level and the pile-structure connections (FH or HH); and 2) the ability of the superstructure to resist any differential horizontal movements of the foundation at the ground surface. When the frame is centred above the tunnel, TPSI analysis pile head rotation distributions are qualitatively opposite to the first derivative of the frame settlement curve (see Figure 6.7(a) and (g) and note that a positive pile head rotation is anticlockwise). Pile-structure connection type (hinged or fixed) has only a marginal influence on results for this case. This happens because ground level columns, which have relatively low bending stiffness, resist differential horizontal

movements between piles (i.e. drag pile heads horizontally) resulting in pile head rotations. On the other hand, for a simple beam, there is a remarkable difference in the rotations induced by hinged and fixed pile-structure connections. When the pile heads are fixed to the beam, the rotation distribution has to follow the first derivative of the settlement curve in Figure 6.7(a) because of the high degree of fixity at the pile heads provided by the beam bending stiffness. For hinged pile heads, relative pile-beam rotations are allowed and the rotation curve shape is similar to that induced by a frame but with higher maximum values because the simple beam is more efficient at reducing horizontal differential movements. Similar interaction mechanisms for pile head rotation are observed when the tunnel is not centred below the building (Figure 6.7(h) and (i)).

Overall, the results shown in Figure 6.7 illustrate that the choice of the structural model can have an important effect on results in a tunnel-pile-building interaction analysis.

6.4 Deflection ratio and horizontal strain modification factors

To put results in the context of the limiting tensile strain framework, this section presents a study of the effects of relative building stiffness on deflection ratio and horizontal strain reduction factors. A parametric study was carried out for both simple beams and framed structures considering several structural configurations, foundation detail (number and length of piles) and building eccentricities. The two-stage analysis Winkler-based method G was used. For each analysis, the computation of the deflection ratios and horizontal strains was performed using greenfield settlements and vertical displacements of the structures at the pile head locations. Horizontal strains were obtained by normalising differential horizontal displacements between two consecutive locations by their relative distance. For the calculation of the building distortions, (Mair et al., 1996) suggested that the considered length of the building should be limited to the practical extent of the settlement trough, which is approximately equal to $2.5i$. The offset of the inflection point at the surface, i, was estimated using $i/R = 1.15\left(z_t/2R\right)^{0.9}$, as suggested by Loganathan and Poulos (1998). This criterion was added to the analyses performed to assess the greenfield and building distortions as well as the modification factors. The results for the framed structures are compared with simple beams using a newly proposed method for determination of relative bending and axial stiffness that accounts for the structural configuration and pile geometrical distribution beneath the building (detailed in the following section). Tables 6.3, 6.4 and 6.5 indicate the range of parameters and structural configurations assumed for the parametric analyses. The previous section (see Figure 6.7), illustrated the importance of pile-structure connections on the global tunnel-pile-structure interaction for simple beams. Therefore, the analyses of the simple beams were performed for two cases: hinged (HH) and fixed (FH) pile head. Frames were only analysed for fixed pile-structure connections because of the secondary role that the rotational restraint has on the global interaction (see Figure 6.7).

Table 6.3 Investigation of modification factors: combination of stiffness for simple beams.

Simple Beam (15 cases)			min	max
Bending stiffness	EI	(kN m^2)	10^4	10^{11}
Axial stiffness	EA	(kN)	10^4	10^{11}

Table 6.4 Investigation of modification factors: soil, tunnel and foundation parameters and configurations.

Tunnel			Foundation and soil		
z_t	(m)	20	E_s	(MPa)	24
R	(m)	3	ν_s	$(-)$	0.5
$V_{l,t}$	(%)	1	E_p	(GPa)	30
e/B	0;0.25;0.5		d_p	(m)	0.5
			L_p	(m)	5;15
			S_t	(m)	5
			# piles		5;11

Table 6.5 Investigation of modification factors: framed structure configurations.

Structure		A	B	C	D
E	(GPa)	30	30	30	30
# storeys			2;4;10;15;30		
h	(m)	3	3	3	3
l	(m)	5	5	5	5
b_cxd_c	(m)	0.2x0.2	0.3x0.3	0.5x0.5	0.7x0.7
b_bxd_b	(m)	0.2x0.2	0.3x0.5	0.5x0.8	0.7x1.0
b_{bg}xd_{bg}	(m)		Absent		

For each analysis, the computation of the greenfield and building deflection ratio in the sagging and hogging zones was performed by: 1) curve fitting the greenfield settlements and structure vertical displacements at the pile head location; 2) identifying the inflexion points of the two curves; 3) calculating, in the hogging and sagging zone, the relative deflection as the maximum distance between the settlement curve and the segment connecting the edges of the hogging/sagging zone; and 4) normalizing the relative deflections by the length of the building in the hogging/sagging zone to obtain the deflection ratio. On the other hand, greenfield and structural horizontal strains were calculated, respectively, at the locations of the pile heads and at the pile heads. Strains were obtained by normalizing the greenfield and structural horizontal differential displacement between two consecutive locations by their distance.

6.4.1 Deflection ratio and relative bending stiffness

6.4.1.1 New relative bending stiffness parameters for piled structures

For piled foundations, it is not possible to simplify the problem to a plane-strain condition. In order to define a suitable relative bending stiffness factor, the problem of a structure on a single pile row foundation is first considered (see Figure 6.8(a)). For a single transverse pile row the entire superstructure contributes to the stiffening of the soil-foundation system, leading to the necessity to consider EI rather than EI^* (per m run) as defined by Franzius et al. (2006) and Farrell (2010). Therefore, in these cases, the use of the following relative bending stiffness parameters are more appropriate:

$$\rho^r_{sag} = \frac{EI}{E_s B^3_{sag}} \quad || \quad \rho^r_{hog} = \frac{EI}{E_s B^3_{hog}} \quad [\text{m}] \tag{6.8}$$

This relative stiffness parameter ρ^r, where the superscript r denotes a single pile row, has dimension of length. It is not possible to use a dimensionless term for this problem because a superstructure of finite longitudinal length interacts with the soil only through the pile row that is discrete along the longitudinal tunnel direction.

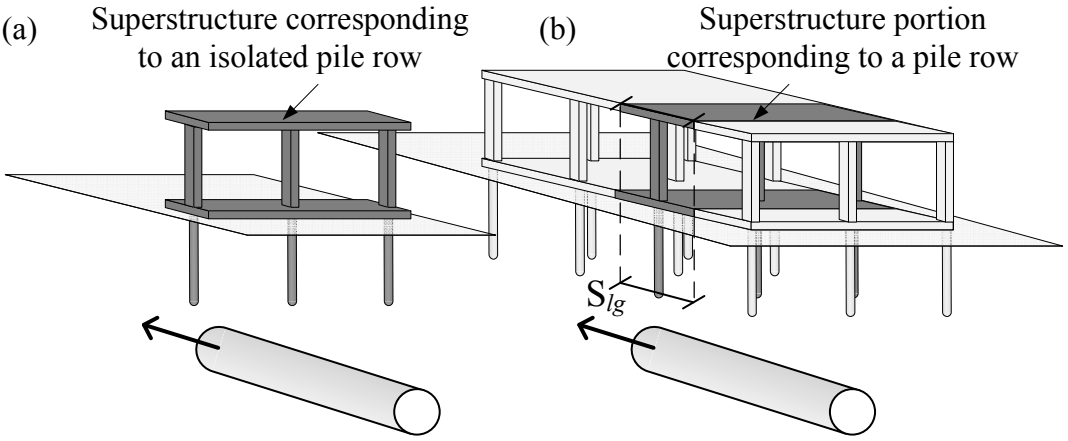

Fig. 6.8 Simplified approach to reduce m x n piled foundation problem to a single pile row.

On the other hand, pile foundations are generally composed of multiple transverse pile rows. In these cases, the analysis may be simplified to that of a single pile row beneath a portion of a building or an equivalent frame. For instance, the building may be separated into independent portions corresponding to each transverse pile row (see Figure 6.8(b)). This simplification is sensible when only the final building transverse deformation profile is considered (i.e. when the tunnel has passed the location of the building). By multiplying the expressions shown in Equation (2.58) by the ratio between longitudinal spacing of transverse pile rows, S_{lg}, and building longitudinal length, L, the following definitions of relative bending stiffness of buildings with multiple pile rows are obtained

$$\rho^p_{sag} = \frac{EI}{E_s B^3_{sag}} \frac{S_{lg}}{L} \quad || \quad \rho^p_{hog} = \frac{EI}{E_s B^3_{hog}} \frac{S_{lg}}{L} \quad [\text{m}] \tag{6.9}$$

where $EI(S_{lg}/L)$ is the bending stiffness of the superstructure portion corresponding to the considered transverse pile row (in kN m^2). This approach permits a direct comparison of ρ for shallow foundations to ρ^p for pile foundations. By definition, the relative stiffnesses may be evaluated from

$$\rho_{sag} = \frac{\rho^{p;r}_{sag}}{S_{lg}} \qquad || \qquad \rho_{hog} = \frac{\rho^{p;r}_{hog}}{S_{lg}} \tag{6.10}$$

This definition will be used in a subsequent section to relate design charts proposed for buildings on shallow foundations to the outcomes of the tunnel-pile-structure interaction analyses presented here. Moreover, to facilitate the description of the results, the terms primary and secondary deformation modes are used as follows: for low eccentricity cases, primary=sagging and secondary=hogging; for high eccentricity cases, primary=hogging and secondary=sagging.

6.4.1.2 Deflection ratio of simple beam and frame models

The deflection ratio modification factors calculated from the parametric study results, M^{DR} (Equation (2.55)), are plotted against the relative bending stiffness in Figures 6.9 and 6.10. Because the analyses are performed for a single pile row, relative bending stiffness is described in terms of ρ^r, defined in Equation (6.8), rather than ρ^p. Figures 6.9 and 6.10 present the results for a building with a transverse width $B = 20$ and 50m, respectively. In each case, two pile lengths, $L_p = 5; 15$m, corresponding to relatively short and long piles with respect to the tunnel depth ($L_p/z_t = 0.25; 0.75$) were implemented and three normalised eccentricities were considered ($e/B = 0; 0.25; 0.5$). In these analyses, the building deformation mode is primarily sagging for $e/B = 0$ whereas it is mainly hogging for $e/B = 0.5$. In order to demonstrate the effectiveness of the column stiffening factor (Equation (2.61)) in predicting the frame equivalent bending stiffness, Equation (2.62) was used to estimate EI of the framed structures and results from the frame analyses are plotted together with those from simple beam analyses. Modification factors of frames are plotted as points whereas those of simple beams are represented with a curve. Finally, the upper charts display the variation in M^{DR} for hinged pile-simple beam connections (HH) whereas the lower charts refer to fixed pile-simple beam connections (FH). Frames are only analysed for fixed pile-structure connections (FH) because, as shown in the validation section, pile-structure connections have secondary effects on the response of framed buildings.

Figures 6.9 and 6.10 illustrate that reduction factors are highly dependent on building eccentricity, e/B. Another important parameter is the relative pile length, L_p/z_t; data show a marked rise of M^{DR} for a given case with an increase of L_p/z_t in both primary and secondary deformation modes (e.g. Figures 6.9 and 6.10(a) and (d)), except for the secondary sagging deformations at high normalised eccentricity $e/B = 0.5$ (see Figures 6.9 and 6.10(c) and (f)). Therefore, relatively long piles represent a greater potential for building damage in this context.

Furthermore, in both Figures 6.9 and 6.10, the modification factor trends reveal qualitative differences between the case of simple beams and framed buildings. Framed buildings undergo a gradual reduction of M^{DR} with relative bending stiffness in both hogging and sagging zones;

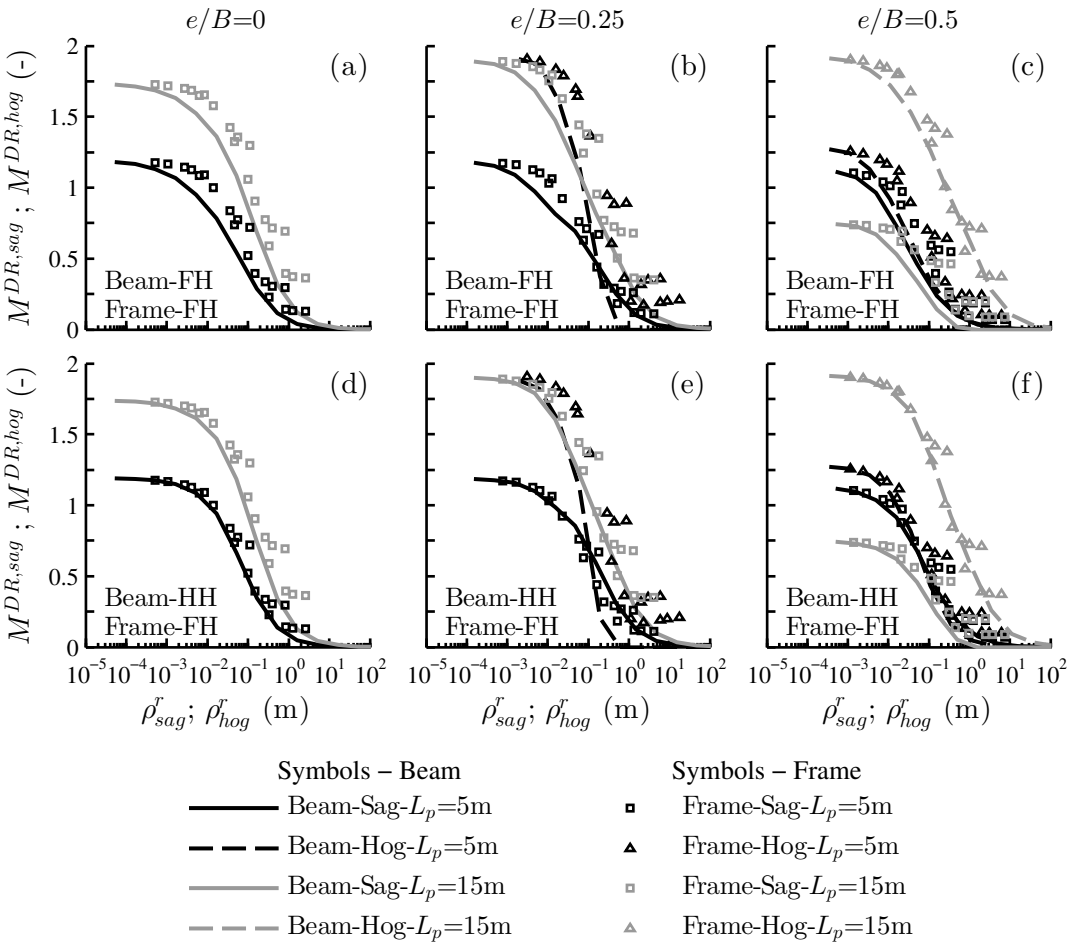

Fig. 6.9 Effects of building stiffness on M^{DR} for $E_s = 24$MPa and B=20 m.

on the contrary, in the case of simple beams with both fixed and hinged pile connections, the charts show that the structural deformation follows a more complex pattern, which is due to the structural continuity of the building, preventing it from responding independently in the hogging and sagging zones. For instance, in the case of a central tunnel ($e/B = 0$) and building width $B = 50$m (see Figures 6.10(a) and (d)) hogging and sagging curves show complex and interrelated trends. After an initial decrease of both reduction factors, at approximately $\rho^r = 10^{-1}$m, there is a sharp drop of the hogging curve whereas the sagging one remains steady up to $\rho^r = 10^0$m. When the hogging reduction factor reaches a value close to zero, which means that the structure is undergoing a fully sagging deformation mode, any increase in structural bending stiffness contributes to further reduce the sagging reduction factor. Figure 6.10 demonstrates that, for simple beams in both sagging and hogging greenfield zones, the structural stiffness is more efficient in the reduction of the secondary deformation mode (the hogging *DR* for low eccentricity buildings and the sagging *DR* for high eccentricity buildings). This outcome agrees with the results of centrifuge and numerical modelling analyses performed by Franzius et al. (2006) and Farrell et al. (2014), who studied the deformation induced by tunnelling on simple shells and plates, respectively. On the other hand, this may not be true for framed structures that,

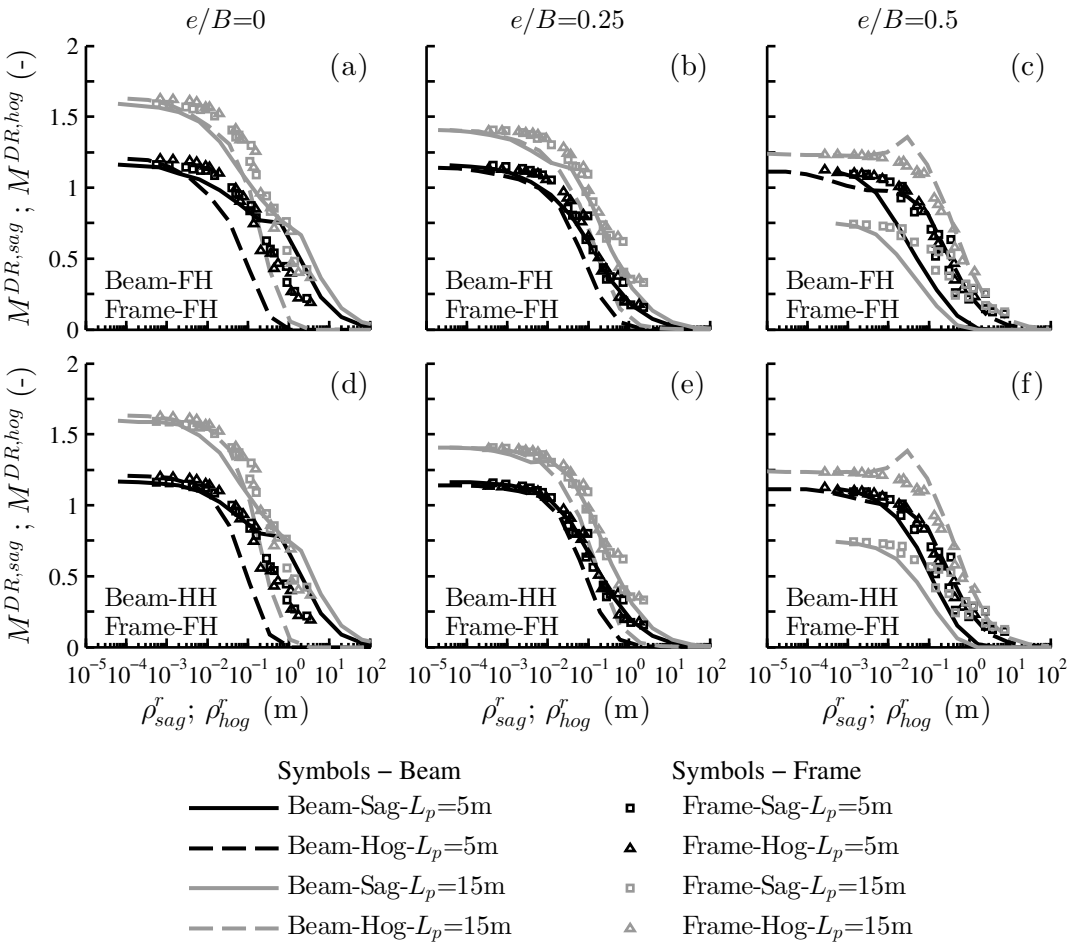

Fig. 6.10 Effects of building stiffness on M^{DR} for $E_s = 24$MPa and B=50 m.

in this study, show a gradual reduction of DR in both deformation zones with the increase of relative stiffness. In general, although the relative stiffness ρ^r accounts indirectly for the tunnel location through B_{sag} and B_{hog}, detailed design charts should be a function of e/B and structural configuration.

Additionally, comparison of results for frames and simple beams illustrates the importance of the pile-structure connection condition. For both sagging and hogging deformation modes, when beams are fixed to the pile heads (FH), most modification factors of the frames are higher than the respective curves for simple beam models (i.e. simple beams have a stiffer response than frames). When hinged connections (HH) are adopted for the simple beams, the difference reduces and results of both structural configurations show a fair agreement (as long as the reduction trends do not diverge due the structural configuration). These results suggest that the structural scheme based on simple beams pinned to the pile heads is the most suitable to be used as an equivalent structure for piled framed buildings without horizontal structural elements at the ground level, although a different building response to tunnelling should still be expected. This occurs because frames without a stiff raft are not able to provide a high level of bending resistance at the pile heads. Secondly, fixed pile-structure connections contribute more than hinged connections to the

stiffening effect of the superstructure; this is because the bending stiffness of the piles contributes to the resistance against building deformation, whereas for hinged connections there would not be this stiffening contribution of the pile foundation.

6.4.2 Horizontal strains and relative axial stiffness

Because tunnelling results in the horizontal displacements of a deep foundation with a free-pile head condition, simple beams and framed buildings with piled foundations may undergo significant horizontal strains. This section investigates the effects of structural configuration and pile-structure connections on horizontal strain modification factors, M^{ε}, defined by Equation (2.56), and introduces a unique dimensionless axial stiffness parameter for both simple beams and frame buildings. As for the analysis of relative bending stiffness, the case of a structure on a single pile row is considered. When the building has multiple transverse pile rows, it is necessary to distribute the building stiffness between the pile rows, as shown in Figure 6.8(b), in order to consider the appropriate portion of the building. To account for the axial stiffness of either a simple beam or a horizontal structural element connecting pile heads in framed buildings, the structural scheme shown in Figure 6.11 was considered. This consists of a portal with a beam at the ground level connecting two pin-supports. The axial stiffness of this beam is referred to as EA_{bg}. As shown in the validation section, for piled foundations, the pile-structure connection has a negligible effect on horizontal movements and therefore strains. As a result, the conservative structural scheme based on pin-supports may be considered to be representative. Similar to Goh and Mair (2014), the frame stiffness factor, α_f, is defined by imposing a unit differential horizontal displacement, Δ, between the pin-supports and calculating the external horizontal reaction force, H', resulting in

$$\alpha_f = \frac{H'}{\Delta} = \frac{3K_bK_c}{h^2\,(2K_b+3K_c)} + \frac{EA_{bg}}{l} \qquad [\mathrm{kN/m}] \tag{6.11}$$

The first term of α_f represents the contribution of the portal to the overall axial stiffness of the building at the ground level whereas the latter relates to the contribution of a simple beam. To account for the soil stiffness, it would be appropriate to define the relative axial stiffness as

$$\alpha_f^* = \frac{1}{E_s}\left[\frac{3K_bK_c}{h^2\,(2K_b+3K_c)} + \frac{EA_{bg}}{l}\right] \qquad [\mathrm{m}] \tag{6.12}$$

Interestingly, the second term of this expression is similar to $\alpha^*_{mod} = EA/(E_sBL)$ (Equation (2.57)), with the bay length l instead of the building width B and the longitudinal building length L omitted (which is sensible considering that the soil interacts with the piles and not directly with the entire superstructure).

The cases presented in Tables 6.3, 6.4 and 6.5 were also used for this analysis. Figure 6.12 plots, for both beams and frames, the calculated values of $M^{\varepsilon h}$ against α_f^*, defined using Equation (6.12). Results illustrate that horizontal strain reduction factors are not affected by the pile length, L_p, but are influenced by building transverse width, B, and building normalised

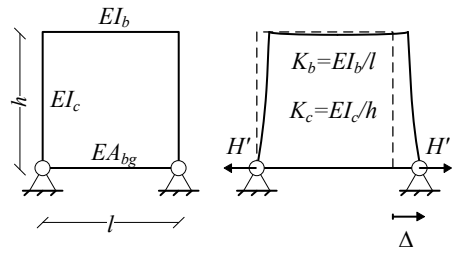

Fig. 6.11 Portal response analysis to a differential horizontal displacement of the supports.

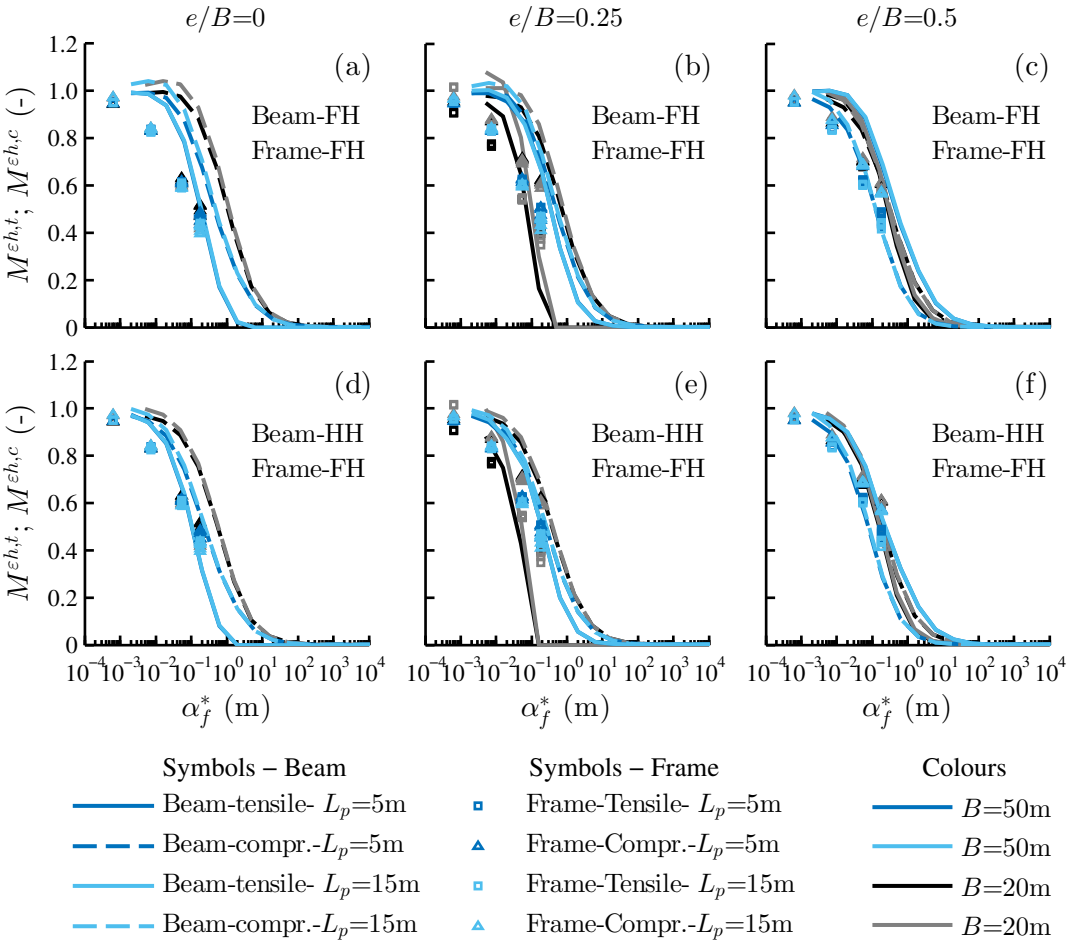

Fig. 6.12 Effects of building stiffness on $M^{\varepsilon h}$ for $E_s = 24$MPa and B=20, 50 m.

eccentricity, e/B. Moreover, Figure 6.12 indicates three notable points. Firstly, the distribution of the results demonstrates the efficiency of horizontal ground level structural elements to reduce horizontal strains (for the given soil-pile foundation system, a wide range of simple beams are able to achieve a value of $M^{\varepsilon h} = 0$, whereas the stiffest frames are only able to reduce $M^{\varepsilon h}$ to 0.4). Secondly, despite the similar trend of results for simple beams and frames, most results from the frames are below those of the simple beams; this may be due to the assumed simplified structural scheme that consists of a single-span one-storey portal, which neglects the frame complexity. The α_f^* term does not accurately account for the structural configuration; the design charts proposed in the following section are therefore a function of the structural configuration. Finally, the minor

effects of pile head connection (hinged or fixed) to the superstructure, discussed in the previous section, is once again confirmed (by comparing results in Figure 6.12(a), (b) and (c) with results in Figure 6.12(d), (e) and (f)). However, in general, for simple beam structures, at a given relative axial stiffness, the reduction factors $M^{\epsilon h}$ are slightly higher for the fixed pile-structure condition than for the hinged connection.

6.4.3 Proposed envelopes for modification factors

An additional extensive parametric analysis was conducted to provide design charts for estimation of the modification factors due to tunnelling beneath piles. Attention was focused on the geotechnical domain by considering a wide range of parameters for the piled foundations and the soil; Table 6.6 summarises the considered soil-pile foundation configurations. The superstructure properties, both simple beams and frames, were defined as in the previous section (see Tables 6.3 and 6.5). Only fixed pile-structure connections were implemented. The relative bending stiffness ρ^r and the relative axial stiffness α_f^* indicated in Equations (6.8) and (6.12) were adopted. Because the tunnel-building eccentricity influences the modification factors, results for different values of e/B are distinguished in the proposed charts with different marks. The proposed envelopes may be useful for engineers to conduct a preliminary risk assessment.

Table 6.6 Parameters and configurations for the parametric study.

Tunnel			Foundation and soil		
z_t	(m)	20	E_s	(MPa)	5;25;100
R	(m)	3	ν_s	$(-)$	0.5
$V_{l,t}$	(%)	1	E_p	(GPa)	30
e/B	0;0.25;0.5		d_p	(m)	0.5;1
			L_p	(m)	5;15
			S_t	(m)	5;10
			# piles		5;10;25

6.4.3.1 Deflection ratio modification factors

The results of M^{DR} from the full parametric study are plotted in Figure 6.13 against ρ^r, which is equivalent to $S_{lg}\rho$ (Equation (6.10)). Included in the figure is a proposed upper and lower design envelope. Reduction factors associated with an absolute value of DR_{gf} lower than $2 \cdot 10^{-3}\%$ were omitted because they do not have potential for damage and the ratio M obtained with a small denominator should not be considered representative. The results in sagging and hogging regions are provided in the left and right plots of the figure, respectively. To highlight the influence of relative pile length L_p/z_t on the global interaction, results are distinguished between relatively short and long piles. Considering the relative bending stiffness of the building, the outcomes suggest that for piled structures, a fully flexible response is expected up to about $\rho^r = 10^{-3} - 10^{-2}$m, depending on relative pile length (Figure 6.13). Note that the values of the

upper and lower envelopes begin to decrease for $\rho^r > 10^{-2}$m. This indicates that performing a tunnel-pile interaction analysis, which neglects the contribution of the structure, may be overly conservative when $\rho^r > 10^{-2}$m. Buildings start to experience negligible deformations (i.e. a fully rigid response) within the range of about $\rho^r = 10^0 - 10^2$m. At a given relative building stiffness, buildings on relatively long piles are more likely to undergo higher deflection ratios than buildings on short piles. Generally, the increase of M^{DR} with L_p/z_t is due to subsurface movements having a greater effect. However, this does not apply to the estimation of $M^{DR,sag}$ in the case of relatively long piles where $e/B = 0.5$ (see Figure 6.13(a) where values of $M^{DR,sag}$ fall below the lower envelope). The presence of these outliers is probably due to the efficiency of simple beams to reduce deformations due to the secondary deformation mode.

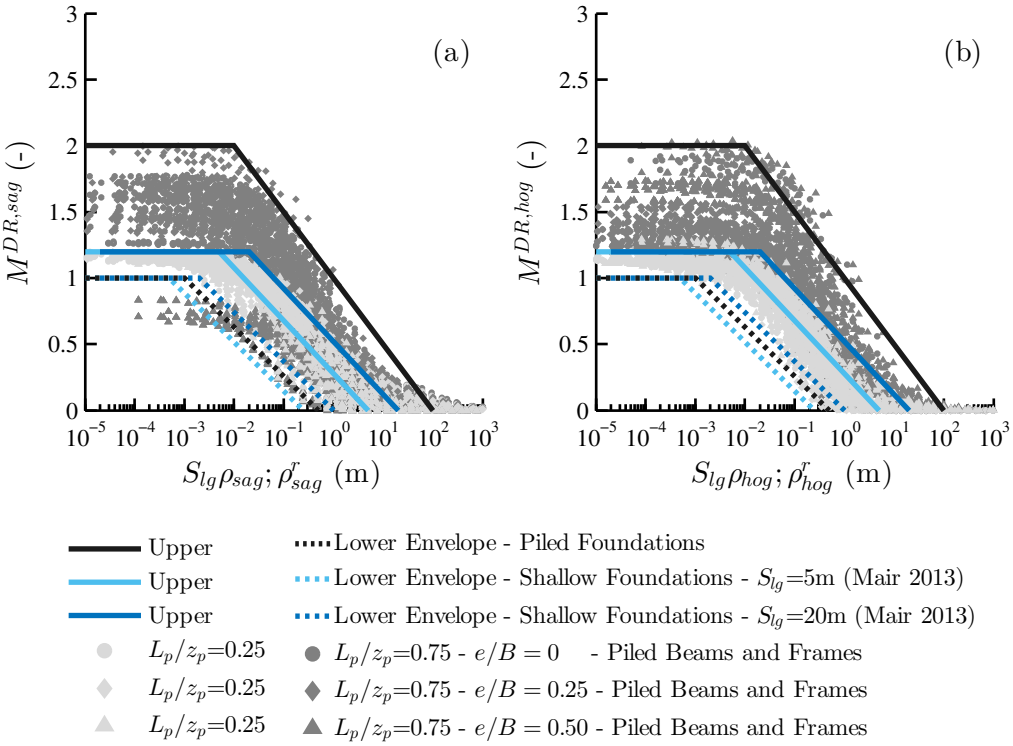

Fig. 6.13 Proposed envelopes for the estimation of M^{DR} for piled foundations.

To highlight the effect of piles, the envelopes suggested by Mair (2013) for shallow foundations are also plotted in Figure 6.13 considering $\rho^r = S_{lg}\rho$ and assuming a longitudinal spacing between pile rows of $S_{lg} = 5$ and 20m to cover a realistic range of pile spacing. In the chart, the magnitude of the envelope translation due to S_{lg} is minor because of the logarithmic scale of the x-axis. The proposed lower envelope is comparable to that obtained by Mair (2013) for shallow foundations; this is probably due to the fact that relatively short piles are mostly affected by the distributions of surface greenfield movements, similar to the case of buildings on rafts and footings. In contrast, the upper envelopes for shallow and deep foundations illustrate the considerable detrimental role played by piled foundations in tunnel-building interaction, especially for flexible structures.

6.4.3.2 Horizontal strain modification factors

Upper and lower envelopes of the horizontal strain modification factor, $M^{\varepsilon h}$, are plotted in Figure 6.14 together with results of the full parametric investigation. Results are distinguished between relatively short and long piles and for simple beam and frame models.

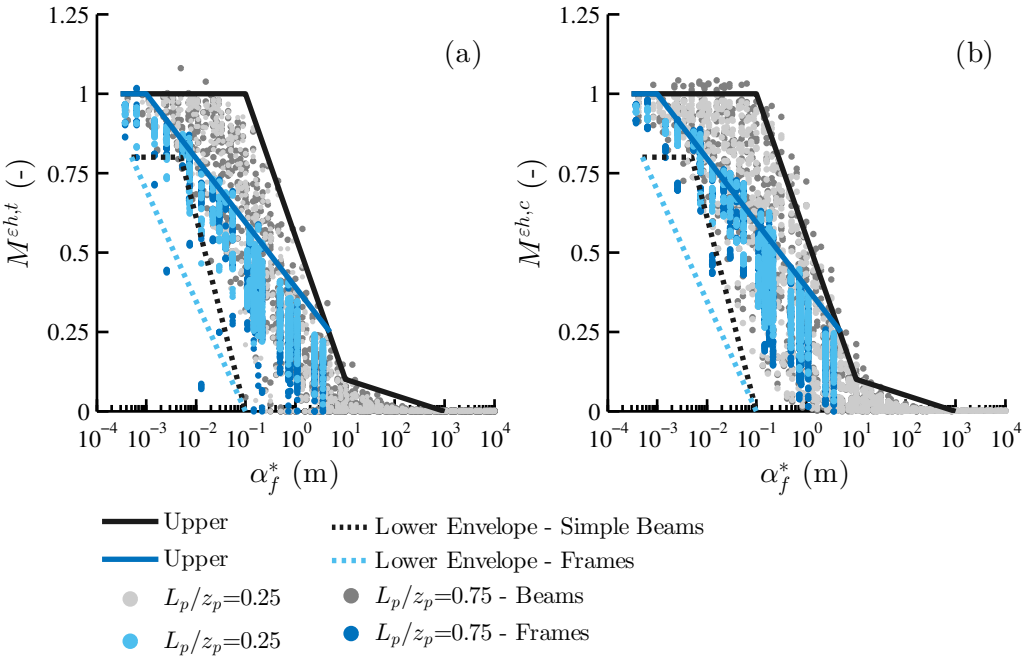

Fig. 6.14 Proposed envelopes for the estimation of $M^{\varepsilon h}$ for piled foundations.

Results in Figure 6.14 illustrate the secondary effect of L_p/z_t on $M^{\varepsilon h}$. On the contrary, there is a marked difference in the reduction trends of piled beam and frame models: $M^{\varepsilon h}$ for beam models may be higher than for frames at a given relative axial stiffness. Despite this, Figure 6.14 indicates the suitability of the dimensionless modification factor α_f^* in describing the building contribution to the reduction of differential horizontal displacements between pile heads for several soil and foundation configurations. To account for the structural scheme, two distinct upper envelopes are proposed for beams and frames, as shown in Figure 6.14. In general, neglecting the effects of piles for fully flexible structures may be adequate because the maximum recorded value of $M^{\varepsilon h}$ was only slightly higher than unity. On the other hand, for partially flexible beams with $\alpha_f^* > 10^{-1}$m and partially flexible frames with $\alpha_f^* > 10^{-3}$m, reduction factors decline steadily; assuming greenfield horizontal strains would be overly conservative in these cases. A rigid building response should be expected for $\alpha_f^* > 10^{3}$m.

Based on the envelopes for simple beams shown in Figure 6.14, it is interesting to notice that a rigid response is observed in most practical cases of piled structures with horizontal structural elements at the ground level. For instance, a simple beam with a 0.25×0.25m^2 cross-section and $E = 30$GPa has an axial stiffness of $1.9 \cdot 10^6$kN. If the building model consists only of these beams and E_s and l are assumed to be 25MPa and 5m, respectively, the relative axial stiffness of the system is $\alpha_f^* = 1.5 \cdot 10^1$m, which is associated with very low value of $M^{\varepsilon h}$ in Figure 6.14.

Therefore, horizontal ground strains transferred into a piled superstructure with continuous horizontal structural elements at the ground level would be negligible unless an unrealistically small axial stiffness is considered. On the contrary, as indicated by Goh and Mair (2014) for frames on single footings, in the case of piled frame structures without ground level strips or rafts, differential horizontal movements between pile heads are expected, which may induce damage in non-structural elements, such as infill walls, or to the ground floor columns. However, horizontal strains should be negligible at the first floor level (i.e. at the top of the ground level columns) because of the constraint provided by the axial stiffness of the first-floor beam/slab.

6.5 Conclusions

A study of the tunnel-piled building interaction has been presented in this chapter based on elastic Winkler-based Two-Stage Analysis Methods (TSAMs). Analyses were limited to the case of tunnelling beneath piled elastic frame structures or simple equivalent beams. Results for varying levels of soil and structural stiffness, structural configuration, and relative foundation-tunnel location compared well with results from 3D FEM numerical models. The Winkler-based TSAMs allow for a remarkable reduction of the computational cost compared to 3D FEM analyses and represent a reliable and versatile tool for parametric studies. The proposed analysis approach allows for a detailed structural analysis that can evaluate the deformations of each member of the superstructure (i.e. beams and columns). This results in a more detailed damage assessment compared to a preliminary analysis based on the limiting tensile strain method, which only evaluates the overall degree of damage within the building.

Extensive parametric analyses highlighted the role of tunnel-pile interaction and the superstructure in the global tunnel-soil-building system response. Design charts were developed as a practical guidance to estimate deflection ratio and horizontal strain modification factors depending on relative bending and axial stiffness, respectively. New bending and axial relative stiffness factors were proposed to account for the presence of the piles and allow comparison of frame axial stiffness to that of simple beams. To reduce the gap between the upper and lower envelopes in design charts and provide a more efficient assessment, it would be necessary to define a relative stiffness factor able to account for tunnel-structure eccentricity, structure configuration and further pile foundation parameters. The following conclusions can be drawn from the results provided in the chapter.

- Vertical settlements are mainly induced by tunnel excavations beneath piled structures. The stiffness of buildings has a significant effect on the pile settlements and the resulting building deflections; assuming that the building as a fully flexible structure (i.e. performing a tunnel-pile interaction analysis) can be overly conservative. Tunnelling-induced horizontal strains in the superstructure are negligible in the case of a continuous foundation at the ground level (i.e. strips or raft) whereas they may be significant in framed buildings when pile heads are not connected by horizontal structural elements. In this case, the horizontal

movement distribution obtained with the tunnel-pile-structure interaction analysis is a moderated version of the displacements resulting from the tunnel-pile interaction.

- The structural configuration is very important; a different response for a piled simple beam and a piled frame is expected. In particular, the structural stiffness of simple beams was found to be more efficient in reducing deformations associated with the secondary inflection mode (i.e. hogging for low eccentricity cases and sagging for high eccentricity cases). Framed structures exhibited a gradual reduction of deformations in hogging and sagging but preserved the shape of the settlement curve even for relatively stiff structures. Neither the response nor the damage of framed buildings can be fully described using a simple beam model.

- The pile-structure connection (hinged or fixed pile heads) plays an important role in tunnel-pile-structure interaction for simple beams and structures whose stiffness is concentrated at the ground level (i.e. frame structure with piled raft foundation). The pile-to-structure connection effect is secondary for framed buildings when pile heads are isolated or connected by slender elements, which is probably due to the relatively low bending stiffness of columns. Furthermore, the results of tunnel-pile-structure interaction analyses suggest that hinged pile-structure connections should be adopted in equivalent simple beam analyses of framed building with relatively low bending stiffness at the ground level (for instance, without continuous strips or a raft).

The results provided in this chapter are based on the simplifying assumptions of soil linearity and perfect bonding between the pile and soil. Therefore, this work represents a first step towards the understanding of the global tunnel-pile-structure interaction. Further investigations should be carried out to clarify the influence of ground conditions, tunnel volume loss level, superstructure self-weight, and tunnel head excavation advancement on the global tunnel-pile-structure interaction. However, the chapter provides important insight into the problem of tunnelling beneath piled structures and contributes to the definition of the key interaction phenomena and parameters involved in the tunnel-piled building response.

Chapter 7

Tunnelling beneath piles and piled frames

Previous research has provided methods for the prediction of settlements and loss of bearing capacity of existing piles due to tunnel excavation; however, few studies have recognised the importance of pile safety factor and load redistribution due to superstructure action on the tunnel-pile foundation interaction. Therefore, the understanding of the contribution of deformable superstructures (in terms of stiffness and self-weight) to the global response has not yet been achieved.

This chapter aims to illustrate the response to tunnelling of axially loaded displacement and non-displacement pile foundations for various and complex construction scenarios. Data are provided from a series of geotechnical centrifuge tests carried out at 60g of tunnel excavation beneath piles and piled frames in dry silica sand. Tunnelling beneath piles is a critical scenario because there is potential for pile failure and differential pile settlements amongst a transverse row of piles within a foundation system. This group of tests (referred to as series 2) was performed using the coupled centrifuge and numerical modelling (CCNM) technique and the experimental equipment illustrated in Section 3.3.

The performed tests are listed in Table 7.1, which provides details on pile load conditions, geometry and tested configurations (shown in Figure 7.1). The note column of Table 7.1 is used to describe the tests with TPI = tunnel-pile interaction, TPGI = tunnel-pile group interaction, TPSI = tunnel-pile structure interaction. Single piles and pile foundations were tested at varying levels of initial safety factor (ratio between pre-tunnelling bearing capacity and applied service loads) and, in the case of piled frames, for varying load redistributions due to superstructure stiffness. In group 2C, piles in positions 1, 2, and 3 were tested (see Figure 7.1 for the position definition). Note that only piles in positions 1 and 2 have their tips located within the influence zones defined by Jacobsz et al. (2004) where large pile settlements may be induced by tunnelling. In test group 2D, the transverse pile row consisted of four piles located in positions 1, 2, 3, and 4. The prototype superstructure consisted of an 8 storey concrete frame ($E = 30$GPa) with a storey height, h, and a span length, S_t, of 3 and 4.5m, respectively. Four different superstructures were implemented; FR00 indicates a fully flexible frame (which does not provide reaction forces to base displacements); FR30, FR50 and FR70 indicate frames in which beam and column elements have square cross-sections of 0.3×0.3m, 0.5×0.5m, and 0.7×0.7m, respectively. Initial pile

loads, P_0, were set equal to 500N, which corresponds to 1.8MN at prototype scale (this is a likely value for an 8 storey frame and is compatible with the foundation performance resulting in $SF_0 = 1.5$ and 2 for non-displacement and displacement piles, respectively).

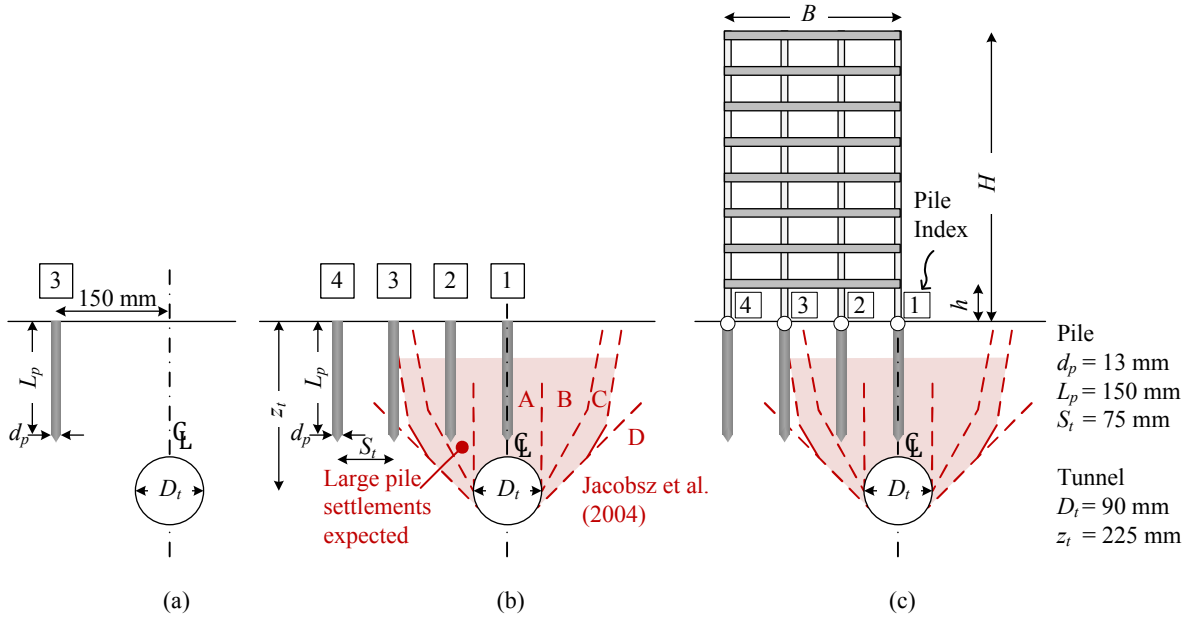

Fig. 7.1 Test layout (in model scale): (a) loading tests, (b) tunnelling beneath a single pile, and (c) tunnelling beneath a piled frame (the geotechnical domain is modelled in the centrifuge, whereas the frame is modelled numerically).

This chapter is structured as follows. Section 7.1 reports results of test groups B and C; this section describes the pre-tunnelling load-displacement curves of isolated displacement and non-displacement piles, followed by a discussion of the influence of installation method, pile location and pile safety factor on tunnelling-induced settlements of isolated piles. Section 7.2 investigates the response of piled frames to tunnelling for a building stiffness varying from fully-flexible to rigid; in particular, load redistribution mechanisms are assessed and their effects discussed. In both sections, the greenfield settlements are used for comparison. Section 7.3 discusses current definitions of pile failure and the role of pile-pile interaction in the global tunnel-piled building interaction. Finally, Section 7.4 summarises the main findings of the chapter. All results and model dimensions are reported in model scale unless stated otherwise.

Table 7.1 Summary, in model scale dimensions, of centrifuge experiments for test series 2 performed at 60g.

Test series	Label (# tests performed)		Pile type †	Pos. #	Offset x (mm)	Serv. Load P_0 (N)	Capacity‡ Q_0 (N)	SF_0 (-)	Note
2A	GF	(1)	-	-	-	-	-	-	GF
2B	LP	(3)	N	3	150	-	-	-	Loading
2C	N1SF1.5	(1)	N	1	0	493	740	1.5	TPI
2C	N1SF2.5	(1)	N	1	0	296	740	2.5	TPI
2C	D1SF1.5	(1)	D	1	0	667	1000	1.5	TPI
2C	D1SF2.5	(1)	D	1	0	400	1000	2.5	TPI
2C	N2SF1.5	(1)	N	2	75	493	740	1.5	TPI
2C	N2SF2.5	(1)	N	2	75	296	740	2.5	TPI
2C	D2SF1.5	(1)	D	2	75	667	1000	1.5	TPI
2C	D2SF2.5	(1)	D	2	75	400	1000	2.5	TPI
2C	N3SF1.5	(1)	N	3	150	493	740	1.5	TPI
2C	N3SF2.5	(1)	N	3	150	296	740	2.5	TPI
2C	D3SF1.5	(1)	D	3	150	667	1000	1.5	TPI
2C	D3SF2.5	(1)	D	3	150	400	1000	2.5	TPI
2D	NGSF1.5FR00	(1)	N	1-4	0-225	500	740	1.5	TPGI
2D	NGSF1.5FR30	(1)	N	1-4	0-225	500	740	1.5	TPSI
2D	NGSF1.5FR50	(1)	N	1-4	0-225	500	740	1.5	TPSI
2D	NGSF1.5FR70	(1)	N	1-4	0-225	500	740	1.5	TPSI
2D	DGSF2.0FR00	(1)	D	1-4	0-225	500	1000	2.0	TPGI
2D	DGSF2.0FR30	(1)	D	1-4	0-225	500	1000	2.0	TPSI
2D	DGSF2.0FR50	(1)	D	1-4	0-225	500	1000	2.0	TPSI
2D	DGSF2.0FR70	(1)	D	1-4	0-225	500	1000	2.0	TPSI

† N: non-displacement piles; D: displacement piles

‡ The reported values do not account for the influence of the pile offset

7.1 Tunnelling beneath single piles

This section analyses the response of single displacement and non-displacement piles (test group 2C) with the support of the data collected in test groups 2A and 2B, which relate to tunnelling under greenfield conditions and loading tests, respectively. The main aims of test groups 2A, 2B, and 2C were to assess the impact on settlements due to tunnel excavation of installation method and initial pile safety factor, $SF_0 = Q_0/P_0$, where Q_0 is the pre-tunnelling ultimate pile bearing capacity and P_0 is the service load. In these tests the traditional approach of modelling a constant pile head load, P_0, was implemented. This load condition was applied by the versatile load-control system developed for the CCNM, which is also able to actuate (after the in-flight pile installation sequences) a constant user-defined load demand.

To investigate the effects of varying initial safety factor, it was necessary to measure the bearing capacity of the model piles, Q_0. For non-displacement piles, it was assumed that Q_0 was equal to the load required to push a pile a distance of 10% of the pile diameter (Terzaghi, 1942). For displacement piles, Q_0 was set to the maximum installation force measured at the end of the jacking process (Marshall and Mair, 2011). It is important to note that Q_0 could be measured during each test of group 2C involving displacement piles whereas the assessment of Q_0 for non-displacement piles required the additional pile loading centrifuge tests of group 2B. In the following section, Q_0 is assessed by analysing the measured pre-tunnelling load-settlement curves.

7.1.1 Pre-tunnelling load-settlement curves

In test series 2B, three loading test were performed. An isolated non-displacement pile, located in position 3 and installed prior to spin-up to its design embedment depth, was tested (layout illustrated in Figure 7.1(a)). The measured load-settlement curves, representative of non-displacement piles, are displayed in Figure 7.2; results achieved by repeating the pile loading test three times with the same configuration were consistent. The average $Q_0 = 740$N at a settlement of $10\%d_p$ (shown in the figure with a grey line) was measured.

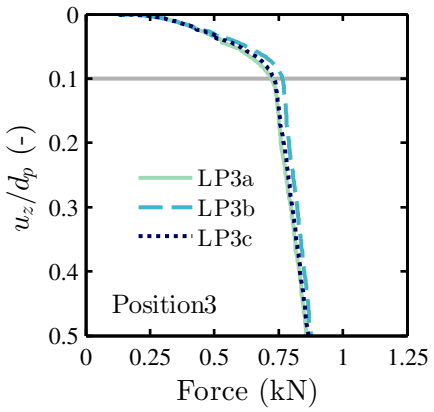

Fig. 7.2 Pile loading tests (LP) for non-displacement pile (position 3).

Figure 7.3 displays the load-normalised settlement curves (Force$-u_z/d_p$) measured during the pile installation/loading phase of test series 2C carried out at the end of the spin-up and prior to tunnelling (note that the model tunnel was isolated by closing the solenoid valve during pile loading). Results for non-displacement and displacement piles in positions 1, 2, and 3 are reported (non-displacement piles-solid lines; displacement piles-dashed lines). The darker the line colour, the higher the pile safety factor, SF_0. The service loads, P_0, applied at the end of the installation/loading phase are reported in Table 7.1.

Results for non-displacement piles (top sub-plots in Figure 7.3) show similar trends in the three different locations; the increase in applied load results in greater pile settlement (the greater the load, the lower the safety factor). Note that in general data are consistent with the curves displayed in Figure 7.2: pile settlements due to the applied load of $P_0 = Q_0/SF_0$ are lower than $10\%d_p$.

It is interesting to discuss the outcomes of the displacement pile installations (bottom sub-plots in Figure 7.3). Firstly, it is important to note that the value of Q_0 assumed for all displacement piles (shown in Table 7.1) was assessed from tests D2SF1.5 and D2SF2.5 (pile at location 2). The reference value $Q_0 = 1000$N was measured at the end of the installation procedure consisting of driving in-flight the pile a distance of $2d_p$ up to the design embedment depth, L_p (note that the pile was pre-installed prior spin-up with an embedment depth of $L_p - 2d_p$). Secondly, installations repeated at position 2 with the same configuration (i.e. tests with varying SF_0 where only the applied value of P_0 after pile driving was changed) gave similar results, illustrating good repeatability of tests. On the other hand, the pile position (i.e. relative tunnel-tip location) had a great effect on Q_0, which is neglected by assuming a fixed reference value of Q_0. In particular, Q_0 measured during tests D3SF1.5 and D3F2.5 was slightly lower than 1kN (Figure 7.3(c)), whereas the bearing capacity of piles in position 1 was highly affected by the tunnel presence (Figure 7.3(a)). Results shown in Figure 7.3(a) display a stabilisation followed by a decrease in load within the installation range $1 - 2d_p$. This unrealistic response of the piles in position 1 is due to the combined used of a water-filled membrane as a model tunnel (that does not contribute to increasing the pile installation force as much as soil) and a displacement pile being installed close to the tunnel periphery. On the other hand, pile bearing capacity in position 2 being higher than in position 3 may be due to the increased stress state at the pile tip in position 2 due to $K = 1$ for the water-filled membrane, which would result in a slightly higher mean effective stress in the ground at the location of the pile tip and, thus, a greater pile capacity.

It is worth noting that the aim of test series 2C is to assess the impact of installation method and pile initial safety factor on tunnel-single pile interaction. Furthermore, the construction scenario characterised by a limited tunnel crown-pile distance is probably the situation of greatest interest to tunnel engineers because of the potential for pile failure. Despite the effects of the water-filled model tunnel on the results, test conditions were consistent within a test series; therefore, these tests still provide insights into the tunnel-single pile interaction mechanisms, especially with regard to the case of a ground loss concentrated in the proximity of the pile tip.

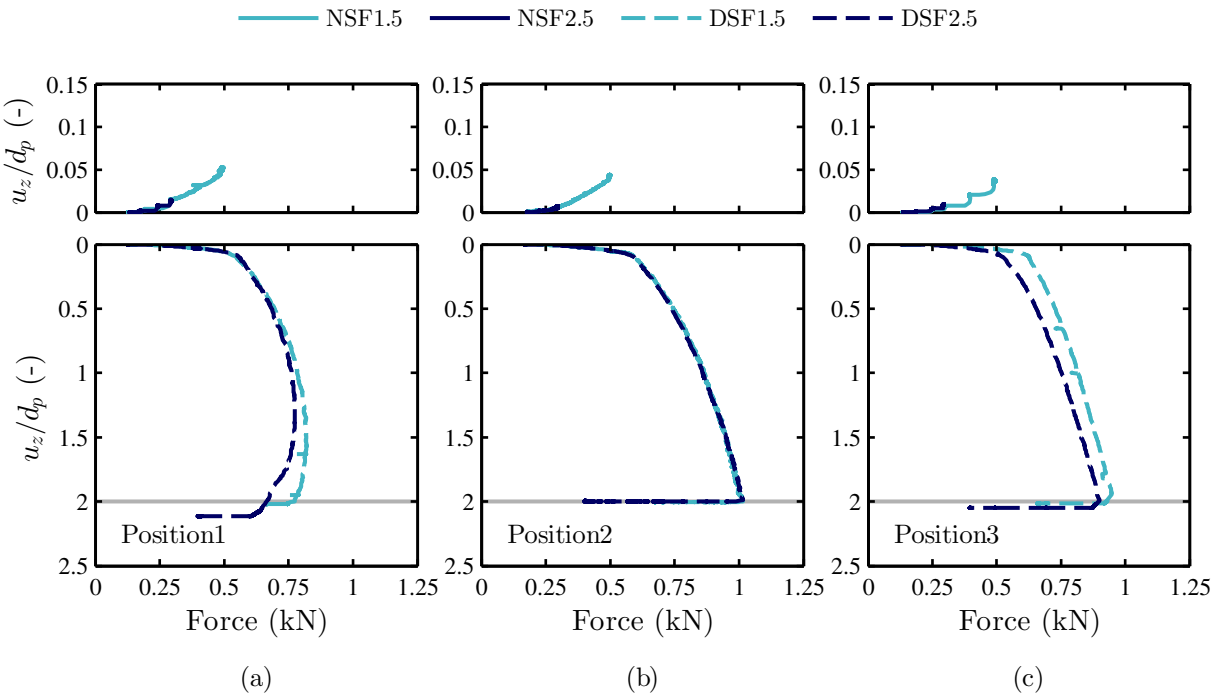

Fig. 7.3 Load versus normalised settlement curves during pile installation/loading for non-displacement piles (top) and displacement piles in positions (a) 1, (b) 2, and (c) 3 during test series 2C.

Finally, it should be noted the use of a rigid lined mechanic model tunnel would have resulted in an unrealistic high stiffening effect of the soil and greater bearing capacity of the pile in position 1. Therefore, to avoid any disturbance, an "ideal" physical model should replicate the actual excavation in-flight (after the pile installation) rather than modelling the tunnel ground loss with either flexible or rigid model tunnels.

7.1.2 Tunnelling-induced settlements

In loading tests, the state of pile failure is often identified as the point when there is a significant reduction of pile stiffness corresponding to a load increment (i.e. the increase of pile settlements for a given increment of load has a sharp rise). This state is associate with both a load and a settlement value that are, respectively, the pile bearing capacity and the ultimate settlement. Pile ultimate vertical movement is generally expressed as a percentage of the pile diameter. Similarly, geotechnical pile failure induced by tunnelling should be described as the moment when the rate of increase of the pile settlement with tunnel volume loss shows a significant increase.

Previous research illustrated that, because of tunnelling, there is a decrease of the pile bearing capacity Q (i.e. $\Delta Q < 0$). If we assume a constant pile load (P = constant), pile failure occurs when the pile bearing capacity reaches the value of the applied load ($Q \rightarrow P$). At this stage, because of the equilibrium condition, the pile bearing capacity has to be equal to the applied load ($Q = P$) and any further decrease of bearing capacity caused by an increment of tunnel volume

loss has to be compensated by pile settlements. If the pile settlement is not able to satisfy the equilibrium condition ($Q < P$), the pile does not stabilise and potentially large settlements occur (Jacobsz et al., 2004; Marshall and Mair, 2011). This framework implies that the initial pile safety factor, $SF_0 = Q_0/P$, influences the failure mechanism.

In the following, the term "pile failure" is used to indicate this increase in pile settlement rate with volume loss due to a loss of bearing capacity. It should be noted that, this phenomenon, may occur at large values of tunnelling-induced vertical movements. Therefore, in this work, the reference values of 20mm (at prototype scale) and $10\%d_p$ are adopted to indicate settlement thresholds that are not compatible with the requirements of the superstructure.

In this section, the centrifuge test dataset is used to investigate the variation of pile settlement-tunnel ground loss curves with initial safety factor. From test series 2C, single pile settlements (bottom sub-plots) and tunnel inner pressure (top sub-plots) are plotted against volume loss in Figure 7.4 with the same x-axis scale. Pile settlements are normalised by the tunnel diameter (u_z/d_p), whereas tunnel pressures are normalised by the initial value measured during the greenfield test ($\sigma_t/\sigma_{t,0}^{GF}$). Sub-plots (a), (b) and (c) are used to illustrated the results obtained for tests with piles in positions 1, 2 and 3, respectively. Regarding pile settlements, for practical purposes, as suggested by Jacobsz et al. (2004), an arbitrary prototype settlement value of 20mm may define the threshold of "large" settlements, which corresponds to $0.026d_p$ at model scale for these tests. Furthermore, the value of $0.10d_p$ is used in this chapter to refer to "very large" settlements, which relate to performance-based requirements of structures. "Large" and "very large" are indicated in the chart with grey horizontal bands. In these figures, greenfield displacements (green lines) at the locations of the pile head and tip are also plotted because they are often used as a reference for tunnel-pile interaction analyses.

Interestingly, the tunnel inner pressure results do not differ notably within the test series, whereas a great variability of settlements is illustrated. The following observations can be drawn from analysing the settlement-volume loss curves in Figure 7.4.

- Settlements of piles in positions 1 and 2 are generally within the range defined by the greenfield displacements at pile head and tip at low volume losses ($V_{l,t} < 1\%$), whereas pile settlements are larger than greenfield movements at higher volume losses. The rate of displacement increases with volume loss for piles in positions 1 and 2, whereas it decreases for piles in position 3. This trends could probably be generalised to the tunnel influence zones defined by Jacobsz et al. (2004).

- Pile initial safety factor, SF_0, has a great influence on the tunnelling-induced settlements. The higher the value of SF_0, the lower the pile displacement for both displacement and non-displacement piles. Interestingly, this statement also describes pile settlement variation at low and medium volume losses.

- Only displacement piles in positions 1 and 2 and the non-displacement pile in position 2 with $SF_0 = 1.5$ underwent failure (see light blue lines). For $SF_0 = 1.5$, the displacement pile in position 1 (sub-plot (a)) failed suddenly with a brittle mechanism for a $V_{l,t} < 0.5\%$,

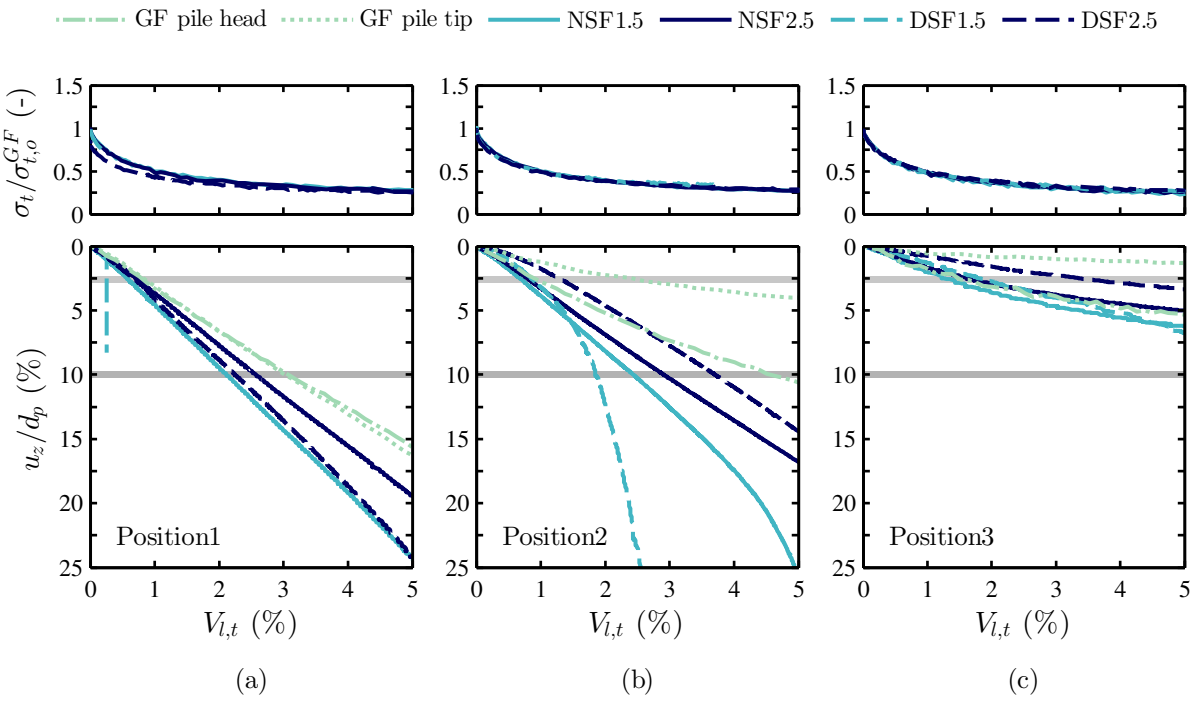

Fig. 7.4 Normalised tunnel pressure and normalised settlement during tunnelling beneath single non-displacement and displacement piles in positions (a) 1, (b) 2, and (c) 3.

whereas displacement and non-displacement piles in position 2 (sub-lot (b)) display a sharp increase in rate of displacement after 1% and 4% volume loss, respectively. Therefore, there is experimental evidence that $V_{l,t}$ at failure is higher for non-displacement piles than for displacement piles for a given SF_0. This is probably due to the fact that the percentage of end-bearing capacity mobilised in displacement piles is greater than in non-displacement piles, in which base capacity is secondary, and the fact that the pile tip is more affected by tunnelling-induced stress relief because it is closer to the tunnel than most of the area of the shaft.

- The failure of piles in position 2 is not as brittle as that of piles in position 1. This phenomenon is due to the capability of large pile settlement at failure in restoring bearing capacity (piles in position 1 have a water-filled membrane beneath their tips, whereas piles in position 2 have soil). Additionally, failure of piles in position 2 was less brittle than the results reported by Marshall and Mair (2011) for tunnelling in dense sands (see Figure 2.20(b)); this may be partially due to the contractive soil behaviour in these tests resulting from its low relative density ($I_d = 30\%$).

- The "very large" settlement threshold ($10\%d_p$) should not be used as a basis to define an ultimate failure criterion; for instance, non-displacement piles in positions 1 and 2 have approximately a constant rate of settlement with $V_{l,t}$ even for vertical displacements greater than this threshold, indicating additional residual bearing capacity is available. In these

cases, the piles are not failing (based on an ultimate limit stare criterion), they are simply moving with the tunnelling-induced ground displacements.

The results shown in Figure 7.4 provide important insights into tunnel-single pile interaction. Overall, the risk of failure of piles located within the tunnel influence area is low for non-displacement piles and needs assessment for displacement piles (high pre-tunnelling safety factor may guarantee a residual bearing capacity greater then service loads even for displacement piles). On the other hand, the magnitude of tunnelling-induced settlements of piles depends considerably on the initial safety factor. In general, it could be suggested that the closer the value of SF_0 to unity, the more likely it is that pile settlements will be greater than the greenfield values at the location of the pile axis.

7.2 Tunnelling beneath pile foundations and piled frames

In this section, the results of test group D that modelled the response of piled frames to tunnelling are analysed. These tests were carried out using the real-time load-controlled coupling of numerical and centrifuge modelling (see Section 3.3). The CCNM used a finite element model to simulate the framed structure whereas the tunnel-ground-foundation system and the structural loads were modelled within the centrifuge. For a given self-weight of the superstructure, tests simulated tunnelling beneath a transverse row of four displacement or non-displacement piles subjected to the frame action of four different superstructures, whose stiffness resulted in a response to tunnelling that varied from fully-flexible to rigid.

The main objectives of test group 2D are [i] the understanding of the effect of load redistribution among piles due to superstructure action (overly conservative outcomes are obtained by simplifying the global tunnel-piled structure interaction with a constant pile head load condition), [ii] the application of the CCNM technique to a geotechnical problem.

7.2.1 Pile installation

Figure 7.5 displays the force$-u_z/d_p$ curves measured during pile installation/loading prior to the ground loss process. Note that in test group 2D, all four piles were installed/loaded during each test. The installation sequence of displacement piles was pile 4, 3, 2 and, 1 (i.e. starting from the external pile and progressing towards the centreline), whereas the loading sequence of non-displacement piles was pile 1, 2, 3 and, 4 (i.e. it starting from the centreline and progressing towards the external pile). As in Figure 7.3, results for non-displacement and displacement piles are plotted, respectively, in the top and bottom sub-plots with solid and dashed lines. Although a colour scale is adopted to distinguish between tests, the installation/loading phase of data presented in each sub-plot was carried out with the same procedure and the same configuration. It can be observed that a good consistency was obtained between different tests.

The results for displacement piles (bottom sub-plots) are similar to the data measured during the installation phase of a single pile (see Figure 7.3 for comparison). Piles in position 1 required a decreasing installation force during the final part of the jacking process because of the model tunnel effects on the soil stresses, whereas the loads measured during jacking of piles in position 2 are slightly higher than for piles in positions 3 and 4.

With reference to non-displacement piles (top sub-plots), pile displacements resulting from the initial loading phase were influenced by pile-pile interaction. As shown in the top sub-plots, the curves display an additional settlement that occurred prior to tunnelling at a constant load, $P_0 = 500$N. This additional settlement (in the following referred to as "interaction settlement") is mostly due to pile-pile interaction and is greatest for pile 1, which is the first pile loaded in the group, than piles in positions 2 and 3. It should be noted that displacements were also affected by creep phenomena (note settlements at $P_0 = 500$N of the pile in position 4). It is difficult to explain the causes of these creep settlements. However, their magnitude is secondary with respect to immediate displacements due to loading and pile-pile interaction; therefore, they were neglected

in this analysis for the sake of simplicity. In general, as shown in the charts, piles in positions 2, 3, and 4 undergo a final displacement $u_z/d_p \approx 5\%$ due to the application of the four service loads, P_0, on the foundation which is comparable with the results in Figure 7.3. On the other hand, the responses to initial loading of non-displacement piles in position 1 differ significantly from the data obtained for isolated piles (compare solid lines in Figures 7.3(a) and 7.5(a)). In Figure 7.5, during the loading phase of piles in position 1, the load-settlement curves display an approximately linear trend up to the target load of 500N associated with $u_z/d_p = 5-7\%$. Because of the interaction settlements, the final value of u_z/d_p due to loading of other piles ranged between $8-13\%$. The impact of higher settlements in the response of the pile group to tunnelling is analysed in a later section.

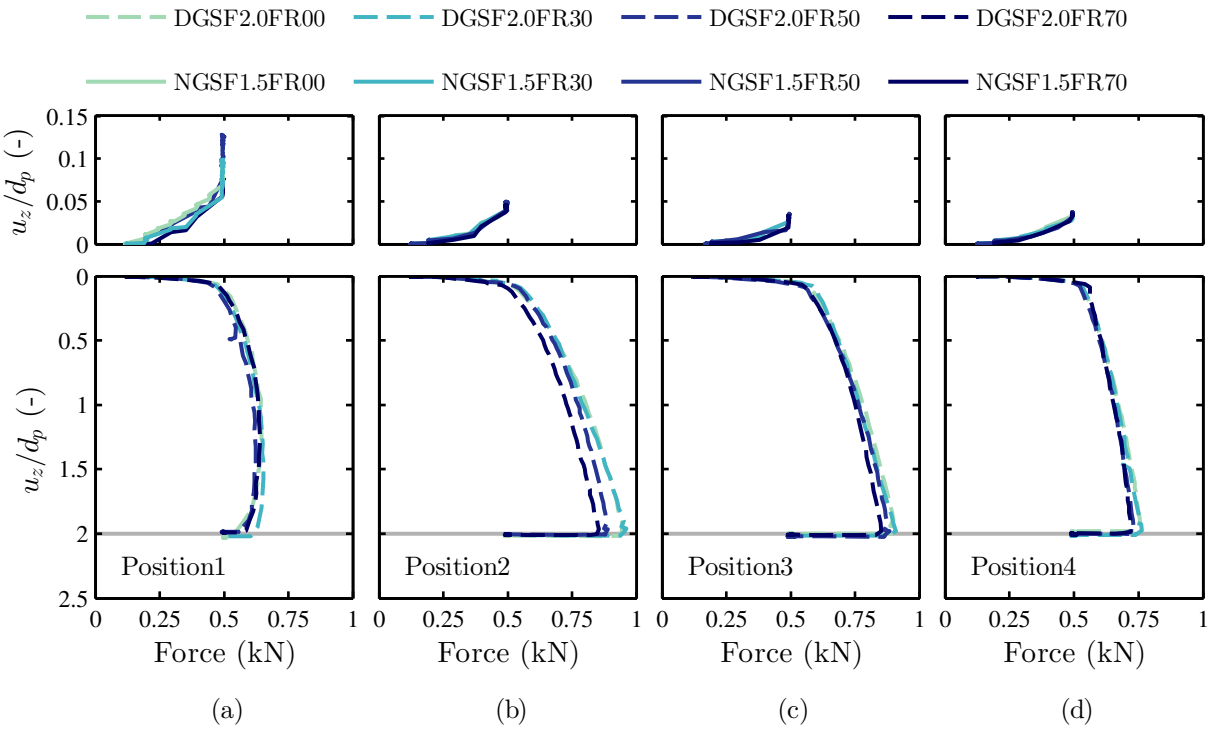

Fig. 7.5 Load versus normalised settlement curves during pile row installation/loading for non-displacement piles (top) and displacement piles in positions (a) 1, (b) 2, (c) 3, and (d) 4.

7.2.2 Comparison between greenfield and pile foundation settlements

The first step towards understanding the global tunnel-piled structure interaction should consist of defining the response to tunnelling of the pile foundation subjected to the superstructure weight and assuming a fully-flexible building (i.e. no load redistribution among piles). In the latter stage of this analysis (see Section 7.2.3), the effects of load redistribution are assessed. In this way, it is possible to isolate the contribution of the building self-weight and stiffness.

To analyse the variation of the greenfield input displacement field that results from the pile-soil interaction, Figure 7.6 compares settlements and tunnel pressures from a greenfield test

(GF) and tests NGSF1.5FR00 and DGSF2.0FR00 with constant pile group head loads and fully-flexible structures. Non-displacement and displacement pile settlements are shown, respectively in Figures 7.6(a) and (b). In the bottom sub-plots, displaying normalised settlement curves, varying line styles are used to indicate measurements corresponding to different pile positions (labelled P1, P2, P3 and P4 in the legend). Results of tests NGSF1.5FR00 (non-displacement

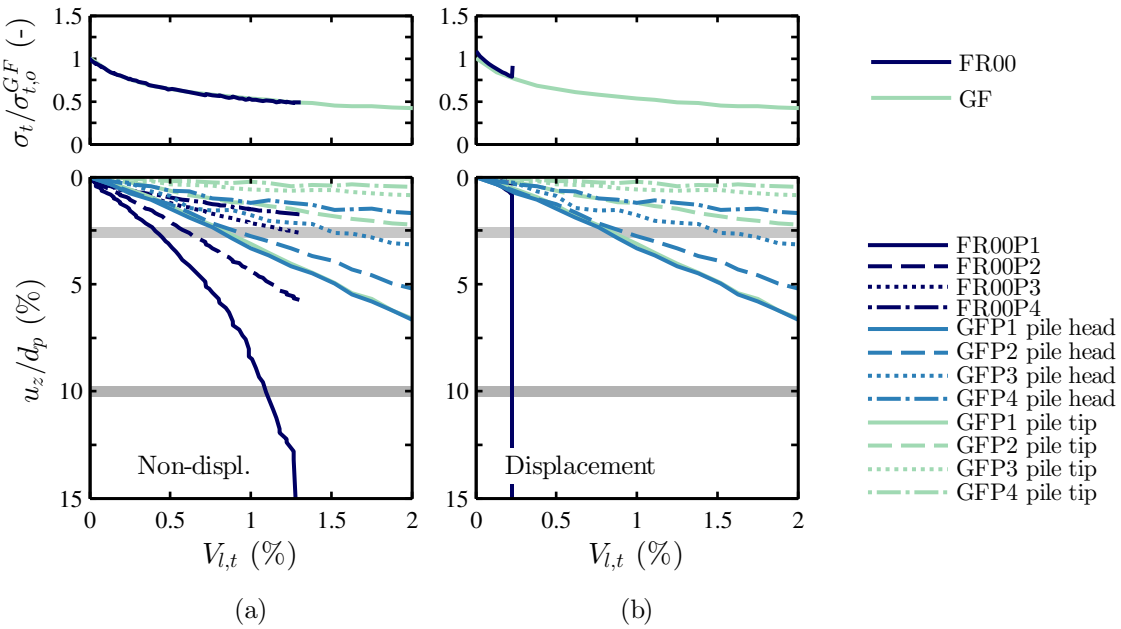

Fig. 7.6 Comparison between greenfield and pile row normalised settlements due to $V_{l,t}$: (a) non-displacement and (b) displacement piles.

pile foundation) and GF (greenfield test) in Figure 7.6(a) show the following.

- Piles 1 and 2 (with their tip within the tunnel influence zone) display settlements larger than the greenfield scenario, whereas piles 3 and 4 (outside the tunnel influence area) settle slightly more than the surface in the greenfield condition. This is interesting because it does not fully agree with the indication that piles with their tip outside the main tunnel influence zone should settle less than the greenfield. This may be partially due to the group effect (according to an elastic analysis the group effect would result in piles above the tunnel and externally located with respect to the tunnel settling less and more than isolated piles, respectively).

- Normalised tunnel pressure trends are similar for the two tests.

- The pile group undergoes failure: the settlement rate with $V_{l,t}$ of the pile in position 1 increases at volume losses higher than 1% and an unstable equilibrium condition is experienced by the pile at $V_{l,t} \approx 1.25\%$. Failure was not observed during test N1SF1.5 (see Figure 7.4). This difference between tests N1SF1.5 and NGSF1.5FR00 is probably a consequence of the pre-tunnelling state of piles in position 1 (compare Figures 7.3 and 7.5)

On the other hand, test DGSF2.0FR00 displayed in Figure 7.6(b) was interrupted at $V_{l,t} \approx 0.2\%$ because of the brittle failure of pile 1. This agrees with the jacking and unloading curve reported in Figure 7.5(a) and the brittle failure of the isolated displacement pile ($SF = 1.5$) shown in Figure 7.4. However, it is interesting to highlight that an increase in the tunnel inner pressure was induced by the brittle failure of the displacement pile foundation. To conclude, Figure 7.6 illustrates that, for the given scenario, a critical response to tunnelling of both displacement and non-displacement pile foundations should be expected in the case of a fully-flexible superstructure.

7.2.3 Effects of load redistribution due to frame action on pile settlements

In this section, the importance of the superstructure stiffness in the global tunnel-piled building interaction is investigated. In general, previous work on tunnel-pile interaction has neglected that the structural stiffness can redistribute loads. This implies that failure of the pile above the tunnel due to reduction of Q may not be induced because of the decrease in the vertical load P at the location.

Figure 7.7 displays the main outcomes of test series 2D performed using the coupled centrifuge-numerical modelling technique: tunnelling-induced normalised pile settlements and pile head loads against tunnel volume loss. Data measured within the volume loss range $V_{l,t} = 0 - 2\%$ is plotted in this figure because the assumption of linear elastic behaviour of the superstructure would not be compatible with displacements resulting from larger volume losses. The reliability of the CCNM is confirmed because of the lack of outliers and relatively smooth curves. On the other hand, it should be noted that test NGSF1.5FR70 was interrupted at $V_{l,t} \approx 1.3\%$ because it reached an unstable condition; this is a limitation of a coupled centrifuge-numerical system that is based on a load-controlled approach while implementing a very rigid superstructure.

In Figure 7.7, sub-plots (a), (b), (c), and (d) are used to report the measurements of the piles in positions 1, 2, 3, and 4, respectively. Top sub-plots show the variation of the applied pile head load, P, in relation to the pre-tunnelling serviciability value $P_0 = 500$N (indicated with black lines), whereas the bottom sub-plots display normalised settlements u_z/d_p. As in Figure 7.4, 'large" and "very large" thresholds are indicated with grey horizontal bands in the plots. To simplify the discussion of the data, solid and dashed lines are used to indicate, respectively, non-displacement and displacement pile foundations whereas a colour scale that associates darker colours to stiffer structures is adopted. Finally, note that greenfield ground movements were omitted to improve the figure readability and measurements of the tunnel inner pressure are not reported for this test series because they do not provide additional information on the interaction mechanism.

The main outcomes that can be seen from Figure 7.7 are [i] the superstructure effectiveness in positively preventing a sudden increase in the pile settlement rate with volume loss (see Figure 7.7(a)) and [ii] the complex pattern of load redistribution due to the superstructure (see top sub-plots). In fact, the superstructure stiffness redistributed the highest portion of the total

building self-weight towards the pile in position 3, whereas the decrease in load of the external pile in position 4 is greater than the reduction experienced by the pile in position 1. In the following, these two outcomes are discussed; it is useful for the discussion to define the force variation as "superstructure reaction force", $\Delta P = P - P_0$.

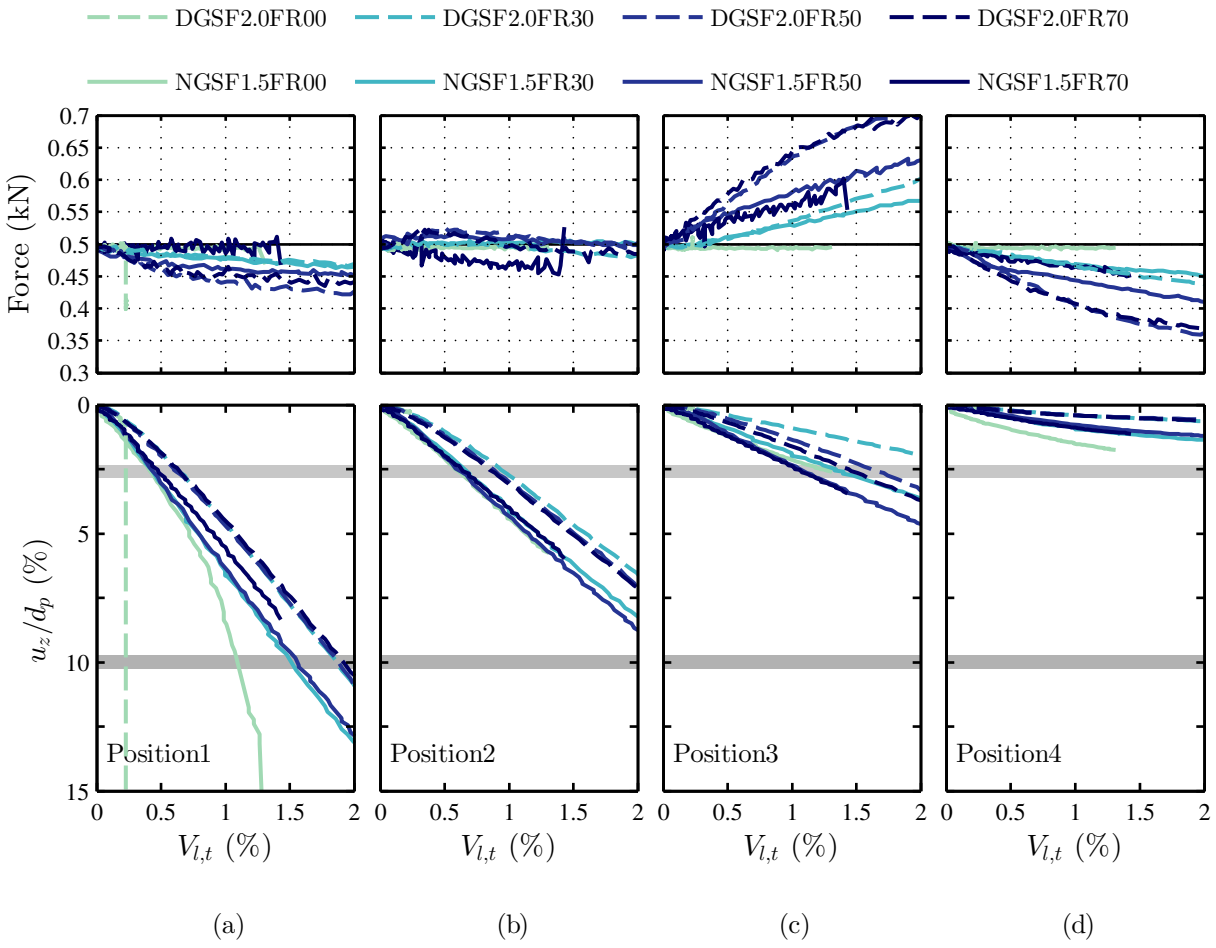

Fig. 7.7 Variation of tunnelling-induced pile normalised settlements and load distribution with frame stiffness: piles in positions (a) 1, (b) 2, (c) 3, and (d) 4.

Firstly, it is interesting to discuss point [i]. Although the maximum decrease of the vertical load at pile 1 above the tunnel is lower than 10% and 20% of P_0, respectively, for displacement and non-displacement pile foundation ($|\Delta P| < 0.1 - 0.2P_0$), the superstructure stiffness is able to prevent pile failure due to excessive loss of bearing capacity (even in the case of the relatively flexible frame FR30). These outcomes represent strong evidence of the need to account for the superstructure during the risk assessment of tunnelling beneath piles. Secondly, to understand the interaction mechanisms responsible for the load redistribution (point [ii]), it is necessary to discuss the cause of ΔP. Reaction forces arise from the bending deformations of the frame which resists the relative deflection of piles rather than the absolute value of the settlements and/or the tilt of the superstructure. This means that a rigid frame (e.g. FR70) would constrain the piles to settle with their heads aligned along a straight line. In the case of an eccentric tunnel-frame condition as in the tested configurations (i.e. frame not located with its centre above

the tunnel centreline), a rigid frame would tilt as well as settle. The complex redistribution of the reaction forces, ΔP, is due to the structure resisting bending deformation while tilting; to obtain a qualitative assessment of ΔP would be useful to constrain the frame base to settle according to a greenfield Gaussian curve (however this approach would only provide qualitative information because of tunnel-pile group interaction). Finally, it is necessary to relate the distribution of reaction forces ΔP with volume loss to the variation in pile settlements with superstructure stiffness. In Figure 7.7, it can be noticed that the higher the increase/decrease in the pile load P, the greater the rise/reduction in the normalised pile settlement u_z/d_p with respect to the configuration with the fully-flexible superstructure FR00.

In summary, results in Figure 7.7 show that the role of the superstructure stiffness in the global tunnel-pile-structure interaction can be significant both in varying the pile settlements and in preventing pile failure due to structural loads exceeding the residual pile capacity. These results suggest that pile failure should be assessed considering (at least in a simplified way) the load redistribution among piles. Although the obtained results are based on the assumption of linear elastic behaviour of the superstore, overall these findings should not be limited by this assumption because most pile settlements in Figure 7.7 are lower than $10\% d_p$. In addition, it could be argued that in real cases the reaction forces necessary to prevent pile failure may not be guaranteed because of possible damage at the pile-structure connection (a tensile reaction force at the pile above the tunnel was induced by the superstructure pulling the pile upwards); however, centrifuge data suggest that limited force reductions with respect to the pre-tunnelling service load (i.e. $|\Delta P| < 0.1 - 0.2P_0$) may be sufficient to avoid brittle pile failure. Despite the insights provided by the use of the simplified elastic approach for the superstructure, further research should investigate the effects of the superstructure non-linearities and the building damage distribution predicted by the coupled centrifuge-numerical model.

7.3 Discussion on settlements, pile capacity loss and pile-pile interaction

This section discusses the concept of pile failure, the criteria relating pile capacity loss with tunnelling-induced settlements, and the role of pile-pile interaction in the global tunnel-pile-structure interaction.

In the literature, tunnelling-induced settlements have been associated with capacity loss and failure. For instance, Dias and Bezuijen (2015) related pile failure to a settlement criteria of $10\%d_p$, whereas Soomro et al. (2015) introduced the apparent loss of pile capacity defined as the pile head load that would induce, according to a pre-tunnelling pile load-settlement curve, a foundation settlement equal to the tunnelling-induced displacement. However, this approach may mislead the tunnel-pile interaction analysis because it neglects the fact that tunnelling-induced pile settlements are due to both the greenfield soil movements and soil stiffness/strength degradation (only the latter component is associated with loss of bearing capacity). For instance, if the greenfield settlement field is approximately constant along the pile length and the tunnelling-induced soil stiffness/strength degradation is negligible, the change in pile capacity $\Delta Q \approx 0$, whereas pile settlements would be equal to the greenfield value. Therefore, it is not possible to correlate pile capacity loss with pile settlements when neglecting the amount of pile settlement that is due to the pile simply following the surrounding settling soil.

To understand the main difference between pile capacity in the tunnelling scenario and the loading test, it is necessary to consider the greenfield displacement field. During a loading test, the pile displaces with respect to a stationary soil (i.e. greenfield soil movements are null). On the other hand, tunnel excavation results in greenfield soil movements associated with soil shear strains and a reduction of ground stresses. If a pile is located near the tunnel, [i] the pile settles with the surrounding soil while the pile axial stiffness acts to average the soil settlement distribution along its length (resulting in relative pile-soil displacements and further soil shear strains). Furthermore, [ii] the pile undergoes additional settlement with respect to the surrounding soil because of soil stress relief due to tunnel volume loss, which induces a reduction of Q, and soil stiffness degradation due to soil shear strains (which are induced by both greenfield tunnelling and relative soil-pile movements). These concepts are illustrated in Figure 7.8.

In addition, it is important to relate the differences in pile-pile interaction mechanisms arising from tunnelling and pile head load to the global tunnel-pile-superstructure interaction. A number of authors have provided a thorough description of pile-pile interaction that has a beneficial and detrimental impact on the pile foundation settlements induced by tunnelling and vertical pile head loads, respectively (pile-pile interaction decreases the pile settlements due to tunnelling and increases the pile group settlement for a given load). To frame this problem, it is useful to refer to the mechanisms resulting from the assumptions of elasticity (plasticity is mostly concentrated at the piles and has secondary effects on pile-pile interaction).

- If a single pile is loaded at the top, the pile settles, dragging with it the surrounding soil. Therefore, the pile behaves as a displacement source, which results in a downward

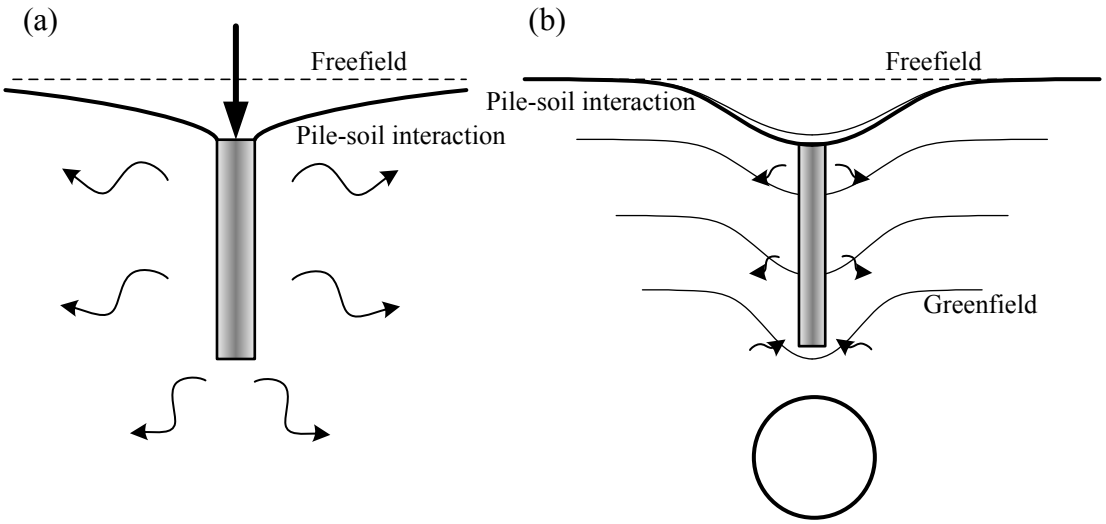

Fig. 7.8 Propagation of pile-pile interaction forces: a) pile loaded externally, b) pile loaded passively by tunnelling-induced soil movements.

.

displacement field that attenuates with distance according to a logarithmic trend. If another pile is in the proximity of the source pile, it settles because of pile-pile interaction.

- If a tunnel excavation is carried out near to a pile, the pile resists differential displacements along its axis with its stiffness resulting in an "averaging effect" of the greenfield input. Locally, the pile propagates displacements resulting from the "shielding effect" (i.e. the pile propagates the difference between the final pile displacement and the greenfield movements); the displacements originating at the pile by the "shielding effect" are lower by definition than the greenfield movements. Additionally, these displacements from the "shielding effect" attenuate with distance.

- If the two scenarios are compared, for a given pile head settlement, the pile head loading condition results in a greater pile-pile interaction effect than tunnelling.

If tunnelling beneath a piled building, there are concerns for building distortions induced by differential displacements. In this scenario, pile-pile interaction mechanisms within the pile foundations arise both from [i] passive loadings due to the greenfield movements and [ii] tunnelling-induced reaction forces provided by the superstructure, which resists to distortions with its stiffness. Previous research has indicated that, if the piles with a high and low offset distance with respect to the tunnel centreline are, respectively, defined as external and central piles, the "shielding effect" in a pile group results in upwards movements of the central piles and downward movements of the external piles, decreasing the distortions of a superstructure. Therefore, contribution [i] is beneficial in the global tunnel-pile-structure interaction. On the other hand, in this scenario, contribution [ii] is also beneficial to the decrease of the building distortions because the presence of pile-pile interaction mechanisms decreases the overall stiffness of the soil-pile foundation system (i.e. the relative stiffness defined as the ratio between the building and soil-pile domain increases).

To conclude, the following general indications may be useful to tunnel engineers.

- The use of simple criteria based on the tunnelling-induced settlements to describe pile capacity loss is questionable. Pile capacity should be evaluated with tools that consider stress relief due to tunnelling (such as cavity expansion/contraction methods or FEMs/FDMs), which is probably the main cause of the reduction of ultimate bearing capacity. On the other hand, pile settlements do provide useful guidance to assess the potential for damage to a superstructure. In this framework, an ultimate tunnelling-induced pile settlement of $10\%d_p$ could be assumed.

- In the case of tunnelling beneath a piled building, pile-pile interaction mechanisms due to both pile "shielding effect" and the superstructure reaction forces (applied at the pile head) are beneficial to the decrease of the superstructure distortions; this agrees with the outcomes of Section 6.1, which illustrate that superstructure distortions from method TPSI-S that neglects pile-pile interactions are greater than from method TPSI-G.

7.4 Conclusions

A key concern of tunnel engineers when tunnelling beneath piled buildings is the limitation of tunnel volume loss to avoid instances of reaching pile failure and superstructure damage. Despite the available guidance based on empirical approaches and simplified analytical methods, there is still a lack of understanding of several aspects of the global tunnel-pile-building interaction, which results in the use of overly conservative design approaches. To provide insights into the interaction mechanism and the loss of bearing capacity due to tunnel excavation, a series of tests was carried out. Centrifuge models and coupled centrifuge-numerical models were used to investigate, respectively, tunnelling beneath single piles and piled frames. In the first set of tests the load was maintained constant on an isolated pile during the entire tunnelling process; in the latter test group, the real-time coupling of numerical and centrifuge modelling was used to assess the impact of load redistribution among piles of a transverse row due to the action of the superstructure. The following conclusions can be drawn from the present study.

- In general, this chapter provides support for the conceptual premise that the initial pile safety factor (i.e. the ratio between initial bearing capacity and applied load) plays an important role in determining tunnelling-induced settlements of piles and the potential for pile failure. The outcomes of centrifuge investigations illustrate that the lower the initial safety factor, the greater the tunnelling-induced settlements.

- The outcomes illustrated the importance of pile installation method, which affects both the tunnelling-induced settlements of the pile and failure process. Strong experimental evidence was provided that the installation method (displacement versus non-displacement piles) results in a greater potential for pile failure of displacement piles; this agrees with previous studies pointing out the importance of load redistribution between pile shaft and base when tunnelling near to piles. In general, results highlighted that pile failure is a critical aspect for displacement piles with relatively low initial safety factors. For a given initial safety factor, non-displacement pile failure is expected at a higher value of volume loss than for displacement piles. Furthermore, in the case of constant service loads, piles in sands with an initial safety factor $SF_0 \geq 2.5$ may not experience failure due to loss of bearing capacity up to relatively high volume losses (i.e. residual $SF > 1$ for $V_{l,t} = 2-5\%$).

- Large pile settlements should be expected for both displacement and non-displacement piles when the pile tip is located within previously defined tunnel influence zones (Jacobsz et al., 2004). Interestingly, displacement and non-displacement piles in this position may settle more than the greenfield soil along the pile axis due to soil non-linearities and plasticity.

- Taken together, the results of tunnel-single pile and tunnel-pile group interaction suggest that there may be a detrimental role of the pile group effect on the pile bearing capacity.

However, more research on this topic needs to be undertaken before this group effect is more clearly understood.

- Another important finding with practical implication is that the piled building/foundation response to underground excavations is highly affected by the superstructure contribution. Tunnelling induces differential pile settlements that result in superstructure distortions and, thus, in the redistribution of building self-weight loads among piles. In the case of piles, the load redistribution due to the superstructure is clearly able to modify the behaviour of the foundation in terms of settlements (also at low volume losses) and failure. In fact, centrifuge data suggest that a limited relative reduction in the pile load with volume loss ($\approx 10-15\%$ of the pre-tunnelling value) could prevent failure of piles with tips close to the tunnel periphery.

- A novel method that enhances geotechnical centrifuge capabilities through real-time coupling of numerical and centrifuge modelling was used to study the impact of tunnelling beneath existing piled frames with displacement and non-displacement pile foundations, which is a complex SSI problem. The overall performance of the CCNM technique was very satisfactory and gives confidence that the methodology can be used for a wide spectrum of building typologies and stiffnesses. Despite the insights achieved with the use of the linear elastic approach for the superstructure, this work provides a basis for further studies. Future research should investigate the effects of the superstructure non-linearities on the global interaction and the building damage distribution predicted by the coupled centrifuge-numerical model.

Chapter 8

Conventional centrifuge modelling of piled structure response to tunnelling

In this chapter, the global tunnel-pile-structure interaction is investigated through conventional centrifuge modelling. The tests were performed at 80g. The adopted equipment and the testing plan are described in Section 3.6. The test series plan is summarised in Table 8.1. Piled buildings were modelled in the centrifuge as an equivalent aluminium plate, with varying stiffness and self-weight, supported by aluminium piles. The series of centrifuge tests presented in this chapter includes additional tests (test group 3D) compared to the dataset published by Franza and Marshall (2016) (test group 3C) to better isolate the contributions of structural stiffness and self-weight. The main aims of this work are to understand the key aspects of the superstructure contribution to the global interaction; additionally, this work provides a benchmark dataset that may be used by other researchers in the future for numerical modelling applications. In the following, both the model dimensions and results are reported in model scale.

In the first part of this chapter (Section 8.1), the results of the centrifuge tests that simulate the effect of tunnel excavation beneath piled structures are described. The greenfield deformation patterns and the results of pile loading tests, characterising the pile ultimate capacity, are illustrated. Tunnelling-induced vertical and horizontal displacement profiles of the superstructure are compared with greenfield surface and subsurface ground movements. The variation of the building displacement profiles with plate stiffness, self-weight and tunnel volume loss illustrates the main effects of tunnel-pile interaction (TPI), and the contribution of the superstructure to the global tunnel-pile-structure interaction (TPSI).

Table 8.1 Summary of centrifuge test series 3 performed at 80g (model scale dimensions).

Test series	Name (# test)		Plate t (mm)	Plate mass (kg)	Pile extra mass (kg)	Total weight † (N)	Note
3A	GF	(1)	-	-	-	-	Greenfield
3B	SP	(3)	-	-	-	-	Pile loading
3C	t1	(1)	1.6	0.55	0	398	Plate
3C	t3	(3)	3	1.03	0	745	Plate
3C	t6	(3)	6	2.05	0	1491	Plate
3C	t12	(1)	12.3	4.21	0	3056	Plate
3D	t1.w12	(1)	1.6	0.55	0.26	3056	Plate + weights
3D	t3.w12	(1)	3	1.03	0.23	3056	Plate + weights
3D	t6.w12	(1)	6	2.05	0.15	3056	Plate + weights
† Self-weight computed considering the variation of g-level within the model							

In the second part of the chapter (Section 8.2), the effects of structural stiffness and self-weight on the response of piled buildings to tunnelling are described in terms of deformations. The building deflection ratio, DR, and the deflection ratio modification factors, M^{DR}, were used as indicators of the building deformations in order to include results within the limiting tensile strain framework. The bending relative stiffness parameter introduced in Section 6.4, ρ^p, is used to compare the centrifuge outcomes presented in this chapter with the elastic envelopes proposed in Chapter 6. To conclude, the main findings are summarised in Section 8.3.

8.1 Centrifuge modelling results

In Section 8.1.1, the repeatability of the test procedure is assessed. In the latter part (Sections 8.1.2 and 8.1.4), the ground movements and plate displacements measured during tunnel excavation are illustrated to highlight the key results of centrifuge test series 3 (Table 8.1). Additionally, in Section 8.1.3, the outcomes of the pile loading tests are reported to characterise the ultimate pile bearing capacity, thus the pre-tunnelling safety factor of the pile foundations.

8.1.1 Repeatability

To illustrate that good repeatability of results was achieved with the simplified model preparation procedure (described in Section 3.4.2), the pile loading test and two different piled building configurations were tested three times (tests LP, t3 and t6). Because of the greater complexity of configuration t3 and t6, this section focuses on the results obtained for tunnelling beneath the piled plate. However, it should be noted that the pile loading tests (test group 3B) also provided similar results for the given tested configuration, as displayed in Figure 8.3.

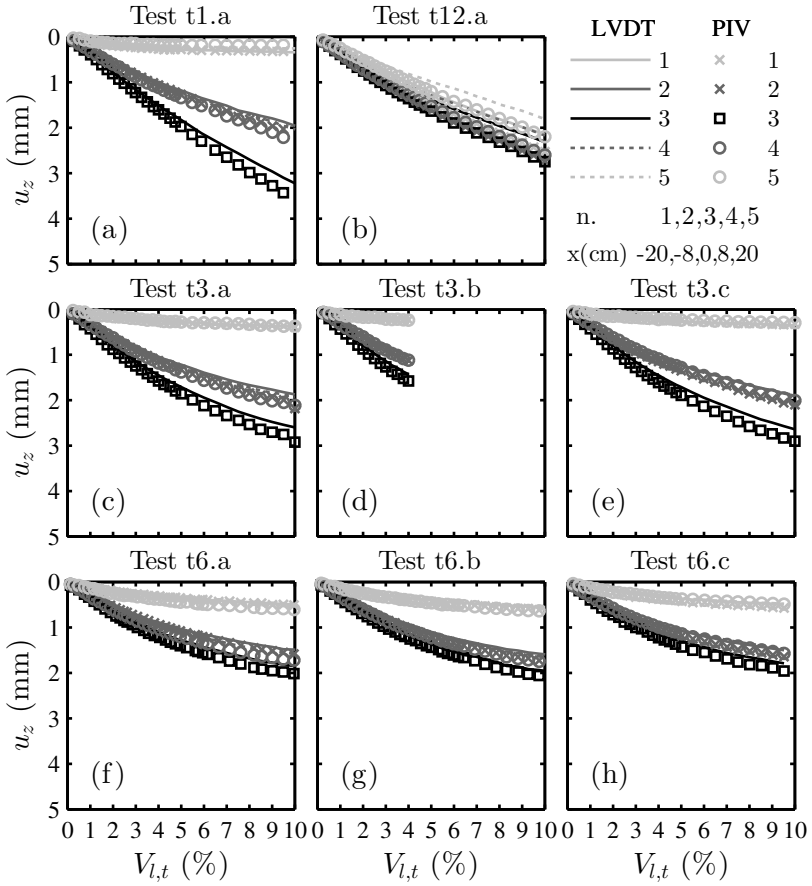

Fig. 8.1 Test repeatability: comparison of PIV and LDVT measurements of plate settlements.

The building displacements measured with the GeoPIV technique and the LVDTs at five locations (corresponding to offset values of 0, ±80 and ±200mm) during the centrifuge test

group C are compared in Figure 8.1. Results display good agreement between PIV measured settlements and LVDT readings and good repeatability within the test series. The scatter of results obtained from repeated tests is smaller than the variation between different configurations (i.e. the results obtained for different test configurations are clearly distinguished). However, the higher the plate stiffness, the greater the difference between PIV and LVDT measurements (PIV data being greater). This can be partly explained by non-uniform deformations across the length L of the plate (along the tunnel longitudinal axis), which does not act as a perfect beam under the actions of the attached piles. This hypothesis was confirmed by elastic finite element analyses of the plate. Further remarks regarding the variation of the settlement rate with plate properties and ground loss are provided later in the discussion of Figure 8.6, which plots the results of both test groups C and D.

8.1.2 Greenfield test

As previously discussed, greenfield ground movements are often used as a reference term for soil-structure interaction analyses. Therefore, measurements of vertical and horizontal soil movements during the greenfield test (test group 3A) are displayed in Figure 8.2 for two values of $V_{l,t}$, which are representative of the investigated range of ground losses. The results are normalised by $R \times V_{l,t}$ to highlight the variation of the deformation pattern with volume loss. Figure 8.2 shows: i) the concentration of ground settlements at the tunnel crown, which results in the narrowing of the settlement troughs with depth, ii) the distribution of the settlements becomes narrower with tunnel volume loss and iii) the magnitude of the horizontal displacements is noticeable at the surface and negligible at greater depth.

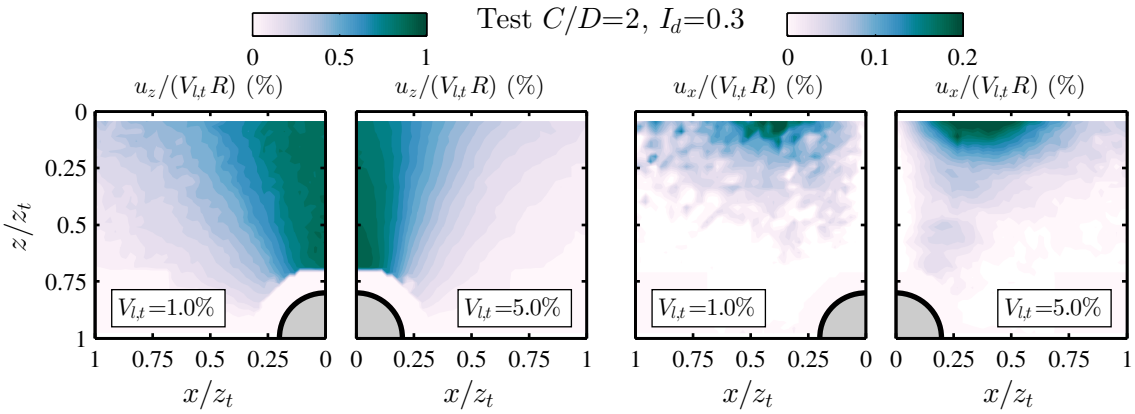

Fig. 8.2 Greenfield distributions of tunnelling-induced vertical (left) and horizontal (right) soil movements at $V_{l,t} = 1$ and 5%.

8.1.3 Load-settlement curve of single piles

Determining the ultimate bearing capacity of the model pile foundation prior to tunnelling was important in order to assess the initial safety factor of the pile foundation, which was loaded

by the equivalent plate. Therefore, a series of centrifuge pile load tests (group 3B) was carried out. The bearing capacity of isolated non-displacement piles was assessed from three tests with the same configuration to check repeatability. Figure 8.3 provides the measured load-settlement curves. Although the tunnel presence disturbs the stress condition within the soil, the results are consistent throughout the three tests (i.e. pile 1 and 2 show approximately the same response to loading) and the scatter between the curves of the two piles is secondary (overall, pile 1, which is closer to the tunnel, shows a lower reaction force to driving). The ultimate bearing capacity of an isolated pile was assumed equal to 495N, which is the average value of the measurements corresponding to a pile head settlement equal to $10\%d_p$, shown in the figure with a dashed line Terzaghi (1942).

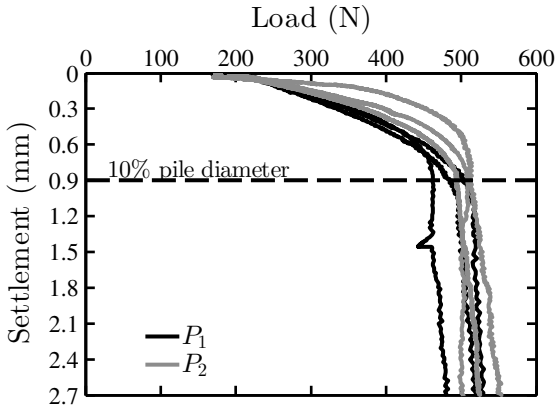

Fig. 8.3 Measured load-settlement curves of single piles during test series 3B. The location of pile 1 and 2 is illustrated in Figure 3.16(a).

8.1.4 Tunnelling beneath a piled structure

The centrifuge data presented by Franza and Marshall (2016) (test group C) suggested that tunnelling-induced settlements of piled structures depend on both the building weight and its stiffness; therefore, the relationship between the relative soil-building stiffness and the tunnelling-induced deformations should account for the building weight. In this research, it was possible to distinguish the effects of the structural stiffness and the building weight by comparing the full dataset composed by test groups C and D, in which a part of the results refers to a building of a given self-weight and varying stiffness and the other to equivalent plates subjected to different loading conditions.

In the case of pile foundations, it is useful to describe the pile safety factor due to the building weight using the initial safety factor of the foundation, SF_0, where initial refers to the pre-tunnelling condition. This is an important parameter that assesses the residual capacity of the system from pile failure due to tunnelling. For each test, the initial safety factor of the foundation, SF_0, was computed as the ratio between the ultimate bearing capacity of the pile group and the total self-weight of the superstructure (accounting for the variation of g-level within the reduced scale model). The ultimate bearing capacity of the pile group foundations in test group 3C and

3D was evaluated as the summation of the bearing capacity of isolated piles, which was assessed in the group 3B. This approach for the calculation of the foundation bearing capacity is valid because, in these experiments, the pile spacing is over 8 d_p and the pile length to diameter ratio, L_p/d_p, is 15. The block failure of the pile group (i.e. failure of the entire soil within the pile group as a block) is generally associated with close spacing of piles and is not likely for relatively short piles in sands (Fleming et al., 2009). Therefore, block failure is not likely to be the failure mechanism and the pile group capacity is not reduced with respect to the isolated configuration.

As summarised in Table 8.2, the initial safety factor SF_0 ranged between 17.4 and 2.3. In particular, the configurations testing plates of varying stiffness and constant self-weight (t12 and group 3D) have a $SF_0 = 2.3$, which indicates that the foundation is well designed for the building loadings. On the other hand, the tests with a SF_0 greater than 2.3 simulated a scenario where the foundation bearing capacity was over-designed with respect to the superstructure and, thus, pile failure is unlikely to be induced by the stress relief due to tunnelling.

Table 8.2 Initial safety factor of the pile foundation, SF_0, in the test groups 3C and 3D.

Test series	Name (# test)		Plate t	Plate mass	Pile mass	Total weight †	Pile capacity	SF_0‡
			(mm)	(kg)	(kg)	(N)	(N)	(-)
3C	t1	(1)	1.6	0.55	0	398	495	17.4
3C	t3	(3)	3	1.03	0	745	495	9.3
3C	t6	(3)	6	2.05	0	1491	495	4.6
3C	t12	(1)	12.3	4.21	0	3056	495	2.3
3D	t1.w12	(1)	1.6	0.55	0.26	3056	495	2.3
3D	t3.w12	(1)	3	1.03	0.23	3056	495	2.3
3D	t6.w12	(1)	6	2.05	0.15	3056	495	2.3

† Self-weight computed considering the variation of g-level within the model
‡ Pile group safety factor

8.1.4.1 The effect of superstructure stiffness

A comparison of the vertical (u_z) and horizontal (u_x) displacement curves of the plates with varying stiffness and constant weight ($SF_0 = 2.3$) is presented in Figure 8.4. These displacements were measured at $V_{l,t} = 1$ and 5%. For comparison, greenfield displacement curves at $z = 0$ and $z/L_p = 1$ (the surface and the pile tip level, respectively) are also shown. Building displacement curves were approximately symmetric except for tests t12 and t1.w12, which showed higher displacements on the left side and a global horizontal translation of the plate towards the right (i.e. linear trend of horizontal movements with x). The variation of the building settlement curves with plate stiffness t and $V_{l,t}$ in Figures 8.4(a) and (b) illustrates the main effects of tunnel-pile interaction (TPI) and the contribution of the superstructure stiffness to the global tunnel-pile-structure interaction (TPSI).

To understand the TPI, it is necessary to analyse the response of flexible superstructures, where the superstructure influence is minimal. The settlement curves of t1.w12 and t3.w12 are characterised by having both hogging and sagging regions. Furthermore, the settlements of the building in all cases are equal to or greater than the greenfield movements at the pile tip depth and the building settlement curves are not intermediate between the surface and subsurface greenfield settlement troughs. These outcomes show that the TPI mechanism is due to both the interaction of the piles with subsurface ground movements along the pile axis and the non-linear and plastic behaviour of the soil. This results in the pile settlements being greater than greenfield values. Additionally, because the piles with their tips above the tunnel should settle more than the surface, whereas piles outside this region should settle less than the surface, there is an increase of the relative deflection of the more-flexible structures compared to shallow foundations that would deform according to surface greenfield settlement troughs.

On the other hand, the effects of the plate stiffness increment (soil-pile-structure interaction), which is evident for the stiffest building t12, are (i) the reduction of the plate relative deflection, Δ, and (ii) a decrease of the portion of the plate undergoing the secondary deformation mode (i.e. hogging deformations for building centred above the tunnel) due to the increase of i_{bldg} (defined in Figure 2.27). Effect (i) is due to the plate resisting the central deflection through its own stiffness and the residual bearing capacity of the external piles (i.e. those furthest from the tunnel), which is a function of the SF of the pile foundation. To restrain the downwards movement of the central piles, the plate applies tensile axial forces (due to tunnelling) near the head of the central piles, resulting in an upwards pile movement relative to the soil. The plate redistributes load to the external piles, which are consequently driven into the soil. This mechanism would induce a redistribution of the loads towards the external piles. If the superstructure is stiff and the load redistribution results in the total load after tunnelling on an external pile increasing to the residual pile bearing capacity (i.e. residual $SF = 1$), the pile (and entire plate) undergoes significant settlements; this is illustrated by comparing Figures 8.4(a) and (b) for test t12 whose external pile undergoes a remarkable increase in the settlement rate with respect to t6.w12. Effect (ii) was also noticed by Farrell et al. (2014), who performed centrifuge tests to study the deformations induced by tunnelling on a plate. Overall, effects (i) and (ii) result in a reduction of the building distortions with plate stiffness; on the other hand, the load redistribution due to stiff structures may result in remarkable settlements if the loads reach the residual bearing capacity. Therefore, tunnelling may pose a threat to the serviceability state of rigid piled buildings in terms of absolute displacements (and tilting in the case of eccentric tunnels).

For the same dataset, Figures 8.4(c) and (d) show the horizontal displacements of the plates. Despite the scatter of the data, the results confirm that the axial stiffness of the superstructure prevents significant horizontal strains of the superstructure (i.e. horizontal displacement curves show approximately a linear trend with the horizontal offset x) and only marginal horizontal differential displacements arise in the flexible plate t1.w12. In general, the distribution of horizontal tunnelling-induced strains was negligible across the entire dataset (groups 3C and 3D). These outcomes agree with the findings of previous researches, which indicate negligible

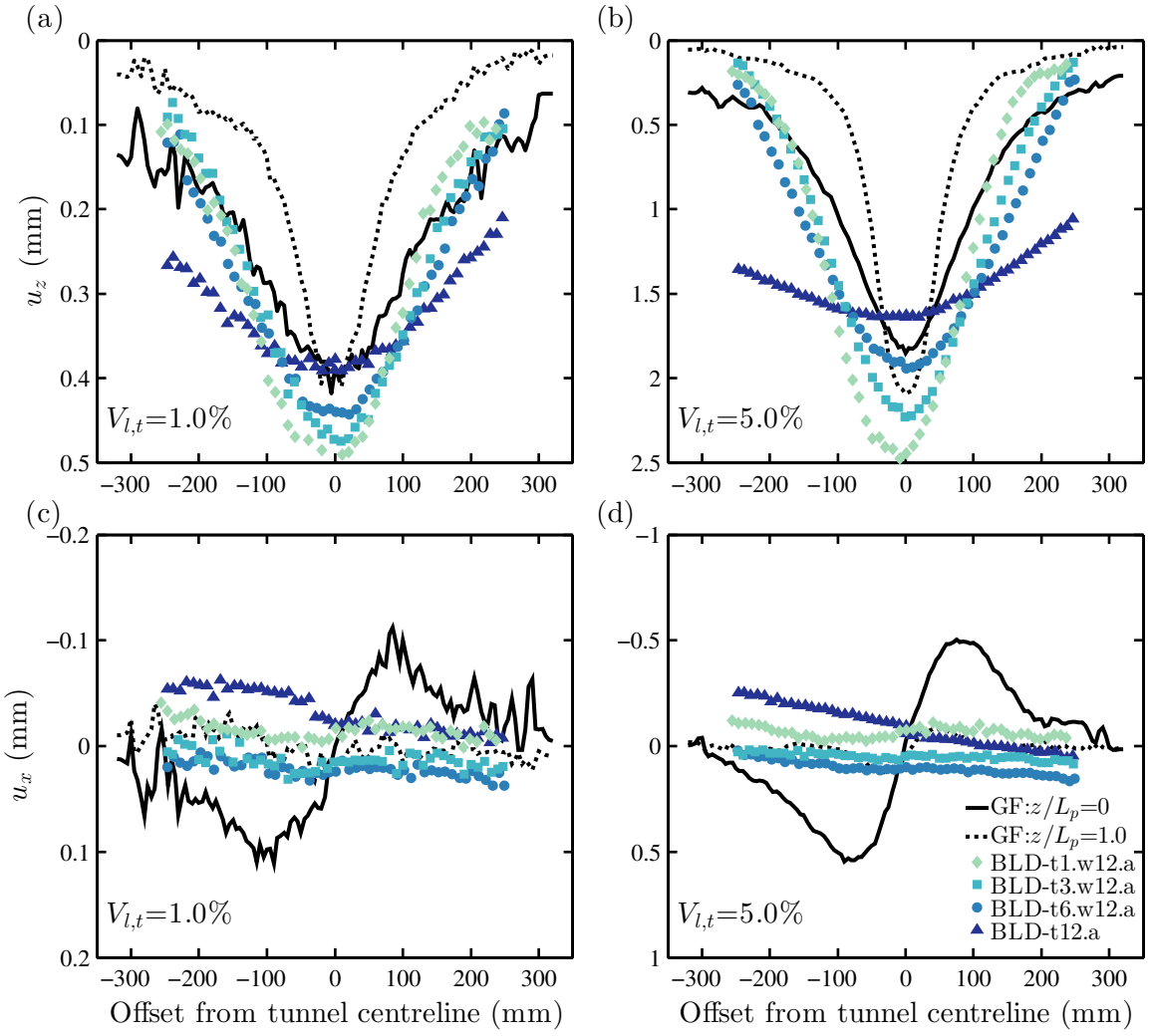

Fig. 8.4 Vertical and horizontal displacements of the soil (in greenfield conditions) and the piled plates with a given self-weight.

horizontal strains for buildings on continuous footings. However, these conclusions should not be generalised to buildings without horizontal structural elements connecting the pile heads (Goh and Mair, 2014).

8.1.4.2 The effect of superstructure weight

Figure 8.5 shows the effect of the superstructure weight on the settlement curves of two different plates (t1 and t6) subjected to a varying loading condition at medium and high volume losses. The results corresponding to the configurations t1, t1.w12, t6 and t6.w12 are shown. For tests t1.w12 and t6.w12, the initial safety factor SF_0 is 2.3, whereas for tests t1 and t6 performed with a simple plate $SF_0 = 17.4$ and 4.6, respectively. Because the plate thickness was maintained constant whilst changing the building weight (by adding masses at tops of the piles), it is possible with this dataset to isolate the effects of building self-weight on the TPI (in the case of the flexible superstructure) and the global TPSI. However, it should be noted that the percentage increase in

SF_0 is different for the two plates; therefore, the comparison of the settlement increase between plates t1 and t6 is only qualitative. In this figure, the greenfield settlement troughs at $z = 0$ and $z/L_p = 1$ are also plotted.

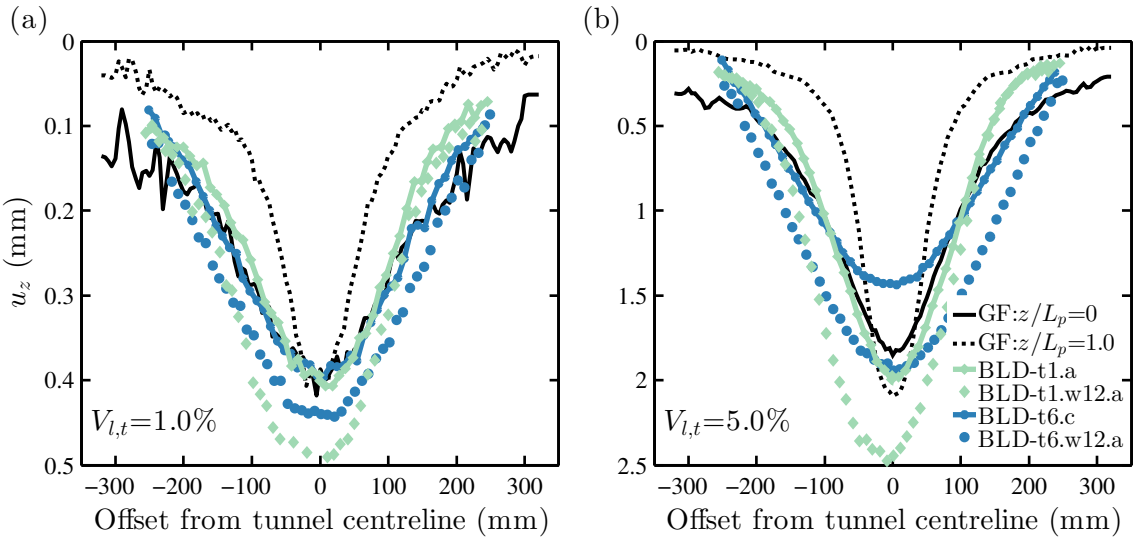

Fig. 8.5 Vertical displacements of the soil (in greenfield conditions) and the piled plates t1 and t6 for a varying self-weight.

The results illustrate that the greater the building self-weight, the higher the settlements of the building, especially in the portion of the building above the tunnel (in the sagging zone). Therefore, the importance of the building self-weight in the TPSI is demonstrated. Additionally, three aspects characterising the results in Figure 8.5 should be noted. i) The zone of influence tends to be narrower for the flexible structure t1 than for the relatively rigid structure t6; this is due to the difference in bending stiffness between the two plates. ii) Overall, the shape of the settlement curves is not highly affected by the building weight. iii) The increase in vertical displacements due to building weight is larger at $V_{l,t} = 5\%$ than at $V_{l,t} = 1\%$. This agrees with the centrifuge outcomes discussed in Chapter 7, which display that the settlement-volume loss curves of a given pile under different vertical loads tends to diverge at high tunnel ground loss. It is important to note that the increase in settlements with the building self-weight is probably associated with two phenomena that have opposing effects: a) there is an increase in the relative deflection of the plate, Δ, which induces greater deformations and b) there is a higher degradation of the soil stiffness, which results in a reduction of the building distortions. Therefore, to assess the impact of the self-weight on the building deformations and identify the prevailing phenomenon, it is necessary to analyse the variation of the deformation parameters, DR and M^{DR}, in sagging and hogging zones. This is carried out in the following sections. Finally, the results of test t1, which is a flexible plate with a negligible self-weight, confirm the averaging effect of piles on greenfield soil movements (i.e. building settlements lie between greenfield values at $z/L_p = 0$ and 1) showed by Devriendt and Williamson (2011) elastic tunnel-pile interaction analyses.

8.2 Study of superstructure deformations and settlements

8.2.1 Plate settlement-volume loss curves

Figure 8.6 plots the vertical displacements against $V_{l,t}$ for each tested configuration (in groups 3C and 3D). Firstly, it is interesting to remark that none of the plates experiences a brittle failure (i.e. a sharp increment of the settlement increment rate), which has been previously shown for the case of tunnel-single pile interaction (Marshall and Mair, 2011), despite the fact that the foundation consisted of piles in sands. This is due to two factors: i) the use of non-displacement piles, whose tunnelling-induced settlement-volume loss curve is not as steep as for displacement piles (see Chapter 7), and ii) the load redistribution that depends on the superstructure stiffness and the differential displacements between adjacent piles (i.e. although the thickness of the plate t1 results in a low bending stiffness, EI, the load redistribution may be relevant in the case of high differential pile displacements). To understand the latter component, it is useful to consider the case of a simply supported beam loaded in the middle by a unit force. The maximum settlement of the beam is proportional to the cube of the span length and the inverse of EI. Therefore, the narrower the settlement trough (which may result from the loss of capacity of the central piles), the greater the load redistribution (which prevents pile ultimate failure).

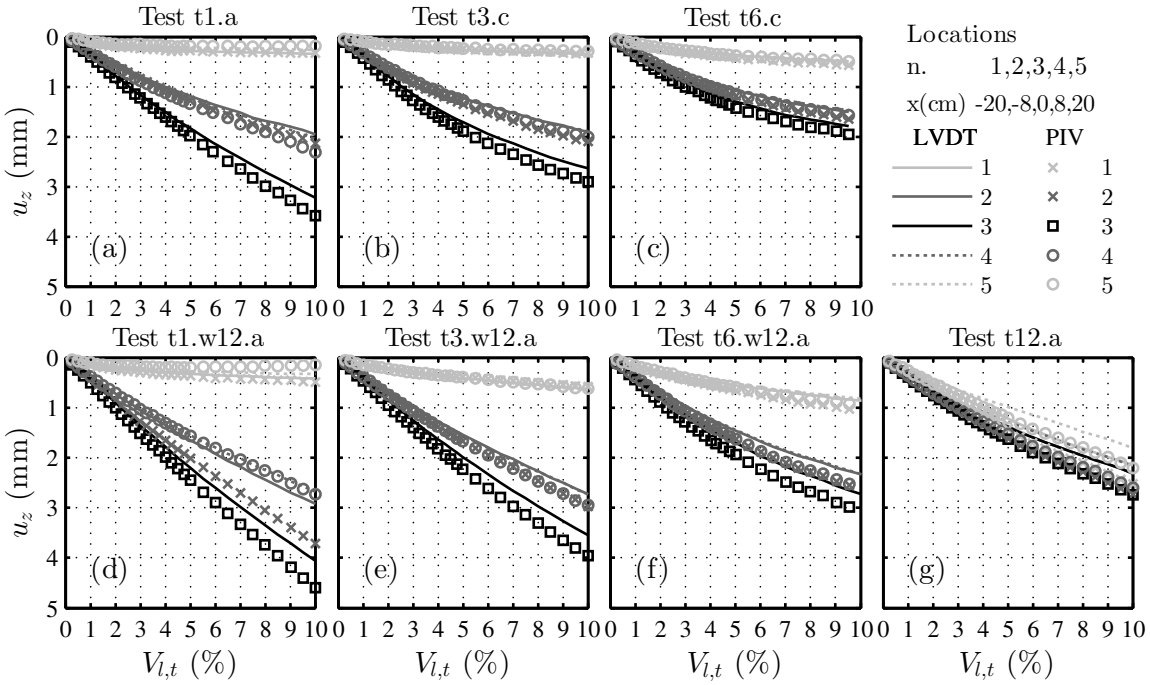

Fig. 8.6 Plate settlement-$V_{l,t}$ curves for varying superstructure self-weight and stiffness.

The results in Figure 8.6 illustrate the influence of the superstructure properties on the settlement increment rate with $V_{l,t}$. The results for a constant building self-weight, shown in Figures 8.6(d), (e), (f) and (g), illustrate a slight and gradual reduction of the plate settlement increment rate with $V_{l,t}$, which is more marked for the configuration t6.w12 than for tests t3.w12 and t1.w12 (it is approximately linear for test t1.w12). This reduction of plate settlement

increment rate with $V_{l,t}$ is probably due to soil plasticity and ground stiffness degradation due to tunnelling and TPSI mechanisms (i.e. the building displaces the piles because of its own stiffness, inducing additional shearing strains at the soil-pile interface). On the contrary, the plate settlement increment rate measured during test t12 is almost constant (Figure 8.6(g)); this is probably due to the combination of superstructure stiffness and the pile head load redistribution that resulted in the external piles, which were subjected to a load close to the residual pile bearing capacity ($SF = 1$), being driven in the soil, as pointed out in Section 8.1.4.1. When the external piles reach the ultimate condition, the superstructure stiffness can only respond to $\Delta V_{l,t}$ with a minor redistribution of the load towards the external piles, which are not able to withstand higher loads, and the entire pile-plate system settles uniformly to balance the effects of $\Delta V_{l,t}$. Therefore, if the external pile settlement is greater then the greenfield values, the decrease in settlement increment rate with $V_{l,t}$ is not possible . On the other hand, the tests performed at constant t and different SF_0 are compared in Figures 8.6(a) and (d), (b) and (e), (c) and (f); the displayed trends are characterised by a steady reduction of settlement increment rates (especially at high $V_{l,t}$) when the building weight is decreased.

In general, despite the influence of stiffness and SF_0 on the settlements, it is possible to conclude that the settlement variability of the central piles is lower than for the external piles (compare Figures 8.6(a) and (g)). This suggests that the building deformations (as DRs) are highly affected by the superstructure properties, whereas the superstructure self-weight and stiffness have a lower impact on the building maximum settlements. Both the building deformations and the maximum settlements are analysed later(see Figures 8.6 and 8.7).

It is important to remark that throughout Section 8.2, the greenfield ground movements are analysed at the normalised depths of $z = 0$ and $z/L_p = 2/3$ to compare the results of the TPSI, respectively, with the comparison terms often used in the case of shallow foundations ($z = 0$) and the empirical approach used for piled structures in the practice ($z/L_p = 2/3$) (Devriendt and Williamson, 2011).

8.2.2 The relationship between maximum plate and greenfield settlements

The building maximum settlement is of great interest for damage assessment at the serviceability limit state. To highlight the influence of the plate stiffness and self-weight on this parameter, the maximum settlements measured at each $V_{l,t}$ increment of the plates ($u^{blg}_{z,max}$) and the greenfield settlement troughs ($u^{gf}_{z,max}$) at $z = 0$ and $z/L_p = 2/3$ are displayed in Figure 8.7(a), whereas the ratios ($u^{blg}_{z,max}/u^{gf}_{z,max}$) between the plate displacement and the surface and subsurface settlement are shown in Figures 8.7(b) and (c), respectively. The latter figures are useful to relate the results of the global interaction with greenfield movements, which can be used as a reference term.

Figure 8.7(a) confirms that the plate stiffness and self-weight tend, respectively, to decrease and increase the maximum settlements of the superstructure within the investigated range of $V_{l,t}$. Note that the critical maximum settlement of $10\%d_p = 0.9$mm is plotted in Figure 8.7(a) for guidance. The results also show that the greenfield settlements, $u^{gf}_{z,max}$, vary almost linearly with $V_{l,t}$ and that the critical settlement of 0.9mm was reached by all the superstructures at

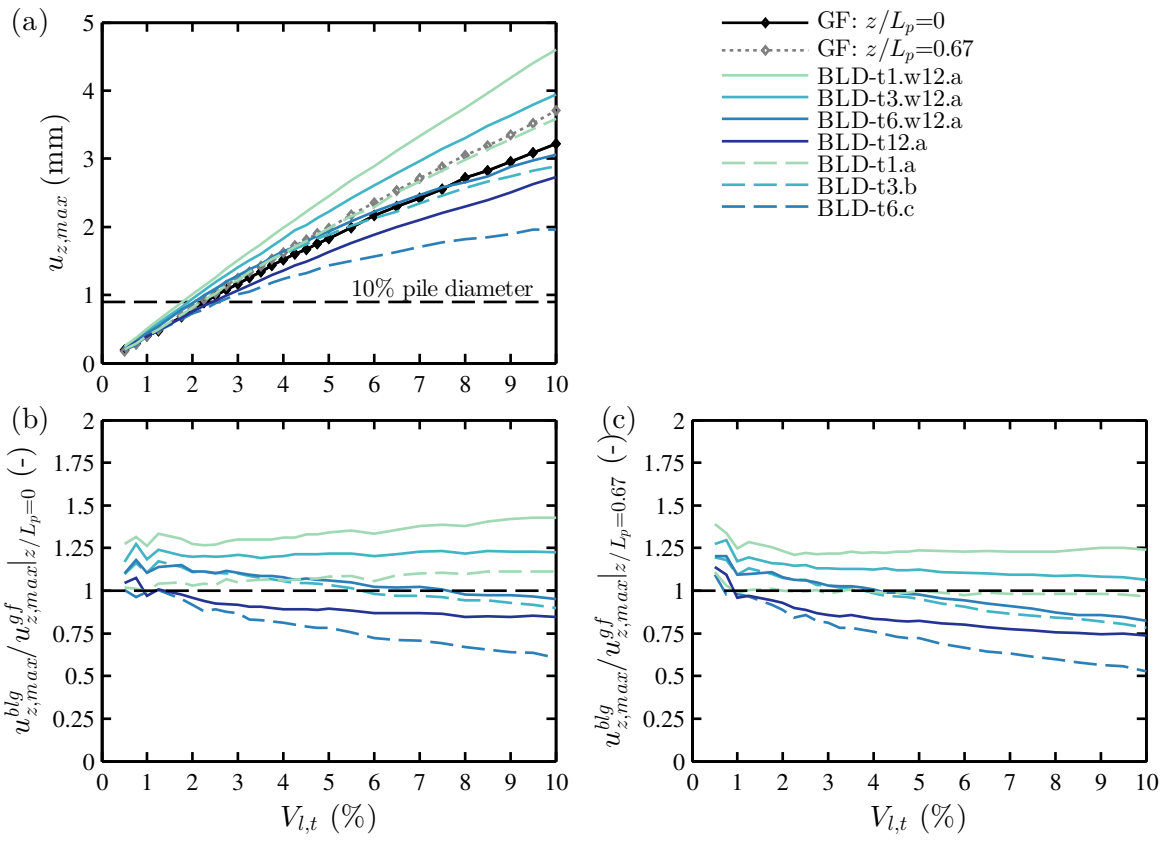

Fig. 8.7 The influence of the plate self-weight and stiffness on the maximum settlements of the superstructure.

$V_{l,t} = 1.5 - 2.5\%$, which is a relatively narrow interval. Furthermore, as shown by the solid lines in Figures 8.7(b) and (c), the dimensionless parameter $u^{blg}_{z,max}/u^{gf}_{z,max}$ ranged within the interval $0.75 - 1.5$ (mostly between 0.85 and 1.3) for the constant self-weight condition, confirming a relatively narrow range of variability of the normalised maximum plate settlements. Therefore, if there is no potential for reaching the pile failure condition, a preliminary assessment of the maximum building settlement could be carried out with a TPI analysis (assuming a fully flexible structure) accounting for the superstructure weight; this type of analysis would lead to a conservative but acceptable estimation for a preliminary design stage.

8.2.3 The variation of *DR* and M^{DR}

In the modification factor approach, to derive the resulting building *DR* values from the greenfield settlement trough, the deflection ratio modification factors, M^{DR}, are used, which are defined and illustrated in Figure 2.27. Note that the location of the greenfield and building inflection points, i and i_{bldg}, may vary with tunnel volume loss, $V_{l,t}$, whereas *DR* is calculated based on the maximum relative deflection, Δ.

In this study, to calculate *DR* and the location of the inflection points, i and i_{bldg}, the settlement curves, obtained from test series 3A, 3C and 3D, were interpolated with modified Gaussian

curves, as previously done by Farrell et al. (2014). In test series 3C and 3D, several curves were not symmetric with respect to the tunnel centreline; therefore, to improve the curve-fitting, two modified Gaussian curves with fixed maximum settlement and different shape parameters were used to interpolate the data corresponding to positive and negative horizontal offsets, x. An example of the achieved curve fitting is shown in Figure 8.8. Note that the curve fitting of the plate settlement curves was limited to the data within $x = \pm 225$mm, corresponding to the maximum pile offset (see Figure 3.16(b)), because the plate behaves as an unloaded cantilever beam outside these points.

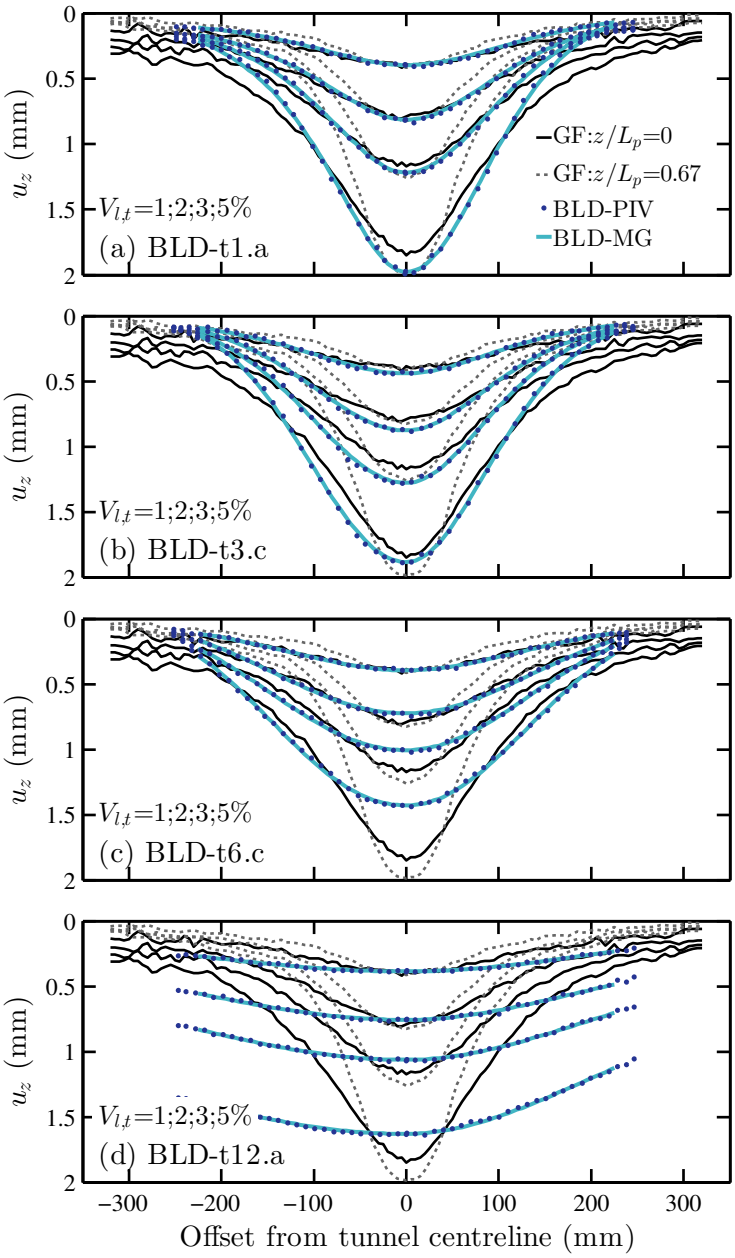

Fig. 8.8 Examples of curve-fitting of Geo-PIV settlement data with modified Gaussian curves.

The influence of the superstructure and $V_{l,t}$ on deflection ratios, DR, and modification factors, M^{DR}, is displayed in Figures 8.9 and 8.10. Figures 8.9 and 8.10 are used, respectively, to

display the effects of the superstructure stiffness and self-weight; sub-plots (a) and (b) shown the building and greenfield *DR*s in both sagging and hogging, whereas sub-plots (c) and (d) show the reduction factors, $M^{DR,sag}$ and $M^{DR,hog}$.

Firstly, the greenfield *DR*s plotted in Figures 8.9 and 8.10 are analysed. Previous researchers have illustrated that greenfield settlement troughs in sands become narrower with the increase of $V_{l,t}$ and suggested that a narrow settlement trough with large maximum settlement poses a higher potential for damage to structures (Marshall et al., 2012). However, for test GF, $DR_{gf,sag}$ and $DR_{gf,hog}$ have approximately linear trends with $V_{l,t}$, rather than increasing non-linearly (exponentially) due to the narrowing of the settlement curves. Note that the DR_{gf} - $V_{l,t}$ relationship should be linear when the shape of the settlement curve does not change with $V_{l,t}$ (typical for undrained clay where volumetric strains are zero). Therefore, the linear trend of $DR_{gf} - V_{l,t}$ during test GF is likely due to the combination of the decrease of i combined with the effects of the volumetric strains. Further investigations are needed to fully understand the effects of I_d, C/D, B, and e/B on the DR_{gf} - $V_{l,t}$ relationship in sands.

Secondly, the influence of the building stiffness is investigated by analysing the configurations with a constant SF_0 (triangle-shaped markers in Figures 8.9(a) and (b)). For the flexible building, the *DR*s measured during test t1.w12 are intermediate between greenfield surface and subsurface values and distributed approximately along a straight line, which indicates that the piles average the greenfield deformation pattern in terms of deformations. On the other hand, for the centrifuge tests t3.w12, t6.w12 and t12, the data follow non-linear distributions that are characterised by decreasing values of *DR* with plate thickness t and a gradual decrease of the increment rate with $V_{l,t}$. Although these results are qualitatively similar to the trends of the maximum settlements shown in Figure 8.7, the curves in Figures 8.9(a) have a marked drop in *DR* with plate thickness. As discussed previously, the observed non-linear trend of the superstructure distortions with volume loss could be attributed to the progressive degradation of the soil stiffness and the relative pile-soil displacements induced by the superstructure.

Finally, the effects of the self-weight on the *DR*s is displayed in Figures 8.10(a) and (b); triangle-shaped markers are used for the configurations with $SF_0 = 2.3$, whereas square-shaped markers are adopted for lower building weight. For all tested plates, the deflection ratios in the sagging zone undergo a notable increase with building self-weight, whereas in the hogging zone, the increase is limited to the flexible plate t1 and there is a reduction of DR_{hog} for the plate t3. Note that both square-shaped and triangle-shaped markers follow non-linear distributions. However, in the case of lower building weights (square-shaped markers), the decrease of the increment rate of *DR* with $V_{l,t}$ results in an asymptotic trend at high volume loss. Interestingly, for this configurations, the higher the value of t, the lower the value of $V_{l,t}$ at which a steady trend of *DR* is reached.

Figures 8.9(c) and (d) show the effects of plate stiffness on the reduction factors, $M^{DR,sag}$ and $M^{DR,hog}$, calculated using surface (solid lines) and subsurface (dashed lines) greenfield settlements. The building self-weight is constant for the dataset in these figures. Despite the influence of non-uniform deformation of the plate in the tunnel longitudinal direction discussed

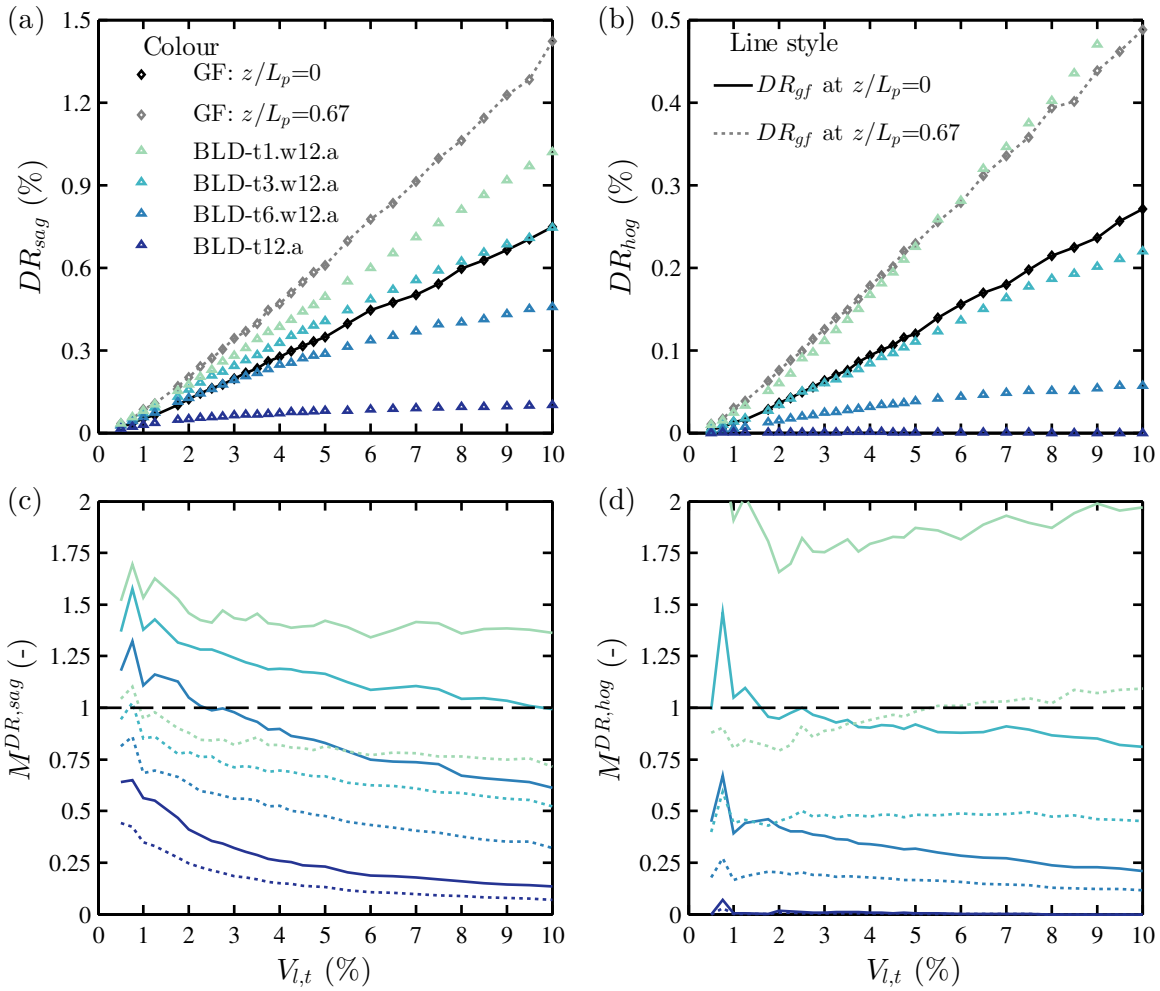

Fig. 8.9 Deflection ratios and modification factors in sagging and hogging for plates t1, t3, t6, and t12 with varying stiffness and constant self-weight.

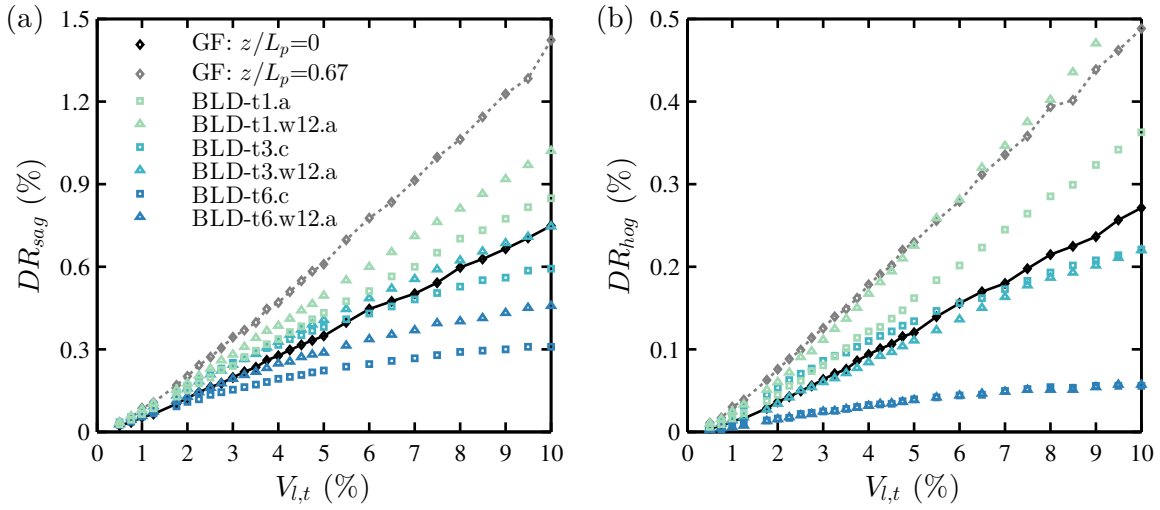

Fig. 8.10 The effects of superstructure self-weight on *DR*s: variation of the deflection ratios of plates t1, t3 and t6 in sagging and hogging.

in Section 8.1.1, from the data normalised with the greenfield surface *DR*s (solid lines), it is apparent that the TPI mechanism results in M^{DR} values greater than unity for flexible structures, whereas structural stiffness contributes to a decrease of the flexural deformations (as discussed earlier). Except for the hogging modification factors, $M^{DR,hog}$, of test t1 that is approximately constant, Figures 8.9(c) and (d) show that the values of M^{DR} are characterised by a steady decrease throughout the entire range of $V_{l,t}$: the thicker the plate, the greater the rate of decrease. Furthermore, as displayed by the dashed lines in Figures 8.9(c) and (d), similar qualitative trends with t and $V_{l,t}$ were obtained for the modification factors $M^{DR,sag}$ and $M^{DR,hog}$ defined using the subsurface greenfield deformations; however, because greenfield settlement troughs are wider at the surface than at greater depth, the magnitudes of dashed lines is remarkably lower than the solid lines. Note that the level of scatter in the GeoPIV measurements for the GF test is relatively high at low volume losses compared to the test with the piled plate; this leads to a scattered trend of the greenfield *DR*s and, thus, of M^{DR} at low volume loss.

Finally, the dashed lines in Figures 8.9(c) and (d) are used to evaluate the performance of simplified empirical TPI analyses described by Devriendt and Williamson (2011) based on the subsurface greenfield settlement profiles (i.e. DR_{gf} at $z/L_p = 2/3$). The modification factors $M^{DR,sag}$ and $M^{DR,hog}$ related to DR_{gf} at $z/L_p = 2/3$ resulted in $M^{DR,sag}$ and $M^{DR,hog} < 1.0$. In particular, during test t12, $M^{DR}_{sag} < 0.5$ and $M^{DR,hog} = 0$ for DR_{gf} measured at $z/L_p = 2/3$. Therefore, these centrifuge tests confirmed that this damage assessment should be reliable and conservative for $SF_0 > 2$ in the case of non-displacement piles. Finally, comparison of Figures 8.6 and 8.7 illustrates the different range of variability of the plate normalised maximum settlements and deformations and the need to account for superstructure stiffness in the assessment of pied building distortions.

8.2.4 The modification factor approach and the relative stiffness factors

8.2.4.1 The relative structure-soil stiffness

In the case of piled foundations, it is not possible to simplify the problem to a plane-strain condition. Therefore, to study the flexural deformations of piled building using the modification factor framework, the relative bending stiffness factor, ρ^p, defined in Equation 6.9 (Section 6.4.1.1) was used in this section.

To define the relative soil-structure stiffness, ρ^p, it is necessary to assess the bending stiffness, EI, of the portion of building corresponding to each transverse pile row, the transverse length, B, of the sagging/hogging zone in the greenfield condition, and the soil stiffness E_s. Firstly, the plate was separated into two independent portions in the longitudinal direction to assess EI corresponding to each pile row. B was measured from the greenfield settlement curves by identifying the offset of the inflection point at each volume loss value. E_s was estimated from the strains induced by the volume loss; the greater the volume loss, the lower the stiffness. The change in soil stiffness with volume loss was assessed following the logic of Marshall et al. (2010) and Farrell (2010), who studied centrifuge tunnelling in sands.

The procedure to assess E_s consists of two parts. a) The stiffness-shear strain relationship was defined from triaxial tests. b) In the case of the presence of the piled structure, the soil shear strains induced by volume loss, γ, were assessed from the displacements measured in the greenfield condition. To account for the spatial variability of E_s, a representative value was assessed at a normalised depth $z/z_t = 0.5$, which was suggested by Franzius et al. (2006) for shallow foundations and accounts for the fact that both the soil at the piles and beneath the tip level are involved in the interaction. Additionally, the strains were averaged along the settlement trough extension ($\pm 2.5i$).

$$\gamma_{avg}\left[z, V_{l,t}\right] = \frac{1}{5i}\int_{-2.5i}^{2.5i} \gamma dx \tag{8.1}$$

where γ_{avg} is the average strain. Note that using greenfield representative conditions results in two approximations: the superstructure self-weight effects on stresses, and thus stiffness, is neglected, and the variation in γ due to the presence of piles and the relative pile-soil displacements induced by the structure load redistribution is neglected. However, the effects of relative stiffness, which is inversely proportional to E_s, on the building distortions are proportional to a logarithmic scale (Franzius et al., 2006); therefore the accuracy of the estimated E_s can be limited to an order of magnitude with negligible error.

To determine the stiffness degradation curve for Fraction E sand, Zhao (2008) performed triaxial tests for $I_d = 70\%$ and $\sigma'_v = 100$kPa. In Figures 8.11(a) and (b), the measured relationships between $E_{v,sec} - \varepsilon_v$ and $G_{sec} - \gamma$ are reported, where G_{sec} and $E_{v,sec}$ are the secant shear stiffness modulus and the vertical Young's modulus of the soil, respectively, and ε_v is the vertical strain. Despite a different soil state (higher density and lower stresses), Marshall et al. (2010) and Farrell (2010) adopted the degradation curve $G_{sec} - \gamma$ measured with the triaxial test for the analysis of their centrifuge results. To evaluate the resulting error, the authors calibrated Equations 8.2 and 8.3, proposed by Lehane and Cosgrove (2000) for siliceous sands and gravels, on the available $E_{v,sec} - \varepsilon_v$ triaxial test data.

$$F\left[e\right] = \frac{\left(2.17 - e\right)^2}{1 + e} \tag{8.2}$$

$$E'_v = \begin{cases} \dfrac{E_{v,0}}{1 + \left(\dfrac{\varepsilon_v - \varepsilon_{el}}{\varepsilon_r - \varepsilon_{el}}\right)^n}, & \text{if } \varepsilon_v \geq \varepsilon_{el} \\ A_E F\left[e\right]\left(\dfrac{\sigma'_v}{p_{atm}}\right)^{0.5} = E_{v,0}, & \varepsilon_v < \varepsilon_{el} \end{cases} \tag{8.3}$$

where $E_{v,0}$ is the maximum stiffness at low strain, ε_v is axial strain, ε_{el} is the strain at which the stiffness-strain curve becomes non-linear, ε_r is a reference strain corresponding to the value of ε_v when E'_v is half of $E_{v,0}$, n and A_E are constants, σ'_v is the vertical effective stress, and p_{atm} is atmospheric pressure (100kPa). Subsequently, Equations 8.2 and 8.3 were used to analyse the variation in $E_{v,sec}$ when the soil density and the stress were varied from the conditions of the

triaxial tests to the centrifuge tests and show that, within the range of strains 0.1-1% generally induced by tunnelling, the variation was limited.

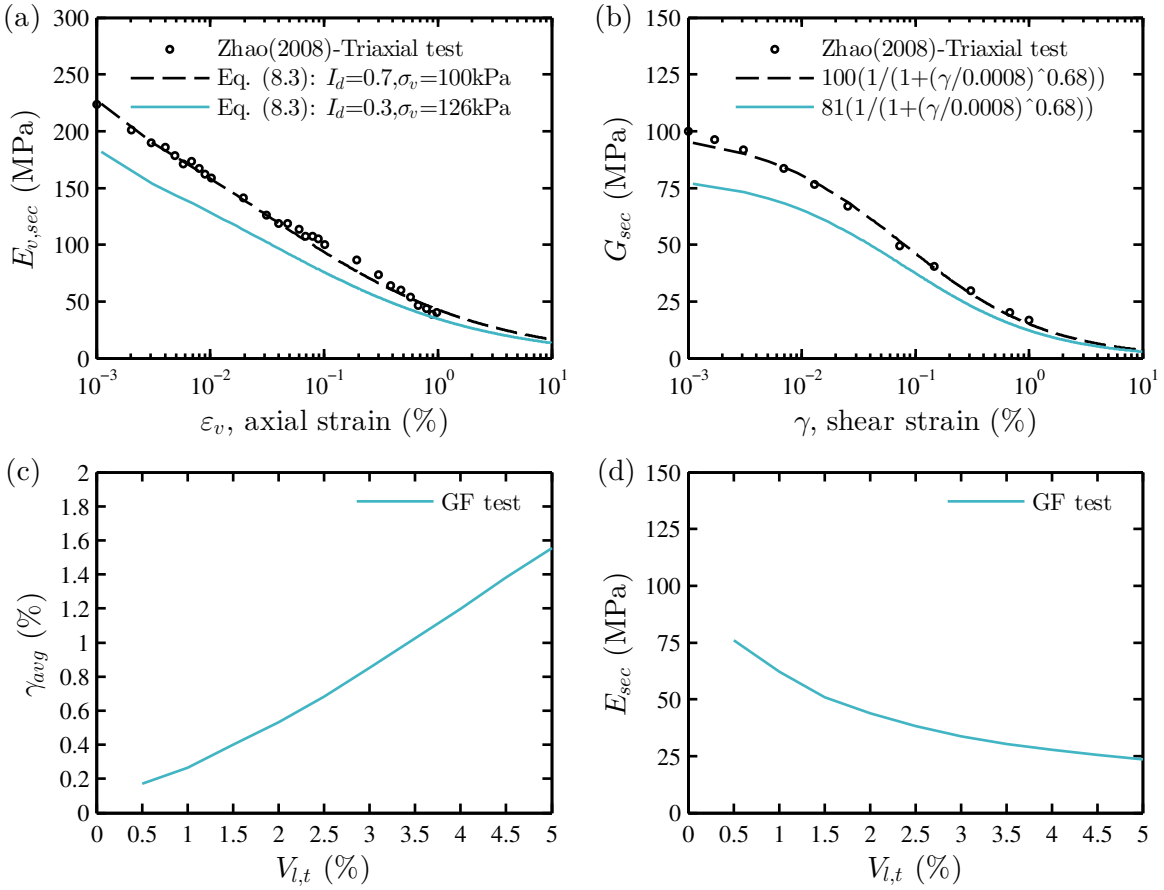

Fig. 8.11 (a) Vertical and (b) shear stiffness degradation with strains, (c) average shear strain and (d) soil stiffness with volume loss.

Following this approach, Equation 8.3 was calibrated on the laboratory test data (see Figure 8.11(a)). The parameters used to curve-fit the data of Zhao (2008) are $A_E = 200$, $n = 0.467$, $\varepsilon_{el} = 1 \cdot 10^{-5}$, and $\varepsilon_r = 4 \cdot 10^{-4}$. Then, the theoretical curve $E_{v,sec} - \varepsilon_v$ corresponding to soil conditions estimated in the greenfield centrifuge test at $z/z_t = 0.5$ ($\sigma'_v = 126$kPa; $I_d = 0.3$) was computed, which is equal to 0.81 times the equation curve-fitted to the triaxial data (see dashed and solid lines in Figure 8.11(a)). As shown in Figure 8.11(b), a stiffness degradation curve $G_{sec} - \gamma$ was curve-fitted to the measured data in the triaxial test (the obtained formula is reported in the legend). To take into account the different soil state between the centrifuge and the triaxial tests, $G_{sec} - \gamma$ curve was corrected with a reduction factor defined as

$$\frac{G_{sec}\left[\gamma, \sigma'_v = 126\text{kPa}, I_d = 0.3\right]}{G_{sec}\left[\gamma, \sigma'_v = 100\text{kPa}, I_d = 0.7\right]} = \frac{E'_v\left[\gamma, \sigma'_v = 126\text{kPa}, I_d = 0.3\right]}{E'_v\left[\gamma, \sigma'_v = 100\text{kPa}, I_d = 0.7\right]} = 0.81 \tag{8.4}$$

Finally, the relationship between shear strain and stiffness was estimated. The soil stiffness E_{sec} was related to the average strains of the soil, measured from the greenfield test at the depth $z/z_t = 0.5$, as follows: [i] it was assumed that $E_{sec}\left[\gamma_{avg}\right] = G_{sec}\left[\gamma_{avg}\right] \times 2(1+\nu)$ with $\nu = 0.25$,

[ii] the $G_{sec} - \gamma$ curve and the relationship $\gamma_{avg} - V_{l,t}$ shown with solid lines in Figure 8.11(b) and (c), respectively, were used. The resulting $E_{sec} - V_{l,t}$ trend, presented in Figure 8.11(d), displays an exponential reduction of soil stiffness with strain, resulting in an asymptotic value at high volume losses.

8.2.4.2 Modification factors against relative stiffness

Figure 8.12 displays the modification factors in sagging and hogging zones, $M^{DR,sag}$ and $M^{DR,hog}$ against the relative bending stiffness ρ^p. $M^{DR,sag}$ and $M^{DR,hog}$ were defined with the measurements of building and surface greenfield settlement curves within the volume loss range $V_{l,t} = 0.5 - 5\%$. Additionally, the envelopes proposed in Chapter 6 from the parametric analysis are also displayed in this figure.

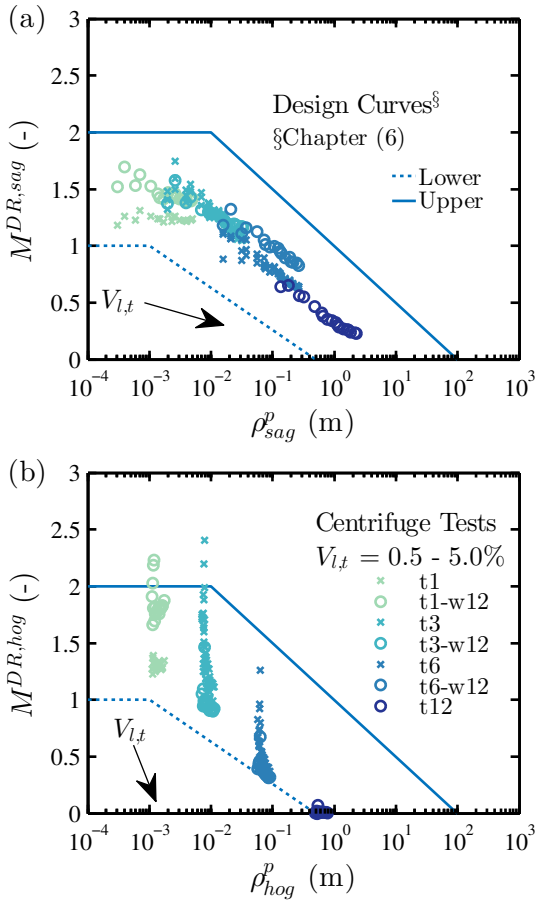

Fig. 8.12 Comparison between centrifuge results and design lines: $M^{DR,sag}$ computed with respect to surface greenfield settlement troughs versus relative building stiffness in (a) sagging and (b) hogging.

The results in Figure 8.12 show that: i) the increase in the relative stiffness decreases the building deformations, ii) the building self-weight increases the modification factors, iii) in sagging zone, the increase in volume loss results in greater ρ^p and lower M^{DR}, and iv) in hogging zone, greater volume losses cause a reduction in M^{DR} whereas their impact on ρ^p is minimal.

The main interaction mechanisms causing these results were described in the previous section, expect for the differences in the effects of $V_{l,t}$ on ρ^p in hogging and sagging zones, which are a consequence of $E_s B^3_{sag}$ decreasing and $E_s B^3_{hog}$ being approximately constant with the ground loss. Interestingly, most results are included between the proposed envelopes and, especially for the sagging zone (the primary deformation mode of the superstructure), the decrease in M^{DR} of the centrifuge data follows the trend indicated by the upper and lower envelopes. However, it should be highlighted that these envelopes were obtained with an elastic Winkler-based analysis method that does not account for the structure self-weight. Therefore, the good fit of the envelopes should not be interpreted as their efficiency in accounting for the building loading condition.

In future works, to account for the dependency of the relationship $M^{DR} - \rho^p$ on the structure self-weight, the relative stiffness parameter used in the x-axis of the charts could be generalised with an approach similar to the Equation (2.58) proposed by Giardina et al. (2015) and assuming that the estimated elastic envelopes correspond to a weightless model of the building. Alternatively, to consider the contribution of the superstructure stiffness in a preliminary risk assessment of TPSI, empirical elastic TPI analyses based on DR_{gf} at $z/L_p = 2/3$ (which do not account for the building weight) or analytical/numerical TPI analyses (that are able to account for the pile loading condition and safety factor) could be used in combination with the envelopes drawn in Figure 8.12 as follows.

- At the first step, the TPI analyses could provide the deflection ratio value DR^{TPI} that does not consider the stiffness of the superstructure.

- At the second step, the deflection ratio accounting for the superstructure contribution to the global interaction, DR^{TPSI}, is calculated as shown in Equation (8.5). The approach consists of multiplying DR^{TPI} by the ratio (≤ 1) between the modification factors $M^{DR}(\rho^p)$ and $M^{DR}(\rho^p \to 0)$, which correspond to the system relative stiffness value and a fully flexible building condition, respectively. $M^{DR}(\rho^p)$ and $M^{DR}(\rho^p \to 0)$ are computed with respect to the design curves in Figure 8.12. Both the curves should be used to define a value of this ratio; the greater DR^{TPSI} should be used for a conservative assessment.

$$DR^{TPSI} = DR^{TPI} \times \max\left(\frac{M^{DR}(\rho^p)|_{\text{upper}}}{M^{DR}(\rho^p \to 0)|_{\text{upper}}}, \frac{M^{DR}(\rho^p)|_{\text{lower}}}{M^{DR}(\rho^p \to 0)|_{\text{lower}}}\right) \tag{8.5}$$

  where the notations "upper" and "lower" refer to the upper and lower curves, respectively.

8.3 Conclusions

This chapter described a series of centrifuge tests performed to study the response of piled buildings to tunnelling in sands. It was demonstrated that the building stiffness and self-weight is important in the assessment of TPSI and that ignoring their influence may lead to erroneous estimations. However, it should be stressed that the performed tests investigated the response of equivalent elastic structures with a non-displacement pile foundation. Therefore, this study does not account for the influence of the structural configuration and the damage-induced non-linear behaviour of real structures (both piles, pile-structure connections, and superstructures) and the brittle tunnelling-induced increase in the settlement rate that is typical of displacement piles. The following conclusions can be drawn, which may provide useful guidance to tunnel engineers.

- Piles can have a detrimental role in the global interaction problem. Piled foundations lead to the narrowing of the building settlement curve in the case of fully-flexible structures because of the pile interaction with subsurface soil movements. This increases the potential for damage with respect to shallow foundations.

- When normalised with greenfield values, the results highlighted that the full range of variability of structural maximum settlements is narrower than the gap between upper and lower values of deflection ratios (compare Figures 8.7(b) and (c) with Figures 8.9(c) and (d)).

- As for shallow foundations, the superstructure stiffness decreases the building maximum settlements and the distortions (both deflection ratios and horizontal strains) resulting from tunnelling. Piled buildings respond critically to tunnelling in terms of flexural deformations, whereas horizontal strains in buildings that are continuous at the ground level are negligible even in the case of low axial stiffness.

- The impact of the weight on the building response is considerable. The increment of the superstructure self-weight results in an increment in the induced flexural distortions and, to a lesser extent, in the structure maximum settlements above the tunnel; therefore, neglecting the impact of the building self-weight is not conservative.

- The overall building settlement curve is dependent on the relationship between the superstructure stiffness, the building self-weight, and the residual safety factor of the piles (i.e. the ratio between residual ultimate and service load). This relationship highly affects the load redistribution mechanism. In general, to obtain load redistribution from the piles above the tunnel to the external ones, it is necessary to have both residual bearing capacity of the external piles and structural stiffness. In particular, with the increase of building self-weight, experiments indicated the possibility that the external piles of rigid structures may settle more than the greenfield scenario. This is due to the loads being transferred by the superstructure from the piles above the tunnel to the external ones, thereby exceeding the residual bearing capacity of the external piles.

- In current preliminary damage assessment procedures for piled buildings, the effects of the structural weight and stiffness is neglected. Assuming the building as a fully flexible structure while considering the building weight (i.e. performing a TPI analysis) can lead to the overestimation of the superstructure *DR* and horizontal strains, whereas it would result in an acceptable and conservative estimation of the maximum structure settlement if there is no potential for reaching pile failure. In particular, when the pile safety factor $SF > 2$, using subsurface greenfield settlement curves at $z/L_p = 2/3$ (i.e. DR_{gf} at $z/L_p = 2/3$), which do not account for the self-weight, leads to a conservative assessment.

- The building flexural distortions were framed within the modification factor approach using a relative structure-soil stiffness factor accounting for the presence of piles. The centrifuge measurement of $M^{DR,sag}$ and $M^{DR,hog}$ were plotted against the relative stiffness together with the design envelopes proposed in Chapter 6. The distribution of the centrifuge data versus the relative stiffness is consistent with the outcomes of the elastic parametric study. Furthermore, the proposed charts confirmed the main interaction mechanisms previously mentioned. Further work is necessary to normalise the distribution of M^{DR} with the building self-weight.

- If there is no potential for pile failure, the increase of $V_{l,t}$ should decrease the building distortions measured with *DR* because of soil stiffness degradation; the greater the plate stiffness the more significant is this decrease.

- For a detailed design, it is important to model the global TPSI accounting for the pile foundation bearing capacity, the service load distribution, and the superstructure self-weight.

Chapter 9

Conclusions and recommendations for further research

Increased urban populations demand further underground space and tunnels for civil infrastructure. Because tunnelling is not only limited to greenfield conditions and often occurs close to existing buried and surface structures, it may compromise the safety or serviceability limit state of these structures. In the case of new tunnel construction, soil-structure interaction analyses are performed by engineers to assess the potential for damage. In particular, a frequent issue in practice is that of excavations beneath pile foundations and piled structures. However, the understanding of the effects of tunnel-structure interaction is far from complete, in particular in the case of pile foundations.

This thesis addressed the problem of tunnelling and its effects on piles and piled buildings. The main aim of the research was to acquire high-quality data during centrifuge testing of tunnelling in sands both in greenfield conditions and near to piles and piled buildings; the development of the experimental apparatus, testing procedures and test plan were described in Chapter 3. In particular, an innovative novel method was developed to study complex soil-structure interaction problems through the real-time coupling of numerical and centrifuge modelling to enhance centrifuge modelling capabilities. This method was used to study the impact of tunnelling beneath existing piled frames, which is a complex SSI problem, providing a direct link between ground and structural engineering. In the author's view, this research has the potential to impact the way in which soil-structure interaction problems are analysed in centrifuge modelling. Finally, it should be noted that, in addition to the experimental work, empirical, analytical and semi-analytical solutions were used to study the tunnelling-induced displacement fields, and simplified elastic analyses were presented that provided insights into the global tunnel-pile-structure interaction mechanisms.

This chapter describes the main findings of the previous chapters and suggests further research that could be undertaken to achieve a better understanding of ground movements and soil-structure interactions resulting from tunnel excavation.

9.1 Conclusions

9.1.1 Greenfield tunnelling in sandy ground

Chapters 4 and 5 dealt with the problem of tunnelling-induced ground movements in sands. Greenfield tunnelling centrifuge tests in a plane-strain condition were performed to investigate relatively shallow and deep tunnels in loose, medium-dense and dense dry sands. The data from these experiments, taken together with comparable datasets from Marshall et al. (2012) and Zhou (2014), allowed for the evaluation of displacement and shear strain distributions around the tunnel. Furthermore, centrifuge test data were analysed within empirical and semi-analytical frameworks, which are based on the use of modified Gaussian curves and the superposition of singularities method, respectively. The main findings regarding greenfield ground movements due to tunnel excavation in sands are summarised in the following.

- The vertical and horizontal displacement mechanisms are notably complex and correlated; in particular, experimental data supports that the displacement mechanisms are the consequences of the soil's capability for arching.

- Settlement trough width and maximum settlement were studied because they are of great interest to engineers for preliminary risk assessment procedures. The maximum settlement at the tunnel centreline increases with tunnel volume loss, decreases with cover-to-diameter ratio, and reduces with soil density both at the surface and subsurface levels. On the other hand, the settlement field width increases with the increase in cover-to-diameter ratio whereas it decreases with increase in tunnel volume loss and normalised depth; these relationships are non-linear because of soil arching and the transition from shallow to deep tunnels.

- The curve-fitting of centrifuge settlement troughs with modified Gaussian curves allowed the study of settlement trough shape. In addition, a new empirical method based on the use of modified Gaussian curves was proposed to predict the main variations in width parameters and soil volume loss with the physical parameters of the problem. However, the predictions of the new set of equations are subject to certain limitations because the empirical approach cannot entirely capture the complexity of the problem.

- The efficiency of the González and Sagaseta (2001) analytical closed-form solution was assessed by comparing its predictions with the centrifuge experiment data. Despite a consistent soil deformation pattern, the analytical solution provided a poor prediction of subsurface displacements.

- To provide a simple and efficient tool to engineers, the elastic analytical displacement field predicted by the González and Sagaseta (2001) solution was modified through a corrective term calibrated using data from a single centrifuge test as a benchmark. It was shown that the proposed semi-analytical formula is able to determine, with reasonable accuracy, the

horizontal and vertical movements around the tunnel as they are affected by tunnel volume loss; however, the modification factor regression should be extended to the entire dataset of centrifuge tests to overcome its limited applicability.

- The differences in the deformation patterns of clay and sandy soils due to tunnelling were also investigated: tunnel ovalization and tunnel volume loss lead to significant differences, particularly with regard to subsurface movements and, in general, at high volume loss.

- The effects of the tunnel modelling technique was analysed by comparing greenfield outcomes of fluid-filled flexible membranes to a rigid boundary model tunnel. In general, the boundary conditions used to simulate tunnel ground loss have a significant impact on the settlement mechanism and stress state. Rigid model tunnels with uniform contraction are not appropriate for a realistic modelling of tunnelling in sands.

9.1.2 The effect of tunnelling on pile foundations

Tunnelling beneath piles is a critical scenario because there is potential for pile failure and differential pile settlements amongst a transverse pile row. Chapters 7 and 8 presented centrifuge test data relating to the study of the response to tunnelling of axially loaded displacement and non-displacement pile foundations with constant head loads (imposed or resulting from fully-flexible structures). These test series provide insights into the pile settlement-tunnel volume loss relationship and the initiation of pile failure.

- Results illustrated the importance of considering [i] pile installation method (displacement versus non-displacement piles) and [ii] initial safety factor (ratio between initial pile bearing capacity and service load) for the estimation of tunnelling-induced pile settlements and the critical tunnel volume loss associated with pile failure; in general the tunnel-pile interaction is affected by both aspects [i] and [ii].

- Centrifuge outcomes showed that the lower the initial safety factor, the greater the tunnelling-induced settlements.

- Large pile settlements should be expected for both non-displacement and displacement piles when the pile tip is located within previously defined tunnel influence zones (Jacobsz et al., 2004). Piles in this position may settle more than the soil along the pile axis in greenfield condition due to soil non-linearities and plasticity.

- Results highlighted that pile failure is a critical aspect for displacement piles with relatively low initial safety factors (initial safety factor lower than 2). Interestingly, piles in sands with an initial safety factor greater than 2.5 may not experience failure due to tunnel excavation. For instance, this would be the case of an unloaded pile.

9.1.3 The effect of tunnelling on piled structures

Chapters 6, 7, and 8 explored the key aspects of complete tunnel-pile-structure interaction due to tunnelling beneath the pile tip depth. Research focused on pile head and structural displacements as well as superstructure deformations that can be used to evaluate building serviceability state. Results of these chapters were also evaluated with the modification factor approach to allow the direct comparison with similar research carried out for buildings on shallow foundations. In Chapter 6 the predictions of a simplified elastic Winkler-based Two-Stage Analysis Method (TSAM) were validated with 3D finite element analyses limited to the case of soil linear elasticity and perfect bonding between the pile and soil. Therefore, the effects of soil non-linearities and building self-weight were not considered. The elastic Winkler-based TSAM provided insights into the main interaction mechanisms (the role of tunnel-pile interaction, superstructure stiffness, structural configuration, and pile-structure connections) and their effects on superstructure deformations. Chapter 7 illustrated the response of piled frames to tunnelling with tests performed using the coupled centrifuge and numerical modelling (CCNM) technique to assess the influence of frame stiffness and pile installation method (displacement and non-displacement piles). This tests series provided, for various configurations, the boundary conditions (settlements and axial loads) shared between the frame (simulated numerically) and the pile foundation (tunnel-ground-foundation system was modelled in the centrifuge). Finally, in Chapter 8, conventional equivalent piled aluminium plates with a non-displacement pile foundation were tested in the centrifuge. Tested configurations isolated the contributions of structural stiffness and self-weight on superstructure displacements.

The following findings should prove to be particularly valuable to engineers for the design of new tunnels beneath piled structures. These conclusions, achieved with different approaches, provide a consistent framework for future investigations.

- This study has found that tunnelling-induced displacements of piled buildings are dependent on the relationship between the superstructure stiffness, the building self-weight, the residual safety factor of the piles and the pile installation method. A detailed design should account for all these factors.

- Elastic numerical analyses and experimental studies identified that piled buildings respond critically to tunnelling in terms of flexural deformations, whereas horizontal strains in buildings that are continuous at the ground level are negligible even where structural elements (i.e. ground level beams) have low axial stiffness.

- This research confirmed that [i] piled foundations increase the risk of structural damage compared to shallow foundations, [ii] the superstructure stiffness decreases building maximum settlements and the distortions resulting from tunnelling (both deflection ratios and horizontal strains), and [iii] the increase in the superstructure self-weight results in greater tunnelling-induced flexural distortions and, to a lesser extent, in the structure maximum settlements. In general, piles have a detrimental role in the global interaction problem

because of the interaction of piles with subsurface soil movements (piled foundations lead to the narrowing of the building settlement curve with respect to the greenfield scenario in the case of constant pile head load). On the other hand, the superstructure stiffness is able to modify the behaviour of the foundation because tunnelling induces differential pile settlements resulting in superstructure distortions and, thus, in the redistribution of building self-weight loads among piles. Finally, it is worth highlighting that neglecting the impact of building self-weight is not conservative.

- Interestingly, the risk of pile failure due to underground excavations is highly affected by the pile head load redistribution due to the superstructure stiffness. Centrifuge data suggest that a limited relative reduction in the pile load with volume loss ($\approx 10-15\%$ of the pre-tunnelling value) could prevent failure of piles. Therefore, analysis methods assessing ultimate tunnel contraction associated with pile failure should account for load redistribution among piles.

- Results of elastic Winkler-based TSAM illustrated that the response of buildings modelled as equivalent beams can differ considerably compared to when they are modelled as framed structures. Therefore, the structural configuration should be considered in a refined risk assessment.

- The building distortions were considered within the modification factor approach. Parametric analyses were carried out with the elastic Winkler-based TSAM. Simple design charts were provided to estimate horizontal strains and deflection ratio modification factors based on newly defined relative axial and bending stiffness parameters which account for the presence of the piles. The envelopes compared well with deflection ratio modification factors measured from the equivalent plate centrifuge tests. However, note that these design charts do no account for the building self-weight.

- In general, centrifuge data illustrated that assuming the building as a fully flexible structure while considering the building weight (i.e. performing a TPI analysis) can lead to the overestimation of the superstructure deflection ratio and horizontal strains, whereas it would result in an acceptable and conservative estimation of the maximum structure settlement if there is no potential for reaching pile failure. In current preliminary damage assessment procedures for piled buildings (neglecting the structural weight and stiffness), the building deflection ratio is evaluated with respect to the subsurface greenfield settlement curves at a depth equal to 2/3 of the pile length. It was confirmed that this estimation is conservative if the safety factor of non-displacement piles is greater than 2.

- In the case of pile foundations, the increase of tunnel volume loss should decrease the building distortions measured relative to the greenfield case because of soil stiffness degradation. However, this statement should not be generalised to cases of low initial foundation safety factor combined with a flexible building; in this scenario, piles may fail resulting in potential high localised superstructure distortions.

- Tunnel engineers should consider that potential risk for the serviceability limit state of buildings and services is associated with both building distortions and absolute settlements. Therefore, absolute building settlements should also be considered. For instance, centrifuge tests highlighted that rigid superstructures combined with a low pre-tunnelling safety factor of the foundation could lead to significant building absolute settlements.

9.2 Further research

This research has shown the importance of investigating soil-structure interaction problems due to underground excavations accounting for both the geotechnical and the structural aspects; simplified modelling that reduces the structural domain to a distribution of constant forces may induce errors as significant as the assumption of a simplistic ground model. There is certainly scope for further work involving tunnelling, tunnelling beneath piled structures and, in general, soil-structure-interaction due to excavations. These are outlined in the following.

- When subsurface and horizontal ground movements are used for tunnel-structure interaction analyses, it is necessary to assume a consistent soil deformation pattern. The proposed semi-analytical solution provides a simple way to assess greenfield movements; however, this approach should be extended to the entire available dataset and its predictions compared with field data. The resulting solution would be of great utility.

- Because the tunnel depth is considered by the normalised cover-to-diameter ratio, the proposed empirical approach for the prediction of settlement troughs does not account for the effects of the confining stresses. Therefore, additional centrifuge tests in the plane-strain greenfield condition could examine, for a given cover-to-diameter ratio and soil relative density, the relation between displacement mechanisms and overburden stress level. Furthermore, the proposed empirical framework should ideally be validated against field data.

- Within this research it was shown that, despite the wide body of literature, the effects of the adopted tunnel modelling technique in centrifuge tests is not well understood. It would be useful to the research community to accurately assess the effect of using flexible and rigid model tunnels in centrifuge tests; this work could result in a framework of good tunnel modelling practice in centrifuge tests.

- It would be interesting to study tunnel-pile-structure interaction considering the excavation advancement in the tunnel longitudinal direction to [i] evaluate the variation of the interaction mechanisms with respect to plane-strain tunnel modelling and [ii] assess the resulting 3D deformations of structures. This may be achieved by performing a series of tests modelling half of the tunnel with the plane of symmetry (Perspex window) parallel to the tunnel longitudinal axis.

- Future research should assess the impact of the displacement field variability in sands on tunnel-structure interaction problems. For instance, further investigations are needed to fully understand the effects of density, tunnel relative depth, and building-tunnel eccentricity on the relationship between superstructure deflection ratio and volume loss.

- The greenfield centrifuge test series in this dissertation focused on tunnelling in dry sand. A subsurface water table is frequently present when tunnelling; therefore, centrifuge

tests modelling water conditions would be interesting to evaluate the variation of the displacement mechanisms induced by the pore pressure and partial saturation of the sand above the water table.

- The Winkler-based TSAM could be improved by implementing non-linear pile-soil load transfer models (considering soil degradation and unloading effects). This advanced TSAM could be validated with the centrifuge dataset of this research and, potentially, it could represent a useful tool to further investigate the effects of tunnel volume loss level, superstructure weight, and tunnel head excavation advancement on the global interaction.

- Design charts were suggested as a practical guidance to estimate deflection ratio and horizontal strain modification factors depending on relative bending and axial stiffness, respectively, accounting for the presence of the piles. [i] Further research on bending and axial relative stiffness factors could narrow the gap between the upper and lower envelopes. For instance, more accurate predictions could be achieved accounting for structural configuration and tunnel-structure eccentricities, which were shown to have a remarkable role in the interaction. [ii] Additionally, bending and axial relative stiffness factors should consider the pile installation, pile initial safety factor (i.e. building self-weight), pile spacing and diameter. [iii] The proposed envelopes are based on an elastic parametric study and were compared with a small data set obtained with centrifuge modelling. To prove its reliability, it would be interesting to evaluate their performance with field data obtained in practice.

- For framed buildings, it would be interesting to perform a detailed structural analysis and compare the actual damage distribution within a frame (considering strains in pillars and beams) with predictions obtained using the limiting tensile strain framework and an equivalent beam model. Furthermore, in the author's view, the process of identification of the equivalent beam/plate should be improved to better account for the superstructure configuration.

- In urban areas, development of infrastructure and new building construction often need temporary works and deep excavations, which may affect existing piled structures. Because there are several similarities in the interaction resulting from deep excavations and tunnelling, it would be interesting to study the problem of the response of piled building to deep excavations using the experimental and analytical tools developed during this research.

- In general, the construction of new tunnels in the proximity of deep foundations raises concerns related to pile failure and associated structural damage (in both the superstructures and the foundation). Because of the uncertainties related to the problem, to minimise tunnelling-induced damage on structures and infrastructure of strategic/historical importance, protection measures such as compensation grouting are often prescribed. In general, limited guidance is available for engineers to evaluate the effects of compensation grouting

on pile foundations; furthermore, there may be cases in which the use of grouting results in unexpected or negative outcomes for deep foundations and superstructures. Further studies and/or centrifuge tests aiming to understand the mechanisms governing the effects of grouting on deep foundations would be a valuable contribution.

- Although this research has investigated the response of pile foundations, the author believes that further work in assessing the effects of the close spacing of piles within a group would aid tunnel engineers. It would be interesting to confirm if the group effect is detrimental or beneficial to the response of piles to tunnelling, both in terms of displacements and residual bearing capacity.

- The research has focused on the response of deep foundations and piled structures to tunnelling considering that the piles are the only structural elements interacting with the soil. However, frequently in urban environments, foundations are designed as a piled raft or as piles with enlarged caps or connection beams. These elements at the pile heads may be designed to increase the stiffness and bearing capacity of the foundation or may be neglected during the foundation design. In both cases, these elements would likely interact with the ground surface due to tunnelling-induced pile settlements. Future research combining centrifuge modelling, field monitoring and numerical modelling is recommended to address this topic, which should have a significant role in the global interaction. In terms of directions for future work, this dissertation may represent a starting point.

- The overall performance of the CCNM technique was very satisfactory and gives confidence that the methodology can be used for a wide spectrum of building typologies and stiffnesses. Future developments should allow the investigation of the effects of superstructure non-linearities and damage; this could be achieved by coupling the centrifuge model with non-linear and/or plastic models of the superstructure. Further applications (e.g. deep excavations) should also be explored.

References

Atkinson, J. H. and Potts, D. M. (1977). Stability of a shallow circular tunnel in cohesionless soil. *Géotechnique*, 27(2):203–215.

Attewell, P. B., Yeates, J., and Selby, A. R. (1986). *Soil movements induced by tunnelling and their effects on pipelines and structures*. Blackie and Son Ltd, UK.

Attewell, P. B. and Yeates, J. O. H. N. (1984). Tunnelling in soil. *Ground movements and their effects on structures*, pages 132– 215.

Basile, F. (2014). Effects of tunnelling on pile foundations. *Soils and Foundations*, 54(3):280–295.

Bjerrum, L. (1963). Allowable settlement of structures. In *Proceedings of the 3rd European Conference on Soil Mechanics and Foundation Engineering*, volume 2, pages 135–137.

Blakeborough, A., Williams, M. S., Darby, A. P., and Williams, D. M. (2001). The development of real-time substructure testing. *Philosophical Transactions of the Royal Society A: Mathematical, Physical and Engineering Sciences*, 359(1786):1869–1891.

Bolton, M. D., Gui, M. W., Garnier, J., Corte, J. F., Bagge, G., Laue, J., and Renzi, R. (1999). Centrifuge cone penetration tests in sand. *Géotechnique*, 49(4):543–552.

Boonsiri, I. and Takemura, J. (2015). Observation of ground movement with existing pile groups due to tunneling in sand using centrifuge modelling. *Geotechnical and Geological Engineering*, 33(3):621–640.

Boscardin, M. D. and Cording, E. J. (1989). Building response to excavation-induced settlement. *Journal of Geotechnical Engineering*, 115(1):1–21.

Broms, B. B. and Bennermark, H. (1967). Stability of clay at vertical opening. *Journal of the Soil Mechanics and Foundations Division*, 93(1):71–94.

Burland, J. B., Broms, B. B., and De Mello, V. F. B. (1977). Behaviour of foundations and structures. In *Proceedings of the 9th International Conference on Soil Mechanics and Foundations Engineering*, volume 2, pages 495–546, Tokyo.

Burland, J. B., Mair, R. J., and Standing, J. R. (2004). Ground performance and building response due to tunnelling. In Jardine, R. J., Potts, D. M., and Higgins, K. G., editors, *Advances in Geotechnical Engineering: The Skempton Conference - Proceedings of a Three Day Conference on Advances in Geotechnical Engineering, organised by the Institution of Civil Engineers*, volume 1, pages 291–344, London, United kingdom. Thomas Telford Services Ltd.

Burland, J. B. and Wroth, C. P. (1974). Settlement of buildings and associated damage. In *Conference on the Settlement of Structures*, pages 611–654.

Celestino, T. B., Gomes, R. A. M. P., and Bortolucci, A. A. (2000). Errors in ground distortions due to settlement trough adjustment. *Tunnelling and Underground Space Technology*, 15(1):97–100.

Chambon, P. c. and Corte, J. F. (1994). Shallow tunnels in cohesionless soil: stability of tunnel face. *Journal of Geotechnical Engineering*, 120(7):1148–1165.

Chen, L. T., Poulos, H. G., and Loganathan, N. (1999). Pile responses caused by tunneling. *Journal of Geotechnical and Geoenvironmental Engineering*, 125(2-3):207–215.

Cheng, C. Y., Dasari, G. R., Chow, Y. K., and Leung, C. F. (2007). Finite element analysis of tunnel-soil-pile interaction using displacement controlled model. *Tunnelling and Underground Space Technology*, 22(4):450–466.

Chi, S.-Y., Chern, J.-C., and Lin, C.-C. (2001). Optimized back-analysis for tunneling-induced ground movement using equivalent ground loss model. *Tunnelling and Underground Space Technology*, 16(3):159–165.

Clough, W. and Schmidt, B. (1981). Design and performance of excavations and tunnels in soft clay. *Soft Clay Engineering*, pages 567–634.

Cording, E. J. (1991). Control of ground movements around tunnels in soil. In *Proceeding of the 9th Pan-American Conference on Soil Mechanics and Foundation Engineering*, volume 4, pages 2195–2244.

Cording, E. J. and Hansmire, W. H. (1975). Displacements around soft ground tunnels. In *Proceeding of the 5th Panamerican conference on soil mechanics and foundation engineering*, pages 571–632.

da Silva, T. S., Elshafie, M. Z., and Madabhushi, G. (2016). Centrifuge modelling of arching in granular soils. In *Proceedings of the 3rd European Conference on Physical Modelling in Geotechnics (Eurofug*, pages 301–306.

Davis, E. H., Gunn, M. J., Mair, R. J., and Seneviratine, H. N. (1980). The stability of shallow tunnels and underground openings in cohesive material. *Géotechnique*, 30(4):397–416.

Devriendt, M. and Williamson, M. (2011). Validation of methods for assessing tunnelling-induced settlements on piles. *Ground Engineering*, pages 25–30.

Dewoolkar, M. M., Santichaianant, K., and Ko, H.-Y. (2007). Centrifuge modeling of granular soil response over active circular trapdoors. *Soils and Foundations*, 47(5):931–945.

Dias, D. and Kastner, R. (2013). Movements caused by the excavation of tunnels using face pressurized shields - Analysis of monitoring and numerical modeling results. *Engineering Geology*, 152(1):17–25.

Dias, T. G. S. and Bezuijen, A. (2015). Data analysis of pile tunnel interaction. *Journal of Geotechnical and Geoenvironmental Engineering*, 141(12):04015051.

Dimmock, P. S. and Mair, R. J. (2007). Estimating volume loss for open-face tunnels in London Clay. *Proceedings of the ICE -Geotechnical Engineering*, January(GE I):13–22.

Dimmock, P. S. and Mair, R. J. (2008). Effect of building stiffness on tunnelling-induced ground movement. *Tunnelling and Underground Space Technology*, 23(4):438–450.

Dyer, M., Hutchinson, M., and Evans, N. (1996). Sudden valley sewer: a case history. In *International symposium on geotechnical aspects of underground construction in soft ground*, pages 671–676, London.

Ellis, E., Cox, C., Yu, H. S., Ainsworth, A., and Baker, N. (2006). A new geotechnical centrifuge at the University of Nottingham, UK. In Ng, Zhang, and Wang, editors, *6th International Conference of Physical Modelling in Geotechnics: ICPMG'06*, pages 129–133, Hong Kong. Taylor & Francis Group, London.

Fargnoli, V., Boldini, D., and Amorosi, A. (2013). TBM tunnelling-induced settlements in coarse-grained soils: The case of the new Milan underground line 5. *Tunnelling and Underground Space Technology*, 38:336–347.

Fargnoli, V., Gragnano, C. G., Amorosi, A., and Boldini, D. (2015). 3D numerical modelling of soil–structure interaction during EPB tunnelling. *Géotechnique*, 65(1):23–37.

Farrell, R. (2010). Tunnelling in sands and the response of buildings. *Ph.D. Thesis, Cambridge University*.

Farrell, R., Mair, R., Sciotti, A., and Pigorini, A. (2014). Building response to tunnelling. *Soils and Foundations*, 54(3):269–279.

Fioravante, V. (2002). On the shaft friction modelling of non-displacement piles in sand. *Soils and Foundations*, 42(2):23–33.

Fleming, W. G. K., Weltman, A. J., Randolph, M. F., and Elson, W. K. (2009). *Piling Engineering*. Taylor & Francis, 3rd edition.

Franza, A., Haji, T., and Marshall, A. M. (2016a). A Winkler-based method for the assessment of tunnelling-induced deformations on piled structures. In Ni, J. C., Yang, J., Chen, S.-l., and Qiu, T., editors, *Proceedings of 4th Geo-China International Conference*, number 260 GSP, pages 259–266, Shandong, China. American Society of Civil Engineers (ASCE).

Franza, A., Idinyang, S., Heron, C., and Marshall, A. M. (2016b). Development of a coupled centrifuge-numerical model to study soil-structure interaction problems. In Thorel, L., Bretschneider, A., Blanc, M., and Escoffier, S., editors, *Proceedings of the 3rd European Conference on Physical Modelling in Geotechnics (Eurofuge 2016)*, pages 135–140, Nantes, France.

Franza, A. and Marshall, A. M. (2015a). Analytical investigation of soil deformation patterns above tunnels in sandy soil. In *Proceedings of the XVI ECSMGE Geotechnical Engineering for Infrastructure and Development*, volume 2, pages 467–472, Edinburgh, United Kingdom.

Franza, A. and Marshall, A. M. (2015b). Semi-analytical prediction of ground movements due to shallow tunnels in sand. In *Proceedings of the XVI ECSMGE Geotechnical Engineering for Infrastructure and Development*, volume 2, pages 461–466, Edinburgh, United Kingdom.

Franza, A. and Marshall, A. M. (2016). Centrifuge modelling of piled structure response to tunnelling. In Thorel, L., Bretschneider, A., Blanc, M., and Escoffier, S., editors, *Proceedings of the 3rd European Conference on Physical Modelling in Geotechnics (Eurofuge 2016)*, pages 313–318, Nantes, France.

Franza, A., Marshall, A. M., Haji, T., Abdelatif, A. O., Carbonari, S., and Morici, M. (2017). A simplified elastic analysis of tunnel-piled structure interaction. *Tunnelling and Underground Space Technology*, 61:104–121.

Franza, A., Zhou, B., and Marshall, A. M. (2016c). The effects of relative tunnel depth and volume loss on vertical settlements above tunnels in dense sands. In Ni, J. C., Yang, J., Chen, S.-l., and Qiu, T., editors, *Proceedings of 4th Geo-China International Conference*, number 260 GSP, pages 125–132, Shandong, China. American Society of Civil Engineers (ASCE).

Franzius, J. N., Potts, D. M., Addenbrooke, T. I., and Burland, J. B. (2004). The influence of building weight on tunnelling-induced ground and building deformation. *Soils and Foundations*, 44(1):25–38.

Franzius, J. N., Potts, D. M., and Burland, J. B. (2006). The response of surface structures to tunnel construction. *Proceedings of the ICE - Geotechnical Engineering*, 159(1):3–17.

Garnier, J., Gaudin, C., Springman, S. M., Culligan, P. J., Goodings, D., Konig, D., Kutter, B., Phillips, R., Randolph, M. F., and Thorel, L. (2007). Catalogue of scaling laws and similitude questions in geotechnical centrifuge modelling. *International Journal of Physical Modelling in Geotechnics*, 7(3):1–23.

Garnier, J. and König, D. (1998). Scale effects in piles and nails loading tests in sand. In *Proceedings of the international conference Centrifuge 98*, number 205-210.

Gaudin, C., Kong, V., and Cassidy, M. J. (2012). An overview of spudcan reinstallation near a footprint. In *Offshore Technology Conference, Houston*, number 2004, Houston, Texas.

Giardina, G. (2013). *Modelling of settlement induced building damage*. PhD thesis, Technische Universtiteit Delft.

Giardina, G., DeJong, M. J., and Mair, R. J. (2015). Interaction between surface structures and tunnelling in sand: Centrifuge and computational modelling. *Tunnelling and Underground Space Technology*, 50:465–478.

Goh, K. H. and Mair, R. J. (2011). Building damage assessment for deep excavations in Singapore and the influence of building stiffness. *Geotechnical Engineering Journal of the SEAGS & AGSSEA*, 42(3):1–12.

Goh, K. H. and Mair, R. J. (2012). The horizontal response of framed buildings on individual footings to excavation-induced movements. In *Proceedings of the 7th International Symposium on Geotechnical Aspects of Underground Construction in Soft Ground*, pages 895–902, Rome.

Goh, K. H. and Mair, R. J. (2014). Response of framed buildings to excavation-induced movements. *Soils and Foundations*, 54(3):250–268.

González, C. and Sagaseta, C. (2001). Patterns of soil deformations around tunnels. Application to the extension of Madrid Metro. *Computers and Geotechnics*, 28(6–7):445–468.

Grant, R. J. and Taylor, R. N. (2000). Tunnelling-induced ground movements in clay. *Proceedings of the ICE - Geotechnical Engineering*, 143(1):43–55.

Hsiung, B. C. B. B.-C. (2011). A case record of bored tunnels in sand based on the Kaohsiung mass rapid transit system project. *Journal of GeoEngineering*, 6(3):113–123.

Huang, M., Zhang, C., and Li, Z. (2009). A simplified analysis method for the influence of tunneling on grouped piles. *Tunnelling and Underground Space Technology*, 24(4):410–422.

Iglesia, G. R., Einstein, H. H., and Whitman, R. V. (2014). Investigation of soil arching with centrifuge tests. *Journal of Geotechnical and Geoenvironmental Engineering*, 140(2):04013005.

Jacobsz, S. W. (2002). The effects of tunnelling on piled foundations. *Ph.D. Thesis, Cambridge University*.

Jacobsz, S. W., Bowers, K. H., Moss, N. A., and Zanardo, G. (2005). The effects of tunnelling on piled structures on the CTRL. In *Proceedings of the 5th International Symposium on Geotechnical Aspects of Underground Construction in Soft Ground*, pages 115–121, Amsterdam.

Jacobsz, S. W., Standing, J. R., Mair, R. J., Hagiwara, T., and Sugiyama, T. (2004). Centrifuge modelling of tunnelling near driven piles. *Soils and Foundations*, 44(1):49–56.

Jones, B. (2010). Low-volume-loss tunnelling for London ring main extension. *Proceedings of the ICE -Geotechnical Engineering*, 163(3):167–185.

Jongpradist, P., Kaewsri, T., Sawatparnich, A., Suwansawat, S., Youwai, S., Kongkitkul, W., and Sunitsakul, J. (2013). Development of tunneling influence zones for adjacent pile foundations by numerical analyses. *Tunnelling and Underground Space Technology*, 34:96–109.

Kaalberg, F. J., Teunissen, E. A. H., van Tol, A. F., and Bosch, J. W. (2005). Dutch research on the impact of shield tunnelling on pile foundations. In Bakker, K. J., Bezuijen, A., Broere, W., and Kwast, E. A., editors, *Proceedings of the 5th International Symposium on Geotechnical Aspects of Underground Construction in Soft Ground*, pages 123–131, Amsterdam, the Netherlands. Taylor & Francis - Balkema.

Kimura, T. and Mair, R. J. (1981). Centrifugal testing of model tunnels in soft clay. *Proceedings of the 10th international conference on soil mechanics and foundation engineering*, 1:319–322.

Kirsch, G. (1898). Die theorie der elastizitaet und die bedeurfnisse der festigkeitslehre. *VDI Zeitschrift*, 42:797–807.

Kitiyodom, P., Matsumoto, T., and Kawaguchi, K. (2005). A simplified analysis method for piled raft foundations subjected to ground movements induced by tunnelling. *International Journal for Numerical and Analytical Methods in Geomechanics*, 29(15):1485–1507.

Klar, A. (2006). The effect of tunnel buoyancy on ground surface settlement in elastic soil. *Electronic Journal of Geotechnical Engineering*, 11 C.

Klar, A. and Marshall, A. M. (2008). Shell versus beam representation of pipes in the evaluation of tunneling effects on pipelines. *Tunnelling and Underground Space Technology*, 23(4):431–437.

Kutter, B., Chang, J., and Davis, B. (1994). Collapse of cavities in sand and particle size effects. In C. F. Leung, F. Lee and Tan, T., editors, *Proceedings of International Conference Centrifuge '94*, pages 809–815, Singapore. Balkema.

Leca, E., New, B., and Reporter, G. (2007). Settlements induced by tunneling in Soft Ground. *Tunnelling and Underground Space Technology*, 22(2):119–149.

Lee, C. J. (2012). Three-dimensional numerical analyses of the response of a single pile and pile groups to tunnelling in weak weathered rock. *Tunnelling and Underground Space Technology*, 32(0):132–142.

Lee, C. J. and Jacobsz, S. W. (2006). The influence of tunnelling on adjacent piled foundations. *Tunnelling and Underground Space Technology*, 21(3-4):430.

Lee, C.-J., Wu, B.-R., and Chiou, S.-Y. (1999). Soil movements around a tunnel in soft soils. *Proceedings of the National Science Council, Republic of China, Part A: Physical Science and Engineering*, 23(2):235–247.

Lee, C.-J. J. and Chiang, K.-H. H. (2007). Responses of single piles to tunneling-induced soil movements in sandy ground. *Canadian Geotechnical Journal*, 44(10):1224–1241.

Lee, K. M., Rowe, R. K., and Lo, K. Y. (1992). Subsidence owing to tunnelling. I. Estimating the gap parameter. *Canadian Geotechnical Journal*, 29(6):929–940.

Lee, Y.-J. and Bassett, R. H. (2007). Influence zones for 2D pile–soil-tunnelling interaction based on model test and numerical analysis. *Tunnelling and Underground Space Technology*, 22(3):325–342.

Lehane, B. and Cosgrove, E. (2000). Applying triaxial compression stiffness data to settlement prediction of shallow foundations on cohesionless soil. *Proceedings of the ICE - Geotechnical Engineering*, 143(4):191–200.

Loganathan, N. and Poulos, H. G. (1998). Analytical prediction for tunneling-induced ground movements in clays. *Journal of Geotechnical and Geoenvironmental Engineering*, 124(9):846–856.

Loganathan, N., Poulos, H. G., and Stewart, D. P. (2000). Centrifuge model testing of tunnelling-induced ground and pile deformations. *Géotechnique*, 50(3):283–294.

Loganathan, N., Poulos, H. G., and Xu, K. J. (2001). Ground and pile-group responses due to tunnelling. *Soils and Foundations*, 41(1):57–67.

Losacco, N., Burghignoli, A., and Callisto, L. (2014). Uncoupled evaluation of the structural damage induced by tunnelling. *Géotechnique*, 64(8):646–656.

Madabhushi, S. P. G., Haigh, S. K., Ali, A., Williams, M., Ojaghi, M., Lamata, I., Blakeborough, T., Taylor, C. A., and Dietz, M. (2010). Distributed testing of soil-structure systems using web-based applications. In Springman, S., Laue, J., and Seward, L., editors, *Physical Modelling in Geotechnics - Proceedings of the 7th International Conference on Physical Modelling in Geotechnics 2010, ICPMG 2010*, volume 1, pages 355–360, Zurich. Taylor & Francis Group, London.

Mair, R. (2013). Tunnelling and deep excavations: ground movements and their effects. In Anagnostopoulos, A., Pachakis, M., and Tsatsanifos, C., editors, *Proceedings of the 15th European Conference on Soil Mechanics and Geotechnical Engineering - Geotechnics of Hard Soils - Weak Rocks (Part 4)*, pages 39 – 70, Amsterdam, the Netherlands. IOS Press.

Mair, R. and Williamson, M. (2014). The influence of tunnelling and deep excavation on piled foundations. In Yoo, C., Park, S.-W., Kim, B., and Ban, H., editors, *Proceedings of the 8th International Symposium on Geotechnical Aspects of Underground Construction in Soft Ground*, pages 21–30, Seoul, South Korea. Taylor and Francis - Balkema.

Mair, R. J. (1979). Centrifugal modelling of tunnel construction in soft clay. *PhD Thesis Cambridge University*.

Mair, R. J. (1993). Unwin memorial lecture 1992: developments in geotechnical engineering research: application to tunnels and deep excavations. *Proceedings of the ICE - Civil Engineering*, 97(1):27–41.

Mair, R. J. and Taylor, R. N. (1993). Prediction of clay behaviour around tunnels using plasticity solutions. In Telford, T., editor, *Predictive Soil Mechanics: Proceedings of the Wroth Memorial Symposium Held at St. Catherine's College*, pages 449–463, Oxford.

Mair, R. J. and Taylor, R. N. (1999). Theme lecture: Bored tunnelling in the urban environment. In *14th International conference on soil mechanics and foundation engineering*, pages 2353–2385, (Hamburg. Balkema.

Mair, R. J. and Taylor, R. N. (2001). Elizabeth House: settlement predictions. In *Building Response to Tunnelling: Case Studies from Construction of the Jubilee Line Extension*, volume 1, pages 195–215, London, United Kingdom. Thomas Telford.

Mair, R. J., Taylor, R. N., and Bracegirdle, A. (1993). Subsurface settlement profiles above tunnels in clay. *Géotechnique*, 43(2):315–320.

Mair, R. J., Taylor, R. N., Burland, J. B., and Taylor, R. N. (1996). Prediction of ground movements and assessment of risk of building damage due to bored tunnelling. In Mair, R. J. and Taylor, R. N., editors, *Proceedings of the International Symposium on Geotechnical Aspects of Underground Construction in Soft Ground*, pages 713–718, London, United Kingdom. Balkema, Rotterdam.

Marshall, A. (2012). Tunnel-Pile Interaction Analysis Using Cavity Expansion Methods. *Journal of Geotechnical and Geoenviromental Engineering*, (October):1237–1246.

Marshall, A. and Mair, R. (2011). Tunneling beneath driven or jacked end-bearing piles in sand. *Canadian Geotechnical Journal*, 48(12):1757–1771.

Marshall, A. M. (2009). Tunnelling in sand and its effect on pipelines and piles. *Ph.D. Thesis, Cambridge University*.

Marshall, A. M., Farrell, R., Klar, A., and Mair, R. (2012). Tunnels in sands: the effect of size , depth and volume loss on greenfield displacements. *Géotechnique*, 62(5):385–399.

Marshall, A. M. and Franza, A. (2016). Discussion of "Observation of Ground Movement with Existing Pile Groups Due to Tunneling in Sand Using Centrifuge Modelling" by Ittichai Boonsiri and Jiro Takemura. *Geotechnical and Geological Engineering*, pages 1–5.

Marshall, A. M. and Haji, T. (2015). An analytical study of tunnel-pile interaction. *Tunnelling and Underground Space Technology*, 45:43–51.

Marshall, A. M., Klar, A., and Mair, R. (2010). Tunneling beneath buried pipes: View of soil strain and its effect on pipeline behavior. *Journal of Geotechnical and Geoenvironmental Engineering*, 136(12):1664–1672.

Mindlin, R. D. (1936). Force at a Point in the Interior of a Semi-Infinite Solid. *Journal of Applied Physics*, 7(5):195–202.

Moh, Z. C., Ju, D. H., and Hwang, R. N. (1996). Ground movements around tunnels in soft ground. In *Proceedings International Symposium on Geotechnical Aspects of Underground Construction in Soft Ground*, volume 730, pages 725–730.

Möller, S. (2006). *Tunnelling-induced settlements and structural forces in linings*. PhD thesis, University of Stuttgart.

Monmasson, E., Idkhajine, L., Cirstea, M. N., Bahri, I., Tisan, A., and Naouar, M. W. (2011). FPGAs in Industrial Control Applications. *IEEE Transactions on Industrial Informatics*, 7(2):224–243.

Mroueh, H. and Shahrour, I. (2002). Three-dimensional finite element analysis of the interaction between tunneling and pile foundations. *International Journal for Numerical and Analytical Methods in Geomechanics*, 26(3):217–230.

Mylonakis, G. and Gazetas, G. (1998). Settlement and additional internal forces of grouped piles in layered soil. *Géotechnique*, 48(1):55–72.

O'Reilly, M. P. and New, B. M. (1982). *Settlements above tunnels in the United Kingdom - their magnitude and prediction*.

Pang, C. H., Yong, K. Y., and Chow, Y. K. (2005). Three-dimensional numerical simulation of tunnel advancement on adjacent pile foundation. *Underground Space Use: Analysis of the Past and Lessons for the Future*, 2:1141–1148.

Park, K. H. (2004). Elastic solution for tunneling-induced ground movements in clays. *International Journal of Geomechanics*, 4(4):310–318.

Park, K. H. (2005). Analytical solution for tunnelling-induced ground movement in clays. *Tunnelling and underground space technology*, 20(3):249–261.

Peck, R. B. (1969). Deep excavations and tunnelling in soft ground. In *7th International Conference on Soil Mechanics and Foundation Engineering*, pages 225–290, Mexico City, Mexico.

Pender, M. J. (1980). Elastic solutions for a deep circular tunnel. *Géotechnique*, 30(2):216–222.

Phienwej, N., Hong, C. P., and Sirivachiraporn, A. (2006). Evaluation of ground movements in EPB-shield tunnelling for bangkok MRT by 3D-numerical analysis. *Tunnelling and Underground Space Technology*, 21(3-4).

Photayanuvat, C., Flicke, J., and Hollmann, F. (2006). Outline Design of the Blue Line South Underground Section – Extension of the Existing Bangkok MRT Subway Line. In *Proceedings of the International Symposium on Underground Excavation and Tunnelling*, pages 85–96, Bangkok, Thailand.

Pinto, F. and Whittle, A. J. (2006). Discussion of "Elastic solution for tunneling-induced ground movements in clays" by K. H. Park. *International Journal of Geomechanics*, 6(1):72–73.

Pinto, F. and Whittle, A. J. (2014). Ground Movements due to Shallow Tunnels in Soft Ground. I: Analytical Solutions. *Journal of Geotechnical and Geoenvironmental Engineering*, 140(4):04013040.

Pinto, F., Zymnis, D. M., and Whittle, A. J. (2014). Ground Movements due to Shallow Tunnels in Soft Ground. II: Analytical Interpretation and Prediction. *Journal of Geotechnical and Geoenvironmental Engineering*, 140(4):1–11.

Potts, D. M. (1976). Behaviour of lined and unlined tunnels in sand. *Ph.D. thesis, Cambridge University*.

Potts, D. M. and Addenbrooke, T. I. (1997). A structure's influence on tunnelling-induced ground movements. *Proceedings of the ICE - Geotechnical Engineering*, 125(2):109–125.

Poulos, H. G. and Deng, W. (2004). An Investigation on Tunnelling-Induced Reduction of Pile Geotechnical Capacity. In *Proceeding of the 9th Australia New Zealand Conference on Geomechanics*, volume 1, pages 116–122, Auckland, NZ. NZ Geotechnical Society & Australian Geomechanics Society.

Randolph, M. F., Dolwin, J., and Beck, R. (1994). Design of driven piles in sand. *Géotechnique*, 44(3):427–448.

Randolph, M. F. and Wroth, C. P. (1979). An analysis of the vertical deformation of pile groups. *Géotechnique*, 29(4):423–439.

Randolph, M. F. and Wroth, P. C. (1978). Analysis of deformation of vertically loaded piles. *Journal of the Geotechnical Engineering Division*, 104(12):1465–1488.

Ritter, S., Giardina, G., DeJong, M. J., and Mair, R. J. (2016). Experimental challenges of modelling structure response to tunnelling. In *Proceedings of the 3rd European Conference on Physical Modelling in Geotechnics (Eurofuge 2016)*, pages 349–354.

Rowe, R. and Kack, G. (1983). A theoretical examination of the settlements induced by tunnelling: four case histories. *Canadian Geotechnical Journal*, 20(2):299–314.

Sagaseta, C. (1987). Analysis of undrained soil deformation due to ground loss. *Géotechnique*, 37(3):301–320.

Schuller, H. and Schweiger, H. (2002). Application of a Multilaminate Model to simulation of shear band formation in NATM-tunnelling. *Computers and Geotechnics*, 29(7):501–524.

Selemetas, D. (2005). The response of full-scale piles and piled structures to tunnelling. *Ph.D. Thesis, Cambridge University*.

Simulia (2010). ABAQUS Analysis User's Manual. Dassault Systèmes, Providence, RI, U.S.A.

Skempton, A. W. and MacDonald, D. H. (1956). The allowable settlements of buildings. *Proceedings of the ICE*, 5(6):727–768.

Soomro, M. A., Hong, Y., Ng, C. W. W., Lu, H., and Peng, S. (2015). Load transfer mechanism in pile group due to single tunnel advancement in stiff clay. *Tunnelling and Underground Space Technology*, 45:63–72.

Strack, O. b. and Verruijt, A. (2002). A complex variable solution for a deforming buoyant tunnel in a heavy elastic half-plane. *International Journal for Numerical and Analytical Methods in Geomechanics*, 26(12):1235–1252.

Strack, O. E. (2002). Analytic solutions of elastic tunnelling problems. *PhD thesis, Delft Univ. of Technology*.

Sugiyama, T., Hagiwara, T., Nomoto, T., Nomoto, M., Ano, Y., Mair, R., Bolton, M., and Soga, K. (1999). Observations of ground movements during tunnel construction by slurry shield method at the Docklands Light Railway Lewisham Extension-East London. *Soils and Foundations*, 39(3):99–112.

Takahashi, K., Fukazawa, N., Hagiwara, T., and Hosoda, M. (2004). Observational control of slurry shield tunnels with super close spacing under the nearby bridge abutments loads. *Tunnelling and Underground Space Technology*, 19(4):390.

Taylor, R. N. (1995a). *Geotechnial centrifuge technology*. Blackie Academic & Professional, London.

Taylor, R. N. (1995b). Tunnelling in soft ground in the UK. In *Underground construction in soft ground*, pages 123–126, Balkema.

Teparaksa, W., Tangpraprutgul, T., Boonsong, C., and Boonard, J. (2006). Ground and bridge displacement due to epb shield tunnel bored underneath bridge pile foundation. In *Proceedings of the International Symposium on Underground Excavation and Tunnelling*, pages 299–307, Bangkok, Thailand.

Terzaghi, K. (1942). Discussion of the progress report of the committee on the bearing value of pile foundations. *Proceedings of the American Society of Civil Engineers*, 68:311–323.

Timoshenko, S. and Goodier, J. N. (1970). *Theory of Elasticity*. New York.

Ullmann, M., Hübner, M., Grimm, B., and Becker, J. (2004). An FPGA run-time system for dynamical on-demand reconfiguration. In *Proceedings - International Parallel and Distributed Processing Symposium, IPDPS 2004*, volume 18, pages 1841–1848.

van Jaarsveld, E. P., Plekkenpol, J. W., and van de Graaf, C. A. M. (1999). Ground deformations due to the boring of the Second Heinenoord Tunnel. In *Geotechnical engineering for transportation infrastructure. Proceedings of the 12th European conference on soil mechanics and geotechnical engineering*, volume 1, pages 153–159, Amsterdam. A.A.Balkema.

Verruijt, A. (1997). A complex variable solution for a deforming circular tunnel in an elastic half-plane. *International Journal for Numerical and Analytical Methods in Geomechanics*, 21(2):77–89.

Verruijt, A. and Booker, J. (1996). Surface settlements due to deformation of a tunnel in an elastic half plane. *Géotechnique*, 46(4):753–756.

Verruijt, A. and Booker, J. (1998). Discussion - Surface settlements due to deformation of a tunnel in an elastic half plane. *Géotechnique*, 48(5):709–713.

Verruijt, A. and Strack, O. (2008). Buoyancy of tunnels in soft soils. *Géotechnique*, 58(6):513–515.

Vesic, A. B. (1961). Bending of beams resting on isotropic elastic solid. *Journal of the Engineering Mechanics Division*, 87(EM2, Part 1):35–53.

Vorster, T. E. B., Klar, A., Soga, K., and Mair, R. J. (2005). Estimating the Effects of Tunneling on Existing Pipelines. *Journal of Geotechnical and Geoenviromental Engineering*, 131(11):1399–1410.

White, D., Take, W., and Bolton, M. (2003). Soil deformation measurement using particle image velocimetry (PIV) and photogrammetry. *Géotechnique*, 53(7):619–631.

Williamson, M. G. (2014). Tunnelling effects on bored piles in clay. *Ph.D. Thesis, Cambridge University*.

Xu, K. and Poulos, H. (2000). General elastic analysis of piles and pile groups. *International Journal for Numerical and Analytical Methods in Geomechanics*, 24(15):1109–1138.

Xu, K. J. and Poulos, H. G. (2001). 3-D elastic analysis of vertical piles subjected to "passive" loadings. *Computers and Geotechnics*, 28(2001):349–375.

Yoo, C. (2013). Interaction between tunneling and bridge foundation – A 3D numerical investigation. *Computers and Geotechnics*, 49(0):70–78.

Zhang, R., Zheng, J., Pu, H., and Zhang, L. (2011a). Analysis of excavation-induced responses of loaded pile foundations considering unloading effect. *Tunnelling and Underground Space Technology*, 26(2):320–335.

Zhang, R. J., Zheng, J. J., and Yu, S. (2013). Responses of piles subjected to excavation-induced vertical soil movement considering unloading effect and interfacial slip characteristics. *Tunnelling and Underground Space Technology*, 36:66–79.

Zhang, R. J., Zheng, J. J., Zhang, L. M., and Pu, H. F. (2011b). An analysis method for the influence of tunneling on adjacent loaded pile groups with rigid elevated caps. *International Journal for Numerical and Analytical Methods in Geomechanics*, 35(18):1949–1971.

Zhao, Y. (2008). In situ soil testing for foundation performance prediction. *Ph.D. Thesis, Cambridge University*.

Zhou, B. (2014). Tunnelling-induced ground displacements in sand. *Ph.D. Thesis, University of Nottingham*.

Zhou, B., Marshall, A. M., and Yu, H.-S. (2014). Effect of relative density on settlements above tunnels in sands. In *2014 GeoShanghai International Congress: Tunneling and Underground Construction*, volume 242 GSP, pages 96–105, Shanghai, China. American Society of Civil Engineers.

Appendix A

Empirical formulas for tunnelling-induced settlement troughs

Despite its use in previous research, a complete framework has not been provided to adopt modified Gaussian curves for settlement trough prediction. The modified Gaussian curve suggested by Vorster et al. (2005) is defined as

$$\begin{aligned} u_z &= u_{max}\frac{n}{(n-1)+\exp\left[\alpha\left(x/i\right)^2\right]} \\ n &= e^{\alpha}\frac{2\alpha-1}{2\alpha+1}+1 \end{aligned} \tag{A.1}$$

where $\alpha > 0$, $n > 0$ and $i \neq 0$ to guarantee the physical sense of the equation as a settlement trough. This curve has three degrees of freedom (α and i defining the shape and u_{max} defining the magnitude). In the empirical approaches of Marshall et al. (2012) and Section 4.3, the modified Gaussian curve shape was defined with the points $\left(x^*, \frac{1}{\sqrt{e}}u_{max}\right)$ and $\left(x^{**}, \frac{1}{2\sqrt{e}}u_{max}\right)$, where $\frac{1}{\sqrt{e}}u_{max}$ is the settlement corresponding to the inflection point of the standard Gaussian curve (i.e. if $n = 1$, $x^* = i$). x^* and x^{**} were related to the depth of interest, z, through

$$\begin{aligned} x^* &= K^*\left(z_t - z\right) \\ x^{**} &= K^{**}\left(z_t - z\right) \end{aligned} \tag{A.2}$$

where $K^* = f\left[C/D, I_d, z/z_t\right]$ and $K^{**} = f\left[C/D, I_d, z/z_t\right]$ (defined in Section 4.3 by Equations (4.6) and (4.9)). The settlement magnitude was determined in terms of soil volume loss, $V_{l,s}$, with Equation (4.12).

In this appendix, the degrees of freedom of the modified Gaussian curve (α, i, u_{max}) are related to the parameters of the empirical method (K^*, K^{**}, $V_{l,s}$) presented in Section 4.3. The set of equations necessary to estimate the three degrees of freedom from the empirical formulas is suggested. Finally, figures comparing experimental data and empirical predictions are displayed.

A.1 Shape parameters

The objective of this section is to define a relationship between the width parameters, K^* and K^{**}, and the two degrees of freedom of the settlement trough shape, α and i. From the definition of x^* and x^{**}, Marshall et al. (2012) showed that

$$\left(\frac{x^*}{i}\right)^2 = \frac{\ln\left[n\sqrt{e}-(n-1)\right]}{\alpha} \tag{A.3}$$

$$\left(\frac{x^{**}}{i}\right)^2 = \frac{\ln\left[2n\sqrt{e}-(n-1)\right]}{\alpha} \tag{A.4}$$

Combining these equations results in

$$\frac{\ln\left[2n\sqrt{e}-(n-1)\right]}{x^{**2}} = \frac{\ln\left[n\sqrt{e}-(n-1)\right]}{x^{*2}} \tag{A.5}$$

Considering Equations (A.2) and (A.5), the ratio between the width parameters, K^*/K^{**}, is related to the shape parameter n by

$$\left(\frac{K^*}{K^{**}}\right)^2 = \frac{\ln\left[n\sqrt{e}-(n-1)\right]}{\ln\left[2n\sqrt{e}-(n-1)\right]} \tag{A.6}$$

Equation (A.6), which relates $n = f[\alpha]$ and K^*/K^{**}, can be approximated with the following relationship

$$\alpha = 10^{-7}\exp\left[-17.5\left(\frac{K^*}{K^{**}}\right)^2 + 35.5\left(\frac{K^*}{K^{**}}\right)\right] - 0.12 \qquad \text{for}\left(\frac{K^*}{K^{**}}\right) = 0.53-0.75 \tag{A.7}$$

Note that $K^*/K^{**} = 0.53-0.75$ covers the typical range of $\alpha = 0.001-1$. The upper limit of $K^*/K^{**} = 0.75$ corresponds to $\alpha = 1.8$. The lower limit of K^*/K^{**} was obtained from

$$\lim_{n\to 0}\left(\frac{K^*}{K^{**}}\right)^2 = \lim_{n\to 0}\frac{\ln\left[n\sqrt{e}-(n-1)\right]}{\ln\left[2n\sqrt{e}-(n-1)\right]} = \frac{\sqrt{e}-1}{2\sqrt{e}-1} \tag{A.8}$$

Therefore, to guarantee $\alpha > 0$ and $n > 0$

$$\left(\frac{K^*}{K^{**}}\right) > \sqrt{\frac{\sqrt{e}-1}{2\sqrt{e}-1}} \approx 0.53 \tag{A.9}$$

From Equation (A.3), the inflection point offset is given by

$$i = \pm\sqrt{\frac{\alpha x^{*2}}{\ln\left[n\sqrt{e}-(n-1)\right]}} \tag{A.10}$$

A.2 Settlement trough magnitude

It was displayed by Marshall (2009) that

$$\begin{aligned} V_s &= u_{max} T i \\ T \approx \bar{T} &= \exp\left[1.699 + 0.522\alpha - 1.472\sqrt{\alpha}\right] \end{aligned} \tag{A.11}$$

Therefore, Equation (A.12) can be used to calculate u_{max} from $V_{l,s}$, i and α.

$$u_{max} = \frac{1}{\bar{T} i} \times \frac{V_{l,s} \pi R^2}{100} \tag{A.12}$$

A.3 Summary

To summarise, to estimate the degrees of freedom α, i, and u_{max} of Equation (A.1), the following set of equations can be used.

$$\begin{aligned} &K^* = f\left[C/D, I_d, z/z_t\right] \text{ from Equations (4.6) and (4.9)} \\ &K^{**} = f\left[C/D, I_d, z/z_t\right] \text{ from Equations (4.6) and (4.9)} \\ &\alpha = 10^{-7} \exp\left[-17.5\left(\frac{K^*}{K^{**}}\right)^2 + 35.5\left(\frac{K^*}{K^{**}}\right)\right] - 0.12 \\ &\frac{i}{z_t} = \pm\sqrt{\frac{\alpha\left(K^*\left(1 - z/z_t\right)\right)^2}{\ln\left[n\sqrt{e} - (n-1)\right]}} \\ &u_{max} = \frac{1}{\bar{T} i} \times \frac{V_{l,s} \pi R^2}{100} \\ &\bar{T} = \exp\left[1.699 + 0.522\alpha - 1.472\sqrt{\alpha}\right] \\ &V_{l,s} = f\left[C/D, I_d, z/z_t = 0\right] \text{ from Equation (4.12)} \end{aligned} \tag{A.13}$$

Note that the settlement trough can only be predicted at the surface because of the available expression to estimate $V_{l,s}$. Judgement based on data presented in Marshall et al. (2012) and Section 4.3 (see Figure 4.21) could be used to evaluate subsurface values of $V_{l,s}$.

The following figures (Figure A.1-A.5) compare settlement troughs measured during centrifuge tests for $I_d = 0.3$ and 0.9 and empirical predictions obtained with Equation (A.13). Despite the scatter between experimental data and modified Gaussian curves, Equation (A.13) capture part of the complex behaviour of tunnelling-induced settlements in sands than was not described by previous research.

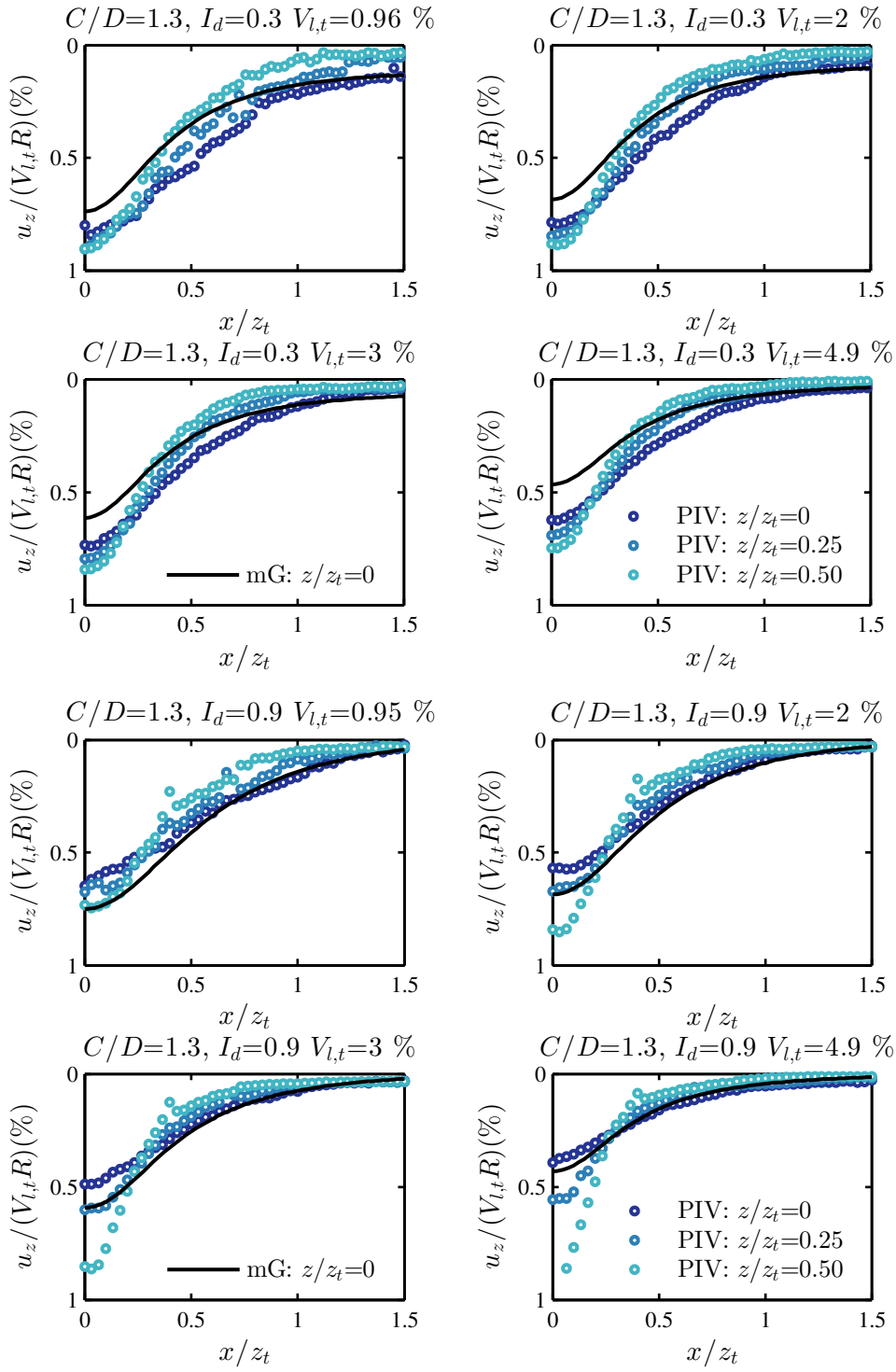

Fig. A.1 Settlement troughs for $C/D = 1.3$: comparison between GeoPIV data and empirical predictions.

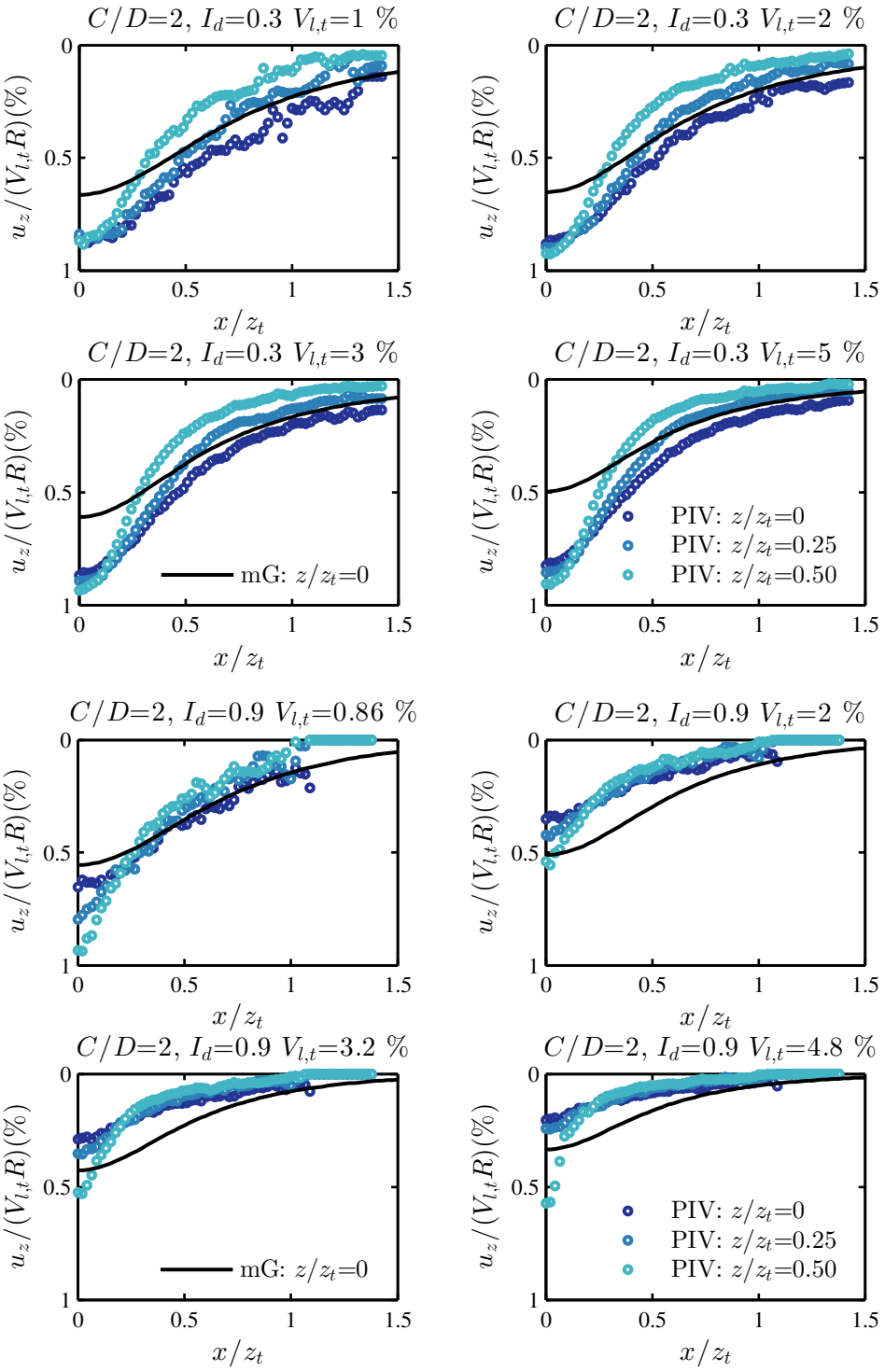

Fig. A.2 Settlement troughs for $C/D = 2.0$: comparison between GeoPIV data and empirical predictions.

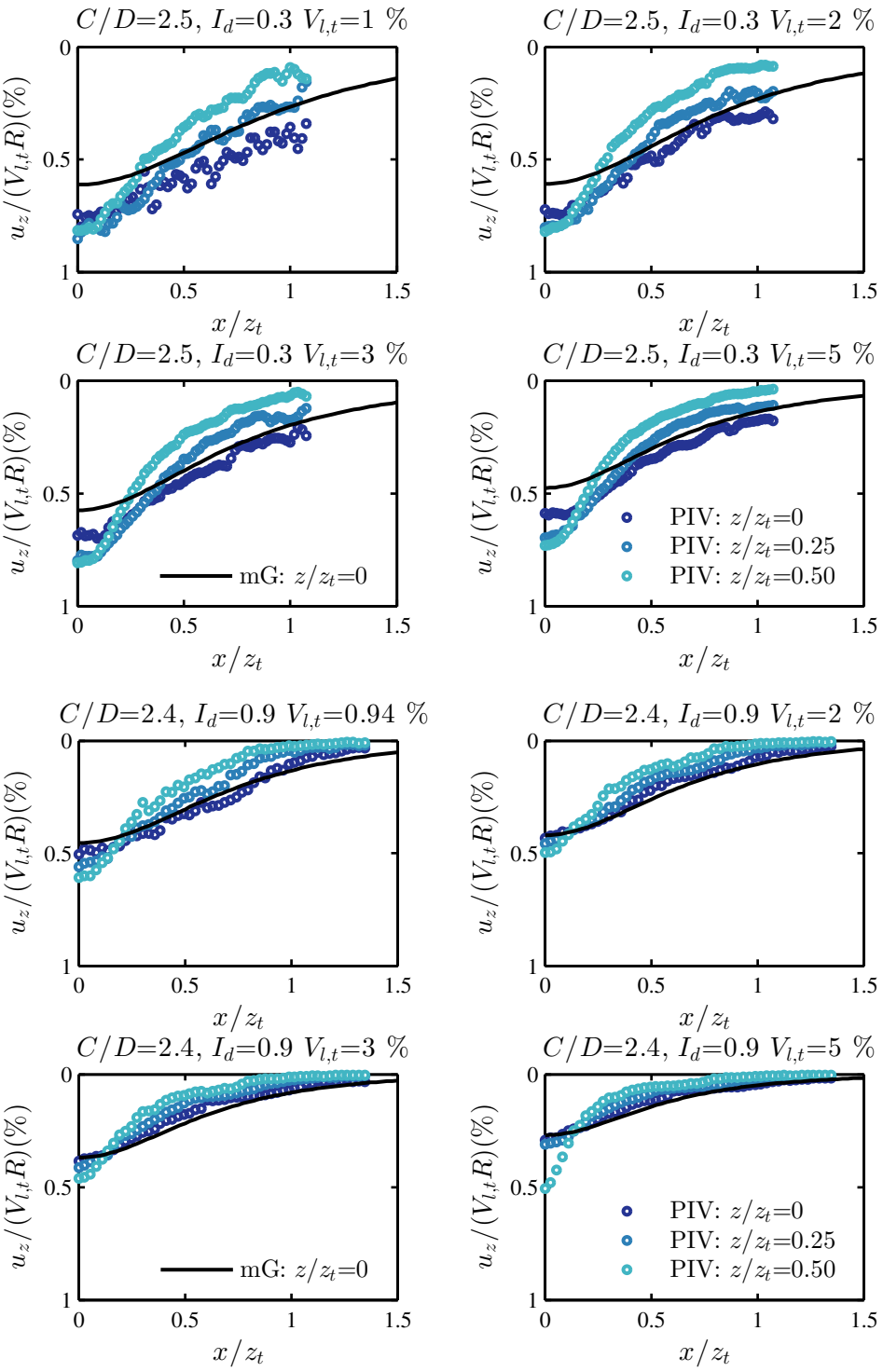

Fig. A.3 Settlement troughs for $C/D \approx 2.5$: comparison between GeoPIV data and empirical predictions.

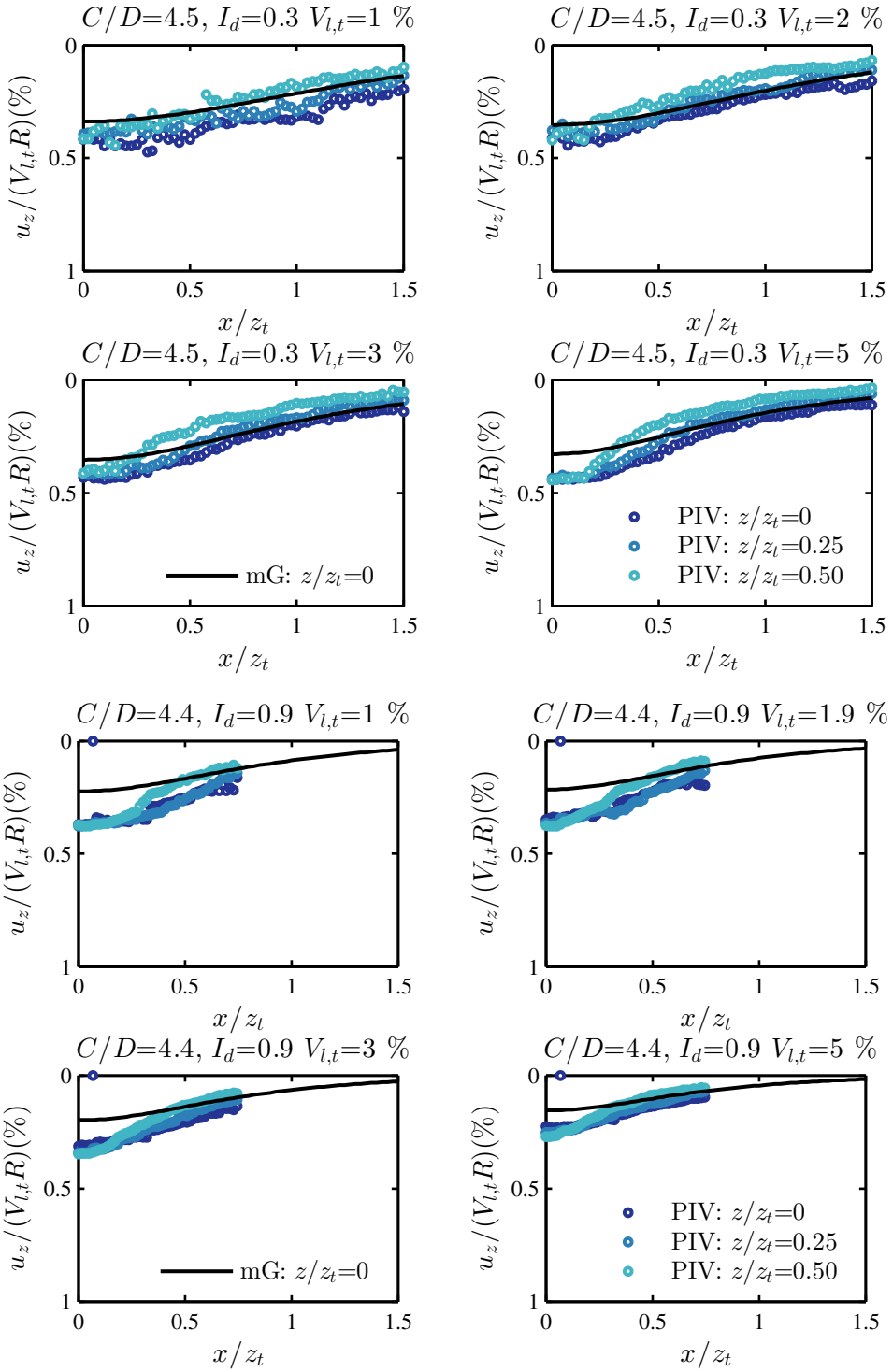

Fig. A.4 Settlement troughs for $C/D \approx 4.4$: comparison between GeoPIV data and empirical predictions.

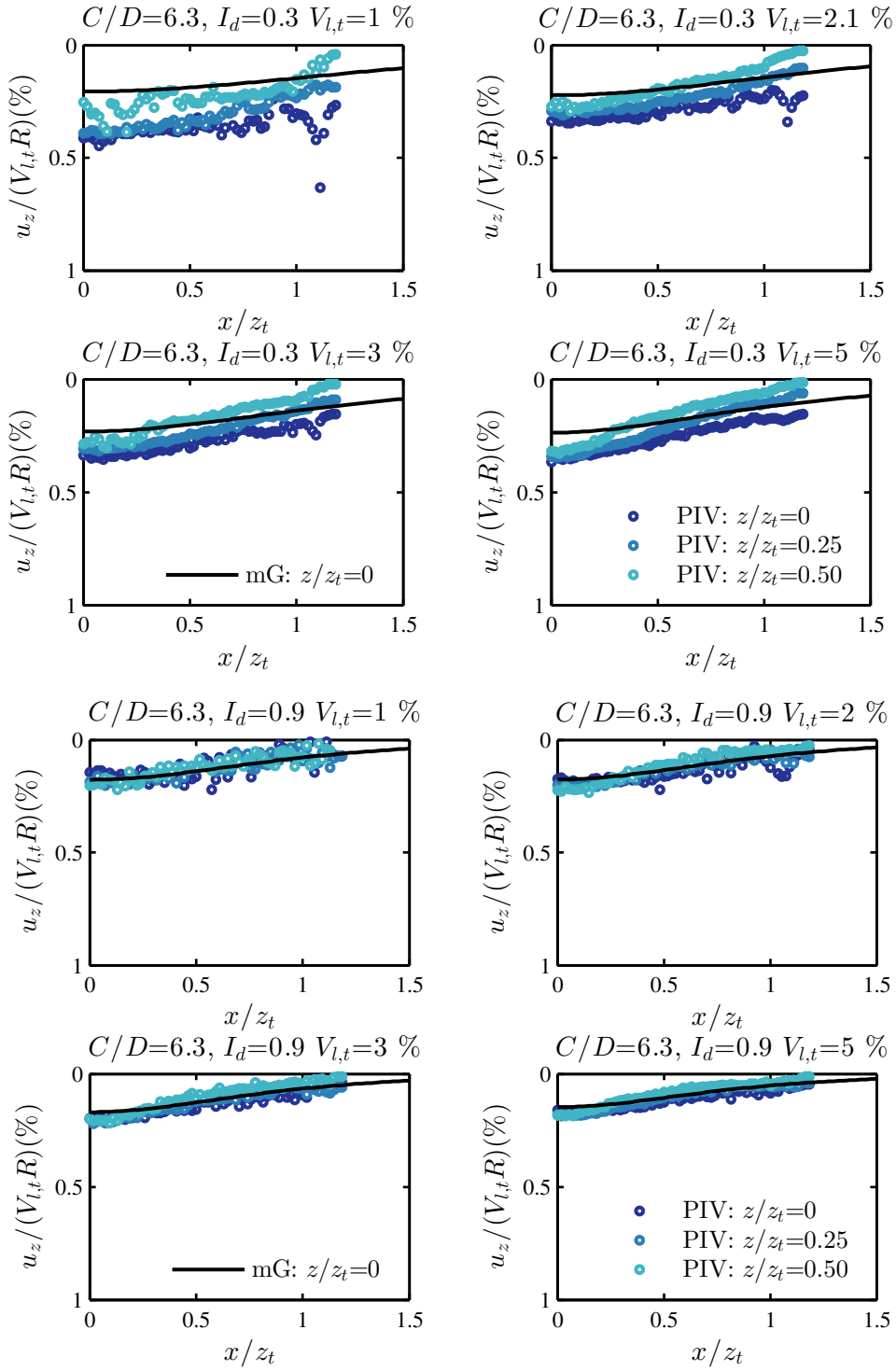

Fig. A.5 Settlement troughs for $C/D = 6.3$: comparison between GeoPIV data and empirical predictions.